

UNIVERSITAT POLITÈCNICA DE VALÈNCIA

DEPARTAMENTO DE COMUNICACIONES



UNIVERSITAT
POLITÈCNICA
DE VALÈNCIA



Doctoral Thesis

**Advanced Techniques for the Design
and Optimization of Multi-Band
and Reconfigurable Microwave
Waveguide Filters**

Juan Carlos Melgarejo Lermas

Julio 2021

Co-directors

Dr. Vicente E. Boria Esbert (Universitat Politècnica de València)

Dr. Santiago Cogollos Borrás (Universitat Politècnica de València)

Tesis Doctoral presentada al Departamento de Comunicaciones,
en el cumplimiento parcial de los requisitos para obtener:
Título de Doctor en Ingeniería de Telecomunicación
por la Universitat Politècnica de València

Fecha: 1 de julio de 2021, Valencia

Esta Tesis Doctoral ha contado con asesoría externa del Dr. Marco Guglielmi (ESA Retired Engineer).

Agradecimientos

Cuando me embarqué en este proyecto, desconocía la magnitud de la tarea que debía llevar a cabo, o la cantidad de obstáculos y dificultades que tendría que salvar. En este espacio, me gustaría dedicar unas palabras a todas aquellas personas sin las cuales no habría llegado hasta aquí.

En primer lugar, me gustaría agradecer a Marco, Santiago y Vicente por su inestimable ayuda y apoyo. Ha sido un verdadero placer aprender de y trabajar junto a vosotros. Me habéis enseñado a mantener la calma (y sangre fría) y afrontar los (no pocos) problemas que han surgido durante estos años. No podría haber pedido mejores mentores. Me llena de alegría poder compartir este momento con vosotros.

También me gustaría agradecer a todo el equipo de la Fundación la Caixa por esta oportunidad, por todos los seminarios y webinars, y especialmente, por haberme presentado al resto de doctorandos. Sois un grupo fantástico y me alegra mucho haber podido compartir tanto mis inquietudes como mis triunfos con vosotros.

Finalmente, quiero dar las gracias a mi familia, pareja y amigos por vuestro inquebrantable apoyo. Habéis compartido mis nervios, mis deadlines y mis quebraderos de cabeza. Me habéis ayudado a desconectar y disfrutar, incluso en los momentos de más presión. Jamás hubiese llegado hasta aquí sin vuestra ayuda. Va por vosotros.

Resumen

El creciente número de dispositivos intercambiando datos ha empujado a las empresas del sector espacial a utilizar bandas de frecuencia cada vez más altas, como Ku, K y Ka, ya que permiten emplear canales de frecuencia más anchos. A medida que disminuye la longitud de onda, el tamaño de los filtros se reduce y, por tanto, son más sensibles a las desviaciones de fabricación. Para compensar estos errores, es necesario emplear elementos de sintonía en la etapa de diseño.

En este contexto presentamos una estrategia de diseño que permite incluir todos los factores no ideales, como elementos de sintonía o esquinas redondeadas, en las simulaciones finales de filtros y multiplexores.

Una vez se han fabricado los filtros es necesario ajustar manualmente los elementos de sintonía hasta recuperar la respuesta objetivo. Sin embargo, para realizar esta tarea con éxito es necesario tener mucha experiencia previa y, aún así, conlleva un tiempo considerable. Por tanto, también proponemos un procedimiento de sintonización eficiente y sistemático que permite a cualquier persona, independientemente de su experiencia previa en sintonización, realizar esta tarea con éxito.

Además del aumento de las tasas de transmisión, otros desafíos del sector espacial son reducir el tamaño y peso de sus componentes, así como dotarlos de capacidad de reconfiguración. Emplear dispositivos multifunción como filtros multibanda o dispositivos reconfigurables es una posible solución. En este contexto, proponemos una nueva familia de filtros multibanda en guía de ondas que puede adaptarse a las futuras necesidades del sector espacial. Con el mismo objetivo, también proponemos una familia de dispositivos reconfigurables de varios estados discretos que pueden modificar su comportamiento de forma remota.

Resum

El creixent nombre de dispositius intercanviant dades ha empès a les empreses del sector espacial a utilitzar bandes de freqüència cada vegada més altes, com Ku, K i Ka, ja que permeten fer servir canals de freqüència més amples. A mesura que la longitud d'ona disminueix, la mida dels filtres es redueix i, per tant, són més sensibles a les desviacions de fabricació. Per compensar aquests errors, és necessari fer servir elements de sintonia en l'etapa de disseny.

En aquest context presentem una estratègia de disseny que permet incloure tots els factors no ideals, com a elements de sintonia o cantonades arrodonides, en les simulacions finals de filtres i multiplexors.

Una vegada s'han fabricat els filtres és necessari ajustar manualment els elements de sintonia fins a recuperar la resposta objectiu. Però, per realitzar aquesta tasca amb èxit és necessari tenir molta experiència prèvia i, així i tot, comporta un temps considerable. Per tant, també proposem un procediment de sintonització eficient i sistemàtic que permet a qualsevol persona, independentment de la seua experiència prèvia en sintonització, realitzar aquesta tasca amb èxit.

A més de l'augment de les taxes de transmissió, altres desafiaments de el sector espacial són reduir la mida i pes dels seus components, així com dotar-los de capacitat de reconfiguració. Emprar dispositius multifunció com filtres multibanda o dispositius reconfigurables és una possible solució. En aquest context, proposem una nova família de filtres multibanda en guia d'ones que pot adaptar-se a les futures necessitats del sector espacial. Amb el mateix objectiu, també proposem una família de dispositius reconfigurables de diversos estats discrets que poden modificar el seu comportament de forma remota.

Abstract

The need for ever increasing data rate of modern communication systems has motivated companies in the space sector to exploit higher frequency bands, such as Ku, K and Ka, in order to offer wider bandwidths to their customers. However, as the frequency increases, the wavelength decreases, and all waveguide hardware becomes smaller and more sensitive to deviations from the ideal dimensions that normally occur when manufacturing the devices. In order to compensate for these deviations (or errors), tuning elements must then be added to the hardware and included in the design process.

In this context, therefore, we focus on the investigation of novel design strategies for filters and multiplexers with the objective of including all necessary non-ideal factors in the design process.

It is important to note in this context that, once the filters are manufactured, the tuning elements are usually adjusted manually until the desired target performance has been achieved. However, successfully performing this task requires a considerable amount of time and very significant previous experience in tuning microwave filters. Consequently, an additional goal of our research work is to propose efficient and systematic tuning procedures so that anyone, regardless of their previous tuning experience, can successfully perform this difficult task.

In addition to the increasing data rates, another current challenge of advanced communication systems is the ability to be reconfigured remotely to adjust to changes in customer demands. The use of multi-function or reconfigurable devices is then an attractive possible solution. In this context, therefore, we also investigate new families of multi-band waveguide filters that can be used to accommodate several pass bands in the same filtering device. Furthermore, we also propose a new family of reconfigurable devices with several discrete states that can be easily controlled remotely.

Contents

Resumen	v
Resum	vii
Abstract	ix
Contents	1
Figure list	5
Table list	15
Acronyms	17
1 Introduction	19
1.1 Motivation	19
1.2 Objectives.	20
2 State of the Art	23
2.1 Basic filter design process	23
2.2 Space Mapping.	27
2.3 Filter tuning.	31
2.4 Multi-band filters	33

2.5 Reconfigurable filters	36
3 Efficient Microwave Filter Design Procedures Based on Aggressive Space Mapping	41
3.1 Efficient Implementation of OS ASM: the Step-by-Step ASM	42
3.1.1 One-Step ASM	42
3.1.2 Step-by-Step ASM	47
3.2 Design of a 6-pole inductive filter	50
3.2.1 One-Step ASM	51
3.2.2 Step-by-Step ASM	54
3.3 Design of a folded 6-pole filter with a cross-coupling	58
3.3.1 One-Step ASM	59
3.3.2 Step-by-Step ASM	63
3.4 Design of a folded 4-pole filter with a cross-coupling	68
3.4.1 One-Step ASM	68
3.4.2 Step-by-Step ASM	72
3.5 Design of a 5-pole filter based on dual-mode coaxial resonators	76
3.5.1 One-Step ASM	79
3.5.2 Step-by-Step ASM	79
3.6 Conclusions	84
4 On Aggressive Space Mapping Techniques for Filter Tuning	85
4.1 Experimental Setup	86
4.2 Tuning procedures	88
4.2.1 Procedure I	89
4.2.2 Procedure II	91
4.2.3 Procedure III	95
4.2.4 Procedure IV	100
4.2.5 Procedure V	102
4.3 Comparison between the different tuning methods	105
4.4 Recovery of the measured performance	106
4.5 Other possible <i>coarse</i> models	110
4.5.1 Using a waveguide <i>coarse</i> model	111
4.5.2 Using a <i>coarse</i> model based on transmission lines and inverters	114
4.6 Conclusions	117
5 Novel Folded Multi-Band Filters	119
5.1 Multi-band filters in a manifold configuration	120

5.2 Proposed topology	123
5.3 Specifications	123
5.4 Design of the independent channels.	125
5.4.1 Folded filters without TZs	125
5.4.2 Folded filters with TZs	129
5.5 Design of the tri-band filter	130
5.6 Practical considerations	136
5.6.1 Closing screws	136
5.6.2 Flanges	138
5.7 High-precision simulations	139
5.8 Experimental validation	141
5.8.1 CMM measurements of the filter	143
5.8.1.1 Combined analysis	143
5.8.1.2 Separate analysis	145
5.8.2 Measurements.	152
5.9 Conclusion	154
6 Reconfigurable Waveguide Components	155
6.1 Filter & Switch based on MTPs	156
6.2 Reconfigurable Waveguide Filters	161
6.3 Specifications and design procedure.	163
6.4 Design procedure for Filter A	164
6.5 Design procedure for Filter B	172
6.6 Experimental Validation	176
6.7 Reconfigurable Diplexer	176
6.7.1 Design procedure for the LA diplexer.	179
6.7.2 Design procedure for the HA diplexer	188
6.8 Experimental Validation	191
6.9 Conclusions	193
7 Conclusions and Future Work	197
7.1 Conclusions	197
7.2 Future work	199
A Manufacturing Plans with Solid Works	201
A.1 Filter example	201
A.2 General idea	203
A.3 3D plans	203

B Publications	215
B.1 Journal publications	215
B.2 Conference publications.	215
Bibliography	217

Figure list

2.1	Low-pass prototype implemented with inverters.	25
2.2	Band-pass filter implemented with inverters.	25
2.3	Distributed model with transmission lines and inverters.	25
2.4	Low accuracy waveguide model.	26
2.5	High accuracy waveguide filter that includes all the non-ideal manufacturing details.	27
2.6	Original Space Mapping method [1].	29
2.7	Circulator channel-dropping method	33
2.8	Equivalent circuit for a triple-mode resonator.	34
2.9	A tri-band HTS filter employing the triplexer concept.	34
2.10	Topology of the in-line tri-band filter.	35
2.11	Cavity with two movable end walls.	36
2.12	Using teflon rods to modify the performance of a waveguide filter.	37
2.13	Using non-resonating cavities as coupling windows.	38
2.14	MEMS-based tuning concept.	39
2.15	Filter & Switch.	39
3.1	Three-pole filter structure.	42
3.2	Aligned responses of the LA and HA models.	44

3.3	Three-pole filter structure with rounded corners.	45
3.4	Aligned responses of the LA (Fig. 3.1) and HA models (Fig. 3.3).	46
3.5	OS-ASM process to design the filter shown in Fig. 3.3	47
3.6	First tuple of the 3-pole filter	48
3.7	Performance of the reduced <i>fine</i> and <i>coarse</i> models after only one ASM iteration.	48
3.8	First two tuples of the 3-pole filter	49
3.9	Performance of the reduced <i>fine</i> and <i>coarse</i> models after only one ASM iteration.	49
3.10	Final model used for the 6-pole inductive filter.	51
3.11	<i>Coarse</i> model used for the 6-pole inductive filter.	51
3.12	Optimized performance of the <i>coarse</i> model and initial <i>fine</i> model's response.	52
3.13	Performance of the <i>fine</i> model after one iteration compared to the target response.	53
3.14	One-Step ASM process to fine tune the filter.	53
3.15	First tuple of elements of the 6-pole filter	54
3.16	Performance of the reduced <i>fine</i> and <i>coarse</i> models after only one ASM iteration.	55
3.17	First two tuples of the 6-pole filter	55
3.18	Performance of the second reduced <i>fine</i> and <i>coarse</i> models.	56
3.19	Performance of the <i>fine</i> model after duplicating half of the structure.	57
3.20	Measured performance of the 6-pole inductive filter compared to the target performance.	57
3.21	Final model for the 6-pole folded filter with a cross-coupling.	58
3.22	<i>Coarse</i> model used for the 6-pole waveguide filter with one cross-coupling.	60
3.23	Responses of the 6-pole filter in the first stage of the One-Step ASM process.	60
3.24	<i>Fine</i> model used for the second One-Step ASM stage.	61
3.25	Responses of the 6-pole filter in the second stage of the One-Step ASM process.	61

3.26 Responses of the 6-pole filter in the third stage of the One-Step ASM process.	62
3.27 First three of elements of the folded 6-pole filter.	63
3.28 Performance of the first reduced <i>fine</i> and <i>coarse</i> models.	64
3.29 Performance of the second reduced <i>fine</i> and <i>coarse</i> models.	64
3.30 Third reduced models used for the 6-pole folded filter.	65
3.31 Performance of the reduced <i>fine</i> and <i>coarse</i> models after only one ASM iteration.	65
3.32 Performance of the <i>fine</i> model after one ASM iteration.	66
3.33 Last ASM iteration considering all design parameters.	67
3.34 Measured performance of the 6-pole folded filter compared to its target performance.	67
3.35 Final model used for the 4-pole single-mode quadruplet filter.	69
3.36 Target performance for the 4-pole single-mode quadruplet filter.	69
3.37 <i>Coarse</i> model used for the 4-pole single-mode quadruplet filter.	70
3.38 Performance of the high precision model with sharp 90° corners after two ASM iterations.	71
3.39 Performance of the high precision model with round corners after five ASM iterations.	72
3.40 First three elements of the first reduced model for the quadruplet.	73
3.41 Performance of the reduced <i>fine</i> and <i>coarse</i> models after only one ASM iteration.	73
3.42 Reduced models used in the second stage of the design of the quadruplet.	74
3.43 Performance of the second reduced models one two iterations.	74
3.44 Performance of the high precision model compared to its target.	75
3.45 Initial model of the 5-pole filter with sharp 90° corners and without tuning elements.	76
3.46 Final model of the 5-pole filter with round corners and tuning elements.	77
3.47 Target performance for the 5-pole filter based on dual-mode coaxial resonators.	77
3.48 Dimensions that are optimized in the design process.	78

3.49	<i>Fine</i> model of the filter using tuning elements.	79
3.50	ASM process to recover the desired performance in the <i>fine</i> model that uses tuning elements.	80
3.51	ASM process to recover the desired performance in the <i>fine</i> model that includes tuning elements and rounded corners.	80
3.52	Second <i>coarse</i> model of the filter.	81
3.53	Second <i>fine</i> model of the filter.	81
3.54	First reduced model of the filter.	82
3.55	ASM process to recover the desired performance in the first reduced <i>fine</i> model.	82
3.56	ASM process to recover the desired performance in the second reduced <i>fine</i> model.	83
3.57	Final performance of the <i>fine</i> model compared to the design target. . .	83
4.1	6-Pole inductive filter with tuning elements.	87
4.2	Precision robotic arm that is used to modify the penetration of the tuning screws.	88
4.3	Performance of the filter when all tuning elements are set to the design depth.	89
4.4	Low precision model that includes tuning elements.	90
4.5	Procedure I: Filter performance after every ASM iteration.	91
4.6	Fast low precision model that does not include tuning elements.	92
4.7	High precision model that includes tuning elements and rounded corners.	92
4.8	Aligned performances of the <i>coarse</i> and <i>fine</i> models.	93
4.9	Procedure II: Filter performance after every ASM iteration.	95
4.10	Aligned performances of the models.	98
4.11	Performance of the high and low precision models after perturbing the first aperture by 0.1 mm.	99
4.12	Performance of the high and low precision models after perturbing the first cavity by 0.1 mm.	99
4.13	Procedure III: Filter's performance after every ASM iteration.	100

4.14	Procedure IV: Filter’s performance after every ASM iteration.	102
4.15	Fast LP model that does not include tuning elements.	103
4.16	Aligned performances of the <i>coarse</i> model and measured response.	103
4.17	Procedure V: Filter performance after every ASM iteration.	104
4.18	Starting point for all procedures.	105
4.19	Simplified tuning example.	106
4.20	Recovered performance with the <i>coarse</i> model.	107
4.21	Elements in the <i>coarse</i> model that are optimized in the process of re- covering the measured performance (darker color).	107
4.22	After one ASM iteration the filter is perfectly tuned.	108
4.23	Elements in the <i>coarse</i> model that are optimized in the process of re- covering the measured performance (darker color).	108
4.24	Recovered performance with both possible <i>coarse</i> models.	109
4.25	After the ASM iteration, two tuning elements are set at the wrong penetration.	109
4.26	Phase of the S11 parameter for both <i>coarse</i> models.	110
4.27	Waveguide 4-pole filter to be tuned.	111
4.28	Initial state of the filter. As we can see, it is very detuned.	112
4.29	Waveguide <i>coarse</i> model of the filter.	112
4.30	Low precision model of the filter that considers tuning elements.	113
4.31	Procedure IV using a waveguide-based <i>coarse</i> model.	113
4.32	<i>Coarse</i> model based on transmission lines and inverters.	114
4.33	Procedure IV using a distributed model.	115
4.34	Recovering the ‘measured’ performance with a distributed model.	116
4.35	Recovering the ‘measured’ performance with a waveguide-based <i>coarse</i> model.	116
5.1	Manifold-based multiplexer.	120
5.2	Manifold-based N-band filter.	121
5.3	Topology of the in-line tri-band.	121

5.4	Performance of the in-line tri-band.	122
5.5	Proposed topology for the filter channels.	124
5.6	Proposed topology for the tri-band filter.	125
5.7	In-line 6-pole filter.	126
5.8	Performance of the independent in-line filters.	127
5.9	Central aperture of the filters.	128
5.10	Folded filter without TZs.	128
5.11	Multipath coupling diagram for a 2-5 cross-coupling.	129
5.12	Performance of one of the channels for different cross-couplings.	130
5.13	Performance the independent channels.	131
5.14	Performance the independent channels with and without TZs.	131
5.15	First channel connected to a double manifold terminated in short circuits.	132
5.16	Performance obtained in the first stage of the design.	133
5.17	Structure after adding the second filter channel.	133
5.18	Performance obtained in the second stage of the design.	134
5.19	Structure after adding the third filter channel.	134
5.20	Performance obtained in the third stage of the design.	135
5.21	Performance of the low-precision model.	135
5.22	Closing M4 screws and pressure well.	136
5.23	Final structure after changing the central channel to the opposite side.	137
5.24	Performance of the low precision model after flipping the central channel.	137
5.25	Flanges for WR-75	138
5.26	Lateral vew of the tri-band filter.	138
5.27	Two H-plane bends have been added to the filter.	139
5.28	Yield analysis.	140
5.29	Final high-precision model.	140
5.30	<i>Coarse</i> and <i>fine</i> models of one of the filer channels.	141
5.31	Performance of the low and high-precision models for the second filter channel.	142

5.32	Performance of the high-precision model after adding the filter channels to the manifold.	142
5.33	Final performance of the high-precision model.	143
5.34	Body and cover of the tri-band filter.	144
5.35	CMM measurements of each filter channel.	145
5.36	Histogram of the errors.	146
5.37	Histogram for the Z errors.	147
5.38	Histogram for the X-Y errors.	148
5.39	Manufacturing deviations.	149
5.40	Threading direction.	150
5.41	Histogram of the positive X-Y errors.	151
5.42	Histogram of the positive X-Y errors (compensated).	151
5.43	Assembled filter fed with WR-75 waveguides.	152
5.44	Measured performance of the tri-band filter compared to the CST simulation.	153
5.45	Insertion loss of the filter compared to the simulated losses in CST. . .	153
6.1	Possible implementation of the Fiter & Switch.	156
6.2	Modified Tuning Pins.	157
6.3	Path P1-P2 of the F&S.	158
6.4	Path P1-P3 of the F&S.	159
6.5	Remote operation of the F&S.	160
6.6	Reconfigurable waveguide filter topology.	161
6.7	State selection with the MTPs.	162
6.8	Waveguide filter channel.	165
6.9	Performance of the independent filter channels.	165
6.10	Filter structure after performing Step 1.	166
6.11	Response of the filter after performing Step 1.	167
6.12	Filter structure after performing Step 2.	168

6.13	Response of the filter after performing Step 2.	169
6.14	Step 3: Set the MTPs of the second filter to the OFF state and add the third filter to the manifold.	169
6.15	Response of the filter after performing Step 3.	170
6.16	Performance of the LA filter.	170
6.17	Final high-precision model for Filter A.	171
6.18	Performance of the high-accuracy model of Filter A.	171
6.19	Proposed topology for Filter B.	172
6.20	Closing screws of Filter B.	173
6.21	LA model of Filter B for the second state.	174
6.22	Performance of the LA model for Filter B.	174
6.23	Performance of the HA model for Filter B.	175
6.24	Body and cover of Filter B. Both pieces have been manufactured in aluminum.	176
6.25	Measured performance of Filter B (State 1).	177
6.26	Measured performance of Filter B (State 2).	177
6.27	Measured performance of Filter B (State 3).	178
6.28	Reconfigurable diplexer.	178
6.29	Step 1: Design both diplexers independently.	180
6.30	Performance of the isolated diplexers. Top: State 1. Bottom: State 2.	181
6.31	Combination of the independent diplexers.	182
6.32	Performance of the 4-port device.	183
6.33	Combination of the common outputs of the branches (part 1).	184
6.34	Performance of the structure shown in Fig. 6.33 after a short optimization.	185
6.35	Combination of the common outputs of the branches (part 2).	186
6.36	Performance of the structure shown in Fig. 6.35 after a short optimization.	186
6.37	E-field at 11.8 GHz of Fig. 6.35.	187
6.38	Introducing an additional pin to short circuit the manifold eliminates the resonance at 11.8 GHz.	187

6.39	Performance of the structure shown in Fig. 6.38.	188
6.40	Low precision model of the reconfigurable diplexer.	189
6.41	Performance of LA reconfigurable diplexer. Top: State 1. Bottom: State 2.	190
6.42	High precision model for the reconfigurable diplexer (HA).	191
6.43	Performance of the HA reconfigurable diplexer (State 1)	192
6.44	Performance of the HA reconfigurable diplexer (State 2).	192
6.45	Reconfigurable diplexer already fed with WR-75 waveguides.	193
6.46	Measured performance of the reconfigurable diplexer (State 1).	194
6.47	Measured performance of the reconfigurable diplexer (State 2).	195
A.1	Folded 6-pole filter with a capacitive a cross-coupling.	202
A.2	Target performance for the filter.	202
A.3	Professional tuner.	203
A.4	Add cylinders on top of the tuning elements	204
A.5	Solid structure at the end of Step 3.	204
A.6	Add the box that contains the filter	205
A.7	Subtract the filter from the box.	206
A.8	Flanges for WR-75	206
A.9	Add additional rectangles to fit the standard flanges.	207
A.10	Add the M4 threaded holes.	207
A.11	Solid that includes standard WR-75 flanges.	208
A.12	Add the rest of the holes.	209
A.13	Separation of the solid in three pieces.	210
A.14	Body of the filter.	212
A.15	Covers of the filter.	213
A.16	Drawing for the top cover.	214

Table list

2.1	Performance specifications for the given filter.	24
3.1	Dimensions of the three-pole inductive filter (LA).	43
3.2	Dimensions of the three-pole inductive filter (HA).	43
3.3	Accuracy settings used for the 6-pole inductive filter.	50
3.4	Performance of both design methods for the in-line 6-pole waveguide filter.	58
3.5	Accuracy settings used for the folded 6-pole filter.	59
3.6	Performance of both design methods for the folded 6-pole waveguide filter with a capacitive cross-coupling.	68
3.7	Accuracy settings used for the 4-pole single-mode quadruplet filter.	70
3.8	Performance of both design methods for the quadruplet.	75
3.9	Accuracy settings used for the 5-pole filter based on dual-mode coaxial resonators.	78
3.10	Performance of both design methods for the 5-pole filter based on dual-mode coaxial resonators.	84
4.1	Performance of Procedure I.	90
4.2	Accuracy settings used for the 6-pole inductive filter.	92
4.3	Performance of Procedure II.	95
4.4	Performance of Procedure III.	98

4.5	Performance of Procedure IV.	101
4.6	Performance of Procedure V.	105
4.7	Comparison of the different tuning methods.	106
4.8	Performance of Procedure IV.	111
4.9	Performance of Procedure IV using a <i>coarse</i> model based on transmission lines and inverters.	114
5.1	Accuracy settings used for tri-band filter.	126
5.2	Parameters of the combined analysis.	143
5.3	Key parameters of the Z errors.	146
5.4	Key parameters of the X-Y errors	147
6.1	Accuracy settings used for Filters A and B.	164

Acronyms

ASM	Aggressive Space Mapping
BFGS	Broyden-Fletcher-Goldfarb-Shanno
CAD	Computer-Aided Design
CMM	Coordinate-Measuring Machine
CNC	Computer Numerical Control
CST	CST Microwave Studio
CWDM	Circular-Waveguide Dual-Mode Filter
EDM	Electrical Discharge Machining
EM	Electromagnetic
FEM	Finite Element Method
FEST3D	3D Full-Wave EM Software Tool
GGW	Groove Gap Waveguide
HA	High-Accuracy
HFSS	High-Frequency Structure Simulator
HP	High-Precision
HTS	High-Temperature Superconductor
IL	Insertion Loss
LA	Low-Accuracy

LP	Low-Precision
MEMS	Microelectromechanical Systems
MEN	Multimode Equivalent Network
ML	Machine Learning
MO	Microwave Office
MTP	Modified Tuning Pin
SM	Space Mapping
TZ	Transmission Zero
VNA	Vector Network Analyzer

Introduction

1.1 Motivation

Waveguide technology is especially suitable for transmitting signals in communication systems in which high power needs to be handled, and when low insertion losses are required. Furthermore, past experience has shown that waveguide technology is indeed the most appropriate for space applications, due to the extreme conditions that satellites must endure both in the launch phase and in the operational phase in the intended orbit.

Besides, the increasing demand for more advanced communication systems with wider channel bandwidths has recently motivated space companies to explore the use of higher frequency bands (such as Ku, K, and Ka) that can easily accommodate higher transmission rates [2].

However, the use of higher frequency bands poses a series of mechanical problems when manufacturing waveguide devices, in particular with respect to waveguide filters. It is, in fact, well known that as the frequency increases, the wavelength decreases, and the physical size of the components becomes smaller. The two major implications are that first, unwanted high power effects are more likely to appear [3, 4], and second, that the devices become much more sensitive to errors in the manufacturing processes, since the mechanical tolerances become significant with respect to the filters' size.

Manufacturing errors are usually compensated using tuning elements in the filter structure that need to be adjusted (or tuned) manually after the filter has been built. In an industrial context, the filters are designed without tuning elements and then, a

‘corrected’ version of the filters is manufactured. For example, in waveguide filters based on resonators coupled with inductive irises, the resonators are pre-shortened and the irises are pre-lengthened. This is an easy way to ensure that the target response can be recovered by inserting the tuning screws a certain (and unknown) amount. Though this is undeniably simple, this solution cannot always be used. It is therefore, necessary to develop novel filter design and tuning strategies that include the presence of the tuning elements from the very beginning of the filter design process.

Furthermore, manually tuning the filters after manufacturing is a time-consuming task that generally requires extensive previous experience. Although many computer-aided tools have indeed been developed to assist with the tuning process, tuning complex filters remains today a very specialized skill. A simplification of this task would therefore be very much appreciated.

A further consequence of the ever increasing demand for higher data rates is the need for reconfigurable payloads. Reconfigurable payloads are, in fact, a must in order to efficiently accommodate variable user needs. In this context, therefore, one possible solution that is investigated in this thesis is the development of multi-function devices, such multi-bandpass filters, or filters with a response that can be modified remotely.

1.2 Objectives

The main objective of this doctoral thesis is to provide solutions for the limitations described in the previous section. In particular, we will discuss:

- A filter design and optimization strategy that includes all non-ideal factors (tuning elements or round corners) in the final filter structure, so that we can obtain a high yield and low cost manufacturing process. The optimization strategy is based on the Space Mapping (SM) [1] and Aggressive Space Mapping (ASM) techniques [5]. The basis of SM is to use two simulation spaces: a fast but inaccurate model (*coarse* model) and a slow and precise one (*fine* model), and to combine them efficiently in order to get the best of these two worlds (or models). The benefit of the proposed technique is that all non-ideal factors can be considered in the final electromagnetic simulations without slowing down the whole design process.

The proposed optimization strategy has been applied to a variety of microwave filters and devices, from in-line inductive waveguide filters to more complex structures like filters based on dual-model coaxial resonators or multi-band filters. By using the proposed design strategy, the whole design process has been sped up by a factor of ten. The results of this part have been presented in [6].

- A novel systematic tuning procedure that can be successfully used also by inexperienced engineers. The proposed tuning procedure also exploits the computational advantages of SM and ASM. It has been proved that is possible to establish a mapping by simulation between a fast *coarse* model that does not include tuning elements and a *fine* model that does. Furthermore, we have shown that such mapping can be effectively used later on when the real filter is being tuned.

In order to demonstrate the benefits of the proposed procedure, an in-line 6-pole inductive filter has been tuned using several tuning methods. The results showed that a filter with these characteristics can be tuned by anyone in less than five minutes. The results of this part of the research have been presented in recognized international conferences and journals [7], [8].

- Flexible filter topologies for the design of multi-band filters. We have also developed a folded manifold configuration that can be used to easily design multi-band filters. The proposed filter topology is, in our opinion, the best approach to obtain complex and scalable multi-band filters. Since the manifold is folded, we can easily introduce cross-couplings in the filter channels we deem necessary. Furthermore, since the filter is based on a manifold, the same well-known optimization strategy discussed in [9] can be used in this case to obtain multi-band filters with as many bands as necessary.

We have validated the proposed topology by designing and measuring a waveguide tri-band filter with two transmission zeros (TZs) in each passband. The results have been published in [10].

- Novel topologies for microwave filters with discrete reconfigurable states that can be easily controlled remotely. We will extend the use of the Modified Tuning Pin (MTP) of the filter and switch shown in [11] to design a series of reconfigurable devices.

Using these MTPs, we have successfully designed two reconfigurable filters with three discrete states. Furthermore, we have also designed a novel diplexer with two selectable states. We have manufactured and measured the first prototypes with outstanding results.

The remarkable feature of these reconfigurable devices is that, while other approaches require bulky and expensive mechanical switches, the MTPs can be used to remotely select between the states with a few light-weight and low-cost servomotors.

State of the Art

After setting the general objectives of this doctoral thesis, it is important to examine what has already been published in the technical literature in the subjects under investigation. In this chapter, we will:

- Review the basic filter design process.
- Review two of the most powerful design techniques: Space Mapping (SM) and Aggressive Space Mapping (ASM).
- Provide some general guidelines on how to manually tune a microwave filter and review the Computer-Aided Design (CAD) techniques that have been used to facilitate this complex and time-consuming task.
- Examine the most commonly used techniques to design multi-band filters, and compare their advantages and disadvantages.
- Finally, we will describe some of the currently available solutions for implementing both continuously tunable and reconfigurable filters.

2.1 Basic filter design process

Microwave filters are normally designed in order to satisfy a list of specifications that define the desired filter performance. The specifications can be generally classified as follows:

- **Performance:** Central frequency of the filter, bandwidth, attenuation levels at different frequencies, group delay variation, insertion loss, power handling, etc.
- **Environment:** Microwave filters must perform in a system that is designed to func-

tion in a specific environment. For space applications, for instance, environmental specifications may include temperature variations, maximum vibrations, outgassing, high pressure conditions, etc.

- **Footprint:** A filter is normally a component of a more complex system. As a consequence, there can be some specifications (or restrictions) regarding the filter's footprint, size, maximum weight, type of input and output connections, etc.
- **Manufacturing:** Each manufacturing process has a unique set of features. For example, using milling will result in a filter structure with rounded concave corners because the cutting tool is cylindrical. This can have a major impact on the performance of the filter and, therefore, the presence of rounded corners must be included in the design of the filter. The final mechanical accuracy of the manufacturing process is also of key importance. If the mechanical accuracy is low, the filter design will also need to include the presence of tuning elements that are needed to compensate for the mechanical inaccuracy.

Table 2.1: Performance specifications for the given filter.

Central frequency (f_0)	11 GHz
Bandwidth (BW)	500 MHz
Return Loss	20 dB
Out-of-band Rejection at $f_0 \pm 600$ MHz	40 dB
Input/Output	WR-75
Material	Aluminum
TZs	No
Topology	Inline
Tuning Elements	$r = 1.6$ mm

To continue our discussion, however, we now assume that the system engineer, considering the whole communication system, has already chosen the topology, the material, and the input-output ports of the filter we need to design. Furthermore, the performance specifications that this filter needs to satisfy are shown in Table 2.1¹. In this context, therefore, a possible procedure that we can use to design this filter can be described as follows [12], [13]:

1. Find a mathematical transfer function (Chebyshev, elliptic, etc.) that complies with the specifications using the equivalent low-pass filter. In this particular case, a Chebyshev transfer function of order $N = 6$ is enough to comply with the specifications.

¹This hypothetical filter has been chosen as a simple example so that we can describe the common steps of any filter design procedure. The very same procedures are, in fact, valid and applicable also to other arbitrarily complex filter structures.

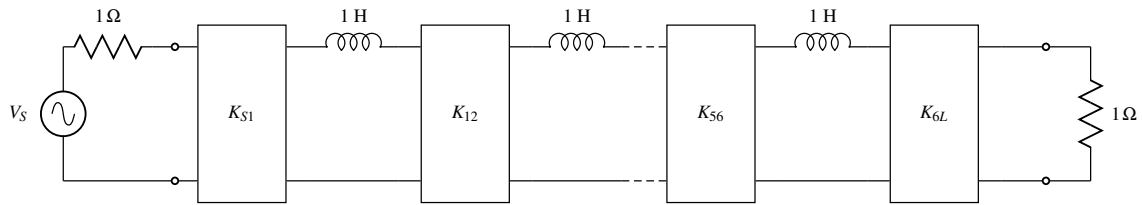


Figure 2.1: Low-pass prototype implemented with inverters.

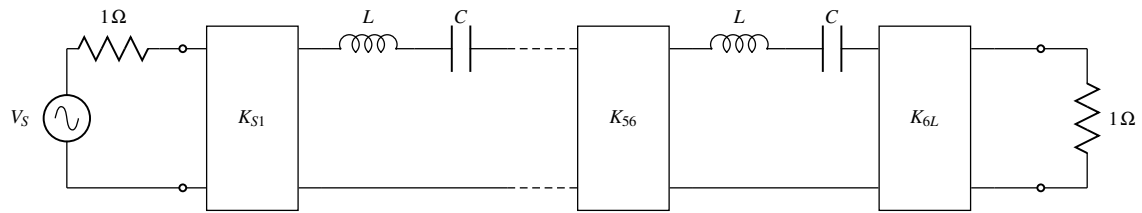


Figure 2.2: Band-pass filter implemented with inverters.

2. Obtain the lumped elements low-pass filter that provides the desired response using the known formulas given in [14], [15], for instance. Fig. 2.1 shows a possible circuit for the low-pass prototype using inverters and 1 H inductors.
3. Perform a frequency transformation to obtain the bandpass filter. Fig. 2.2 shows the transformed circuit.
4. Obtain a distributed model of the filter based on transmission lines and inverters. Fig. 2.3 shows the distributed model of the filter.
5. Optimize a fast, low precision waveguide model of the filter using, for instance, a Multimode Equivalent Network (MEN) simulator [16] until the desired performance is achieved. This model will not consider rounded corners or tuning elements in order to minimize the computation time. The resulting filter is shown in Fig. 2.4. This step can be performed using, for instance, the efficient procedure discussed in [17].

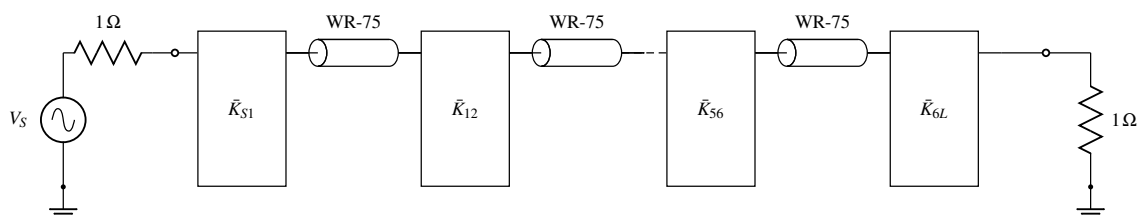


Figure 2.3: Distributed model with transmission lines and inverters.

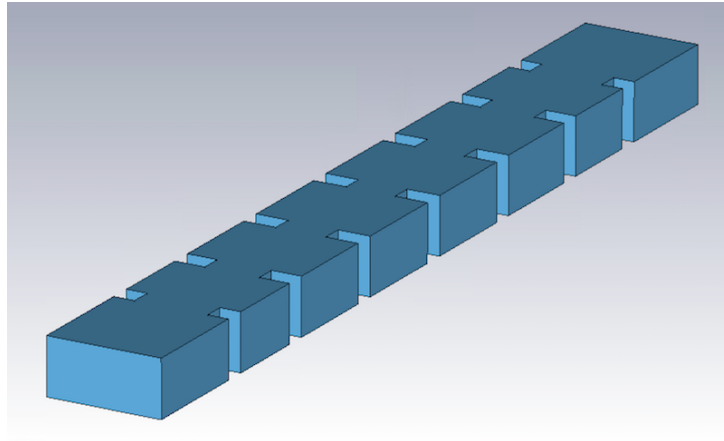


Figure 2.4: Low accuracy waveguide model.

Most CAD packages for designing microwave filters (such as Microwave Office (MO), 3D Full-Wave EM Software Tool (FEST3D), CST Microwave Studio (CST) or High-Frequency Structure Simulator (HFSS)) come with a built-in optimizer where we can select several optimization algorithms to obtain the target performance, like Gradient Descent, quasi-Newton algorithms like Broyden-Fletcher-Goldfarb-Shanno (BFGS), other non-gradient based approaches like Simplex Descent, or even nature-inspired optimization algorithms such as Simulated Annealing, Genetic or Bat Algorithms [18–20]. Since the procedure described in [17] only adjusts a few elements in each step, a gradient-based or a Simplex algorithm will perform very well.

6. Finally, use successive direct electromagnetic optimizations of increasing accuracy to obtain a high precision model that includes all the non-ideal manufacturing details, such as rounded corners and tuning elements, as shown in Fig. 2.5.

Of the steps just described, the most time consuming is Step 6. This is because a single Electromagnetic (EM) high precision simulation of a complex filter using a Finite Element Method (FEM) solver can take hours. Even if the performance of the initial model is relatively close to the desired one, the fine tuning of the filter via direct EM optimization can take days (or even weeks) to be completed. Naturally, the situation can be slightly better if we can use a more efficient high accuracy simulator like FEST3D. In any case, the direct EM optimization of a microwave filter structure is always a very time consuming task.

Fortunately, in 1994, Prof. John Bandler et al. proposed an elegant solution to the problem of direct EM optimization of complex structures, namely, Space Mapping (SM) [1].

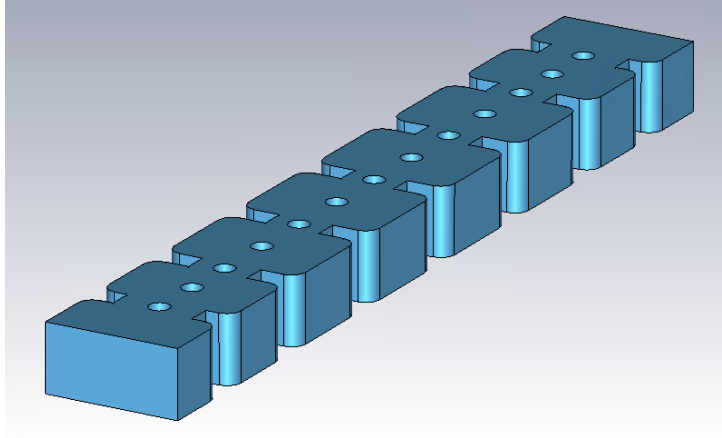


Figure 2.5: High accuracy waveguide filter that includes all the non-ideal manufacturing details.

2.2 Space Mapping

The basic idea behind SM is extremely simple. The method uses a fast, Low-Accuracy (LA) software simulator *or model*, called the *coarse model*, and High-Accuracy (HA), computationally time consuming software tool, which is called the *fine model*. In our previous example, the model shown in Fig. 2.4, or the circuit shown in Fig. 2.3, could be the *coarse model* and the one shown in Fig. 2.5 could be the *fine model*. The heart of SM is to combine the best features of both domains, namely, the low computation time of the *coarse model* and the precision of the *fine model*.

Suppose we are at the end of Step 5 of the filter design procedure we just described. At this point, we already have the optimal dimensions of our *coarse model*, namely, the $N \times 1$ vector \mathbf{x}_{copt} that contains the values of all the dimensions of the filter structure. Suppose now that we call $R_c(\mathbf{x}_{\text{copt}})$ the simulated response of our *coarse model*. Let us also assume that the starting point for the *fine model* is the $N \times 1$ vector $\mathbf{x}_{\mathbf{f1}}$ and that the performance of the *fine model*, given by $R_f(\mathbf{x}_{\mathbf{f1}})$, is far from the desired performance. In mathematical terms we can write $|R_f(\mathbf{x}_{\mathbf{f1}}) - R_c(\mathbf{x}_{\text{copt}})| > \epsilon$ where ϵ is a prearranged small number. Finally, and this is the power of SM, let us also assume that the dimensions of both spaces can be linked with the following linear mapping:

$$\mathbf{x}_c = \mathbf{B} \cdot \mathbf{x}_f + \mathbf{C}, \quad (2.1)$$

where \mathbf{B} is an $N \times N$ matrix and \mathbf{C} is an $N \times 1$ vector. The question is: how do we obtain the optimal dimensions of the *fine model* with the minimum number of evaluations of the *fine model*? The answer to this question is what SM is all about. The SM procedure can be described as follows:

1. Optimize the *coarse* model until the initial (detuned) performance of the *fine* model is matched, or equivalently, find \mathbf{x}_{c1} so that $|R_f(\mathbf{x}_{f1}) - R_c(\mathbf{x}_{c1})| \ll \epsilon$.
2. Slightly perturb the *fine* model around \mathbf{x}_{f1} to obtain a set of m points in the *fine* domain (usually, $m \geq N$). The set of *fine* model points can be written as:

$$S_f = \{\mathbf{x}_{f1}, \mathbf{x}_{f2}, \dots, \mathbf{x}_{fm}\} \quad (2.2)$$

3. Optimize the *coarse* model until the performance of the m points of *fine* model are matched ($|R_f(\mathbf{x}_{fi}) - R_c(\mathbf{x}_{ci})| \ll \epsilon$). The set of *coarse* model points can be written as:

$$S_c = \{\mathbf{x}_{c1}, \mathbf{x}_{c2}, \dots, \mathbf{x}_{cm}\} \quad (2.3)$$

4. When we have m pairs of points, we can rewrite the system in eq. (2.1) as:

$$\begin{bmatrix} \mathbf{x}_{c1} & \mathbf{x}_{c2} & \dots & \mathbf{x}_{cm} \end{bmatrix} = [\mathbf{C}^{(1)} \quad \mathbf{B}^{(1)}] \begin{bmatrix} 1 & 1 & \dots & 1 \\ \mathbf{x}_{f1} & \mathbf{x}_{f2} & \dots & \mathbf{x}_{fm} \end{bmatrix} \quad (2.4)$$

5. Obtain the least-squares solution [21] for $\mathbf{C}^{(1)}$ and $\mathbf{B}^{(1)}$.
6. Obtain the next *fine* point as:

$$\mathbf{x}_{fm+1} = \mathbf{B}^{(1)-1}(\mathbf{x}_{copt} - \mathbf{C}^{(1)}) \quad (2.5)$$

7. If the new *fine* model performance does not match the desired response, optimize another instance of the *coarse* mode until the performance of the new *fine* model is again recovered:

$$|R_f(\mathbf{x}_{fm+1}) - R_c(\mathbf{x}_{cm+1})| \ll \epsilon \quad (2.6)$$

8. Add \mathbf{x}_{cm+1} and \mathbf{x}_{fm+1} to the system in eq. (2.4) and obtain the least-squares solution for $\mathbf{C}^{(2)}$ and $\mathbf{B}^{(2)}$.
9. Obtain the next *fine* model point as:

$$\mathbf{x}_{fm+2} = \mathbf{B}^{(2)-1}(\mathbf{x}_{copt} - \mathbf{C}^{(2)}) \quad (2.7)$$

10. Repeat the steps 7-9 until the desired performance is achieved for the *fine* model.

The beauty of SM is that the linear mapping between the domains is obtained with a very low number of simulations in the time-consuming high precision model. As an example, for an inductive waveguide filter of order 6, we may need to perform hundreds of simulations in the *coarse* model, however we will only need to simulate the high precision model 10 or 15 times. Fig. 2.6 shows a graphic view of the original SM method.

The SM procedure we just described assumes that there is a linear mapping between

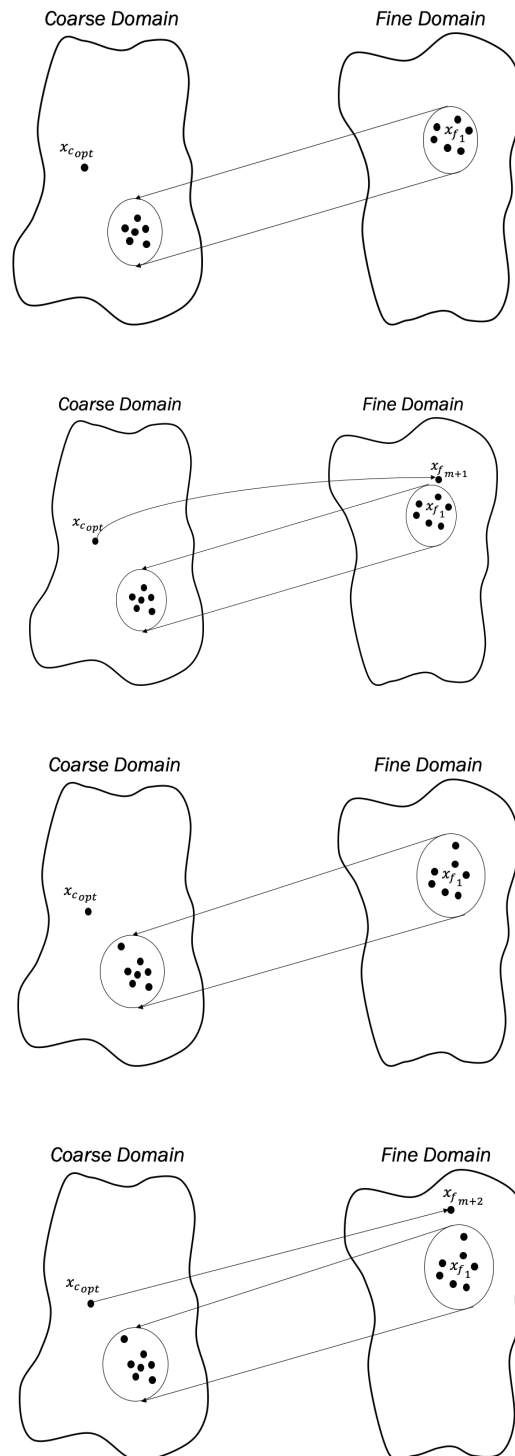


Figure 2.6: Original Space Mapping method [1].

the coarse and the fine domains, however, that is not always the case. If the initial performance of the *fine* model is highly detuned, SM may have problems in converging to the desired solution.

An improved SM strategy, the so-called Aggressive Space Mapping (ASM), was introduced in [22], [5]. ASM is, essentially, a reformulation of the original SM problem so that a Quasi-Newton optimization method can be applied. The goal of ASM is to find \mathbf{x}_f so that:

$$\mathbf{F}(\mathbf{x}_f) = P(\mathbf{x}_f) - \mathbf{x}_{\text{copt}} = \mathbf{0}, \quad (2.8)$$

where the mapping $P(\mathbf{x}_f) = \mathbf{x}_c$ is obtained optimizing the *coarse* model so that $R_c(\mathbf{x}_c) = R_f(\mathbf{x}_f)$.

If we expand $\mathbf{F}(\mathbf{x}_f)$ around the initial point (\mathbf{x}_{fi}) using a one-term Taylor expansion, we obtain that:

$$\mathbf{F}(\mathbf{x}_{fi} + \Delta) \approx \mathbf{F}(\mathbf{x}_{fi}) + \mathbf{J}(\mathbf{x}_{fi})\Delta, \quad (2.9)$$

where $\mathbf{J}(\mathbf{x}_{fi})$ is the Jacobian of \mathbf{F} evaluated at \mathbf{x}_{fi} . The goal is to find the value of Δ so that $\mathbf{F}(\mathbf{x}_{fi} + \Delta) = \mathbf{0}$:

$$\mathbf{0} = \mathbf{F}(\mathbf{x}_{fi}) + \mathbf{J}(\mathbf{x}_{fi})\Delta \quad (2.10)$$

$$\mathbf{J}(\mathbf{x}_{fi})\Delta = -\mathbf{F}(\mathbf{x}_{fi}) \quad (2.11)$$

$$\Delta = -\mathbf{J}(\mathbf{x}_{fi})^{-1}\mathbf{F}(\mathbf{x}_{fi}) \quad (2.12)$$

And therefore, the next *fine* model evaluation must be:

$$\mathbf{x}_{fi+1} = \mathbf{x}_{fi} + \Delta = \mathbf{x}_{fi} - \mathbf{J}(\mathbf{x}_{fi})^{-1}\mathbf{F}(\mathbf{x}_{fi}) = \mathbf{x}_{fi} - \mathbf{J}(\mathbf{x}_{fi})^{-1}(\mathbf{x}_{ci} - \mathbf{x}_{\text{copt}}) \quad (2.13)$$

Instead of estimating the Jacobian by finite differences, the method starts using the identity matrix (\mathbf{I}) as the initial point. The Jacobian is then updated after every iteration using the well-known Broyden formula [23]. It is important to note that if the relation between the spaces is linear:

$$P(\mathbf{x}_f) = \mathbf{B} \cdot \mathbf{x}_f + \mathbf{C}, \quad (2.14)$$

then the Jacobian of (2.8) is, indeed, equal to \mathbf{B} .

$$\mathbf{J}(\mathbf{x}_f) = \frac{\partial \mathbf{F}(\mathbf{x}_f)}{\partial \mathbf{x}_f} = \frac{\partial (P(\mathbf{x}_f) - \mathbf{x}_{\text{copt}})}{\partial \mathbf{x}_f} = \mathbf{B} \quad (2.15)$$

Due to the extreme simplicity, and the power clearly demonstrated in many cases, the ASM has been extensively used by many engineers and researchers. There are indeed countless filters in the literature that have been designed using an ASM-based procedure. As an example, in [24] and [25], ASM was used to design inductive waveguide filters manufactured with rounded corners. Furthermore, ASM has also been used to design multiplexers based on dielectric resonators [26]. ASM has also been used to correct the manufacturing deviations in circular-waveguide dual-mode filters [27, 28]. A great summary can be found in [29] and in [30], where the development of ASM has been tracked in the last 20 years.

During the last few years, researchers have focused their attention on reducing the number of iterations the original ASM method described in [22] requires. A significant effort has been devoted to improve the parameter estimation to achieve a faster convergence [31–33].

Recently, in [34] and [35], it was demonstrated that for resonant structures, an ASM based design procedure may converge to the desired target performance in *just one step*, independently of the number of variables involved in the optimization process (One-Step ASM). Even though this last method has proved to be very effective for simple designs, the efficiency of this approach decreases with the complexity of the filters. Specifically, this method fails when the initial starting point is far from the target performance or when the specifications of the filters are very demanding. In Chapter 3 of this thesis, we will introduce a powerful and robust ASM-based design procedure that provides exceptional results in these situations.

2.3 Filter tuning

As already mentioned in the introduction, every manufacturing process has specific limits for the dimensional accuracy that it can deliver. A very high precision technique, such as Electrical Discharge Machining (EDM), is able to manufacture pieces with an accuracy of a few microns (0.5 - 10 μm). Standard *milling*, on the other hand, may produce errors between 10 and 200 μm . Without a specific analysis, it is difficult to decide what level of error can be tolerated by a given filter. For instance, a 15 μm deviation in any of the filters that are discussed in this thesis would have a massive impact on their performance. So, how should we proceed? There are two options:

1. Use the most accurate, and normally, most expensive manufacturing technique available [36].
2. Use a less accurate technique and add tuning elements to the filter, so that manufacturing errors can be compensated by *manually tuning* the filter.

Minimizing the costs is usually a must in the industrial production of microwave filters, and thus, using a medium precision manufacturing technique along with tuning elements is the most commonly used strategy to reduce the manufacturing cost of a filter [12], [37].

However, it is important to remember that manually tuning a filter after it has been manufactured is a complex task that, in most cases, requires a significant amount of time and expertise [38]. There are, indeed, some guidelines in the technical literature on how to perform this task [39, 40], namely:

1. Adjust the tuning elements of the resonators. After this step, all cavities should be resonating at the central frequency of the filter.
2. Adjust the in-line couplings and try to balance the S11 response of the filter.
3. Finally, adjust the cross-couplings.
4. Repeat these steps until convergence.

Despite these guidelines, the filter tuning process still remains a cumbersome task for a novice tuner. For that reason, there are many computer-aided tools that have been designed to help us with this task. Fuzzy logic was used in [41–43] to tune microwave filters. Machine Learning (ML) techniques have also been developed to automatize the tuning stage [44–47]. Other CAD techniques, like pattern search optimization [48] or particle swarm optimization [49] have also been used for tuning purposes.

In the last decade, Space Mapping (SM) and its aggressive variant (ASM) have also been successfully used for tuning microwave filters. For example, ASM was applied in [50] to tune a varactor-based combline microstrip filter. Another example is [51], where ASM was used to tune a four-pole inductive waveguide filter. Even though these ASM-based approaches are very promising, they all have the same problem: either the mapping matrix is estimated by finite differences at a very detuned initial point or not estimated at all, which means that many ASM iterations are needed to tune the filter.

In Chapter 4, we will show how we can take advantage of different simulation models to obtain a high quality mapping matrix that does not need to be updated, hence considerably speeding up the whole tuning process.

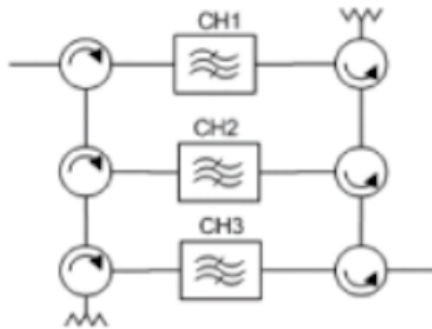


Figure 2.7: Circulator channel-dropping method. Fig. 1 (a) from [54].

2.4 Multi-band filters

The next technical subject discussed in this thesis is the design of filters that exhibit more than one pass-band (*multi-band*) with a single waveguide structure. Multi-band filters are an attractive approach to the implementation of complex satellite payloads [52, 53]. A number of non-contiguous channels may be amplified at once and sent through the same satellite beam to cover a specific area. Consequently, multi-band filters are required to reject the interleaving channels.

The most common approaches to design multi-band filters are described in [54]. The first possible solution is to use circulators to add or drop the channels as shown in Fig. 2.7. Thanks to the circulators, the filters are completely isolated, which makes their design extremely simple and modular. The disadvantages are the cost, insertion loss (IL) and weight of the filter.

Another common approach is to cascade a bandpass filter and one (ore more) band-stop filter(s) [55]. The advantages are the same as in the previous case, the design is simple and modular. However, this approach requires a large footprint.

We can also use in-band transmission zeros (TZs) to divide a high order bandpass filter in several lower order channels [56–58]. The footprint of this approach is not as large as the ones from the previous solutions. However, if a wide separation between the channels is required, this solution is not an option because the coupling levels usually tend to be too large to be realized physically.

One of the most attractive approaches is to use resonators with multiple modes. This approach provides the most compact solution. There are many examples in the literature of dual and triple-mode resonators that have been used to implement multi-band filters. Fig. 2.8 shows the equivalent circuit of the triple-mode resonator used in [54] and [59] to design tri-band filters. In [60] and [61], for instance, a triple-conductor combline

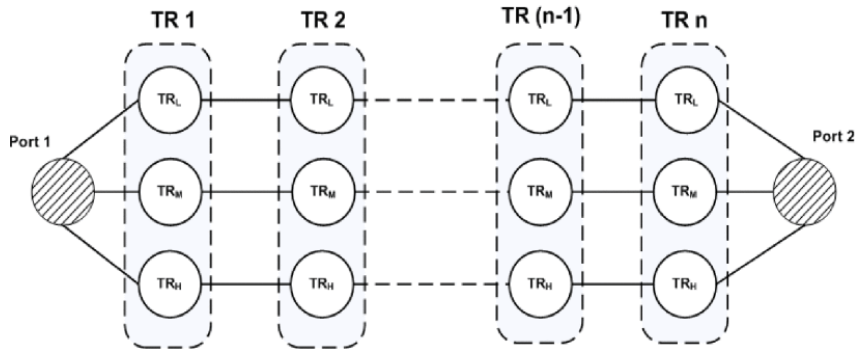


Figure 2.8: Equivalent circuit for a triple-mode resonator. TR stands for triple-mode resonator (Fig. 2 from [54]).

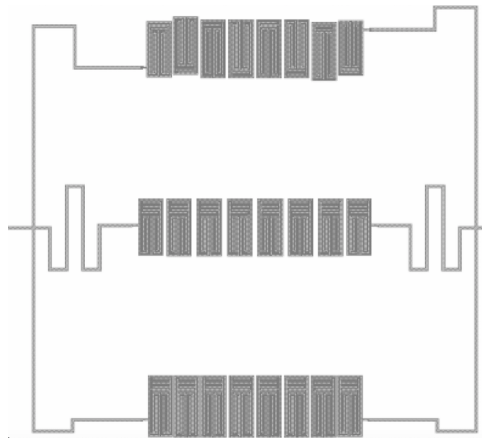


Figure 2.9: A tri-band HTS filter employing the triplexer concept (Fig. 2 of [65]).

resonator was used to implement dual-band filters. A dual-mode filter structure was also used to generate a dual-band filter in [62]. In [63], a new class of dual-band filters and diplexers, based on dual-band resonators was also discussed. Finally, a novel configuration of dual-band filters using side-coupled elliptical cavity resonators was reported in [64]. Although this approach seems very appealing, there is a major drawback: the difficulty of implementing transmission zeros (TZs). Even though TZs have been introduced in standard dual-mode filters with simple cross couplings [64], the same procedure has not been demonstrated for multiple-mode resonator implementations of multi-band filters [54].

The last approach consists on using ordinary filters and to combine their inputs and outputs to generate multi-band filters. There are, indeed, many multi-band filters in planar technology that have been designed with this approach [65]. Fig. 2.9 shows a tri-band HTS filter that was designed with this approach.

Even though this last approach provides the best behavior in terms of insertion

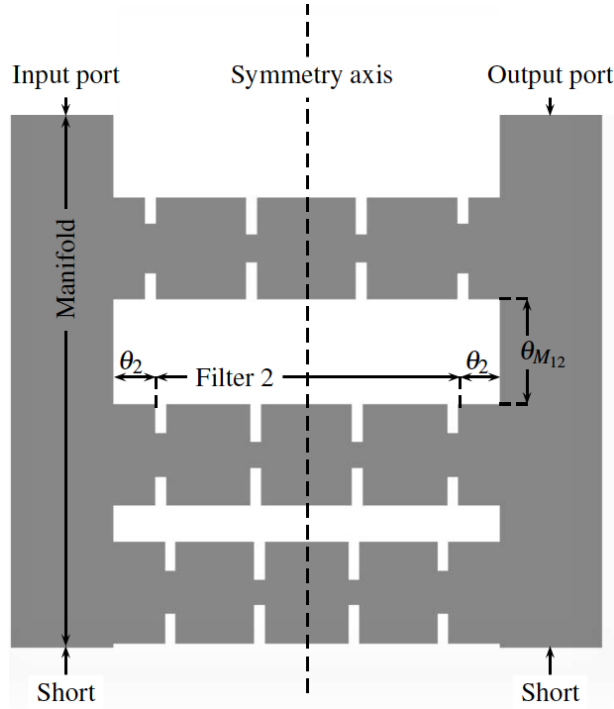


Figure 2.10: Topology of the tri-band filter designed in [66].

loss and group delay, it is specially challenging for waveguide filters (since waveguides are not as malleable as microstrip transmission lines). Recently in [66], it was shown that the well-known multiplexer design technique described in [9] could be used to design multi-band filters in a manifold configuration. It was demonstrated how three independent filters could be combined using a double manifold to implement multi-band filters (see Fig. 2.10). The disadvantages of this approach are that it is not possible to produce in-band transmission zeros and that the sizes of each of the filter channels must be comparable.

In Chapter 5, we will show a novel topology based on a double manifold and folded filters that overcomes all of the limitations mentioned above: it is possible to easily produce in-band transmission zeros, and the order of the filter channels can be as different as necessary. We believe that the topology we propose provides the best performance in terms of flexibility and scalability.

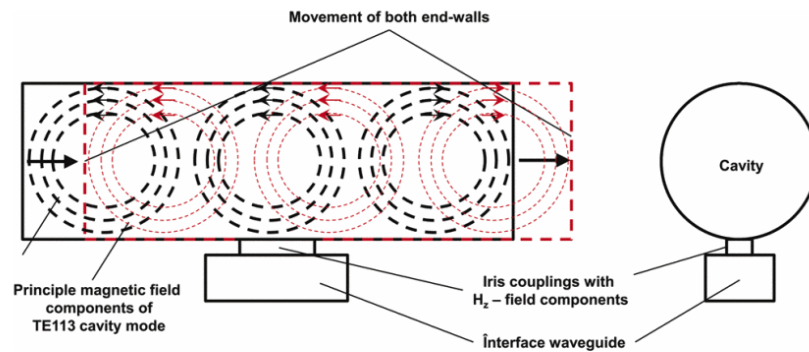


Figure 2.11: Cavity with two movable end walls (Fig. 1 of [69]).

2.5 Reconfigurable filters

Modern communication payloads are currently evolving toward systems that can provide reconfigurable channels to adapt to variable customer demand. New tunable or reconfigurable filter structures are therefore of great interest and have been extensively researched.

One possibility to obtain continuously tunable filters is by changing the size of the cavities. This has, in fact, been demonstrated in [67, 68], where they used two movable cavity end walls to change the effective width of a resonant cavity as shown in Fig. 2.11. In [69], the same approach was used to obtain a reconfigurable output multiplexer.

Another popular approach to design reconfigurable filters is to use metallic or dielectric screws (or *perturbations*) to modify the electric field of a fixed resonator. In [70], for instance, the maximum tuning range of filters in circular and rectangular waveguide technology was explored using metallic screws. Furthermore, the tuning range of a waveguide inductive filter was also studied using teflon rods [71]. Both [70] and [71] use tuning elements both in the cavities and in the coupling apertures to change both the filter center frequency, and the coupling levels (as shown in Fig. 2.12).

Instead of using classic coupling windows, a possible alternative is to use non-resonating cavities [72], [73] (see Fig. 2.13). The resonant frequencies of these cavities are outside of the filter range and thus, they act as impedance inverters. In this context, an extensive review of tuning techniques has been recently discussed in [74].

The last common implementation of flexible input/output networks in communication payloads is to combine mechanical switches with microwave filters [12]. The switches are mostly based on rotary systems [75] or use semiconductor technology or MEMS (microelectromechanical systems) [76]. In [77], RF-MEMS cantilever switches were used to

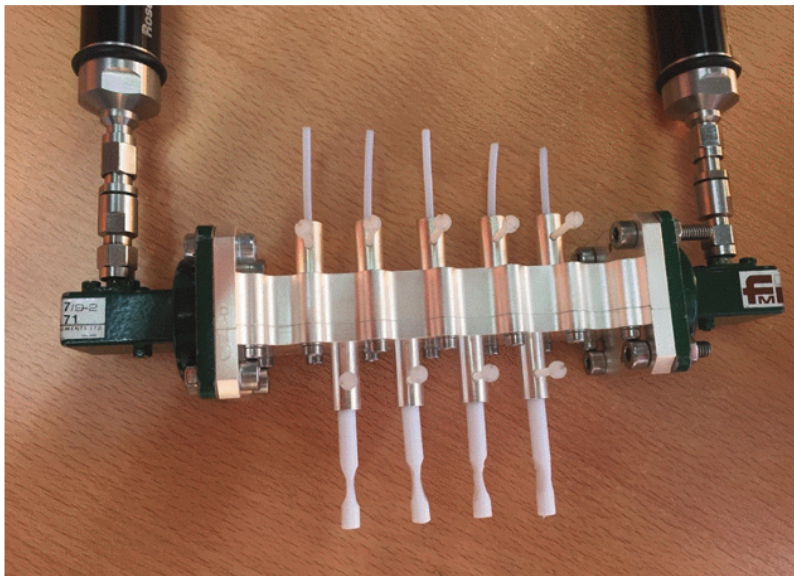
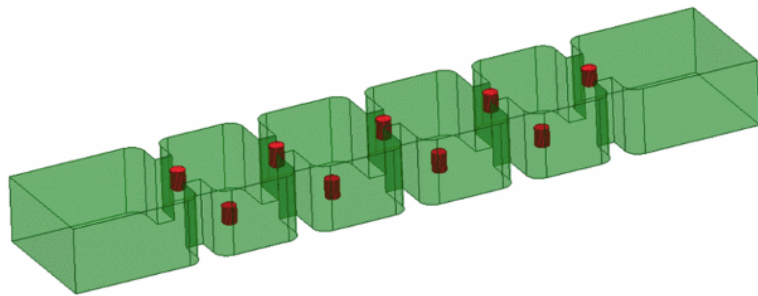


Figure 2.12: Using teflon rods to modify the performance of a waveguide filter (Figs. 1 and 11 from [71]).

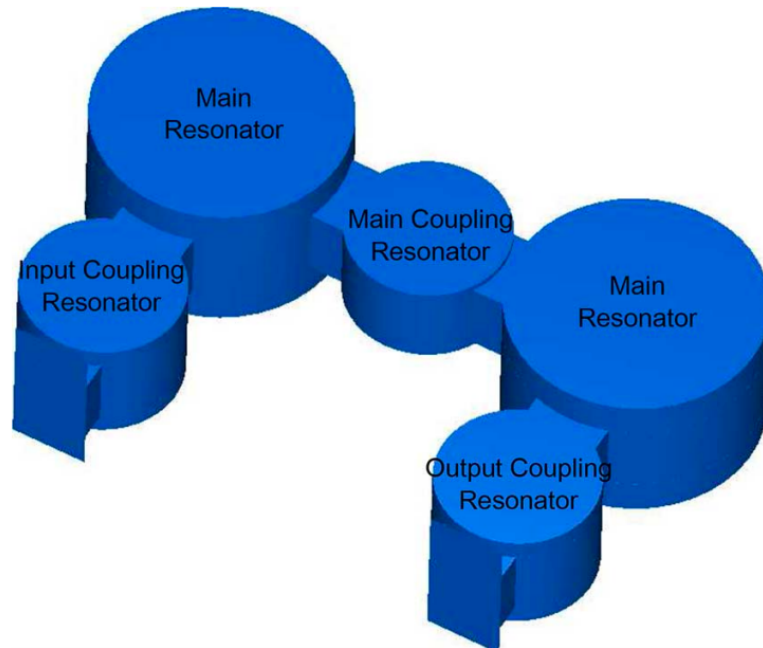


Figure 2.13: Using non-resonating cavities as coupling windows (Fig. 5 from [72]).

connect printed line sections placed over the side wall of a TE₁₀₁ mode cavity to realize an equivalent movable inner wall (see Fig. 2.14). The design of a four-channel switched filter bank in the S- and C-band using p-i-n-diode switches was also described in [78].

Recently in [11], a new device that integrates the functions of a microwave filter and a waveguide switch (F&S) was proposed. Fig. 2.15 shows an implementation of the F&S. It simultaneously behaves as a three-pole filter and as a 1P3T (one-pole triple-throw) switch. By inserting and removing the *modified tuning pins* (MTPs), the signal can be remotely re-routed with simple servo-motors.

In Chapter 6, we will demonstrate how the same concept used in the F&S can be applied to design complex reconfigurable filters and diplexers with discrete states. In order to validate this approach, we have manufactured and measured several prototypes, obtaining excellent results.

After this broad review of the state-of-the-art in different technical areas, we are now ready to discuss in detail the novel contributions that are the result of the work carried out in the context of this doctoral research activity.

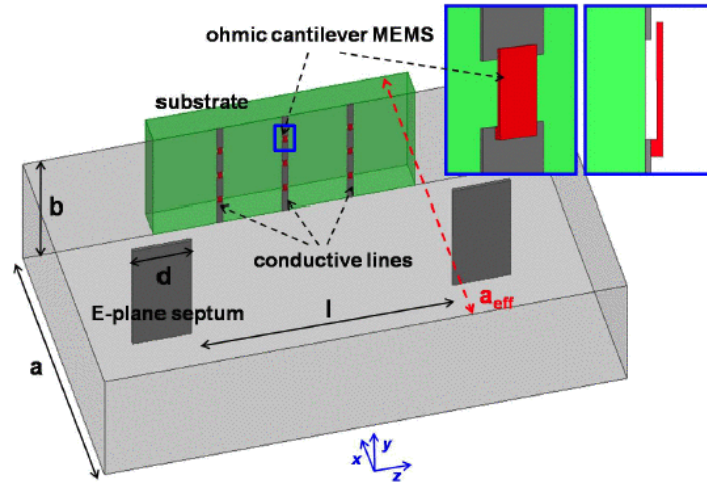


Figure 2.14: The MEMS-based tuning concept proposed in [77].

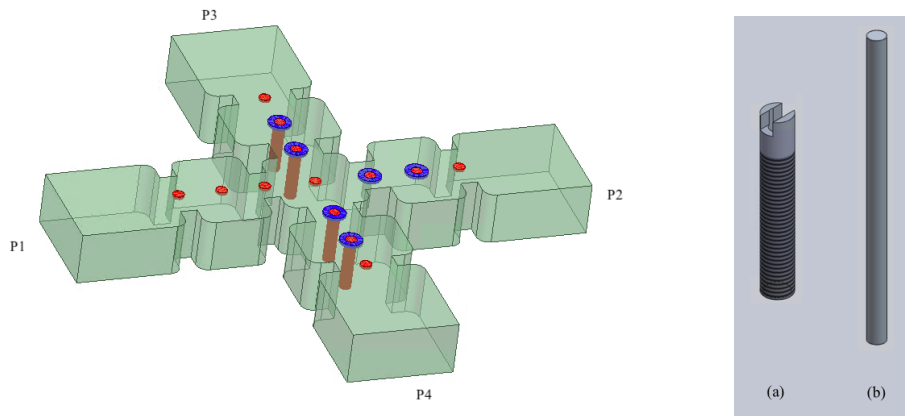


Figure 2.15: Topology of the F&S presented in [11]. Left: F&S. Right: Modified tuning pins (MTPs).

Efficient Microwave Filter Design Procedures Based on Aggressive Space Mapping

In this chapter, we will discuss the results obtained during our investigation in the area of advanced design procedures for microwave filters. It is important to note that some of the results that we discuss have already been presented at the European Microwave Conference in 2020:

- J.C. Melgarejo, M. Guglielmi, S. Cogollos and V. Boria, "An efficient microwave filter design procedure based on space mapping", in *2020 50th European Microwave Conference (EuMC)*, Jan. 2021, pp. 743-746.

Ever since Space Mapping (SM) and Aggressive Space Mapping (ASM) were introduced by Prof. Bandler, they have indeed been very widely used for the design of microwave filters [1, 5, 21, 22, 24, 30, 79–82]. As it was explained in Chapter 2, the key of SM is to use two simulation models (or spaces): a *coarse* and a *fine* model. The *coarse* model is inaccurate but fast and the *fine* model is precise but slow. SM combines the best features of both spaces, so that most simulations are carried out in the computationally inexpensive model, and the precise model is exclusively used for validation purposes.

Recently, in [34] and [35] it was shown that for resonant structures, an ASM based optimization procedure can converge to the desired target performance in *just one step*, independently of the number of variables involved in the optimization process. This

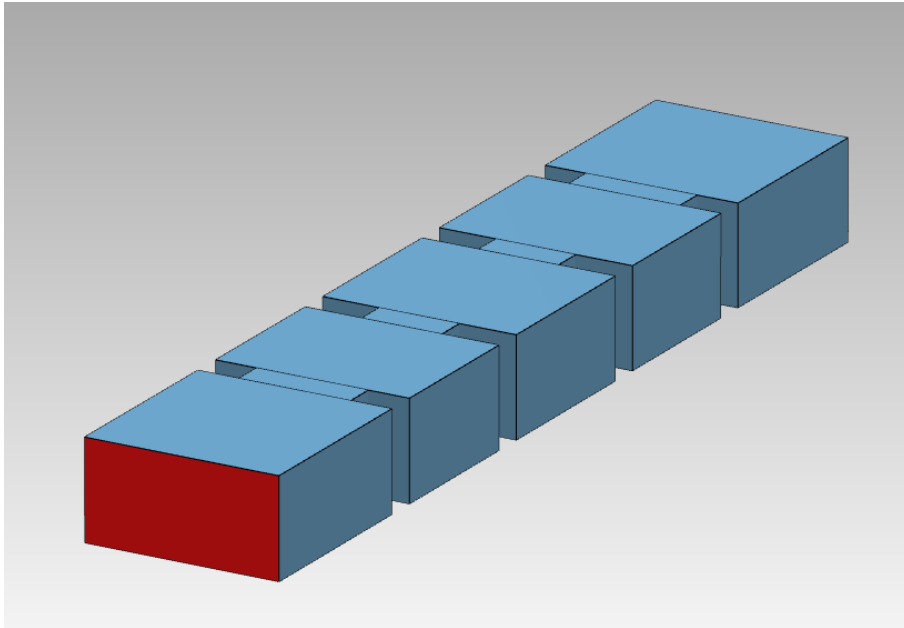


Figure 3.1: Three-pole filter structure.

approach is referred to as One-Step ASM (OS-ASM). Due to the importance of these results in the context of this thesis, we find it appropriate to give further details about the OS-ASM technique.

3.1 Efficient Implementation of OS ASM: the Step-by-Step ASM

3.1.1 One-Step ASM

In the special case where the *coarse* and *fine* models belong to the same physical domain (for example, if they both are waveguide models), the matrix \mathbf{B} can be very well approximated by the identity matrix. An explanation of this remarkable finding was provided in [35] in terms of cavity perturbation theory [83]. In this section, we will verify that same finding by finite differences for the simple three-pole inductive filter shown in Fig. 3.1 (see Table 3.1 for the dimensions of the filter).

Let us now simulate the performance of this filter with a MEN simulator (FEST3D) using two different accuracy setups. The first one will be a low accuracy (LA) setup, using the following set of computational parameters:

- Accessible modes = 4
- Number of basis functions = 12
- Green's function terms = 120

Table 3.1: Dimensions of the three-pole symmetric filter. All apertures have a length of 3 mm and all cavities have a width of 19.05 mm. The dimensions that are given are the lengths of the cavities and the widths of the irises.

Element	Dimension (mm)
Iris 1	10.9849
Cavity 1	15.1736
Iris 2	7.8713
Cavity 2	16.8996

Table 3.2: Dimensions of the three-pole symmetric filter for the HA model. All apertures have a thickness of 3 mm. All cavities have a width of 19.05 mm. The dimensions given are the lengths of the cavities and the widths of the irises.

Element	Dimension (mm)
Iris 1	10.9778
Cavity 1	15.1718
Iris 2	7.8647
Cavity 2	16.9001

A detailed explanation of the meaning of these parameters can be found in [16]. Using this setup, the simulation takes less than 0.08 s. The second setup will be a high accuracy (HA) setup, with the following computational parameters:

- Accessible modes = 50
- Number of basis functions = 150
- Green's function terms = 1500

The HA model will still be relatively fast, it runs in less than 1.05 s. Naturally, since the models use different setups, their performances will not be identical. To continue, we will now optimize the dimensions of the HA model to recover the performance of the LA model. Table 3.2 shows the dimensions of the HA model and Fig. 3.2 shows their two identical (*aligned*) responses.

According to [35], the mapping matrix between the domains could be very well approximated by \mathbf{I} . Let $\mathbf{x}_{\mathbf{c}\mathbf{a}}$ and $\mathbf{x}_{\mathbf{f}\mathbf{a}}$ indicate the aligned waveguide dimensions of the *coarse* and *fine* model, respectively. The relation between the spaces in the vicinity of $\mathbf{x}_{\mathbf{c}\mathbf{a}}$ and $\mathbf{x}_{\mathbf{f}\mathbf{a}}$ can be approximated by:

$$\mathbf{x}_{\mathbf{f}\mathbf{a}} = \mathbf{B} \cdot \mathbf{x}_{\mathbf{c}\mathbf{a}} + \mathbf{C}, \quad (3.1)$$

Let us simulate 4 points ($\mathbf{x}_{\mathbf{f}i}$) that are close to $\mathbf{x}_{\mathbf{f}\mathbf{a}}$. By optimization of the *coarse*

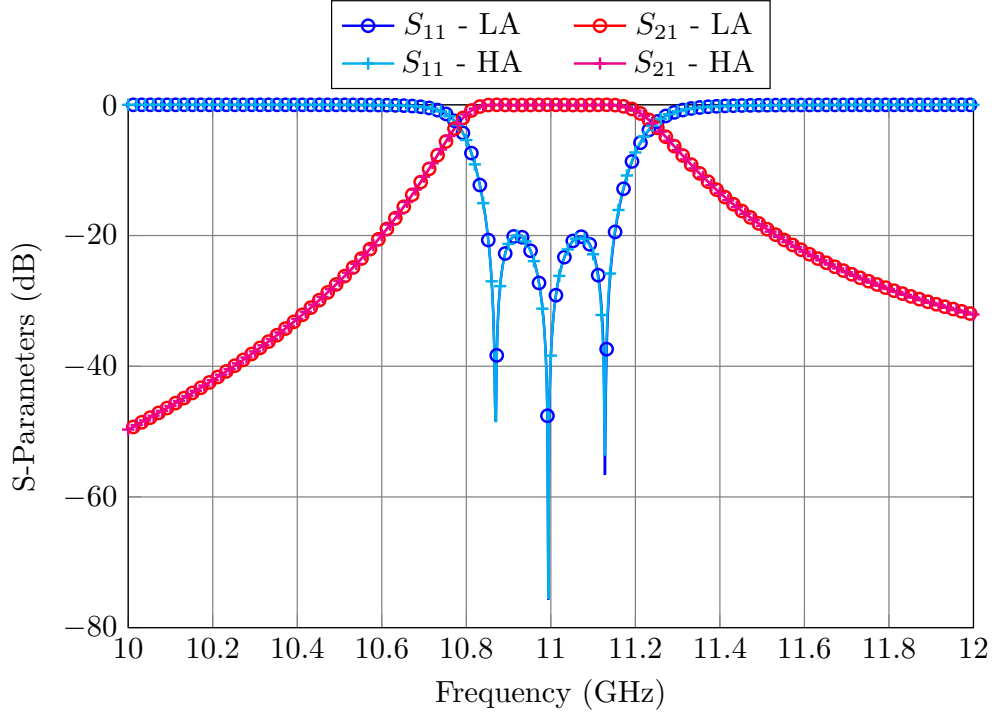


Figure 3.2: Aligned responses of the LA and HA models.

model, we can find the equivalent points (\mathbf{x}_{c_i}) so that $R_c(\mathbf{x}_{c_i}) = R_f(\mathbf{x}_{f_i})$. Then, it is also true that:

$$\mathbf{x}_{f_i} = \mathbf{B} \cdot \mathbf{x}_{c_i} + \mathbf{C}, \quad \forall i = 1, 2, 3, 4 \quad (3.2)$$

Computing the differences between eq. (3.1) and eq. (3.2) we obtain:

$$\Delta_{f_i} = \mathbf{B} \cdot \Delta_{c_i}, \quad \forall i = 1, 2, 3, 4 \quad (3.3)$$

where Δ_{f_i} and Δ_{c_i} are, respectively, $\mathbf{x}_{f_a} - \mathbf{x}_{f_i}$ and $\mathbf{x}_{c_a} - \mathbf{x}_{c_i}$. The previous matrix system can be easily solved for \mathbf{B} , thereby obtaining:

$$\mathbf{B} = \begin{pmatrix} \mathbf{0.9442} & -0.0614 & 0 & 0 \\ 0.048 & \mathbf{1.0513} & -0.0097 & 0 \\ 0 & -0.0078 & \mathbf{0.9898} & 0.0072 \\ 0 & 0 & -0.014 & \mathbf{0.9851} \end{pmatrix} \approx \mathbf{I} \quad (3.4)$$

As we can clearly see from the result given above, it is indeed true that the matrix

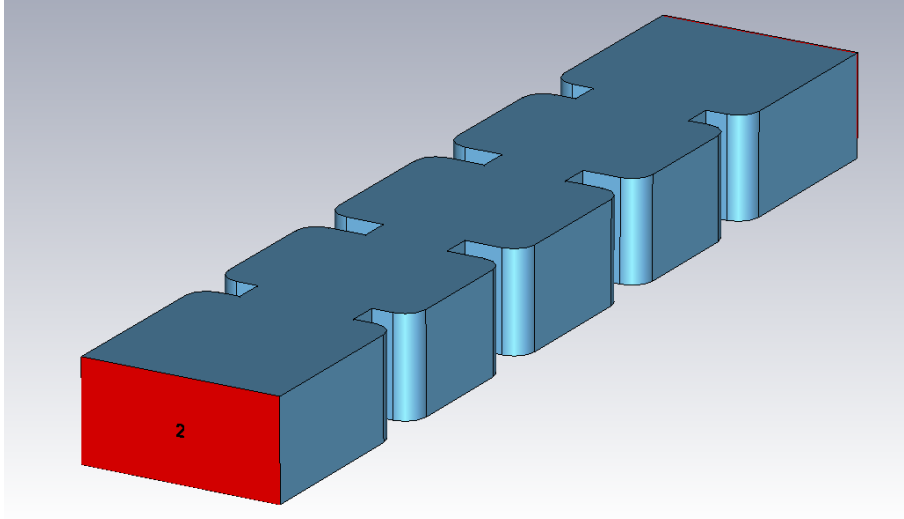


Figure 3.3: Three-pole filter structure with rounded corners.

\mathbf{B} can be approximated by the identity matrix. This is not a surprise since the models are geometrically identical. However, it turns out that the previous approximation is still valid even if the *fine* model is slightly different from the *coarse* model. To prove this, let us take now the dimensions given in Table 3.1, and round the corners of all the cavities (see Fig. 3.3).

If we simulate the structure shown in Fig. 3.3 in a high precision simulator, we will mainly see a frequency shift due reduction of the volume of each cavity. We will then use the LA model from Fig. 3.1 to match the performance of the *fine* model. Fig. 3.4 shows the two aligned responses.

If we now repeat the same process as in Eq. (3.1)-(3.3), we can obtain the \mathbf{B} matrix that relates the two domains, namely:

$$\mathbf{B} = \begin{pmatrix} \mathbf{1.0348} & 0 & 0 & 0 \\ 0 & \mathbf{1.0192} & 0.0016 & 0 \\ 0 & -0.0036 & \mathbf{0.9944} & 0 \\ 0 & 0 & 0.012 & \mathbf{1.0157} \end{pmatrix} \approx \mathbf{I} \quad (3.5)$$

As we can see, even if the *coarse* and *fine* models have small differences (in this case the *fine* model includes rounded corners) the matrix that links the spaces can still be very well approximated by the identity matrix. This result has a massive impact in the overall time required to perform ASM. As an illustration, let us now consider a simple example: the design of a filter as the one shown in Fig. 3.3. The design procedure will be as follows:

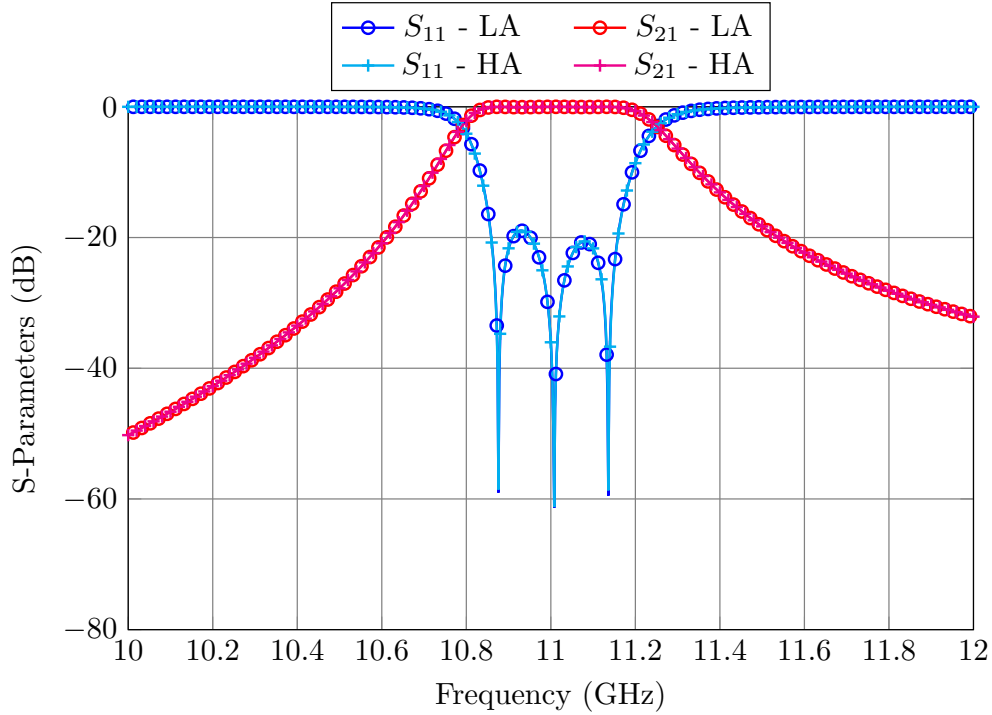


Figure 3.4: Aligned responses of the LA (Fig. 3.1) and HA models (Fig. 3.3).

1. Obtain the optimal solution (\mathbf{x}_{copt}) using the *coarse* model shown in Fig. 3.1.
2. Take those dimensions, add the non-ideal factors (round corners) and simulate the structure with a high precision simulator (the *fine* model). Let us refer to the fine dimensions as \mathbf{x}_{f1} .
3. Optimize the *coarse* model until the performance of the *fine* model has been matched (as in Fig. 3.4). We will refer to these dimensions as \mathbf{x}_{c1} .
4. Set the next *fine* model dimensions to:

$$\mathbf{x}_{\text{f2}} = \mathbf{x}_{\text{f1}} + \mathbf{B} \cdot (\mathbf{x}_{\text{copt}} - \mathbf{x}_{\text{c1}}) \approx \mathbf{x}_{\text{f1}} + (\mathbf{x}_{\text{copt}} - \mathbf{x}_{\text{c1}}) \quad (3.6)$$

5. After only one iteration, we obtain the desired performance in the *fine* domain. As we can see from Fig. 3.5, using only two *fine* model evaluations, the response of the *fine* model is indistinguishable from the desired target.

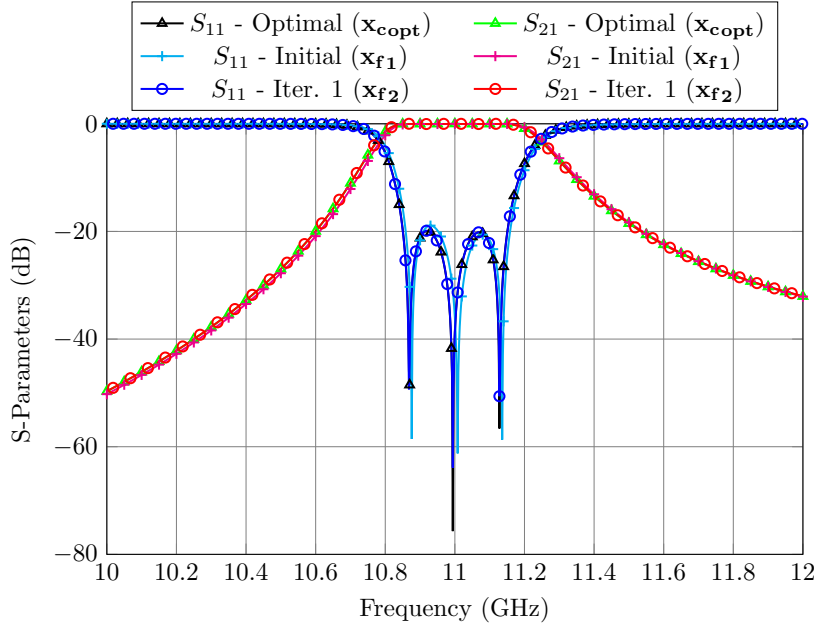


Figure 3.5: OS-ASM process to design the filter shown in Fig. 3.3

3.1.2 Step-by-Step ASM

OS-ASM has proved to be extremely powerful for situations where the initial performance of the *fine* model is relatively close to the desired one. However, for more complex filters, the initial performance of the *fine* model can be very far from the desired target. In this case, the optimizer can very easily get lost during the optimization process.

As a very effective remedy, in this chapter we propose a novel and robust ASM-based technique, namely, the Step-by-Step ASM procedure. The Step-by-Step method that we propose combines the segmentation strategy described in [17] with the power of OS-ASM. The basic idea is to optimize a reduced number of elements at a time, thereby reducing the optimization space from N to two or three parameters at most. The procedure goes as follows:

1. Optimize the dimensions of the *coarse* model until the target performance has been obtained.
2. Simulate the first three elements of the optimized *coarse* model (Fig. 3.6, left). The simulation of this reduced structure will provide the target response that the reduced *fine* model (Fig. 3.6, right) needs to match. Instead of optimizing the *fine* model until the response matches the performance of the *coarse* model (which is what was originally proposed in [17]), we will now exploit the power of OS-ASM. To do that, we will now optimize the reduced *coarse* model until the performance

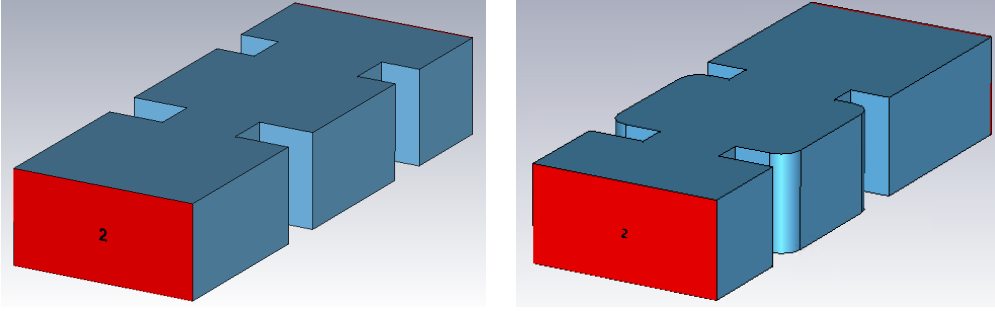


Figure 3.6: Left: First three elements of the *coarse* model. Right: First three elements of the *fine* model.

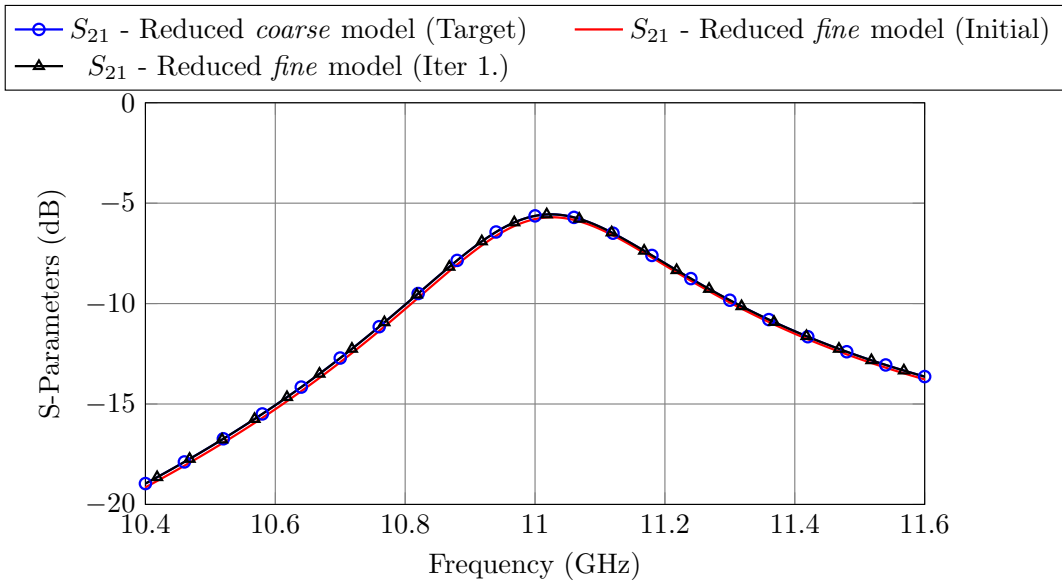


Figure 3.7: Performance of the reduced *fine* and *coarse* models after only one ASM iteration.

of the reduced *fine* model is matched:

$$R_c(\mathbf{x}_{c1}) = R_f(\mathbf{x}_{f1}), \quad (3.7)$$

and then we will modify the dimensions of the reduced *fine* model according to:

$$\mathbf{x}_{f2} = \mathbf{x}_{f1} + (\mathbf{x}_{c\text{opt}} - \mathbf{x}_{c1}) \quad (3.8)$$

Due to the small number of parameters involved (three elements), the reduced *fine* model will provide the same target response in one iteration. Fig. 3.7 shows the performances of the *fine* and *coarse* models after one ASM iteration.

3. Add the next tuple of elements, that is, the next resonator and aperture to the

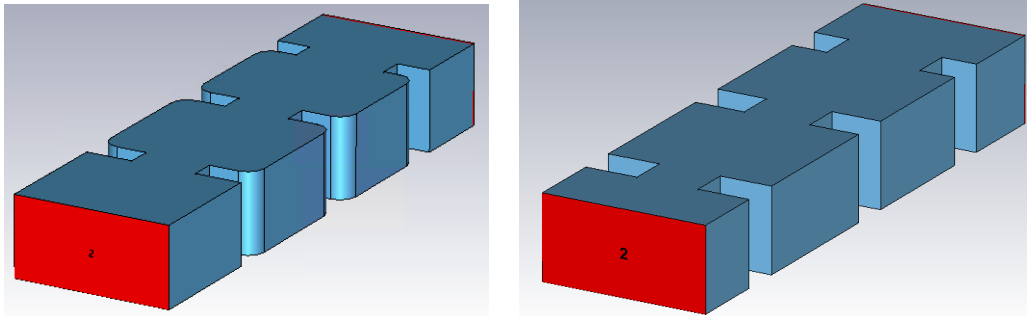


Figure 3.8: Left: Second reduced *fine* model. Right: Second reduced *coarse* model.

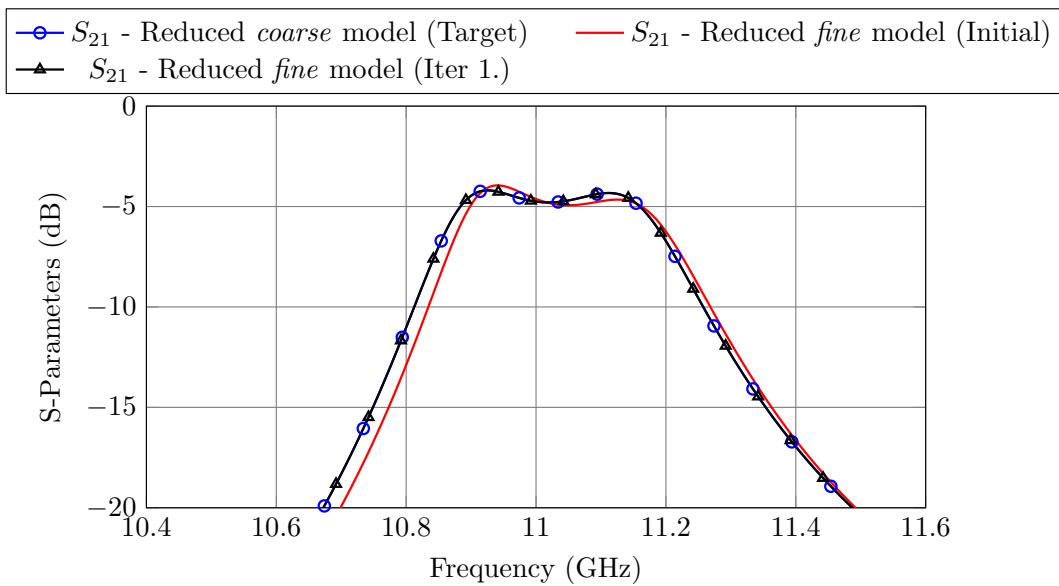


Figure 3.9: Performance of the reduced *fine* and *coarse* models after only one ASM iteration.

fine model and repeat the previous process (see Fig. 3.8). Since the first three elements have already been optimized in the previous step, in most cases, it will not be necessary to readjust them. For the same reason as before, we will recover the target performance in one ASM iteration as shown in Fig. 3.9

4. Finally, duplicate the last reduced *fine* model to obtain the filter¹. In this simple example, the response of the filter after this step matches exactly the target performance. However, in general, we will have to repeat another OS-ASM iteration considering all design parameters.

The advantages of Step-by-Step ASM are not yet visible. If anything, it seems that there are unnecessary steps that slow down the design process. However, it is very

¹This is due to the geometrical symmetry of the filter.

Table 3.3: Accuracy settings used for the 6-pole inductive filter.

Coarse Model	
Simulator	FEST3D
Accessible modes	10
Number of basis functions	30
Green's function terms	300
Fine Model	
Simulator	CST Microwave Studio
Solver	Frequency Domain Solver
Frequency Sweep	General Purpose
Mesh refinement	11 GHz
Error Threshold	0.005
Maximum number of iterations	20

important to note that this is an unrealistically simple filter. In the remainder of this chapter, we will compare the performance of One-Step ASM and Step-by-Step ASM for four different filters, and we will see that the technique that we propose can achieve the desired target performance significantly faster, especially in the most complex cases.

3.2 Design of a 6-pole inductive filter

We will start the comparison with one simple case: the 6-pole inductive waveguide filter shown in Fig. 3.10. The filter is centered at 11 GHz and has a bandwidth of 500 MHz.

A commonly used strategy to reduce the overall cost of a filter is to use a medium precision manufacturing technique (like H-plane milling) along with tuning elements that can be adjusted to compensate for the manufacturing errors. The final simulations must then include a 2 mm curvature radius in all concave corners. The final model must also consider tuning elements (in this case, with a radius of 1.6 mm) set at a fixed depth of 1 mm. This depth is chosen to allow for bidirectional adjustments after manufacturing the prototype.

We will use two simulation tools: FEST3D and CST Microwave Studio. For the *coarse* model(s) we will use FESTD using a low accuracy setting. For the *fine* model(s) we will use CST. Table 3.3 shows the settings for each EM simulator.

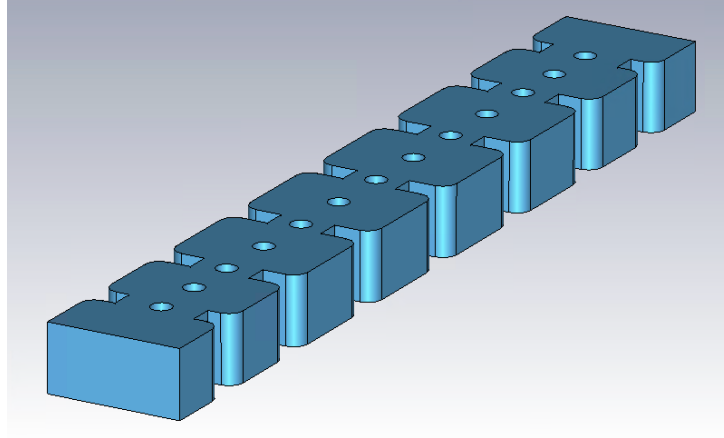


Figure 3.10: Final model used for the 6-pole inductive filter that includes all the non-ideal manufacturing details (*fine* model).

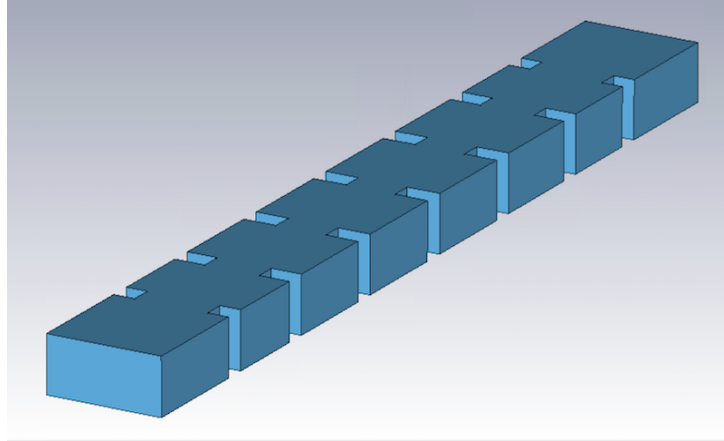


Figure 3.11: *Coarse* model used for the 6-pole inductive filter.

3.2.1 One-Step ASM

The *coarse* and *fine* models used in the One-Step ASM technique are shown in Figs. 3.11 and 3.10, respectively. The design process for this filter using One-Step ASM is as follows:

1. Optimize the dimensions of the *coarse* model (\mathbf{x}_{copt}) until the desired performance is obtained. The parameters that are optimized are the widths of the apertures and the lengths of the cavities.
2. Use the dimensions of the coarse model as a starting point for the *fine* model, that is:

$$\mathbf{x}_{f1} = \mathbf{x}_{\text{copt}} \quad (3.9)$$

Fig. 3.12 shows the performance of the *fine* model compared to its target. It is important to note that the *fine* model includes also rounded corners and tuning

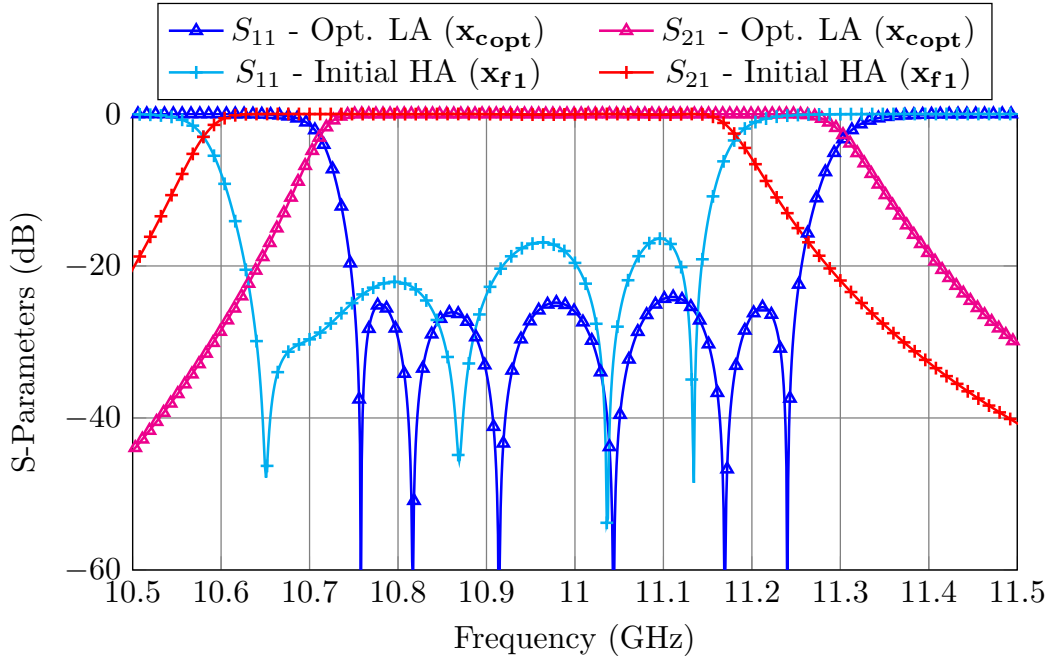


Figure 3.12: Optimized performance of the *coarse* model and initial *fine* model's response.

elements.

3. Optimize a new instance of the *coarse* model until the response of the *fine* model is recovered:

$$R_c(\mathbf{x}_{c1}) = R_f(\mathbf{x}_{f1}) \quad (3.10)$$

4. Set the *fine* model's dimensions to:

$$\mathbf{x}_{f2} = \mathbf{x}_{f1} + \mathbf{B} \cdot (\mathbf{x}_{c_{opt}} - \mathbf{x}_{c1}) \approx \mathbf{x}_{f1} + (\mathbf{x}_{c_{opt}} - \mathbf{x}_{c1}) \quad (3.11)$$

It is important to note that even if the *fine* model includes rounded corners and tuning elements, we can still approximate \mathbf{B} with the identity matrix. The performance of the *fine* model as compared to its target is shown in Fig. 3.13. Even though the response is objectively much closer to the target than before, the filter is still detuned.

5. Repeat the previous steps as many times as necessary. In this case, three iterations are needed to obtain the desired response. Fig. 3.14 shows the performance of the *fine* model in each iteration.

For the 6-pole inductive filter, four ASM iterations were needed to achieve the desired performance. The computation time required can be obtained with the following formula:

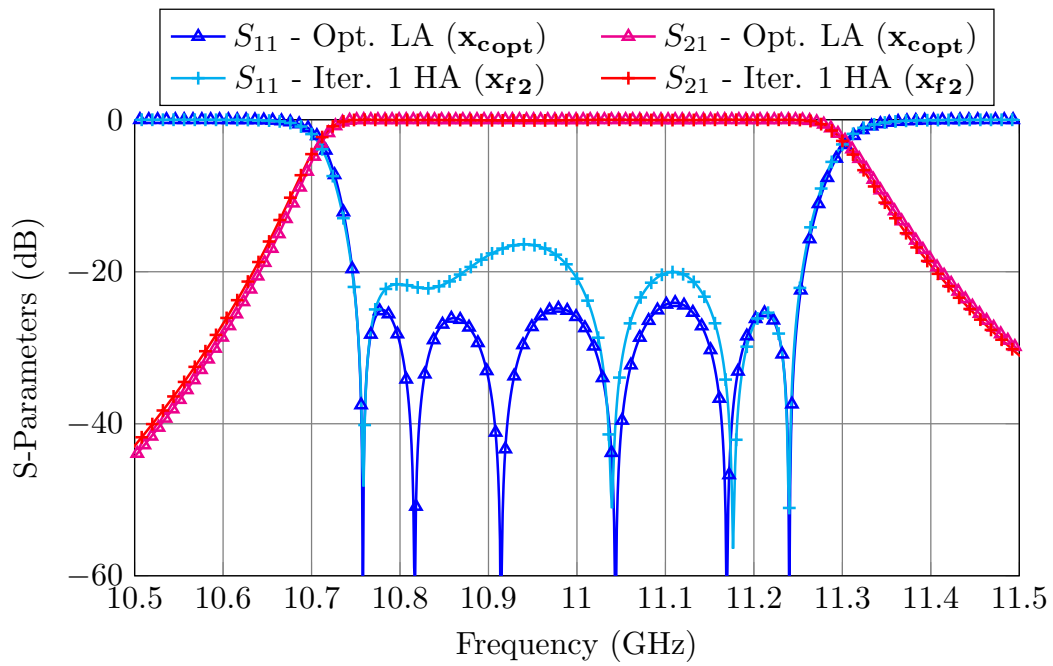


Figure 3.13: Performance of the *fine* model after one iteration compared to the target response.

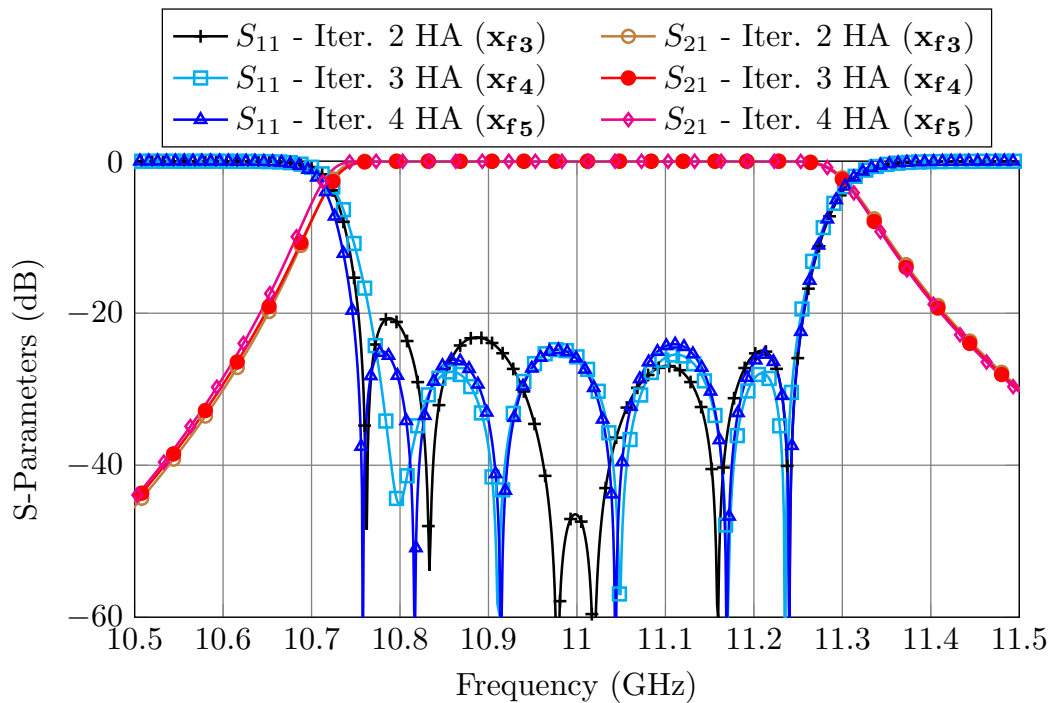


Figure 3.14: One-Step ASM process to fine tune the filter.

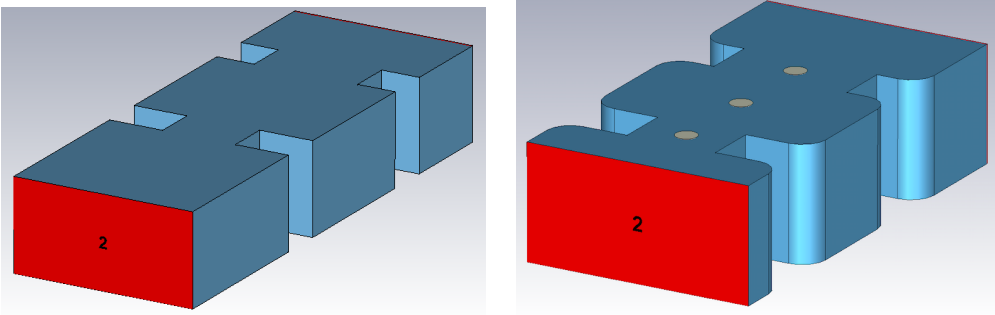


Figure 3.15: Left: First three elements of the *coarse* model. Right: First three elements of the *fine* model.

$$\text{Time} = TF \cdot (NI + 1) + TC \cdot AI \cdot NI = 11 \text{ min. } 35 \text{ s.} \quad (3.12)$$

where TF and TC are, respectively, the computation time of the *fine* and *coarse* model, NI is the number of ASM iterations, and AI is the average number of simulations performed by the Simplex algorithm to recover each of the *fine* model responses.

3.2.2 Step-by-Step ASM

The Step-by-Step procedure for the 6-pole inductive filter is as follows:

1. Optimize the dimensions of the *coarse* model (\mathbf{x}_{copt}) until the desired performance is obtained. The parameters that are optimized are the widths of the apertures and the lengths of the cavities. This step is the same as the first step of the previous procedure.
2. Simulate the first three elements of the optimized *coarse* model (Fig. 3.15, left). The result obtained will provide the target response that the same three elements of the *fine* model (Fig. 3.15, right) need to match. Optimize the reduced *coarse* model until the performance of the reduced *fine* model is matched:

$$R_c(\mathbf{x}_{\mathbf{c1}}) = R_f(\mathbf{x}_{\mathbf{f1}}), \quad (3.13)$$

and then, modify the dimensions of the reduced *fine* model according to:

$$\mathbf{x}_{\mathbf{f2}} = \mathbf{x}_{\mathbf{f1}} + (\mathbf{x}_{\text{copt}} - \mathbf{x}_{\mathbf{c1}}) \quad (3.14)$$

After only one ASM iteration, the reduced *fine* model provides exactly the target performance (see Fig. 3.16). It is important to note that there are only three parameters that are being optimized in the *coarse* model: the widths of the first two apertures and the length of the first cavity.

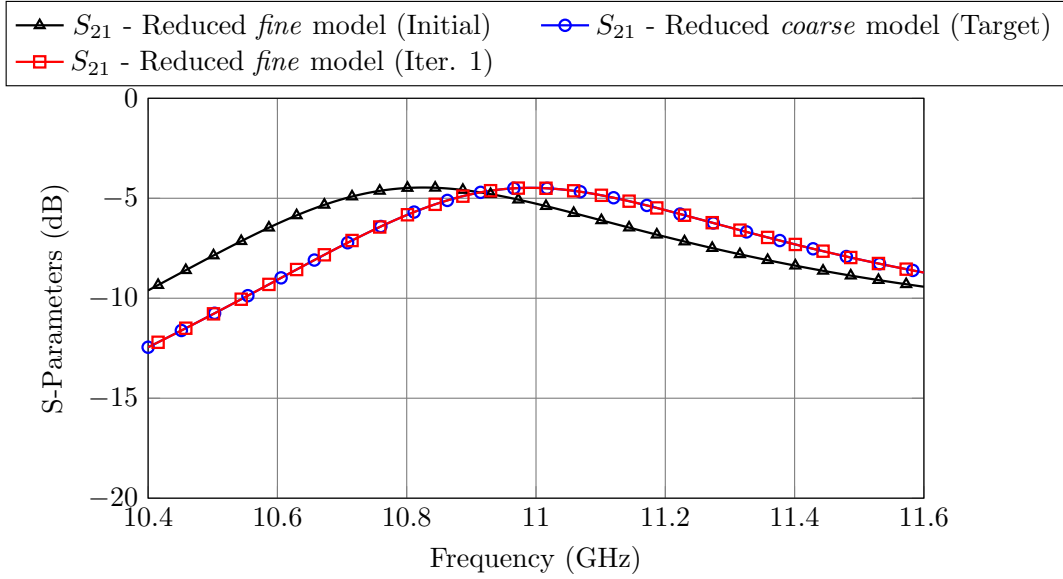


Figure 3.16: Performance of the reduced *fine* and *coarse* models after only one ASM iteration.

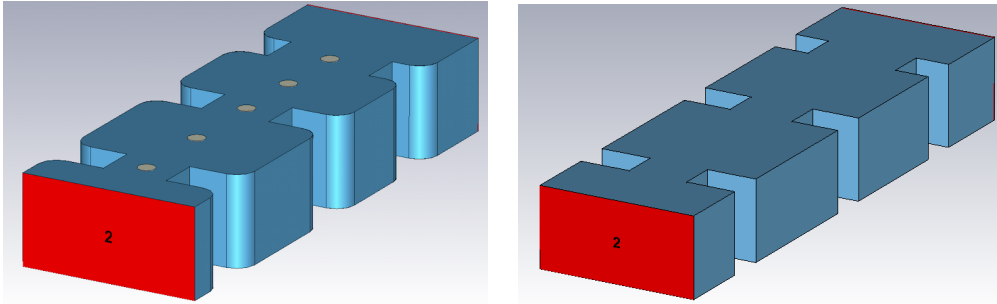


Figure 3.17: Left: Second reduced *fine* model. Right: Second reduced *coarse* model.

3. Add the next two elements (the next cavity and iris) to the reduced *fine* model (see Fig. 3.17, left). We will use the reduced *coarse* model shown in Fig. 3.17, right, to recover the performance of the *fine* model. It is important to note that the variables we optimized in the previous step are now fixed. The only parameters we have to optimize in this stage are the newly added cavity and iris. As it happened in the previous case, one ASM iteration is enough to achieve the desired performance for the high precision model (see Fig. 3.18).
4. We will repeat the last step until we have obtained the dimensions of half of the filter. Then, we will simply apply symmetry to obtaining the structure shown in Fig. 3.10. At this point, we will use the original *coarse* model to recover the *fine* model's response. Since the non-ideal factors have been considered in the previous steps, the first high accuracy simulation of the filter will already be very close to

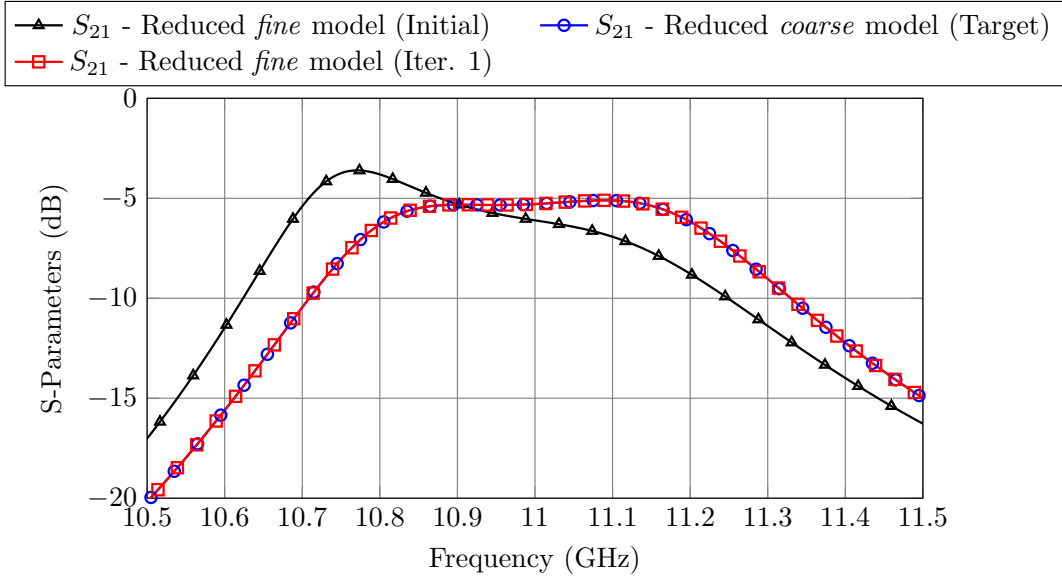


Figure 3.18: Performance of the second reduced *fine* and *coarse* models of Fig. 3.17 after only one ASM iteration.

the target (see Fig. 3.19). One OS-ASM iteration will be enough to obtain the desired performance.

The filter was manufactured and measured (see Fig. 3.20) with excellent results. The key feature of the procedure we have just described is that the non-ideal factors are introduced step by step in the different stages, and each optimization stage involves only a reduced number of variables. This technique has two advantages as compared to the previous one:

- Since there are, at most, only three parameters to optimize, the number of simulations needed to recover each *fine* model's response is greatly reduced.
- The reduced optimization space also makes this method very robust against local minima.

The overall time required to design the 6-pole inductive filter using this approach can be computed as:

$$\text{Time} = \sum_{i=1}^{\text{Stages}} TC_i \cdot I_i + 2 \cdot TF_i = 6 \text{ min. } 20 \text{ s.} \quad (3.15)$$

where TF_i and TC_i represent, respectively, the computation time of the *fine* and *coarse* models in each stage of the procedure, and I_i indicates the number of simulations

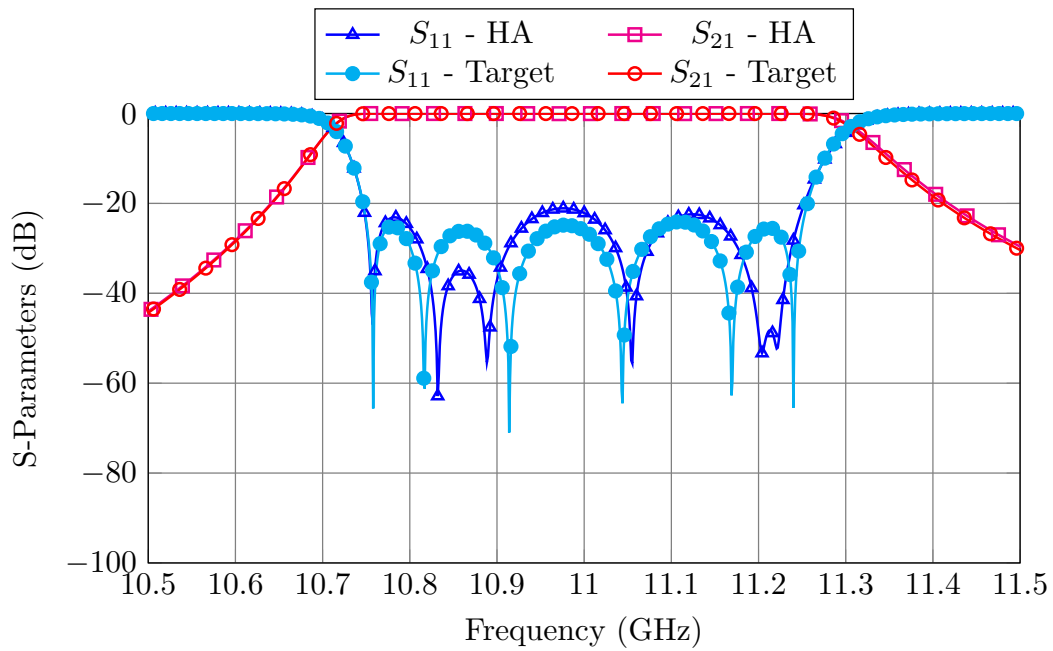


Figure 3.19: Performance of the *fine* model after duplicating half of the structure.

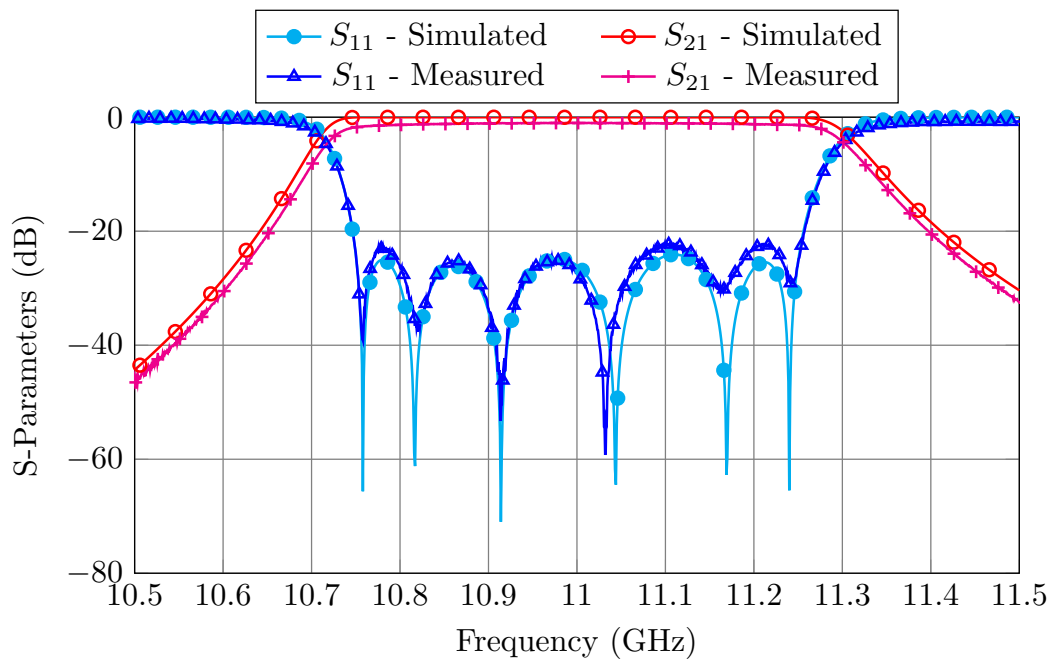


Figure 3.20: Measured performance of the 6-pole inductive filter compared to the target performance.

Table 3.4: Performance of both design methods for the in-line 6-pole waveguide filter.

One-Step ASM		Step-by-Step ASM					
TC	0,23 s.	TC_1	0,1 s.	TF_1	19 s.	$I1$	56
TF	61 s.	TC_2	0,11 s.	TF_2	33 s.	$I2$	71
NI	4	TC_3	0,13 s.	TF_3	41 s.	$I3$	78
AI	424	TC_4	0.26 s.	TF_4	61 s.	$I4$	212
Time	11 min. 35 s.	Time	6 min. 20 s.				

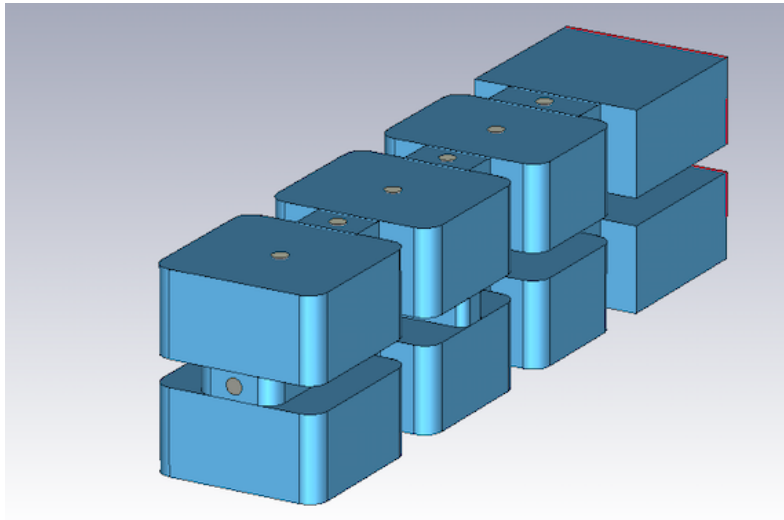


Figure 3.21: Final model used for the 6-pole waveguide filter with one cross-coupling that includes all the non-ideal manufacturing details (*fine* model).

performed by a Simplex algorithm to recover each of the *fine* model's responses. The same result has been obtained **1,83 times faster** than with the One-Step ASM approach. Table 3.4 shows the detailed performance of each procedure.

3.3 Design of a folded 6-pole filter with a cross-coupling

The next case study is shown in Fig. 3.21. It is a more complex folded 6-pole filter with a capacitive cross-coupling. The capacitive coupling between resonators two and five introduces two transmission zeros, one below and one above the pass-band. This filter is centered at 11 GHz and has bandwidth of 200 MHz.

This filter will also be manufactured by H-plane milling in three pieces (a body and two covers). The *fine* model must, therefore, include rounded corners (2 mm radius) in all concave corners. It must also include tuners (0.9 mm radius) set at a fixed depth of 1 mm.

Table 3.5: Accuracy settings used for the folded 6-pole filter.

Coarse Model	
Simulator	FEST3D
Accessible modes	10
Number of basis functions	30
Green's function terms	300
Fine Model	
Simulator	CST Microwave Studio
Solver	Frequency Domain Solver
Frequency Sweep	General Purpose
Mesh refinement	11 GHz
Error Threshold	0.005
Maximum number of iterations	20

3.3.1 One-Step ASM

The *coarse* model used in the One-Step ASM procedure is an ideal waveguide model of the filter with sharp 90° corners, and without tuning elements, as shown in Fig. 3.22. The simulator used for the *coarse* model is FEST3D with the setup shown in Table 3.5.

The *coarse* model only considers 10 accessible modes. However, in the capacitive cross-coupling, many higher order modes are excited and thus, there is a significant difference between the performance of the *coarse* model and the response that the same structure would provide if simulated in CST with a high precision setup (see Table 3.5 for the details). As a consequence, if we tried to consider all non-ideal elements at once in the *fine* model, recovering its performance with the *coarse* model would be rather difficult. It is, therefore, necessary to divide the One-Step ASM procedure into three different steps.

1. The first step consists in obtaining a high precision model with sharp 90° corners and without tuning elements. Three ASM iterations are required to recover the target performance, as shown in Fig. 3.23. The parameters that are being optimized are the lengths of the resonators, and the widths of the apertures.
2. We then can add the tuning elements to the *fine* model (see Fig. 3.24) and repeat the same ASM process. After three ASM iterations, both models provide the same performance (see Fig. 3.25).
3. Finally, we can add the rounded corners to the *fine* model obtaining the final model shown in Fig. 3.21. At this stage, 2 ASM iterations are needed to obtain the desired performance as indicated in Fig. 3.26.

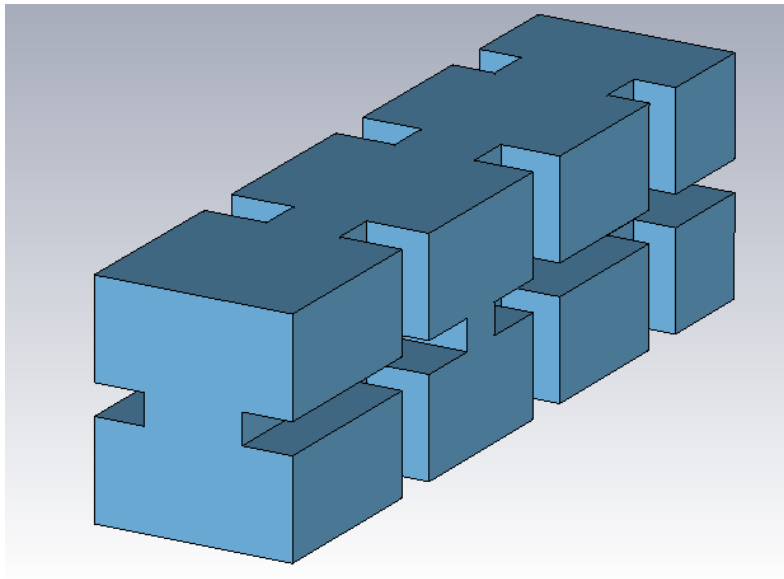


Figure 3.22: Coarse model used for the 6-pole waveguide filter with one cross-coupling. This model includes neither rounded corners nor tuning elements.

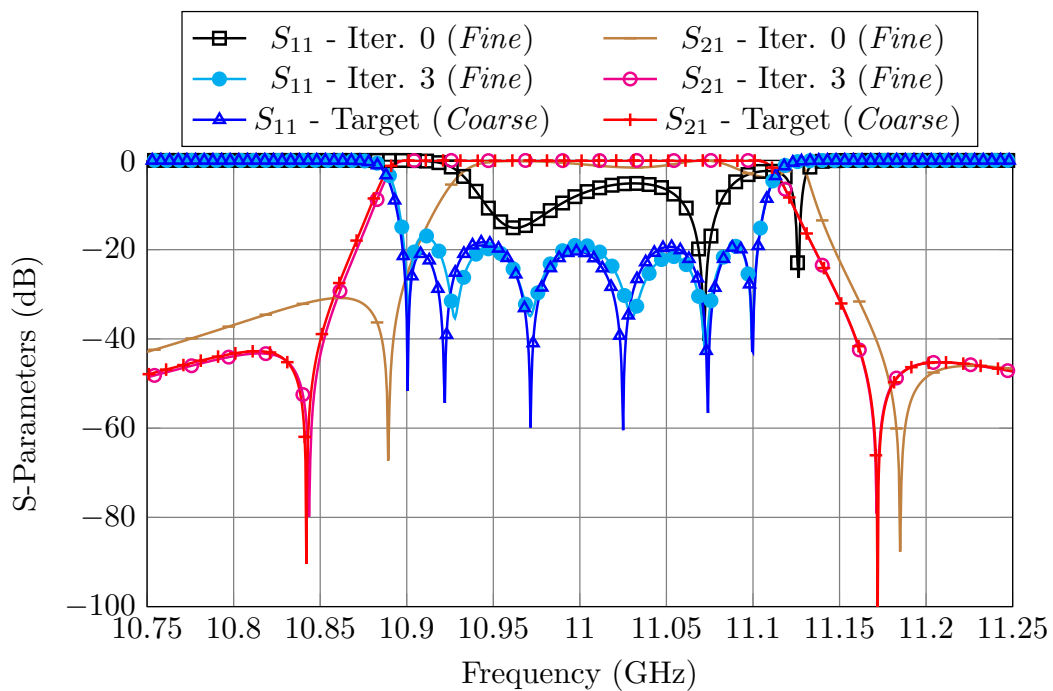


Figure 3.23: One-Step ASM process to obtain the desired performance in the high precision model with sharp 90° corners without tuning elements.

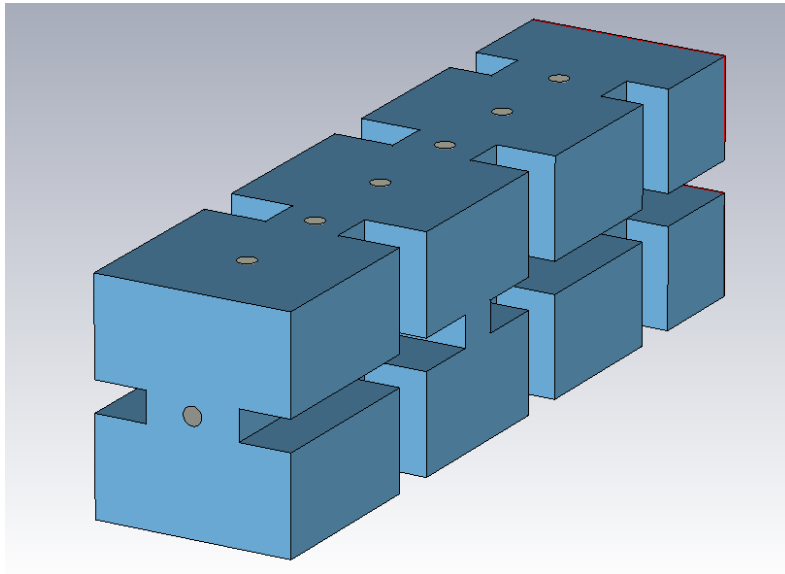


Figure 3.24: *Fine* model used for the second One-Step ASM stage. This model includes tuning elements and it is simulated with CST Microwave Studio.

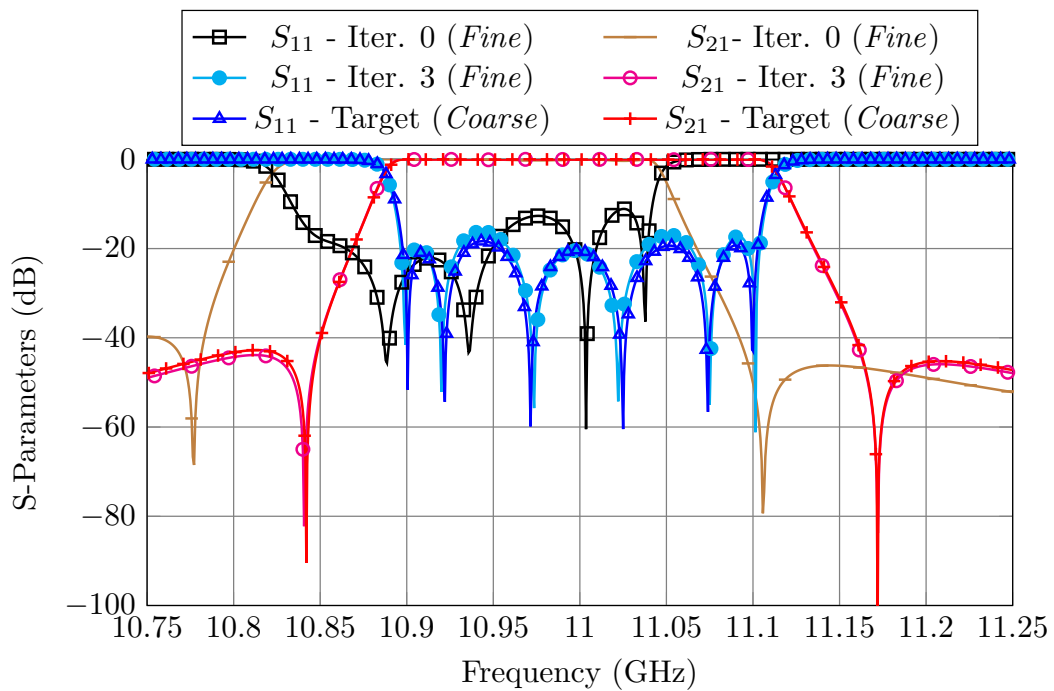


Figure 3.25: One-Step ASM process to obtain the desired performance in the high precision model with sharp 90° corners and tuning elements.

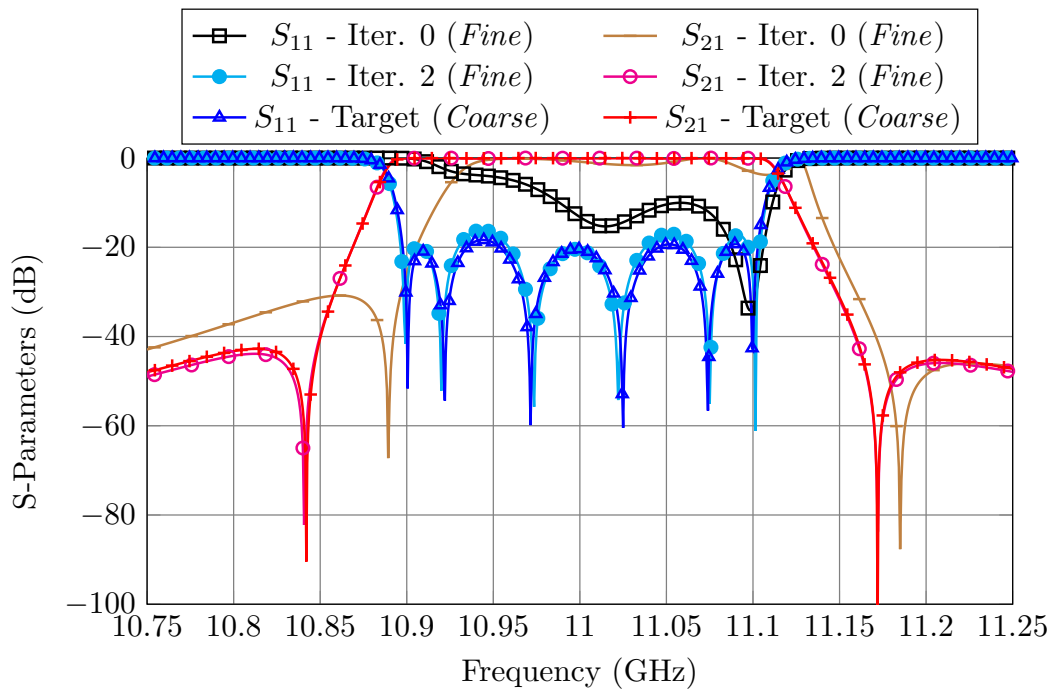


Figure 3.26: One-Step ASM process to obtain the desired performance in the high precision model with rounded corners and tuning elements.

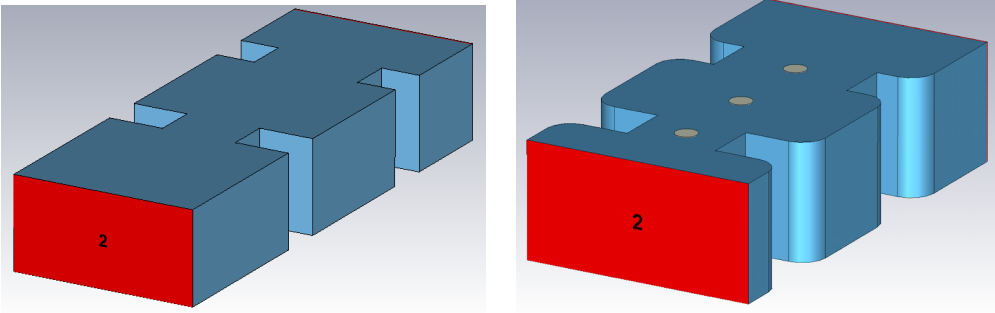


Figure 3.27: First three elements of the first reduced model for the 6-pole folded filter. Left: *Coarse*. Right: *Fine*.

The overall time required to design the 6-pole folded filter using this approach can be computed as:

$$\text{Time} = \sum_{i=1}^{\text{Stages}} TC_i \cdot AI_i \cdot NI_i + (NI_i + 1) \cdot TF_i = 1 \text{ h. } 51 \text{ min.} \quad (3.16)$$

3.3.2 Step-by-Step ASM

We will now use the Step-by-Step procedure. The steps are as follows:

1. Start with reduced *fine* and *coarse* models (see Fig. 3.27) that only include the first three elements of the filter. After only one ASM iteration, both models will provide the same performance, as shown in Fig. 3.28.
2. Add a the next resonator and aperture and repeat the process. Fig. 3.29 shows the performance of the *fine* and *coarse* models after one ASM iteration.
3. Add the next resonator and aperture to the reduced *fine* model (see Fig. 3.30, left) and repeat the ASM process with the reduced *coarse* model shown in Fig. 3.30, right, to obtain the target response. As in the previous cases, one ASM iteration is enough to achieve the target performance, as shown in Fig. 3.31.
4. At this point, we must duplicate the *fine* model and add the capacitive cross-coupling, obtaining the model shown in Fig. 3.21. We will then perform one ASM iteration to recover the desired performance (see Fig. 3.32). It is important to note that even if the initial performance is far from the desired one, we are only optimizing two variables: the width of the capacitive aperture and the length of the resonators it is connected to. After this step, the performance of the filter is already very close to the target performance.
5. After only four ASM iterations with, at most, 3 variables, the performance of the *fine* model is extremely close to the target response. The performance is so close

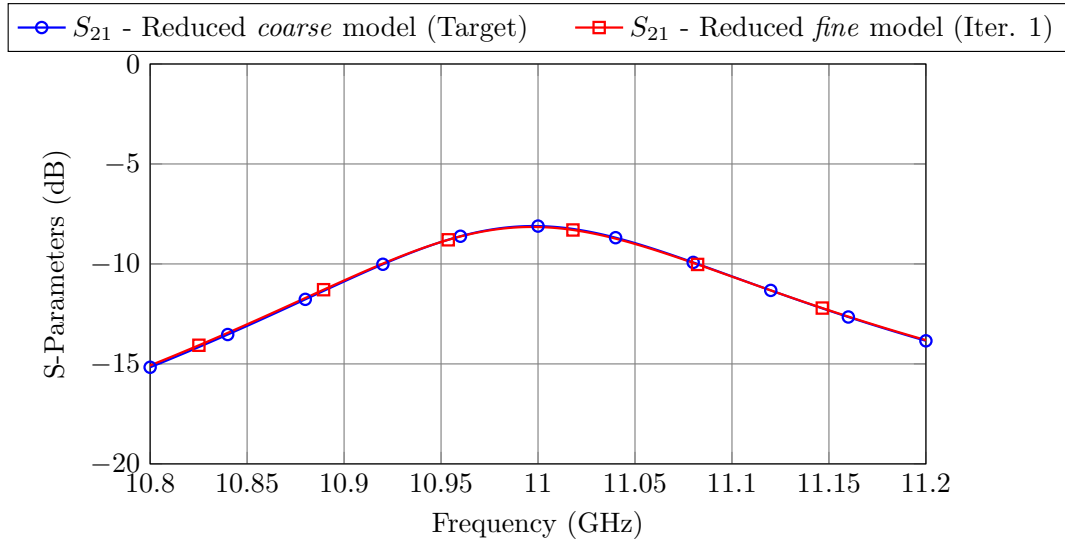


Figure 3.28: Performance of the first reduced *fine* and *coarse* models after only one ASM iteration.

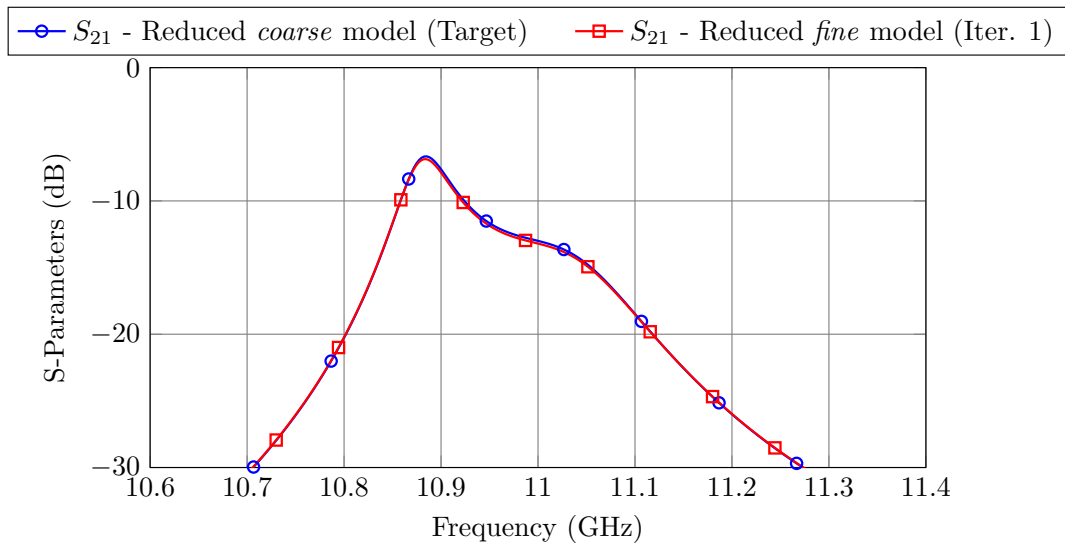


Figure 3.29: Performance of the second reduced *fine* and *coarse* models after only one ASM iteration.

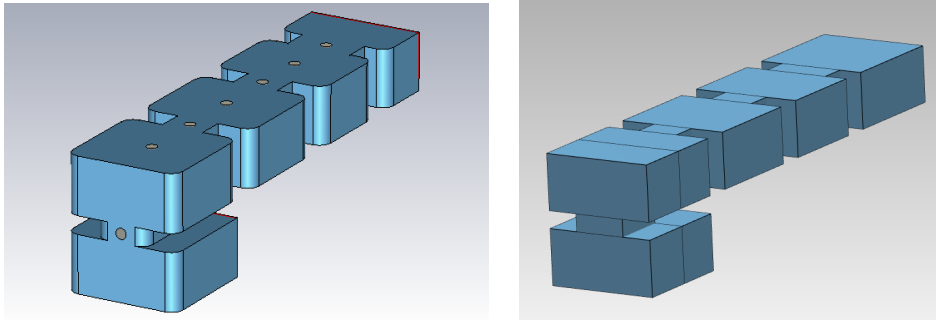


Figure 3.30: Third reduced model for the 6-pole folded filter. Left: *Fine*. Right: *Coarse*.

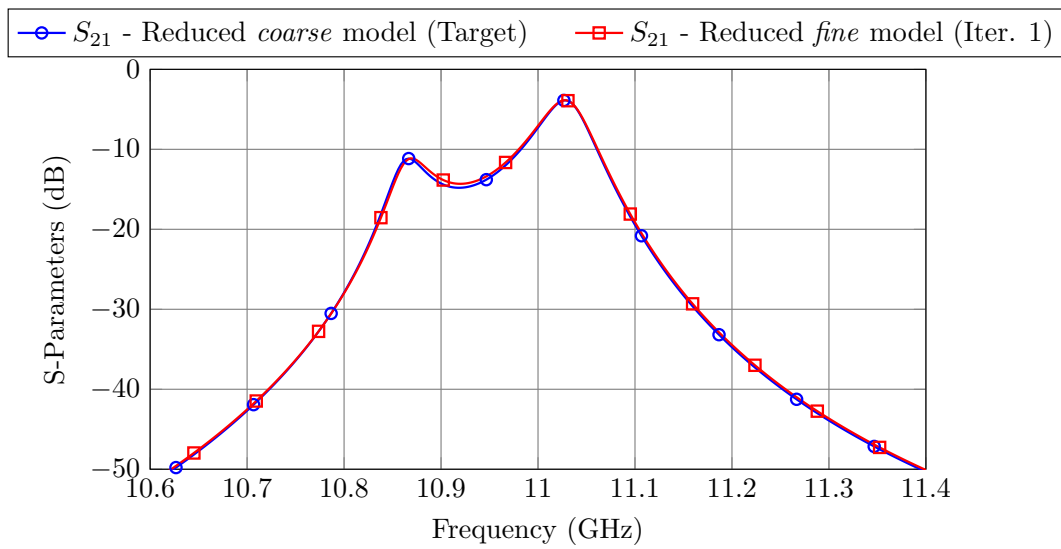


Figure 3.31: Performance of the reduced *fine* and *coarse* models after only one ASM iteration.

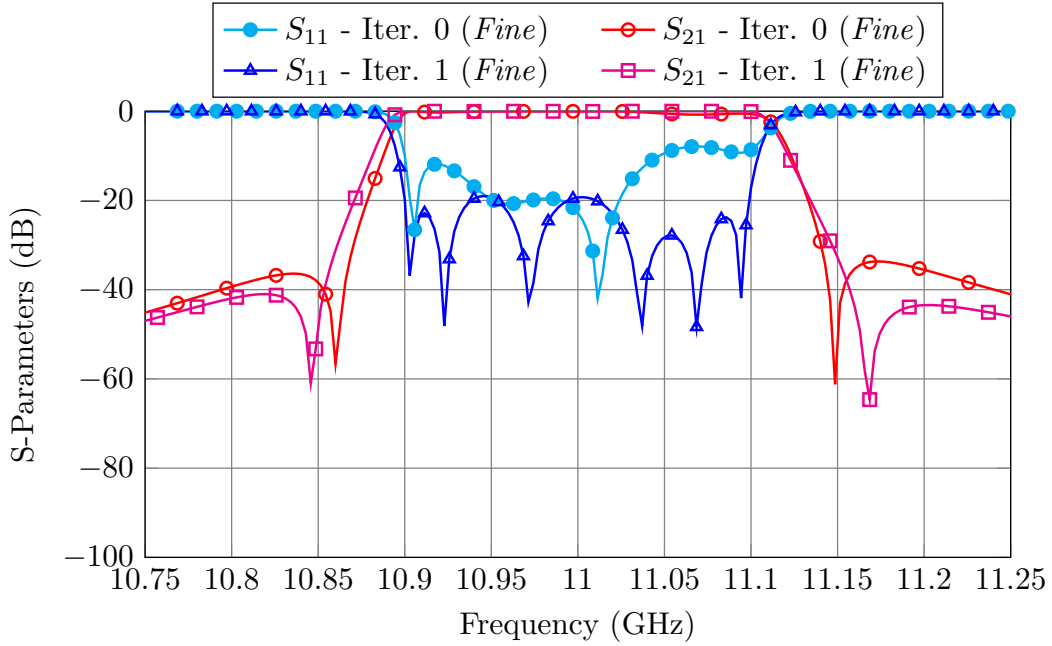


Figure 3.32: Performance of the *fine* model after one ASM iteration.

to the target that we could actually manufacture the filter as is. However, we will perform an additional ASM iteration considering all the parameters so that the performance of the *fine* model matches exactly our target (see Fig. 3.33).

The filter has then been manufactured and measured (see Fig. 3.34) with excellent results.

The overall time required to design the 6-pole folded filter using this approach can be computed as:

$$\text{Time} = \sum_{i=1}^{\text{Stages}} TC_i \cdot I_i + 2 \cdot TF_i = 17 \text{ min. } 30 \text{ s.} \quad (3.17)$$

The same result has been obtained **6.3 times faster** than with the One-Step ASM approach. Table 3.6 shows the time parameters of each procedure.

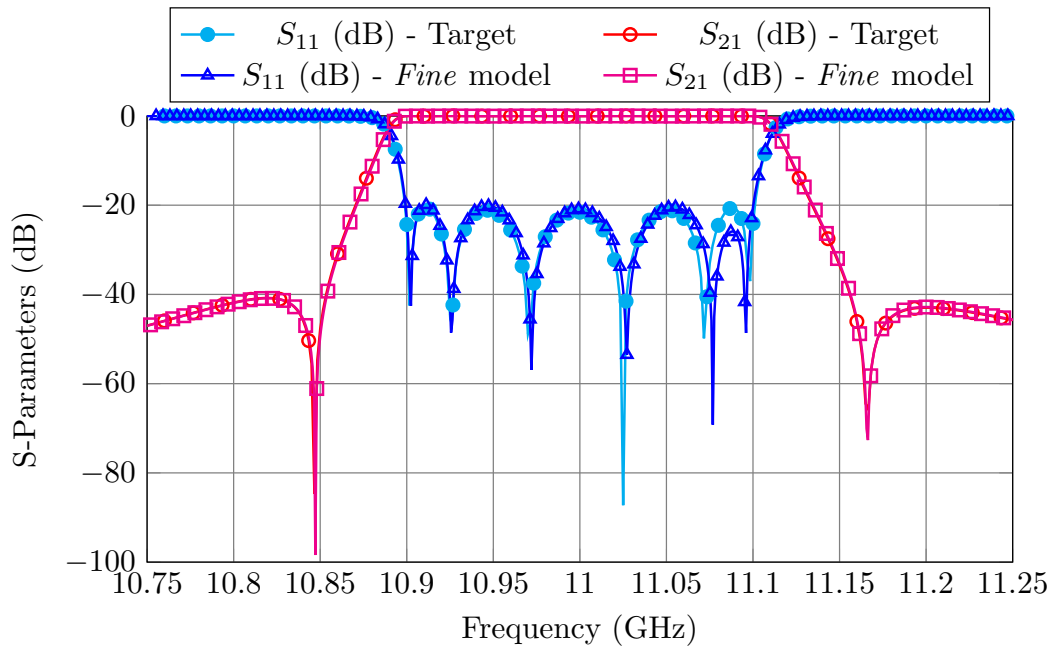


Figure 3.33: Last ASM iteration considering all design parameters.

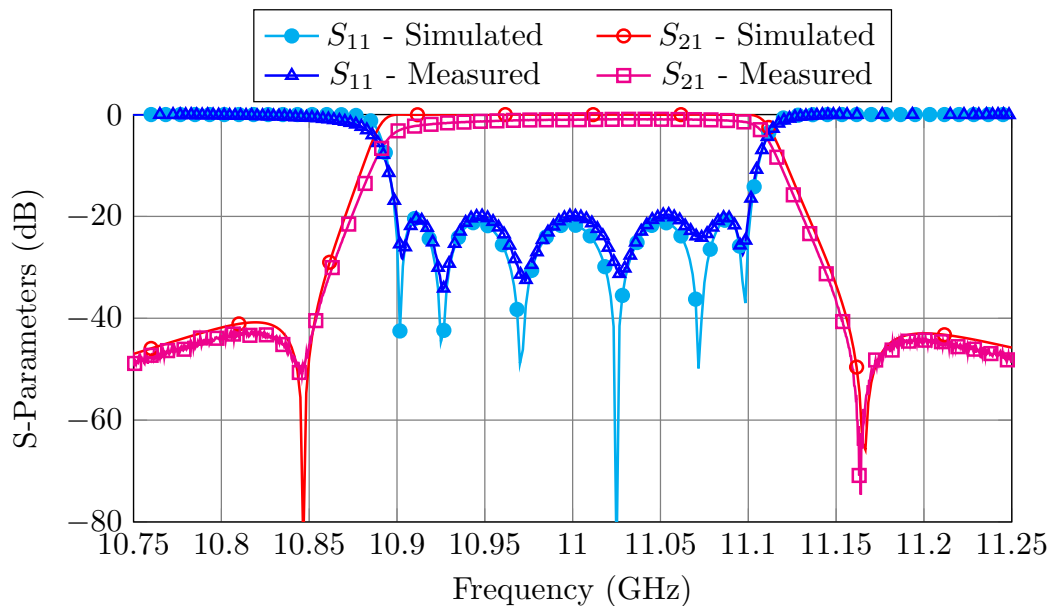


Figure 3.34: Measured performance of the 6-pole folded filter compared to its target performance.

Table 3.6: Performance of both design methods for the folded 6-pole waveguide filter with a capacitive cross-coupling.

One-Step ASM							Step-by-Step ASM						
TC_1	0,26 s.	TF_1	173 s.	AI_1	2314	NI_1	3	TC_1	0,1 s.	TF_1	19 s.	I_1	66
TC_2	0,26 s.	TF_2	181 s.	AI_1	2273	NI_1	3	TC_2	0,11 s.	TF_2	47 s.	I_2	82
TC_3	0,26 s.	TF_3	194 s.	AI_1	2082	NI_1	2	TC_3	0,12 s.	TF_3	91 s.	I_3	127
								TC_4	0.26 s.	TF_4	194 s.	I_4	91
								TC_5	0,26 s.	TF_5	194 s.	I_5	384
Total	1 h. 51 min.						Total	17 min. 30 s.					

3.4 Design of a folded 4-pole filter with a cross-coupling

We will now demonstrate the same procedure for a different filter of a similar complexity as the one shown in Fig. 3.35. This is a 4-pole single-mode quadruplet filter of the same kind that the ones used to design the diplexer described in [84]. It is centered at 19.8 GHz and it has a bandwidth of 200 MHz. Since the filter will be manufactured by standard milling, the high precision model must include rounded corners (2 mm. radius). This filter, however, does not include tuning elements. Fig. 3.36 shows the target performance for the filter.

The settings we will use for each of the *coarse* and *fine* models are similar to the ones we used for the previous cases (see Table 3.7 for more details). The variables to be optimized are:

- The lengths of the resonators.
- The widths of the inductive apertures.
- The position of the capacitive cross-coupling.

We could have kept the cross-coupling at the center of the first resonator and optimized its width. However, that would have led to an unrealizable narrow window. Instead, we fixed its width to 2 mm and optimized its location (or offset) to change the coupling level.

3.4.1 One-Step ASM

The *coarse* model that we used for the OS-ASM procedure is shown in Fig. 3.37. Following the same strategy we used for the folded 6-pole filter, we will perform the OS-ASM in two steps:

1. The first step consist in obtaining the desired performance using a high precision model with sharp 90° corners. After two ASM iterations, the first high precision

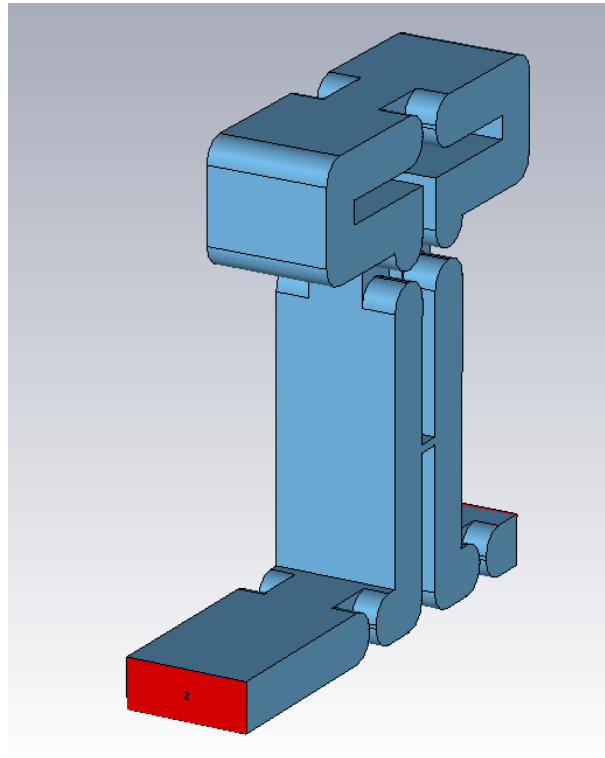


Figure 3.35: Final model used for the 4-pole single-mode quadruplet filter.

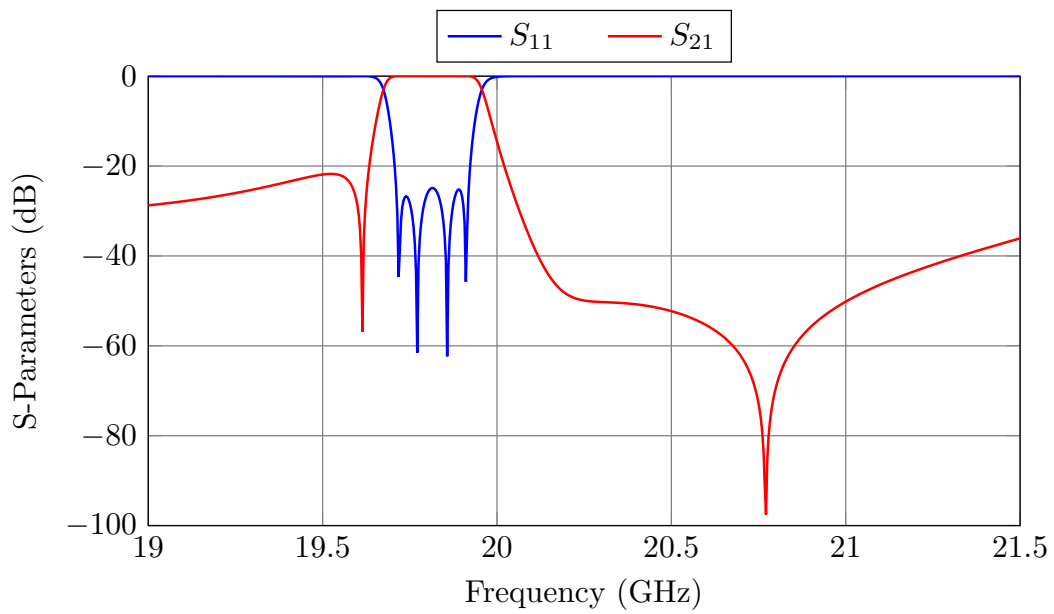


Figure 3.36: Target performance for the 4-pole single-mode quadruplet filter.

Table 3.7: Accuracy settings used for the 4-pole single-mode quadruplet filter.

Coarse Model	
Simulator	FEST3D
Accessible modes	10
Number of basis functions	30
Green's function terms	300
Fine Model	
Simulator	CST Microwave Studio
Solver	Frequency Domain Solver
Frequency Sweep	General Purpose
Mesh refinement	19.8 GHz
Error Threshold	0.005
Maximum number of iterations	20

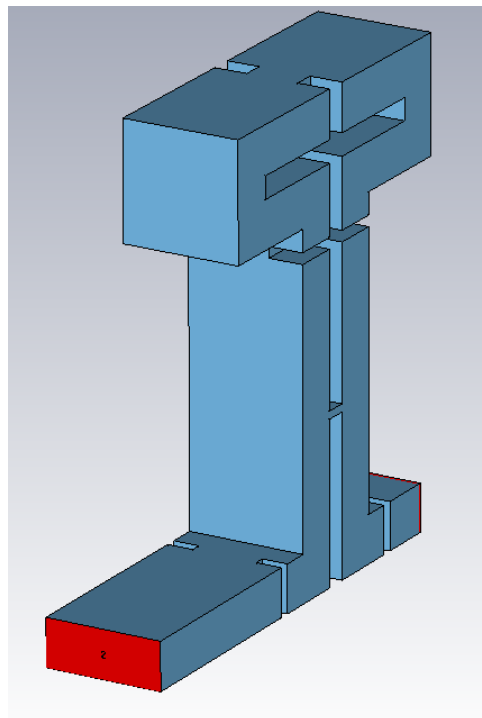


Figure 3.37: Coarse model used for the 4-pole single-mode quadruplet filter.

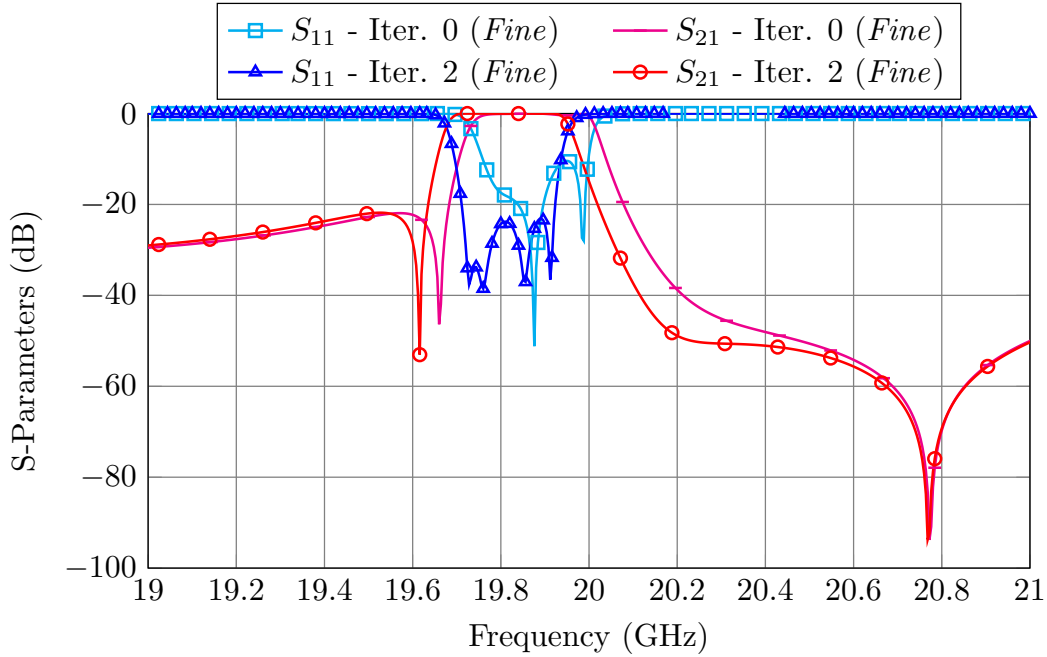


Figure 3.38: Performance of the high precision model with sharp 90° corners after two ASM iterations.

model provides the desired performance (see Fig. 3.38).

2. We can now add the round corners to the *fine* model, obtaining the structure shown in Fig. 3.35. Since the initial performance of the model is very far from the desired target, we now need to perform five ASM iterations in order to recover the desired performance (see Fig. 3.39).

The overall time required to design the 4-pole single-mode quadruplet filter using this approach can be computed as:

$$\text{Time} = \sum_{i=1}^{\text{Stages}} TC_i \cdot AI_i \cdot NI_i + (NI_i + 1) \cdot TF_i = 8 \text{ h. } 33 \text{ min. } 16\text{s.} \quad (3.18)$$

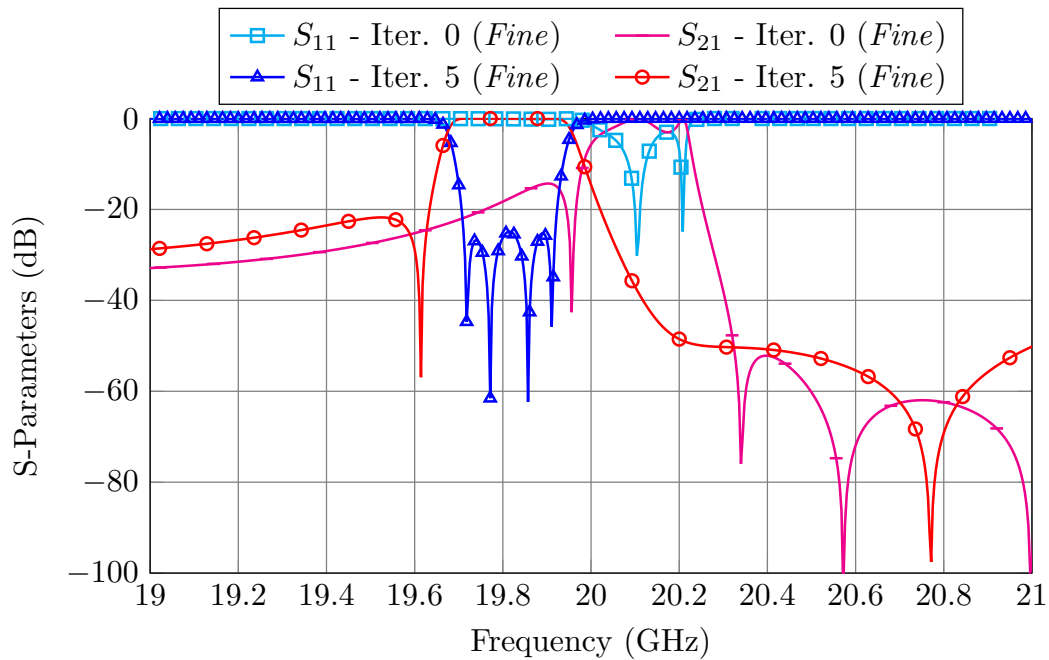


Figure 3.39: Performance of the high precision model with round corners after five ASM iterations.

3.4.2 Step-by-Step ASM

The design process for the quadruplet using the Step-by-Step approach is as follows:

1. Start with the reduced *fine* and *coarse* models shown in Fig. 3.40 that only include the first three elements of the filter. After only one ASM iteration, both models will provide the same performance, as shown in Fig. 3.41.
2. Add then the next two elements of the filter: the second cavity and the third aperture. Fig. 3.42 shows the *fine* and *coarse* models used at this stage. After one ASM iteration with two parameters, both models provide essentially same performance (see Fig. 3.43).
3. At this point we can duplicate the *fine* model and add the capacitive coupling obtaining the structure shown in Fig. 3.35. After one ASM iteration with two parameters (the position (or offset) of the capacitive coupling and the length of the resonators connected to it), the performance of the model is very close to the target.
4. A final ASM iteration using the models shown in Figs. 3.37 (*coarse*) and 3.35 (*fine*) is then performed to obtain the desired target performance. Fig. 3.44 shows the final response of the filter.

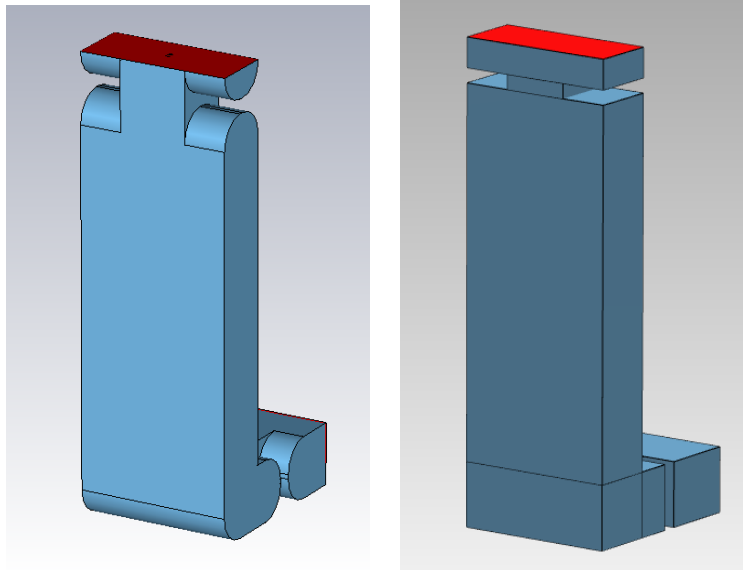


Figure 3.40: First three elements of the first reduced model of the quadruplet. Left: *Fine*. Right: *Coarse*.

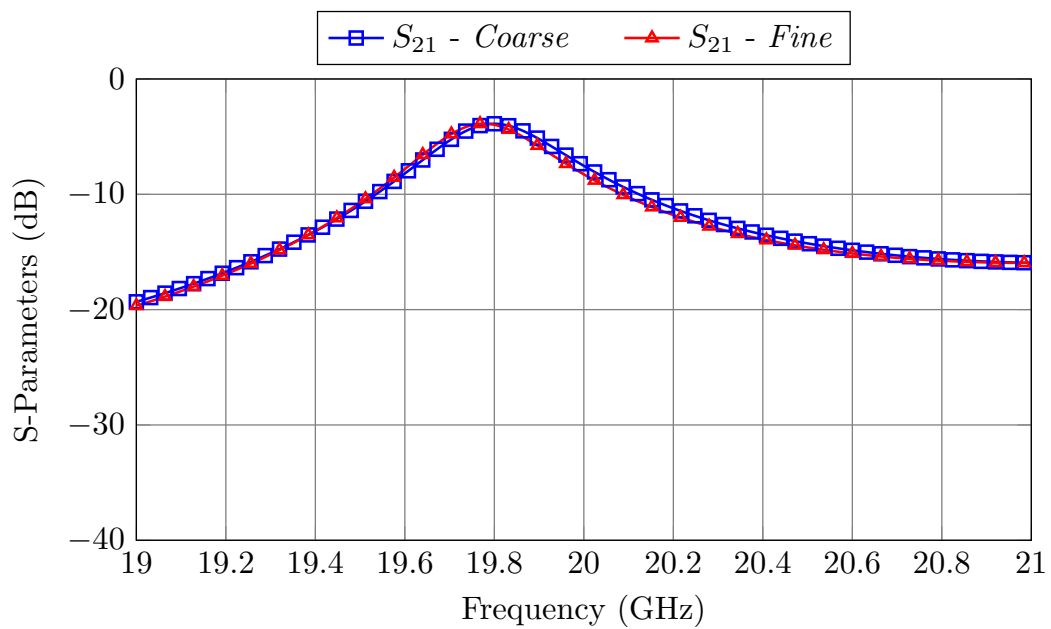


Figure 3.41: Performance of the reduced *fine* and *coarse* models after only one ASM iteration.

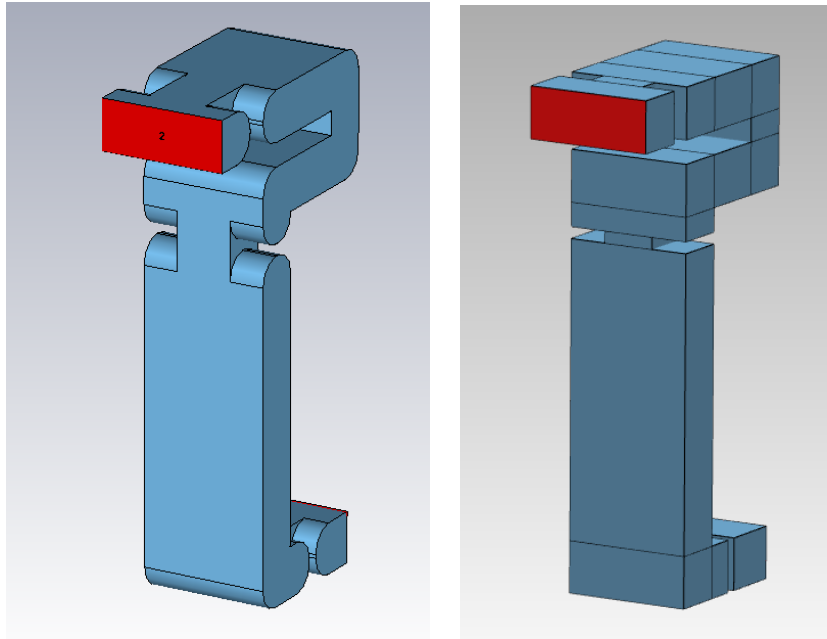


Figure 3.42: Second reduced model for the quadruplet. Left: *Fine*. Right: *Coarse*.

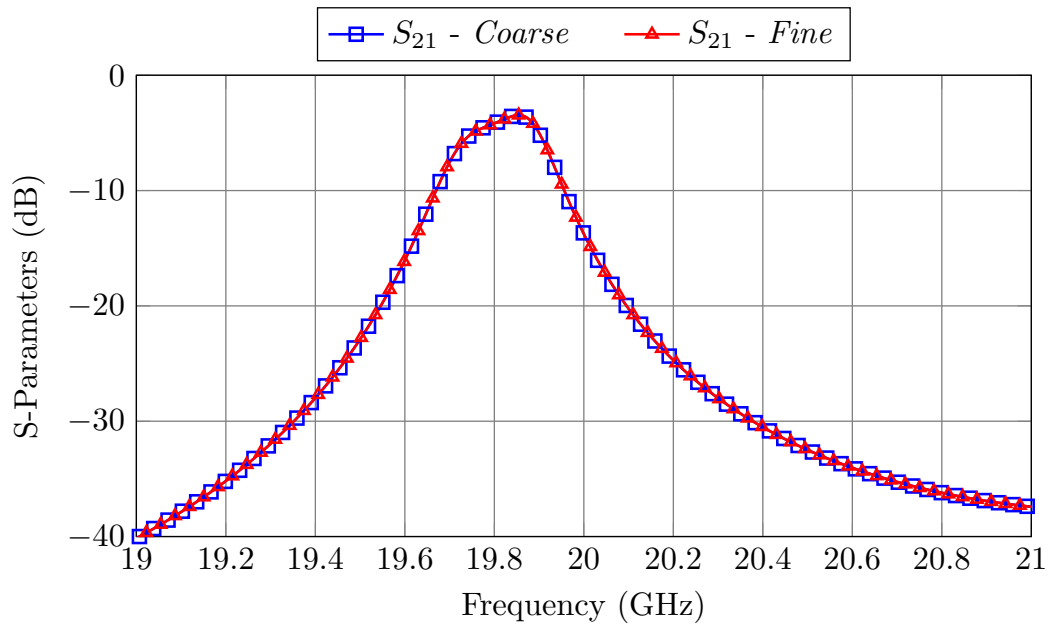


Figure 3.43: Performance of the second reduced *fine* and *coarse* models after only one ASM iteration.

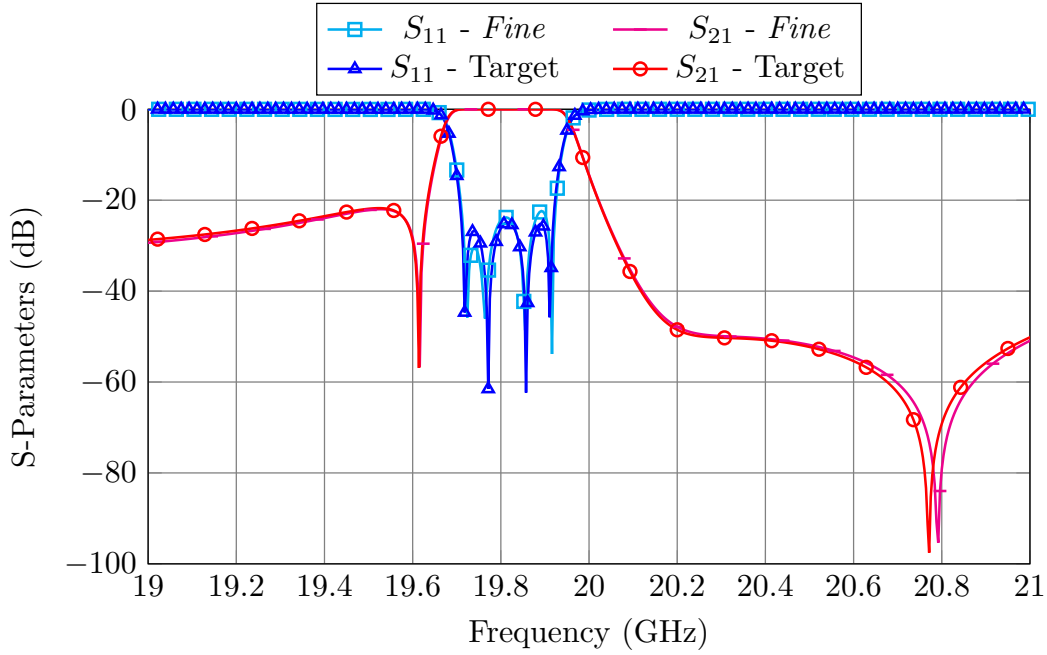


Figure 3.44: Performance of the high precision model compared to its target.

Table 3.8: Performance of both design methods for the quadruplet.

One-Step ASM								Step-by-Step ASM						
TC_1	6.1 s.	TF_1	65 s.	AI_1	675	NI_1	2	TC_1	3.09 s.	TF_1	25 s.	I_1	63	
TC_2	6.1 s.	TF_2	83 s.	AI_1	717	NI_1	5	TC_2	4.57 s.	TF_2	63 s.	I_2	87	
								TC_3	5.4 s.	TF_3	75 s.	I_3	91	
								TC_4	6.1 s.	TF_4	83 s.	I_4	215	
Total	8 h. 33 min. 16 s.							Total	48 min. 7 s.					

The overall time required to design the 4-pole quadruplet is computed as:

$$\text{Time} = \sum_{i=1}^{\text{Stages}} TC_i \cdot I_i + 2 \cdot TF_i = 48 \text{ min. } 7 \text{ s.} \quad (3.19)$$

The Step-by-Step ASM has reached the target performance **10.6 times faster** than OS-ASM. Table 3.8 shows the detailed performance of each procedure.

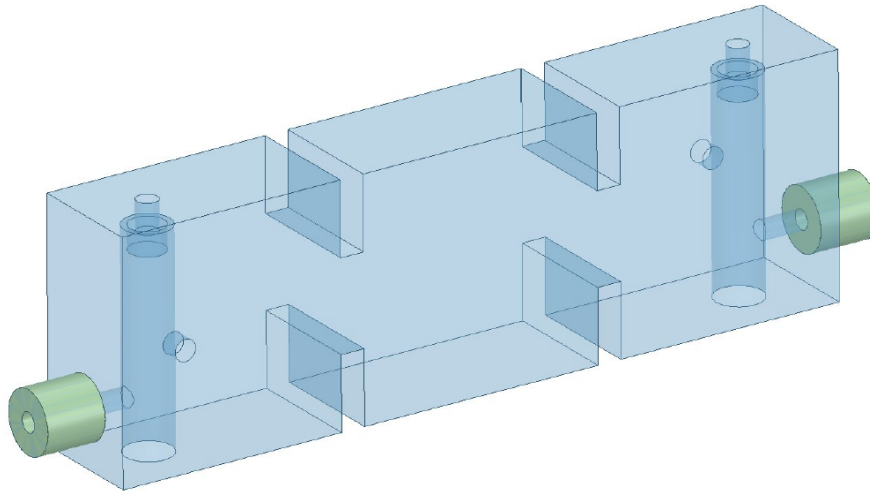


Figure 3.45: Initial model of the 5-pole filter with sharp 90° corners and without tuning elements (Fig. 1 from [85]). Note that the cylinder orthogonal to the post is used to couple the modes of the dual-mode resonator.

3.5 Design of a 5-pole filter based on dual-mode coaxial resonators

The last case study is a symmetric 5-pole band-pass filter based on dual-mode coaxial resonators [85]. Fig 3.45 shows the topology of the filter. There are two modes resonating in the first and last cavity: the second resonance of the re-entrant post and the first resonance of the rectangular cavity (the metallic enclosure). The filter has been manufactured using milling. The final model must therefore include round corners with a radius of 2 mm. It must also include tuning elements (0.9 mm radius) that are set at a fixed depth of 1 mm. Fig. 3.46 shows the the final (*fine*) model of the filter. The filter is centered at 10 GHz and has a bandwidth of 300 MHz. Fig. 3.47 shows the desired target response.

The variables that are optimized are (see Fig. 3.48):

- Lengths of the cavities.
- Widths of the irises (their thickness is fixed to 2 mm).
- Height of the re-entrant post (h_s).
- Height and offset of the cylinder that couples the modes (h_a and l_a).
- Offset of the coaxial input/output (l_c).
- Length of the probe from the coaxial connector to the post (l_p).

The *coarse* model is simulated with FEST3D with a precision setting similar to the one of the previous examples. The high precision model is again simulated with CST. Table 3.9 shows the simulation setups used for each case.

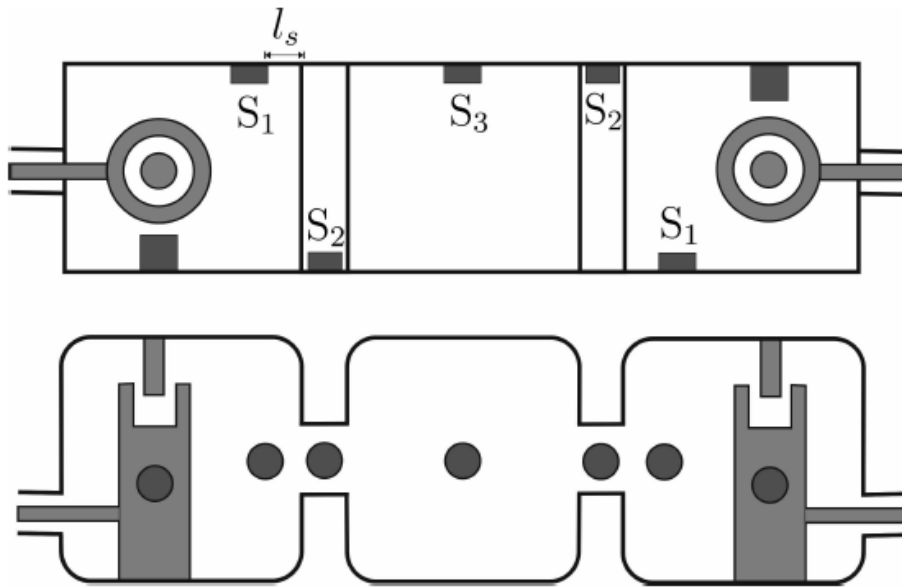


Figure 3.46: Final model of the 5-pole filter with round corners and tuning elements (Fig. 26 from [85]).

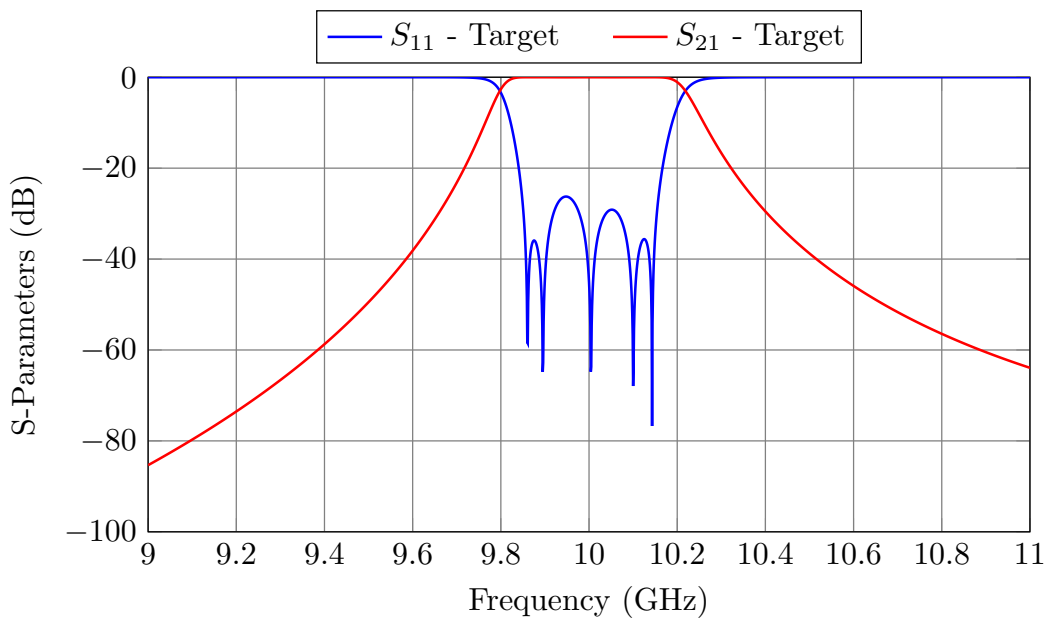


Figure 3.47: Target performance for the 5-pole filter based on dual-mode coaxial resonators.

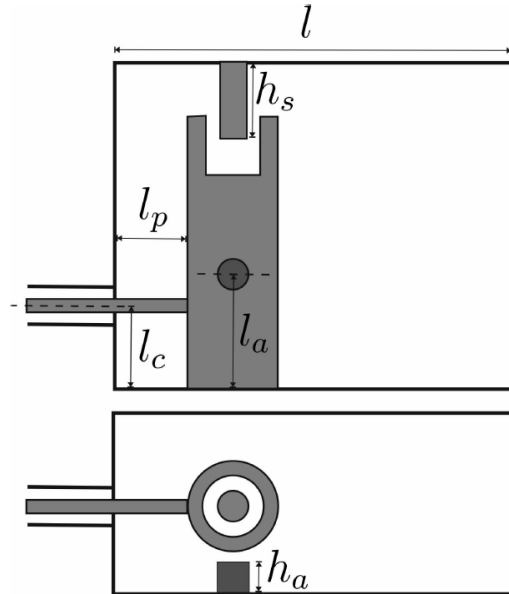


Figure 3.48: Dimensions that are optimized in the design process (Fig. 15 from [85]).

Table 3.9: Accuracy settings used for the 5-pole filter based on dual-mode coaxial resonators.

Coarse Model	
Simulator	FEST3D
Accessible modes	10
Number of basis functions	30
Green's function terms	300
General Cavity's Solver:	BI-RME 3D RWG
Maximum Frequency:	60 GHz
Fine Model	
Simulator	CST Microwave Studio
Solver	Frequency Domain Solver
Frequency Sweep	General Purpose
Mesh refinement	19.8 GHz
Error Threshold	0.005
Maximum number of iterations	20

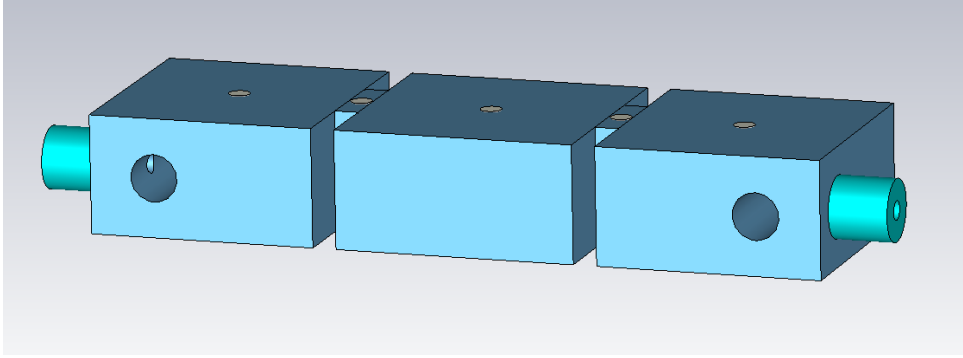


Figure 3.49: *Fine* model of the filter using tuning elements.

3.5.1 One-Step ASM

The One-Step ASM procedure for this particular filter is as follows:

1. Since the *coarse* model simulation in this case is relatively accurate, we can try directly to introduce the tuning elements in the *fine* model (see Fig. 3.49). After three ASM iterations, both models provide a very similar response (see Fig. 3.50).
2. We can now add the rounded corners to the *fine* model (obtaining the structure shown in Fig. 3.46) and repeat the OS-ASM process. After three ASM iterations, the desired performance is recovered (see Fig. 3.51).

The overall time required to design the 5-pole filter based on dual-mode coaxial resonators using this approach can be computed as:

$$\text{Time} = \sum_{i=1}^{\text{Stages}} TC_i \cdot AI_i \cdot NI_i + (NI_i + 1) \cdot TF_i = 19 \text{ h. } 22 \text{ min. } 28\text{s.} \quad (3.20)$$

It is important to note that the *coarse* model is particularly slow due to the presence of the re-entrant posts in the first and last cavity and thus, each ASM recovery takes a long time.

3.5.2 Step-by-Step ASM

In this case, the segmentation of the problem into smaller optimization spaces is more challenging. This is because the first cavity already includes six out of the eight design variables. One possibility to further simplify the design process could be to follow the procedure that was used originally in [85], namely:

1. Obtain first the correct input coupling (optimizing l_c) and the appropriate resonances for the rectangular cavity and post (optimizing l and h_s). To do this, we

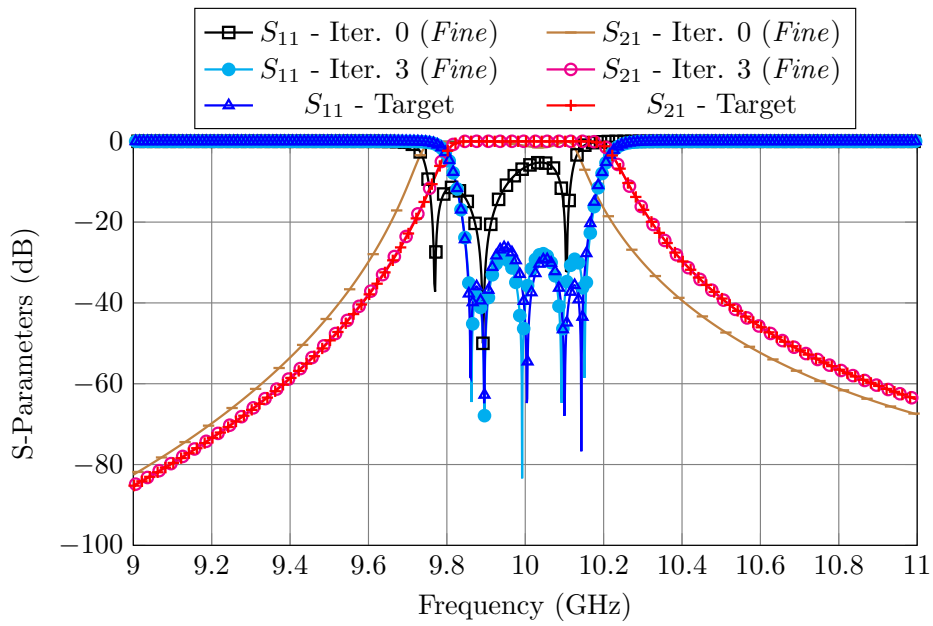


Figure 3.50: ASM process to recover the desired performance in the *fine* model that uses tuning elements.

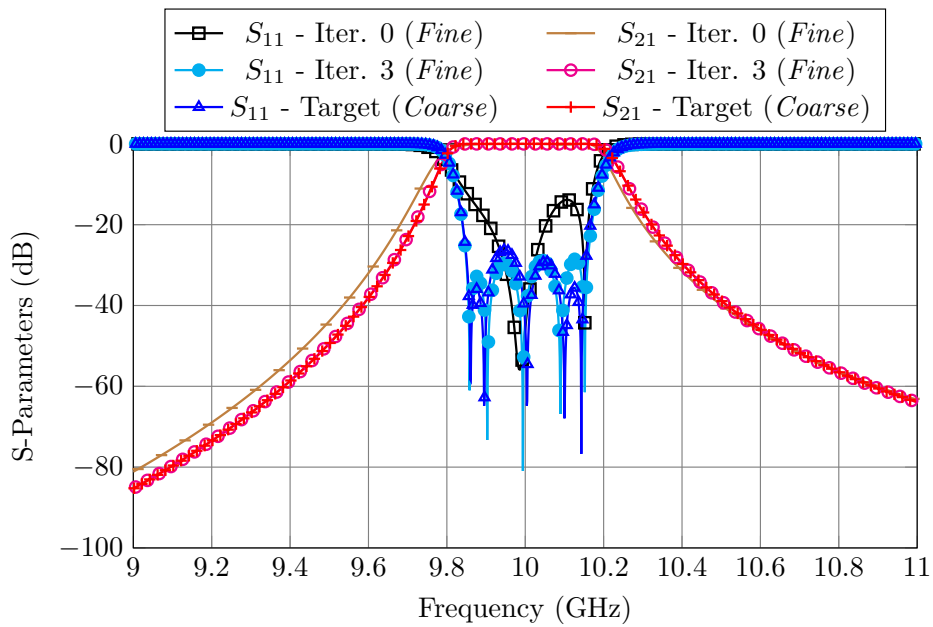


Figure 3.51: ASM process to recover the desired performance in the *fine* model that includes tuning elements and rounded corners.

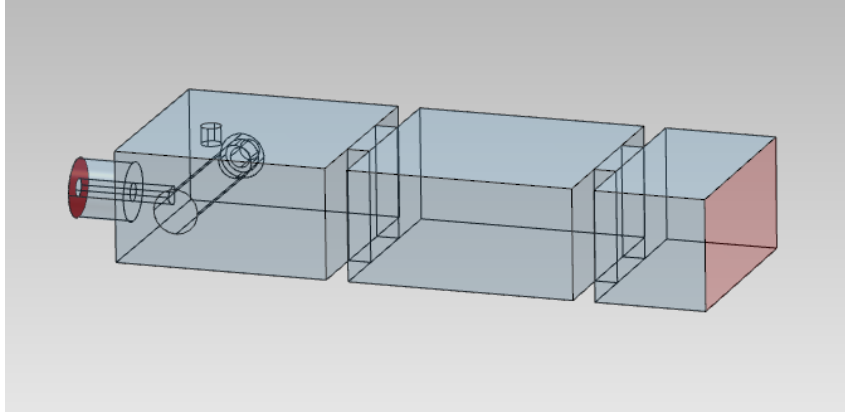


Figure 3.52: Second *coarse* model of the filter.

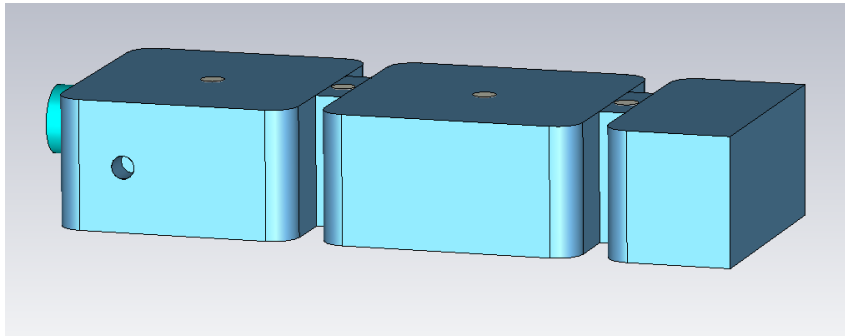


Figure 3.53: Second *fine* model of the filter.

can use the structure shown in Fig. 3.48 for the *coarse* model and a similar one, but including rounded corners and tuning elements, for the *fine* model.

2. Obtain then the correct coupling between the two modes (optimizing h_a , l_a and l_p). To do this we can use the same *coarse* and *fine* models from the previous step.
3. Optimize the coupling from the dual-mode cavity to the central rectangular resonator (optimizing the length of the new cavity and the width of the iris). Figs. 3.52 and 3.53 shows the *coarse* and *fine* models used for this stage.
4. Finally, apply symmetry to the reduced *fine* model to obtain the first high precision model of the filter.

This approach, however, is complicated by the fact that the first 6 variables are not independent. As a consequence, in each stage we would have to re-optimize all design dimensions. The approach that resulted in a much faster design is as follows:

1. Generate a first *fine* fine model of the filter that includes the coaxial input, first cavity (with all its elements) and the first iris (see Fig. 3.54, right). Use the *coarse* model shown in Fig. 3.54, left, and apply the OS-ASM method. After two ASM

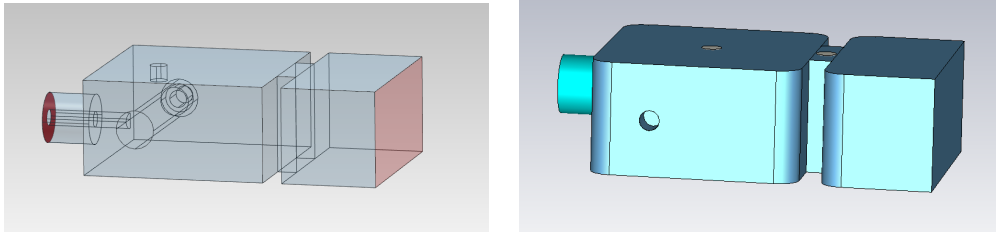


Figure 3.54: First reduced model of the filter. Left: *Coarse*. Right: *Fine*.

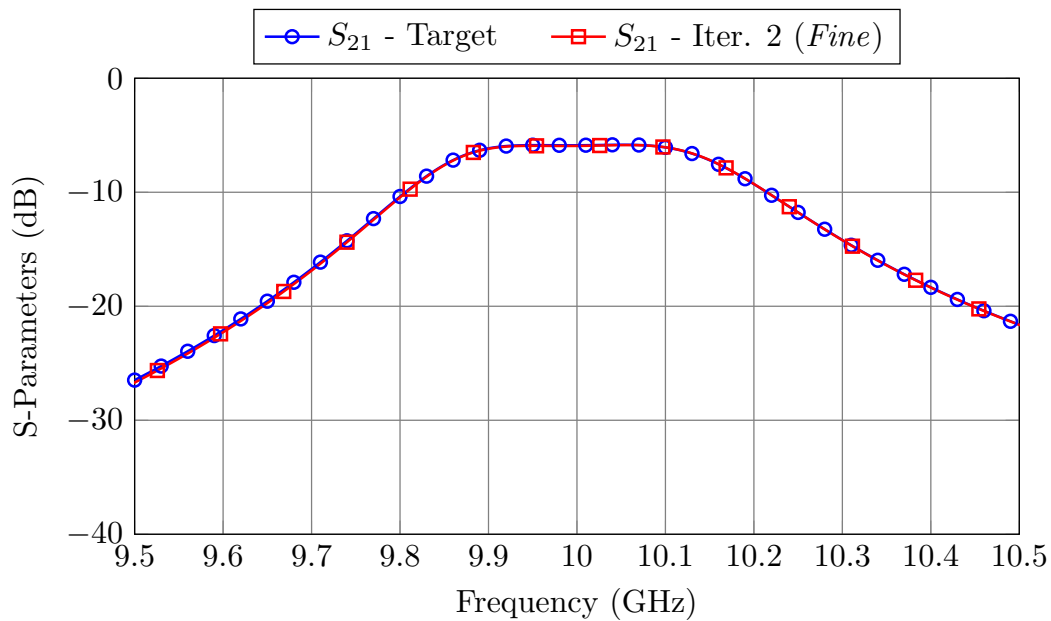


Figure 3.55: ASM process to recover the desired performance in the first reduced *fine* model.

iterations, both models provide the same result (see Fig. 3.55). It is important to note that even if we are optimizing seven parameters (all the dimensions from Fig. 3.54), the *reduced coarse* model is twice as fast as the original *coarse* model.

2. Add then the next resonator and iris to the *fine* model, obtaining the second *fine* model shown in Fig. 3.53. Perform one ASM iteration optimizing, primarily but not exclusively, the newly added elements. Fig. 3.56 shows the performances of the *fine* and *coarse* models after the ASM process.
3. Finally, duplicate the *fine* model to obtain the complete structure (as shown in Fig. 3.46). After only one ASM iteration with all the design parameters, the high precision model gives the desired performance (see Fig. 3.57).

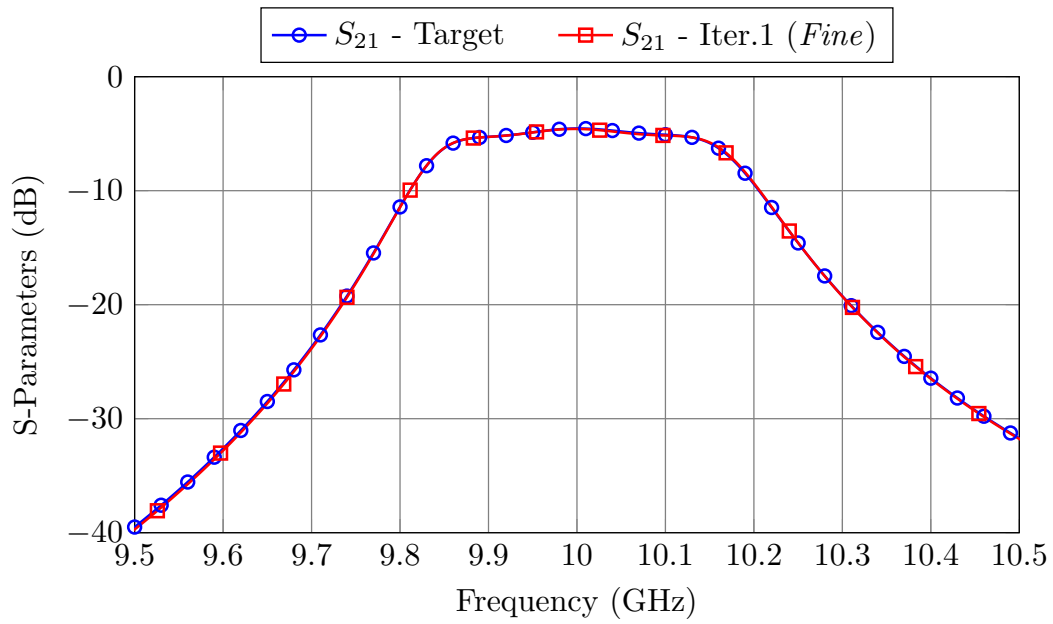


Figure 3.56: ASM process to recover the desired performance in the second reduced *fine* model.

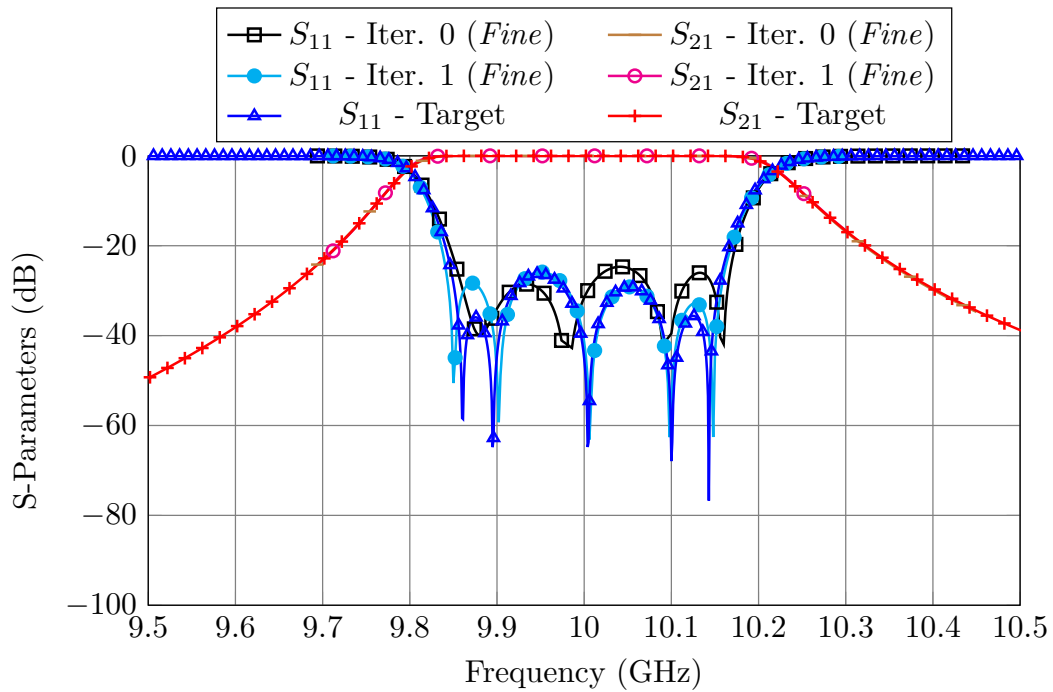


Figure 3.57: Final performance of the *fine* model compared to the design target.

Table 3.10: Performance of both design methods for the 5-pole filter based on dual-mode coaxial resonators.

One-Step ASM							
TC_1	15.74 s.	TF_1	371 s.	AI_1	729	NI_1	3
TC_2	15.74 s.	TF_2	386 s.	AI_1	684	NI_1	3
Total	19 h. 22 min. 28 s.						
Step-by-Step ASM							
TC_1	8.07 s.	TF_1	123 s.	AI_1	251	NI_1	2
TC_2	8.23 s.	TF_2	176 s.	AI_2	204	NI_2	1
TC_3	15.74 s.	TF_3	386 s.	AI_3	372	NI_3	1
Total	3 h. 37min. 58 s.						

The overall time required to design the 5-pole band-pass filter is computed as:

$$\text{Time} = \sum_{i=1}^{\text{Stages}} TC_i \cdot AI_i \cdot NI_i + (NI_i + 1) \cdot TF_i = 3 \text{ h. } 37 \text{ min. } 58 \text{ s.} \quad (3.21)$$

The same result obtained with One-Step ASM approach has now been obtained **5.3 times faster**. Table 3.10 shows the time performance of each procedure.

Even though we could not use a reduced optimization space in each stage of the procedure, we have been able to use smaller circuits (reduced models). As we can clearly see, using partial models does have a massive impact in the overall time required to design the filter.

3.6 Conclusions

In this chapter, we have presented a procedure (Step-by-Step ASM) that allows us to go from the simplest low precision model to the final high precision structure of a filter exploiting the power of both ASM and segmentation techniques.

We have provided four different examples. Two of them have been also validated with experimental measurements. In each case, the new procedure has proved to be significantly faster than the direct OS-ASM method.

Finally, it is important to note is that we have taken advantage of the fact that \mathbf{B} can be approximated by the identity matrix, since the *coarse* and *fine* models belong to the same physical space. However, the segmentation strategy that we have discussed can also be used in situations where the models do not belong to the same space. In that case, after each ASM iteration, it would be necessary to update the required mapping matrix.

On Aggressive Space Mapping Techniques for Filter Tuning

Minimizing the cost of filters is usually a must in any industrial context. As discussed in Chapter 2, a common solution is to use a low accuracy manufacturing technique together with tuning elements to be adjusted manually once the filter is fabricated. However, the manual tuning of microwave filters is a complex task that remains difficult without significant previous experience [39]. For that reason, many CAD procedures have been developed to assist us with the cumbersome filter tuning process.

One of the most promising filter tuning approaches is to use SM and ASM. There are many SM-based tuning procedures in the recent literature. To name a few, ASM was used in [27] to correct the manufacturing errors in a circular-waveguide dual-mode (CWDM) filter. Instead of using tuning screws, rectangular-shaped metal inserts were employed, together with a few SM iterations, to obtain a compliant filter response. In [86], ASM was also used for the fast tuning of a 3D-printed lossy waveguide filter.

Even though these solutions are effective, they all have a common drawback: the mapping matrix between the *coarse* model and the real filter is estimated around a highly detuned point, and thus, the convergence of these methods is slow.

In this chapter, we will show how we can exploit different simulation models to obtain the optimal mapping matrix between a fast *coarse* model and the physical filter, even before the latter is manufactured. In order to do so, we will estimate the mapping matrix between the dimensions of a fast *coarse* model and the tuners' penetrations of a simplified *fine* model. We have proved that this mapping can later be used to tune the

actual filter very efficiently. In the following sections, we will compare five ASM-based tuning procedures by tuning the same six-pole filter, and we will discuss which method is more appropriate for each situation.

The results of our investigation in automated and ASM-based tuning procedures have already been published in the following journals:

- J. C. Melgarejo, M. Guglielmi, S. Cogollos and V. E. Boria, "Space mapping for tuning microwave waveguide filters," in *2019 IEEE MTT-S International Microwave Symposium Digest*, Boston, MA, USA, 2019, pp. 353-356.
- J. C. Melgarejo, J. Ossorio, S. Cogollos, M. Guglielmi, V. E. Boria and J. W. Bandler, "On space mapping techniques for microwave filter tuning," in *IEEE Transactions on Microwave Theory and Techniques*, vol. 67, no. 12, pp. 4860-4870, Dec. 2019.

4.1 Experimental Setup

In order to compare the five different tuning procedures, we will tune the same 6-pole inductive waveguide filter with all of them. Fig. 4.1 shows the body and the assembled filter. The specifications are as follows:

- $f_0 = 11$ GHz.
- Bandwidth (BW) = 500 MHz.
- Return Loss (RL) = 25 dB.
- Tuning elements: Cylindrical tuners with a radius of 1.6 mm. The filter has 13 tuning elements placed at the center of each cavity and aperture.
- Corners rounded with a 2 mm radius.

To implement an automatic tuning procedure, we first need to develop a system that allows us to modify the penetration of the various tuning elements very accurately. To this end, we have built the precision robotic arm shown in Fig. 4.2. The robotic arm has three parts: a movable X-Y table to which the filter is attached, a high precision rotating actuator that can be coupled to the tuning elements, and a computer driven controller to operate the whole machine.

The X-Y table is used to position each tuner under the robotic arm. For the time being, coupling the precision rotating actuator to each tuner is done manually. The theoretical backlash of the tuners is around 2-3°. However, in practice, we have observed that the angular accuracy of the system is around 10°. Since the tuning elements we use have a pitch of 0.397 mm, the uncertainty of the whole system can be obtained with the following expression:

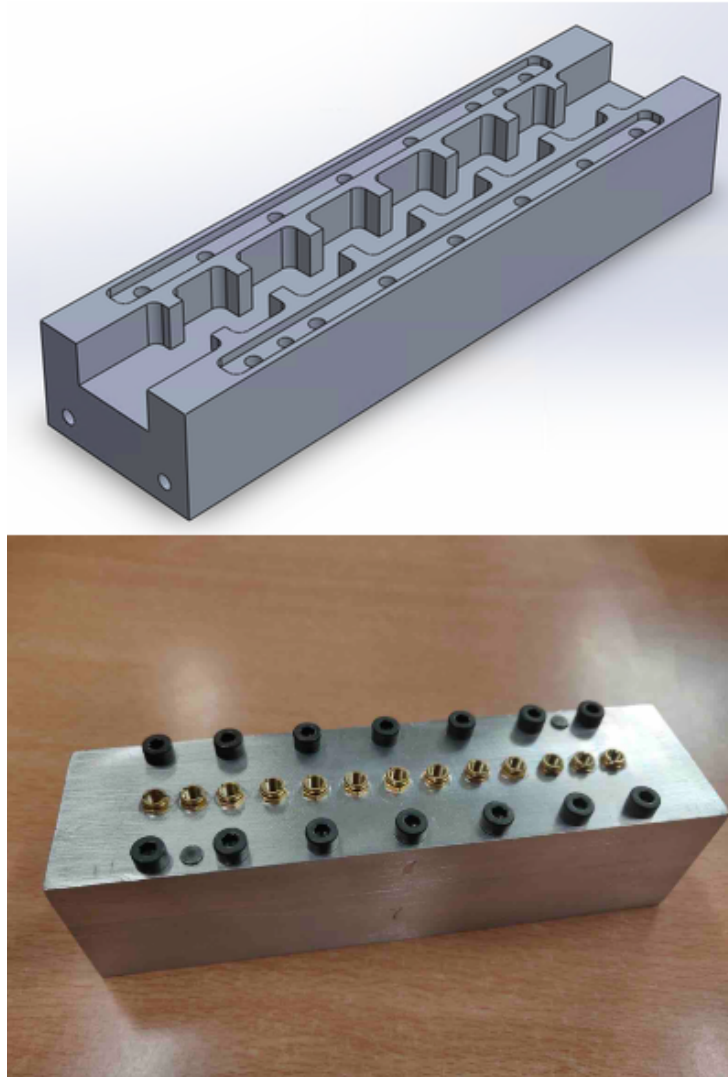


Figure 4.1: 6-Pole inductive filter with tuning elements.

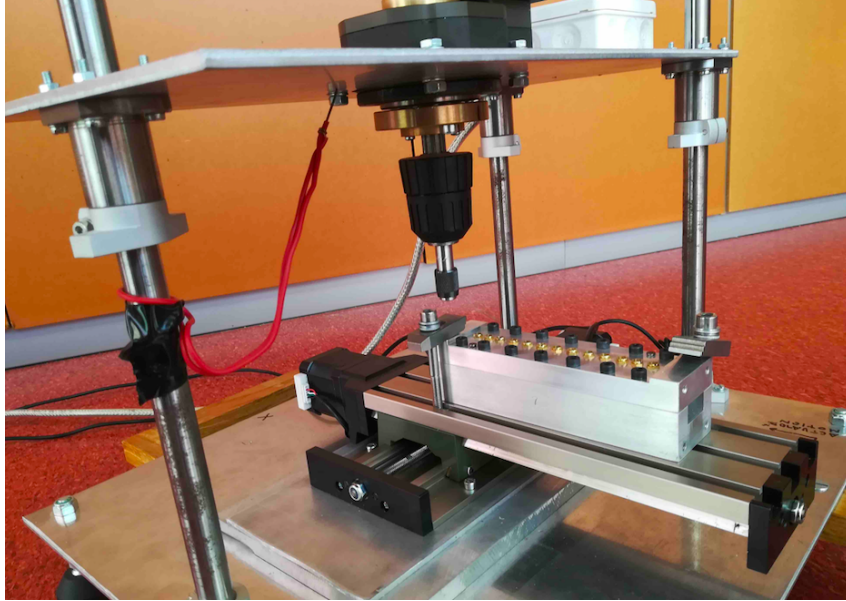


Figure 4.2: Precision robotic arm that is used to modify the penetration of the tuning screws.

$$h_{min} = \frac{10^\circ \cdot 0.397 \text{ mm}}{360^\circ} = 0.011 \text{ mm} \quad (4.1)$$

That means that the maximum tuning accuracy for the penetration depth of each tuner is around $10 \mu\text{m}$. This is, indeed, enough to successfully tune our filter.

4.2 Tuning procedures

In this section, we are going to compare five tuning techniques. The first technique is based on the procedure described in [27] and [35]. It is an ASM-based technique where the *coarse* model includes tuning elements. The penetrations of the tuning elements in the *coarse* model are optimized until the measured performance is recovered, and then, the tuners of the real filter are then modified in the opposite direction. This technique is the simplest and the most time consuming ASM-based procedure we can use. We will only use this technique as a reference to compare the performances of the other four procedures. The methods that we propose (procedures II-V), use a pre-computed estimation of the mapping matrix that can speed the filter tuning process up to 22 times. The key features of these methods are the following:

- The *coarse* model does not include tuning elements and thus, each recovery of the measured performance is significantly faster.
- The estimation of the optimal mapping matrix (around the tuned response) can be

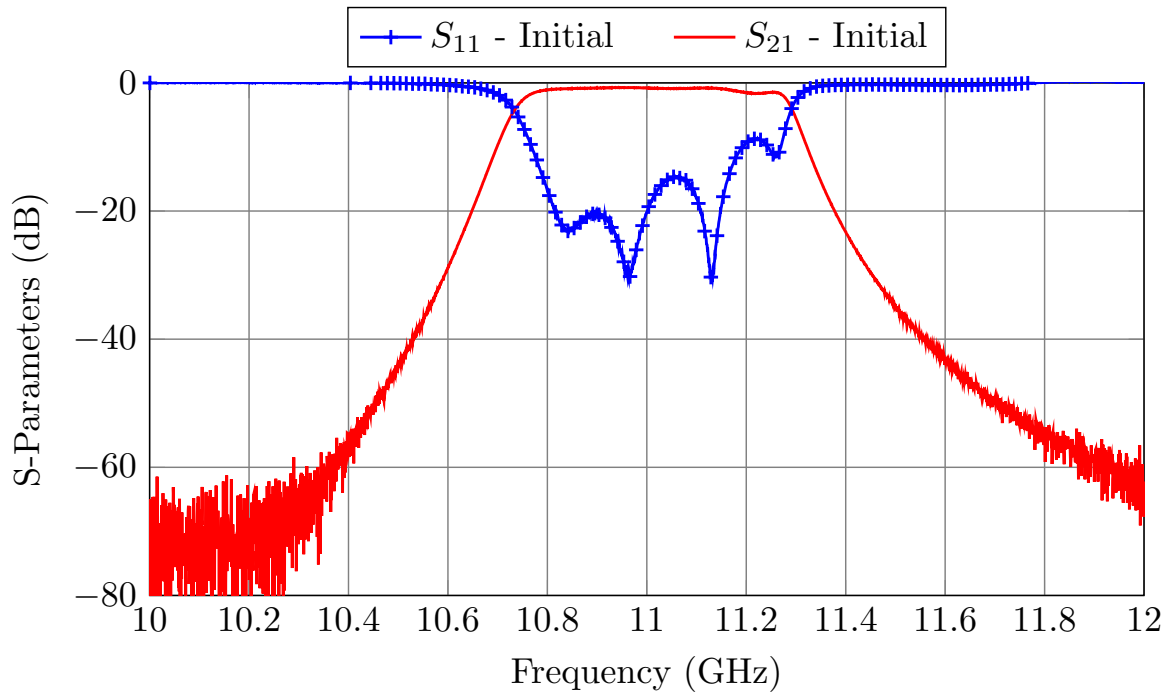


Figure 4.3: Performance of the filter when all tuning elements are set to the design depth.

easily obtained by simulation.

For the starting point of each tuning procedure, we will set all tuning elements to the design depth of 2 mm. The resulting initial performance of the real filter is highly detuned, as we can see in Fig. 4.3.

4.2.1 Procedure I

As it was mentioned above, the *coarse* model of the first tuning procedure is a low precision model that includes tuning elements (see Fig. 4.4). The *fine* model in this case is the measured filter. The *coarse* model is simulated with FEST3D with the following set of parameters:

- Accessible modes = 10
- Number of basis functions = 30
- Green's function terms = 300

The filter tuning procedure is very straightforward: we optimize the penetrations of the tuning elements in the *coarse* model to recover the measured (*fine*) response. We then modify the penetrations of the tuning elements of the real filter in the opposite direction, namely:

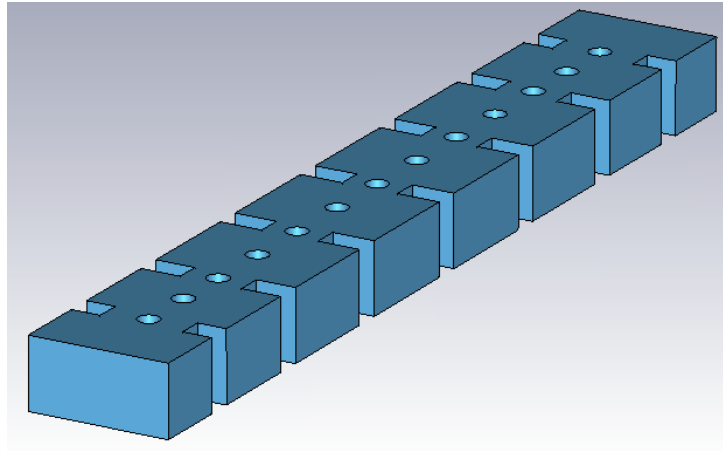


Figure 4.4: Low precision model that includes tuning elements.

Table 4.1: Performance of Procedure I.

TC	NI	AI	$Total$
7.3 s	4	762	6 h 10 min 50 s

$$\Delta = -\mathbf{B}(\mathbf{x}_{\mathbf{cr}} - \mathbf{x}_{\mathbf{copt}}) \approx -(\mathbf{x}_{\mathbf{cr}} - \mathbf{x}_{\mathbf{copt}}), \quad (4.2)$$

where $\mathbf{x}_{\mathbf{copt}}$ is the vector with the design depths (2 mm) and $\mathbf{x}_{\mathbf{cr}}$ are the recovered penetrations of the tuners. Note that since both models (*coarse* and *fine*) belong to the same space (tuning penetrations), the mapping matrix \mathbf{B} can be approximated by the identity matrix. After only four ASM iterations, the filter is properly tuned, as shown in Fig. 4.5.

The filter was indeed tuned in only four iterations. However, each iteration took a considerable amount of time. This is because, since the *coarse* model includes tuning elements, the relevant FEST3D element must be simulated using BI-RME 3D, which increases the simulation time considerably. Table 4.1 shows the performance of this method. The total time is computed as:

$$Total = TC \cdot AI \cdot NI, \quad (4.3)$$

where TC is the computation time of the *coarse* model, NI is the number of ASM iterations and AI is the average number of simulations performed by a Simplex algorithm in order to recover each measured response.

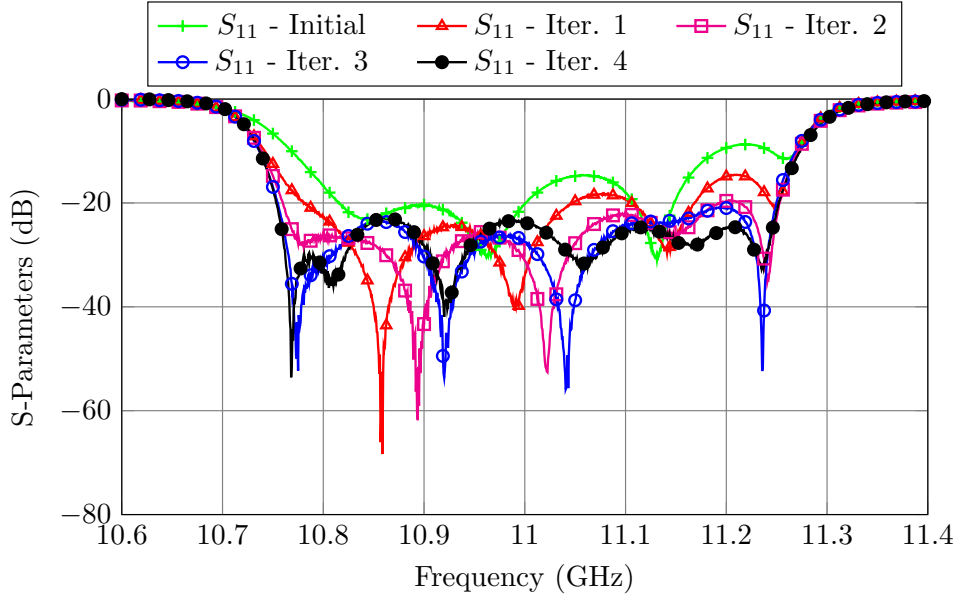


Figure 4.5: Procedure I: Filter performance after every ASM iteration.

4.2.2 Procedure II

A more efficient approach is to use a faster *coarse* model, like the one shown in Fig. 4.6. This model, however, does not include tuning elements, and therefore, we need to estimate the mapping matrix (\mathbf{B}) that relates the penetrations of the screws in the real filter with the waveguide dimensions of the *coarse* model.

Luckily, we can estimate the \mathbf{B} matrix by **simulation**. The final model of the filter (the one that was manufactured) includes both rounded corners and tuning elements (see Fig. 4.7). We have a *fine* (Fig. 4.7) and a *coarse* model (Fig. 4.6) that were already aligned during the design procedure (see Fig. 4.8). In this case, the *coarse* model is simulated with FEST3D and the *fine* model is simulated with CST Microwave Studio (see Table 4.2 for more details regarding the simulation setups).

In the vicinity of the aligned responses ($\mathbf{x}_{f\text{opt}}$ and $\mathbf{x}_{c\text{opt}}$) we can assume that the mapping between the spaces is linear, so that:

$$\mathbf{x}_f = \mathbf{B} \cdot \mathbf{x}_c + \mathbf{C}, \quad (4.4)$$

where \mathbf{x}_f is the $N \times 1$ vector with the penetrations of the N tuning elements in the *fine* model, \mathbf{x}_c is the $N \times 1$ vector with the waveguide dimensions of the *coarse* model and \mathbf{B} and \mathbf{C} are the $N \times N$ matrix and $N \times 1$ vector that define the linear mapping, respectively.

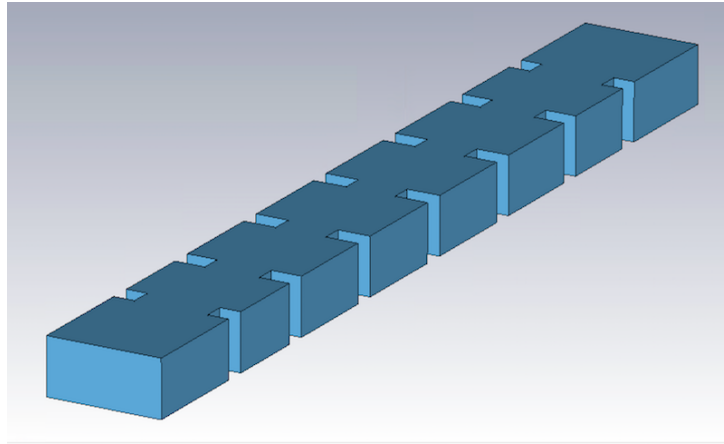


Figure 4.6: Fast low precision model that does not include tuning elements.

Table 4.2: Accuracy settings used for the 6-pole inductive filter.

Coarse Model	
Simulator	FEST3D
Accessible modes	10
Number of basis functions	30
Green's function terms	300
Fine Model	
Simulator	CST Microwave Studio
Solver	Frequency Domain Solver
Frequency Sweep	General Purpose
Mesh refinement	11 GHz
Error Threshold	0.005
Maximum number of iterations	20

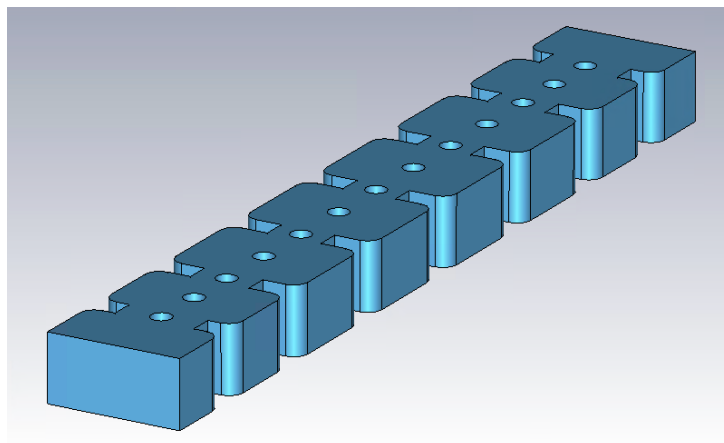


Figure 4.7: High precision model that includes tuning elements and rounded corners.

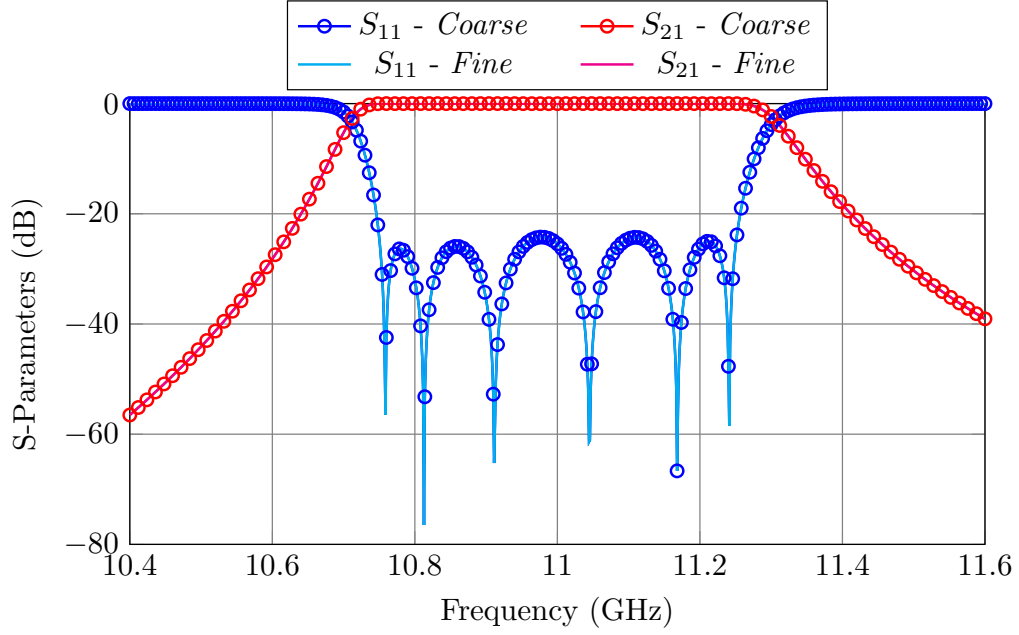


Figure 4.8: Aligned performances of the *coarse* and *fine* models ($\mathbf{R}_c(\mathbf{x}_{c\text{opt}}) = \mathbf{R}_f(\mathbf{x}_{f\text{opt}})$).

In order to compute \mathbf{B} , we will now perturb slightly the *fine* model, one tuning element at a time. Each time we will modify a penetration depth by $+0.1$ mm. We will then optimize the *coarse* model until each *fine* response has been recovered:

$$\mathbf{R}_c(\mathbf{x}_{c_i}) = \mathbf{R}_f(\mathbf{x}_{f_i}) \quad \forall i = 1, 2, \dots, N \quad (4.5)$$

We can now establish differences between the alignment point $\mathbf{x}_{f\text{opt}}$, and \mathbf{x}_{f_i} :

$$\begin{aligned} \mathbf{x}_{f\text{opt}} &= \mathbf{B} \cdot \mathbf{x}_{c\text{opt}} + \mathbf{C} \\ \mathbf{x}_{f_i} &= \mathbf{B} \cdot \mathbf{x}_{c_i} + \mathbf{C} \\ \mathbf{x}_{f\text{opt}} - \mathbf{x}_{f_i} &= \mathbf{B} \cdot (\mathbf{x}_{c\text{opt}} - \mathbf{x}_{c_i}) \end{aligned} \quad (4.6)$$

If we rename $\mathbf{x}_{f\text{opt}} - \mathbf{x}_{f_i}$ as $\Delta\mathbf{x}_{f_i}$ and $\mathbf{x}_{c\text{opt}} - \mathbf{x}_{c_i}$ as $\Delta\mathbf{x}_{c_i}$, we obtain that:

$$\begin{aligned}\Delta \mathbf{x}_{f1} &= \mathbf{B} \cdot \Delta \mathbf{x}_{c1} \\ &\vdots \\ \Delta \mathbf{x}_{fN} &= \mathbf{B} \cdot \Delta \mathbf{x}_{cN}\end{aligned}\tag{4.7}$$

Finally, we can now solve the system for \mathbf{B} . After having computed the mapping matrix between the domains by simulation, we can now easily tune the real filter with the following procedure:

1. Set the tuning elements to the design penetration (in this case, 2 mm), and measure the initial performance (see Fig. 4.3). In the remainder of this section, we will refer to this response as to $R_m(\mathbf{x}_m)$, where \mathbf{x}_m is the vector with the penetrations of the tuning elements in the real filter.
2. We will now optimize the *coarse* model (see Fig. 4.6) until we have recovered the same performance:

$$\mathbf{R}_c(\mathbf{x}_{cm}) = \mathbf{R}_m(\mathbf{x}_m)\tag{4.8}$$

3. We will then set the tuners of the physical filter to the following penetrations:

$$\mathbf{x}_{mopt} = \mathbf{x}_m + \mathbf{B} \cdot (\mathbf{x}_{copt} - \mathbf{x}_{cm})\tag{4.9}$$

4. Go back to Step 2 and repeat the process until the filter is tuned.

After four iterations, the filter is correctly tuned (see Fig. 4.9). Despite the fact that it takes the same number of iteration as in the previous procedure, this approach is considerable faster. The *coarse* model used in this procedure does not include tuning elements, and thus, it is **50 times faster** than the *coarse* model used in the previous approach.

Another benefit compared to other ASM-based tuning techniques is that the mapping is estimated around the optimal tuned performance (Fig. 4.8), and, therefore, **it is not necessary to update the mapping matrix using the Broyden formula [22]**.

Table 4.3 shows the performance of this procedure. Three extra parameters are considered in this case: the computation time of the *fine* model (TF), the average number of simulations performed by a Simplex algorithm to recover each one of the disturbed performances (AD), and the overall time required to estimate the Broyden matrix (TB). The overall time necessary to tune the filter is given by the following expression:

$$\text{Total} = TB + TC \cdot AI \cdot NI,\tag{4.10}$$

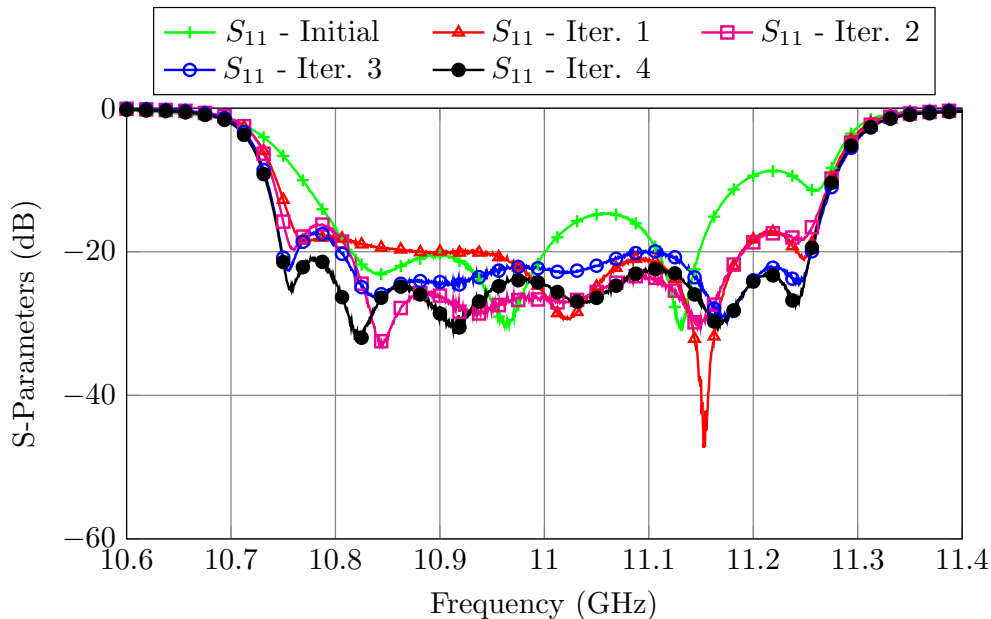


Figure 4.9: Procedure II: Filter performance after every ASM iteration.

Table 4.3: Performance of Procedure II.

TC	TF	AD	TB	NI	AI	$Total$
0.147 s	420 s	245	53 min 12 s	4	703	1 h 5 s

where TB is computed as

$$TB = (TF + AD \cdot TC) \cdot N, \quad (4.11)$$

and where N is the number of disturbances necessary to compute \mathbf{B} . Note that, since the filter is symmetrical, $N = 7$.

The optimal performance is obtained **6 times** faster than with procedure I. It is also interesting to note that the most time consuming task is the estimation of the Broyden matrix (TB), which takes almost 90% of the time required to tune the filter.

4.2.3 Procedure III

In the previous procedure, we used a computationally expensive *fine* model (simulated with CST) that included tuning elements and rounded corners. The *fine* model had to be simulated N times in order to estimate the mapping matrix between the penetrations of the tuning elements and the waveguide dimensions of the fast, low accuracy *coarse* model. However, we can prove that it is not strictly necessary to use a computationally expensive *fine* model.

To do that, we will now establish a number of equivalences between the low precision model simulated with FEST3D that includes tuning elements (see Fig. 4.4), and the high precision model simulated with CST (shown in Fig. 4.7). The dimensions of the models can be related using:

$$\mathbf{x}_f = \mathbf{B} \cdot \mathbf{x}_{fLP} + \mathbf{C}_1, \quad (4.12)$$

where \mathbf{x}_f is a vector with the screw penetrations of the model shown in Fig. 4.7, and \mathbf{x}_{fLP} is a vector with the screw penetration of the low precision model shown in Fig. 4.4. As it has been shown before (in Procedure I and Chapter 3), the mapping matrix in this case can be approximated by the identity:

$$\mathbf{x}_f \approx \mathbf{x}_{fLP} + \mathbf{C}_1, \quad (4.13)$$

From eq. (4.4) we know how \mathbf{x}_f is related to the **waveguide dimensions** of the fast *coarse* model shown in Fig. 4.6, and thus, we can write that:

$$\mathbf{x}_f = \mathbf{B} \cdot \mathbf{x}_c + \mathbf{C} \quad (4.14a)$$

$$\mathbf{x}_{fLP} + \mathbf{C}_1 \approx \mathbf{B} \cdot \mathbf{x}_c + \mathbf{C} \quad (4.14b)$$

$$\mathbf{x}_{fLP} \approx \mathbf{B} \cdot \mathbf{x}_c + (\mathbf{C} - \mathbf{C}_1) \quad (4.14c)$$

This result is extremely powerful. It means that the matrix that links the penetrations of the tuning elements of the low precision model simulated in FEST3D of Fig. 4.4 to the waveguide dimensions of the *coarse* model of Fig. 4.6 is identical to the one obtained in the previous procedure. As a consequence, instead of estimating the mapping matrix by perturbing a computationally expensive model, we can now use a low accuracy model that runs in a few seconds.

We next compare the mapping matrices obtained with procedures II and III. Eq. (4.15) shows half of the matrix \mathbf{B} obtained in Procedure II using the high precision model simulated with CST for the *fine* model. Eq. (4.16) shows the matrix obtained with the new approach.

$$\mathbf{B} = \begin{pmatrix} \mathbf{0.910} & \mathbf{0.187} & 0.061 & 0.004 & -0.002 & -0.001 & -0.010 \\ \mathbf{0.034} & \mathbf{0.471} & \mathbf{0.157} & -0.004 & -0.004 & -0.002 & 0.006 \\ -0.013 & \mathbf{0.008} & \mathbf{1.749} & \mathbf{-0.007} & -0.003 & 0.001 & -0.003 \\ -0.003 & -0.003 & \mathbf{0.139} & \mathbf{0.512} & \mathbf{0.144} & 0.003 & 0 \\ -0.006 & 0.002 & -0.010 & \mathbf{-0.065} & \mathbf{1.985} & \mathbf{-0.052} & 0.006 \\ 0.001 & -0.001 & 0.002 & 0.008 & \mathbf{0.135} & \mathbf{0.502} & \mathbf{0.147} \\ 0.009 & 0.013 & 0.008 & 0.002 & -0.002 & \mathbf{-0.062} & \mathbf{2.134} \\ 0.001 & -0.003 & 0 & 0 & -0.002 & 0 & \mathbf{0.13} \\ 0 & -0.016 & -0.001 & 0.015 & -0.001 & 0.001 & 0.005 \\ 0 & -0.005 & -0.002 & 0 & 0 & 0 & -0.002 \\ -0.002 & -0.002 & -0.006 & 0 & -0.007 & 0 & -0.021 \\ 0.003 & -0.003 & 0 & 0.001 & -0.003 & 0.002 & 0.005 \\ 0 & -0.003 & 0.014 & -0.001 & 0 & -0.003 & -0.031 \end{pmatrix} \quad (4.15)$$

$$\mathbf{B} = \begin{pmatrix} \mathbf{0.945} & \mathbf{0.179} & 0.059 & 0.026 & -0.001 & 0.014 & 0.010 \\ \mathbf{0.028} & \mathbf{0.524} & \mathbf{0.173} & -0.006 & 0.008 & -0.002 & 0.011 \\ -0.005 & \mathbf{0.001} & \mathbf{1.850} & \mathbf{0.024} & 0.021 & 0.028 & -0.017 \\ -0.008 & 0.007 & \mathbf{0.139} & \mathbf{0.537} & \mathbf{0.147} & 0 & 0 \\ -0.032 & 0.082 & 0.029 & \mathbf{-0.069} & \mathbf{2.122} & \mathbf{-0.054} & 0.009 \\ 0.003 & 0 & 0.001 & 0.0103 & \mathbf{0.142} & \mathbf{0.532} & \mathbf{0.150} \\ 0.004 & 0.013 & 0.006 & 0.030 & 0.007 & \mathbf{-0.080} & \mathbf{2.177} \\ 0.002 & -0.002 & 0.002 & 0.002 & 0.002 & 0.006 & \mathbf{0.138} \\ 0.002 & -0.017 & -0.003 & 0.013 & -0.014 & 0.002 & 0.004 \\ 0 & -0.005 & 0 & 0.002 & 0.004 & -0.001 & -0.001 \\ 0.025 & 0 & 0.012 & -0.007 & -0.021 & 0.024 & 0.021 \\ 0.004 & -0.012 & 0.001 & 0.004 & 0.012 & -0.002 & 0.004 \\ 0.019 & 0.006 & 0.014 & -0.002 & -0.005 & 0.0135 & 0.001 \end{pmatrix} \quad (4.16)$$

If we compare the most significant terms (basically the main diagonal, the super diagonal and the sub diagonal), we can verify that the matrices are indeed almost identical.

Another experimental test we can do to assess the validity of the approximation is to disturb the same tuning element in both models (Fig. 4.4 and Fig. 4.7) and plot their performances. Before perturbing the tuning elements, we have to make sure that the two models are aligned (see Fig. 4.10).

Fig. 4.11 and Fig. 4.12 show, respectively, the result of modifying the tuning element

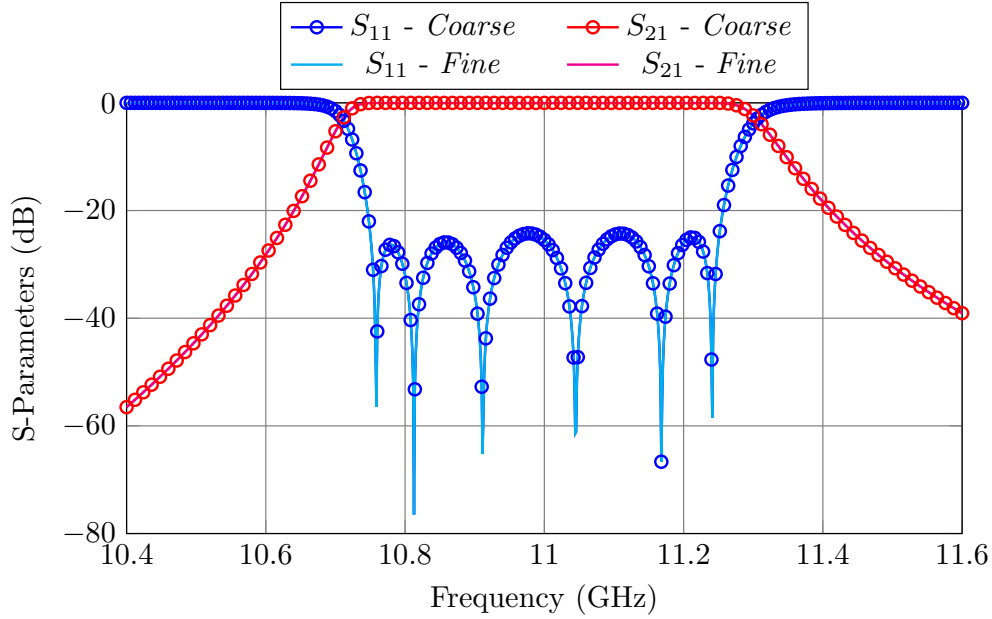


Figure 4.10: Aligned performances of the models ($\mathbf{R}_c(\mathbf{x}_{c\text{opt}}) = \mathbf{R}_f(\mathbf{x}_{f\text{opt}})$).

Table 4.4: Performance of Procedure III.

TC	TF	AD	TB	NI	AI	$Total$
0.147 s	7.3 s	271	5 min 29 s	5	659	13 min 34 s

of the first aperture and cavity by 0.1 mm from the design depth in both models. As we can see, the performance in both cases is almost identical, thereby validating our initial approximation.

After five ASM iterations, the filter is successfully tuned (see Fig. 4.13). Even though it takes one more iteration to obtain the desired performance, **this approach is four times faster** than the previous one. The speed-up in this case is accomplished in the computation of \mathbf{B} (TB). In order to compute \mathbf{B} , we need to disturb 7 tuning elements and, obviously, this is much faster if we use a low precision model. Table 4.4 shows the performance of this tuning procedure.

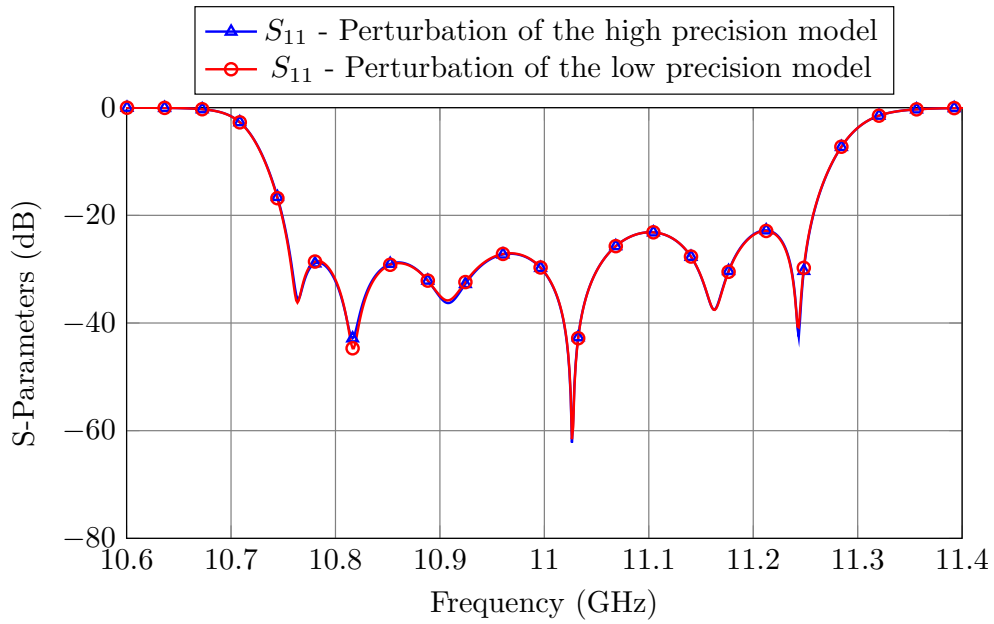


Figure 4.11: Performance of the high and low precision models after perturbing the first aperture by 0.1 mm.

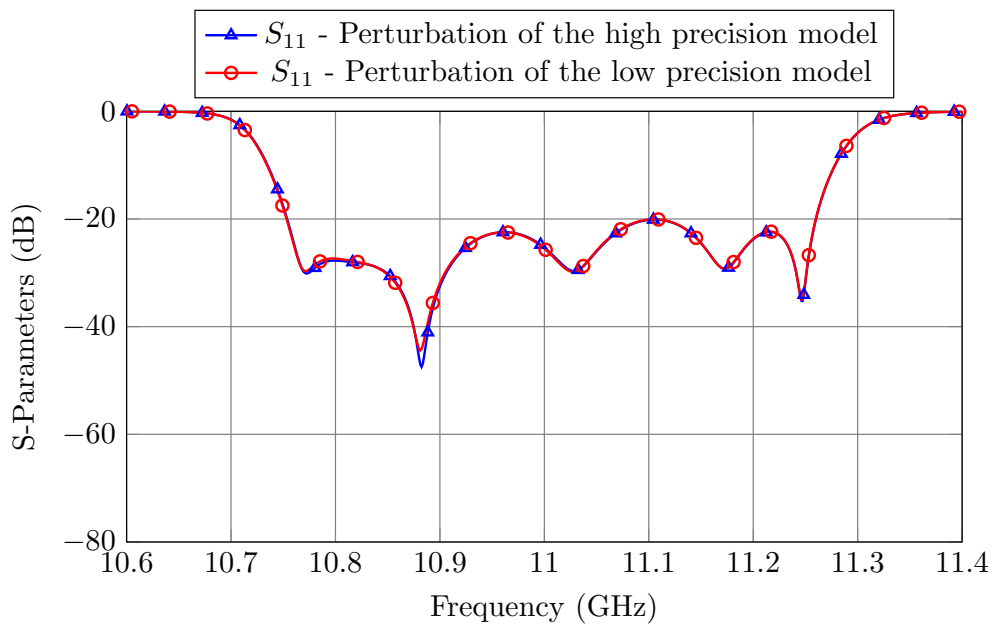


Figure 4.12: Performance of the high and low precision models after perturbing the first cavity by 0.1 mm.

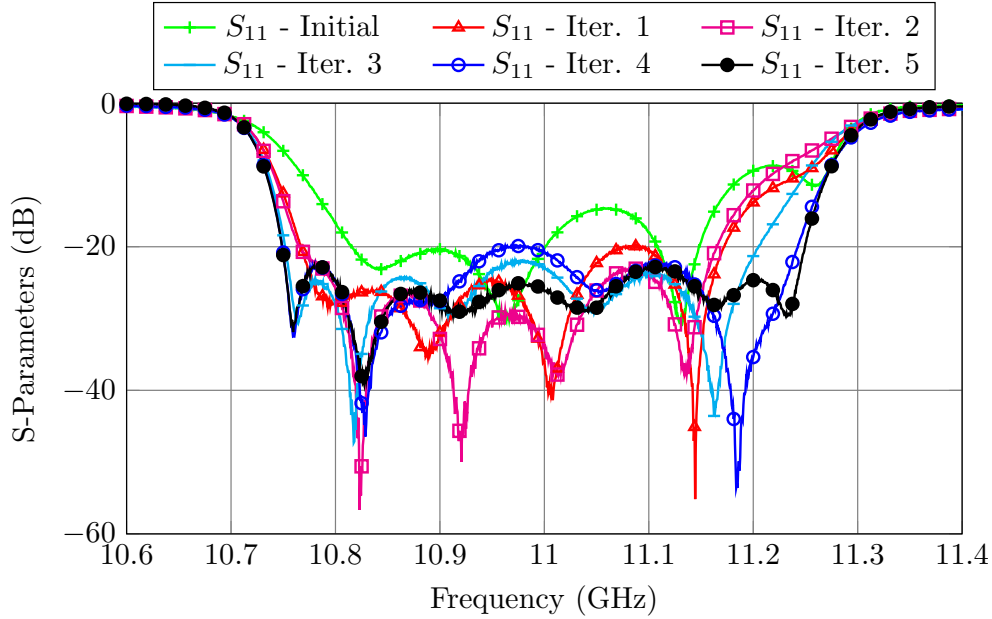


Figure 4.13: Procedure III: Filter’s performance after every ASM iteration.

4.2.4 Procedure IV

By using a low precision model with tuning elements to compute \mathbf{B} (see Fig. 4.4), we have drastically reduced the time needed for the tuning process. The N perturbations of the tuning elements are computed in:

$$TB_{estimate} = TF \cdot N = 7.3 \cdot 7 = 51.1 \text{ s.} \quad (4.17)$$

However, the computation of \mathbf{B} takes up to 5 min. 29 s. The difference is the computational effort required to recover each of the perturbations, which is computed as follows:

$$TB_{recover} = TB - TB_{estimate} = N \cdot TC \cdot AD, \quad (4.18)$$

where AD is the average number of simulations performed by a Simplex algorithm in order to recover each of the disturbances. This average depends on the number of parameters that are optimized in the recovery process. Until now, we have optimized all 13 design variables ($2N + 1$), and thus, it takes an average of 271 simulations to recover each disturbance. However, If we take a closer look to eq. (4.15) and eq. (4.16), we can see that the significant terms are in the main diagonal, the super diagonal and sub diagonal.

That actually makes a lot of sense. Imagine we exclusively perturb the tuning element of the first cavity. By doing that, we are modifying the frequency of resonance of

Table 4.5: Performance of Procedure IV.

TC	TF	AD	TB	NI	AI	$Total$
0.147 s	7.3 s	76	2 min 9 s	4	483	8 min 52 s

that cavity. In order to recover the same performance in the *coarse* model, we mainly have to modify the length of the first cavity, and maybe slightly adjust the adjacent coupling windows. There is no need to optimize, for example, the fourth cavity. We can therefore reduce the optimization space to three variables. As a consequence, we will reduce AD , and thus, we will also reduce TB .

$$\mathbf{B} = \begin{pmatrix} \mathbf{0.931} & \mathbf{0} & 0 & 0 & 0 & 0 & 0 \\ \mathbf{0.052} & \mathbf{0.553} & \mathbf{0.18} & 0 & 0 & 0 & 0 \\ 0 & \mathbf{0} & \mathbf{1.864} & \mathbf{0} & 0 & 0 & 0 \\ 0 & 0 & \mathbf{0.141} & \mathbf{0.538} & \mathbf{0.144} & 0 & 0 \\ 0 & 0 & 0 & \mathbf{0} & \mathbf{2.112} & \mathbf{-0.055} & \mathbf{-0.01} \\ 0 & 0 & 0 & 0 & \mathbf{0.142} & \mathbf{0.530} & \mathbf{0.153} \\ 0 & 0 & 0 & 0 & \mathbf{-0.01} & \mathbf{-0.041} & \mathbf{2.192} \\ 0 & 0 & 0 & 0 & 0 & 0 & \mathbf{0.132} \\ 0 & 0 & 0 & 0 & 0 & 0 & 0.01 \\ 0 & 0 & 0 & 0 & 0 & 0 & 0 \\ 0 & 0 & 0 & 0 & 0 & 0 & 0 \\ 0 & 0 & 0 & 0 & 0 & 0 & 0 \\ 0 & 0 & 0 & 0 & 0 & 0 & 0 \end{pmatrix} \quad (4.19)$$

Eq. (4.19) shows the Broyden matrix obtained using a reduced optimization space. As we can see, it is almost identical to the matrix obtained with the full optimization space (shown in eq. (4.16)). As shown in Fig. 4.14, after only four ASM iterations, the filter is perfectly tuned, thereby validating this approach. Table 4.5 shows the performance of this procedure.

Another advantage of this approach is that it can be scaled. Even if the order of the filter increases, the optimization space will remain fixed to three variables. Therefore, the computational effort to estimate the mapping matrix will not increase as much as if we considered the full optimization space.

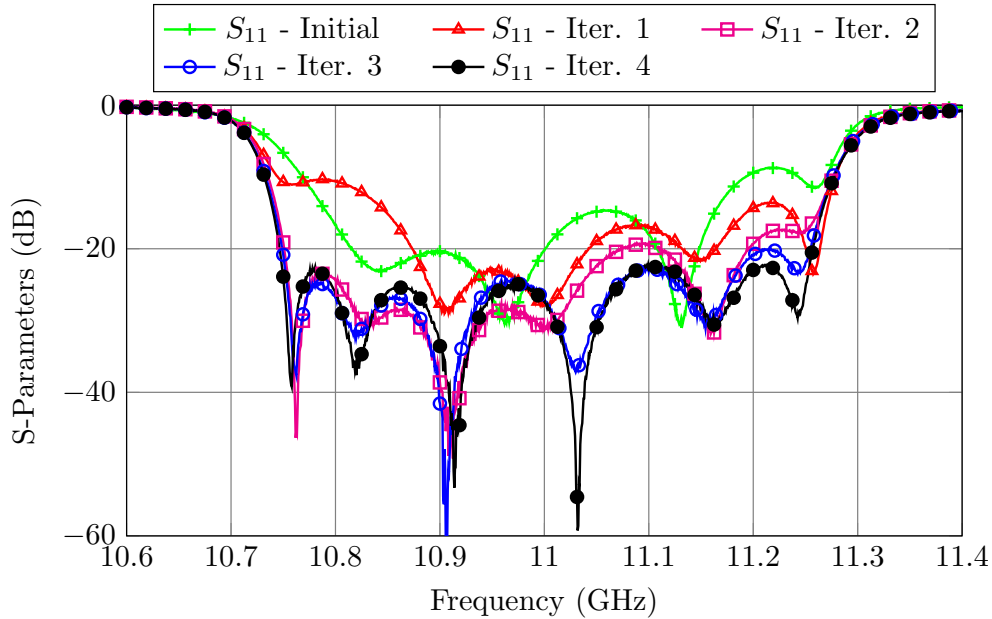


Figure 4.14: Procedure IV: Filter's performance after every ASM iteration.

4.2.5 Procedure V

The last tuning procedure is meant to be used when no advanced simulation tools are available. This case is important to consider because, in most cases, the engineer responsible for tuning the filter is not the same who designed it. In practice, the engineer in charge of tuning is only given the set of S11 and S21 masks that the filter needs to satisfy. The following tuning process can be of real help in this particular situation. The steps involved are as follows:

1. Even though the engineer in charge of tuning the filter might not have the original sophisticated EM simulation models, it is reasonable to assume that they can have at their disposal a *coarse* model of the filter as the one shown in Fig. 4.15. The reason for this change is explained hereunder.
2. The next step is then to optimize the *coarse* model until the measured performance from the Vector Network Analyzer (VNA) is matched, as shown in Fig. 4.16.
3. The tuning engineer must then perturb half of the tuning elements in order to estimate the mapping matrix.
4. Finally, tune the filter using the same approach already discussed in procedures II-IV.

After only three ASM iterations, the filter has been perfectly tuned (see Fig. 4.17). It is important to note that the starting point for this procedure is slightly better than

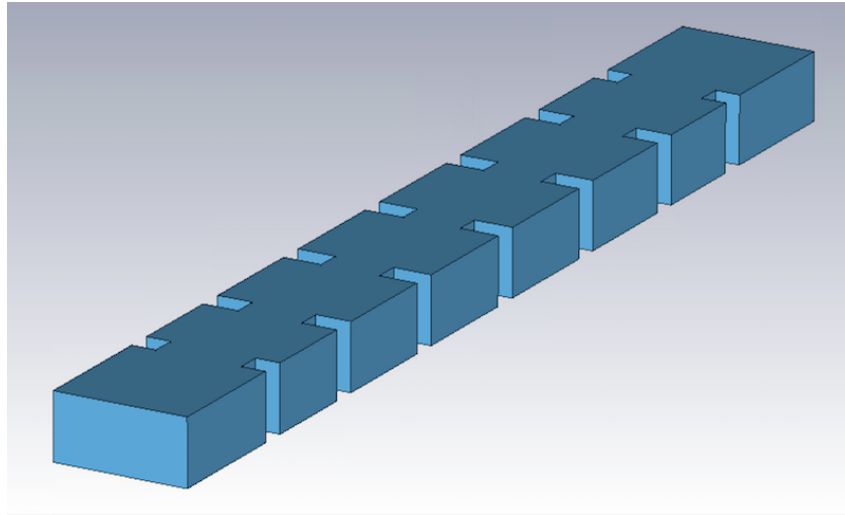


Figure 4.15: Fast low-precision model that does not include tuning elements. Originally in Fig. 4.6 and repeated here for convenience.

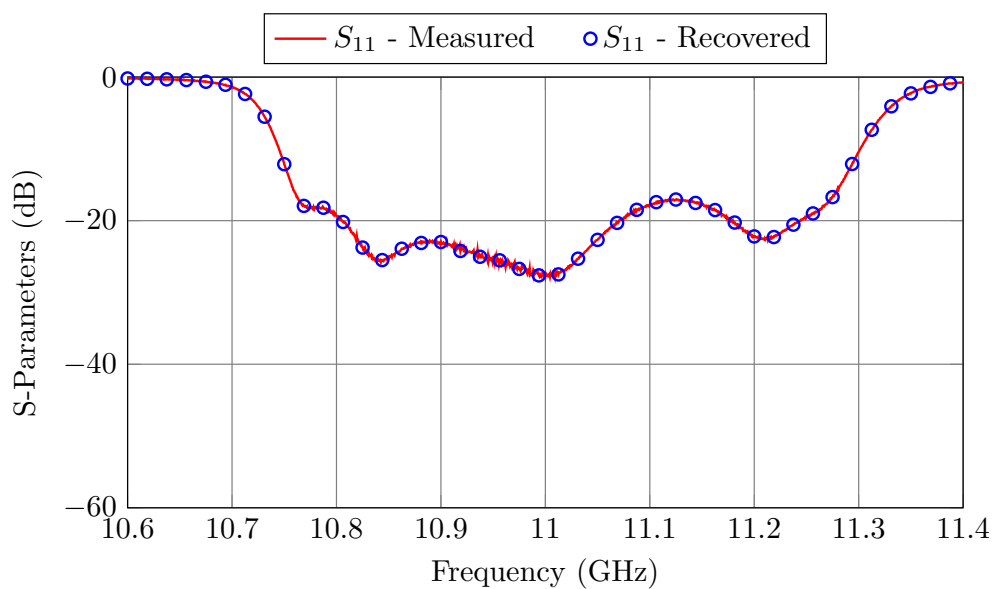


Figure 4.16: Aligned performances of the *coarse* model and measured response.

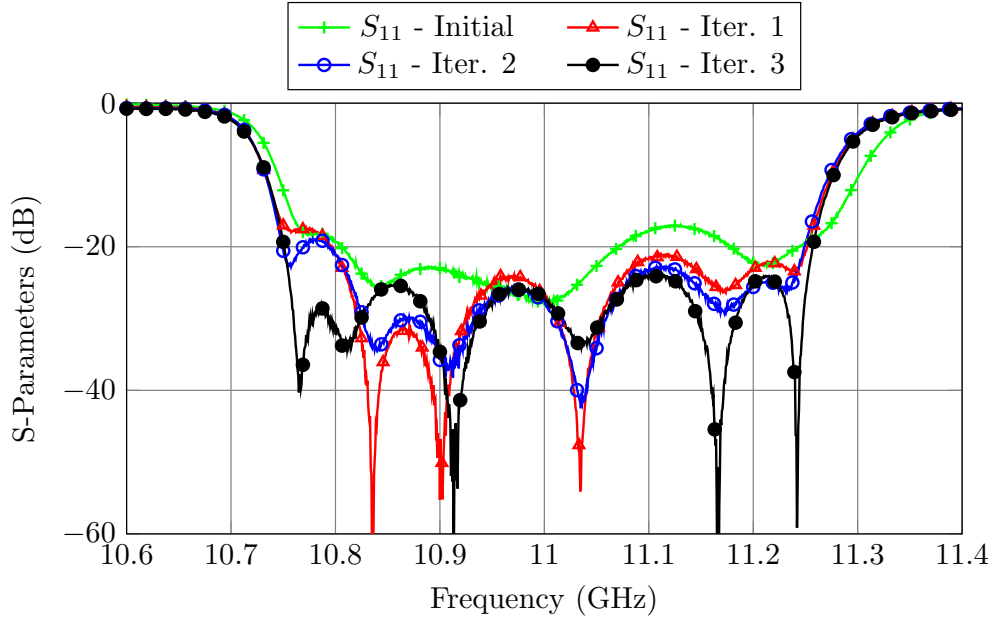


Figure 4.17: Procedure V: Filter performance after every ASM iteration.

the one we have used for the previous tuning methods (see Fig. 4.18).

It is important to recall that the mapping matrix establishes a **linear mapping** between the parameters of two different spaces, and similarly to when we approximate any 2-D $f(x)$ function by $f(a + \Delta x) \approx f(a) + f'(a) \cdot \Delta x$, that is only a valid approximation in the vicinity of the point where the mapping is established (the alignment point shown in Fig. 4.16 or a in the analogous 2-D case). There are, in fact, two different ways in which we could have proceeded:

1. We could have estimated the mapping matrix around the initial starting point for Procedures II-IV. However, that mapping would have only been a good approximation in the vicinity of that point, which is very far from the tuned response. Therefore, we would have needed to update the mapping matrix after each iteration (like it was done in [50], [27] and [86]) or the tuning would have diverged.
2. Another alternative would be to improve manually the starting point and estimate the mapping matrix around this enhanced point.

This last procedure is meant to be used in an industrial contest, and so, we can assume that the engineer in charge of the tuning process could improve the initial starting point with very little effort and thus, the second option is the most pragmatical approach.

Table 4.6 shows the performance of this approach. Since the estimation of the Broyden matrix is done with measurements, we have assumed that TF in this case is

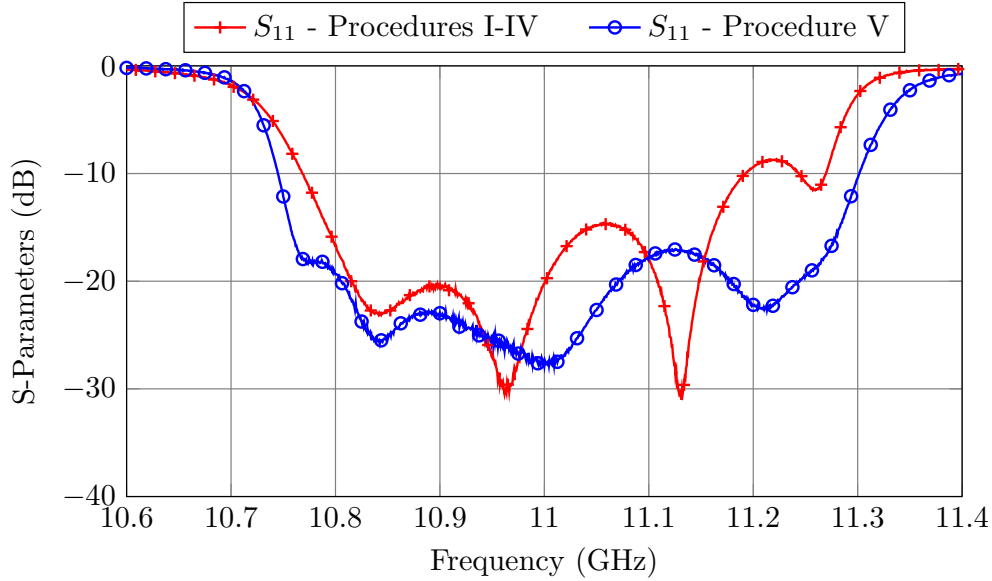


Figure 4.18: Starting point for all procedures.

Table 4.6: Performance of Procedure V.

TC	TF	AD	TB	NI	AI	$Total$
0.147 s	0	67	1 min 9 s	3	604	5 min 35 s

equal to 0 s.

4.3 Comparison between the different tuning methods

In this chapter, we have shown five different tuning techniques based on ASM. In each case we have considered the computation time required to tune the filter with each procedure, but we have not included the time it takes to modify the tuning screws with the robotic arm. Based on our experience, the time we need to modify all tuners is around three minutes, and thus, to each method we have to add an extra amount:

$$\text{Extra} = NI \cdot 180 \text{ s.} \quad (4.20)$$

Finally, we also want to evaluate if the procedures described require of significant tuning experience. Anybody could tune a filter following Procedures I-IV, regardless of their previous experience. However, they might not be able to manually improve the initial point as required for Procedure V. Table 4.7 compares the performance of the different procedures based on these metrics.

Table 4.7: Comparison of the different tuning methods.

Procedure	I	II	III	IV	V
Time	6 h 10 min 50 s	1 h 5 s	13 min 34 s	8 min 52 s	5 min 35 s
Extra	12 min	12 min	15 min	12 min	12 min
Total	6 h 22 min 50 s	1 h 12 min 5 s	28 min 34 s	20 min 52 s	17 min 35 s
Experience	No	No	No	No	Yes

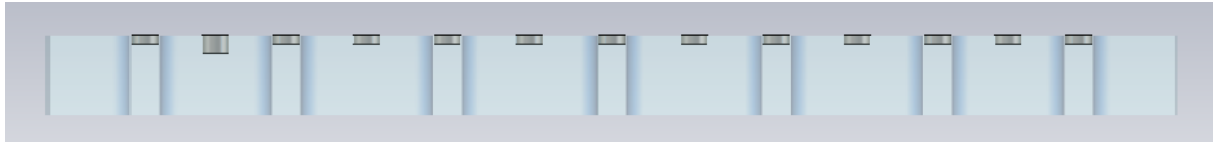


Figure 4.19: The ideal penetration of the tuning element placed in the first cavity is 2 mm. At the moment is set at 2.1 mm. The dimensions have been exaggerated in the drawing for clarity.

From Table 4.7 we can see that Procedure I is clearly the worst one. Procedure II is a great improvement over Procedure I. We would always recommend this procedure over the previous one. Procedures III and IV are further enhancements of Procedure II. Generally, the initial adjustment required in Procedure V will take longer than three minutes and therefore, Procedure IV is the overall best tuning method.

4.4 Recovery of the measured performance

Throughout this chapter, we have repeated several times that, in order to recover each of the measured performances, we have to optimize the *coarse* model until the performance of the measured response is matched. Until now, we have shown in several figures (for example, Fig. 4.16) that the models are aligned when their $|S_{11}(\text{dB})|$ are identical. However, it is important to note that recovering the same phase is just as important.

Let us consider the following simplified case: imagine that the filter is perfectly tuned except for the first cavity (see Fig. 4.19). The optimum penetration for that tuner should be 2 mm, however, as we can see in Fig. 4.19, it is placed at 2.1 mm. Let us apply Procedure IV but in this case disregarding the phase information.

Following Procedure IV, we would optimize the *coarse* model until the same performance is recovered (see Fig. 4.20). Fig. 4.21 shows the elements in the *coarse* model that are modified in order to match the measured performance.

We would then modify the tuning elements according to:

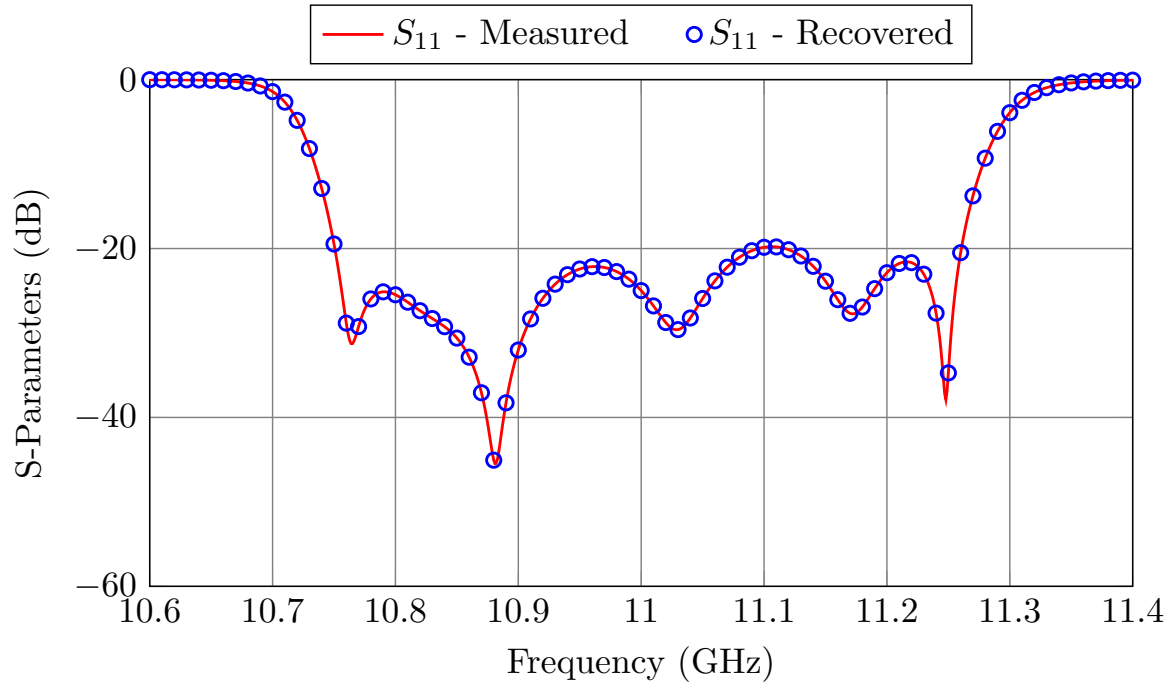


Figure 4.20: Recovered performance with the *coarse* model.

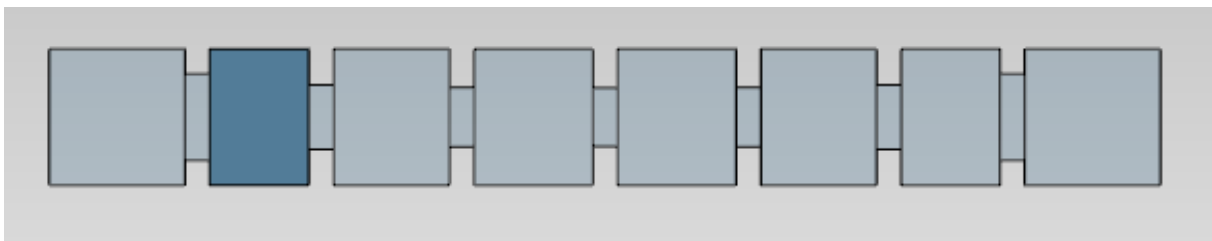


Figure 4.21: Elements in the *coarse* model that are optimized in the process of recovering the measured performance (darker color).

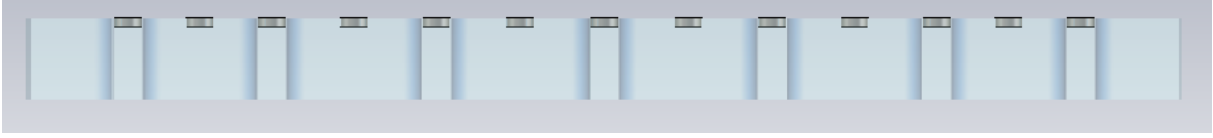


Figure 4.22: After one ASM iteration the filter is perfectly tuned.

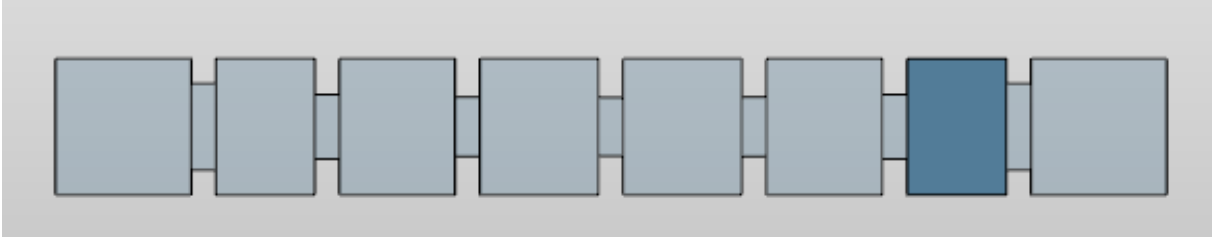


Figure 4.23: Elements in the *coarse* model that are optimized in the process of recovering the measured performance (darker color).

$$\Delta = \mathbf{B} \cdot \Delta_{\mathbf{c}}, \quad (4.21)$$

where $\Delta_{\mathbf{c}} = \mathbf{x}_{\mathbf{c}\text{opt}} - \mathbf{x}_{\mathbf{c}\text{recovered}}$.

After only one iteration, the tuning element of the first cavity is set to the correct depth as shown in Fig. 4.22 and the filter is perfectly tuned.

However, since the filter structure considered is ideal (reciprocal and without losses), the optimizer could have found an alternative solution for the *coarse* model, namely, the one shown in Fig. 4.23. The response in magnitude of the *coarse* model is identical to the one obtained in the previous case (see Fig. 4.24). If we then applied eq. 4.21 to obtain the new penetration of the screws, it would result in the screw penetration shown in Fig. 4.25. As the *coarse* model did not understand which side of the filter it should have optimized, the method modified the wrong tuner, and thus, two tuning elements are now set to the wrong penetration.

A solution that is effective in avoiding this ambiguity is to evaluate the phase of the response in addition to the insertion loss. Fig. 4.26 shows how the phase of the two *coarse* models (Figs. 4.21 and 4.23) is completely different. Since the phase is discontinuous, enforcing any optimizer to also recover the same phase will slow down the recovery process. If the phase is included in the recovery as an additional goal, we would also be creating unnecessary local minima for the optimizer to get stagnated in. The best practice, which is the one that we have used, is as follows:

1. Let the *coarse* model recover the *magnitude* of the measured performance.

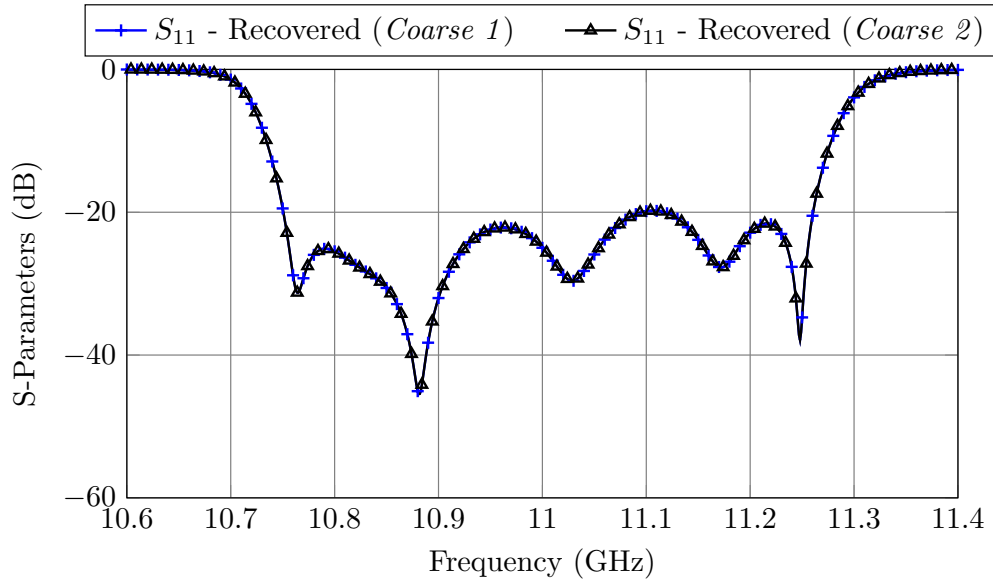


Figure 4.24: Recovered performance with both possible *coarse* models.

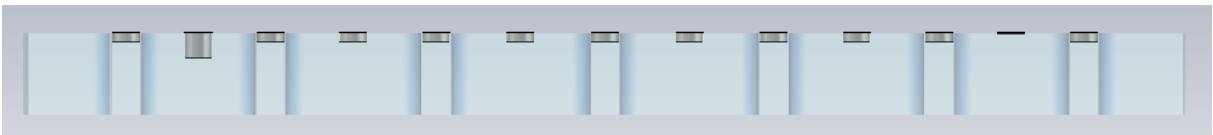


Figure 4.25: After the ASM iteration, two tuning elements are set at the wrong penetration.

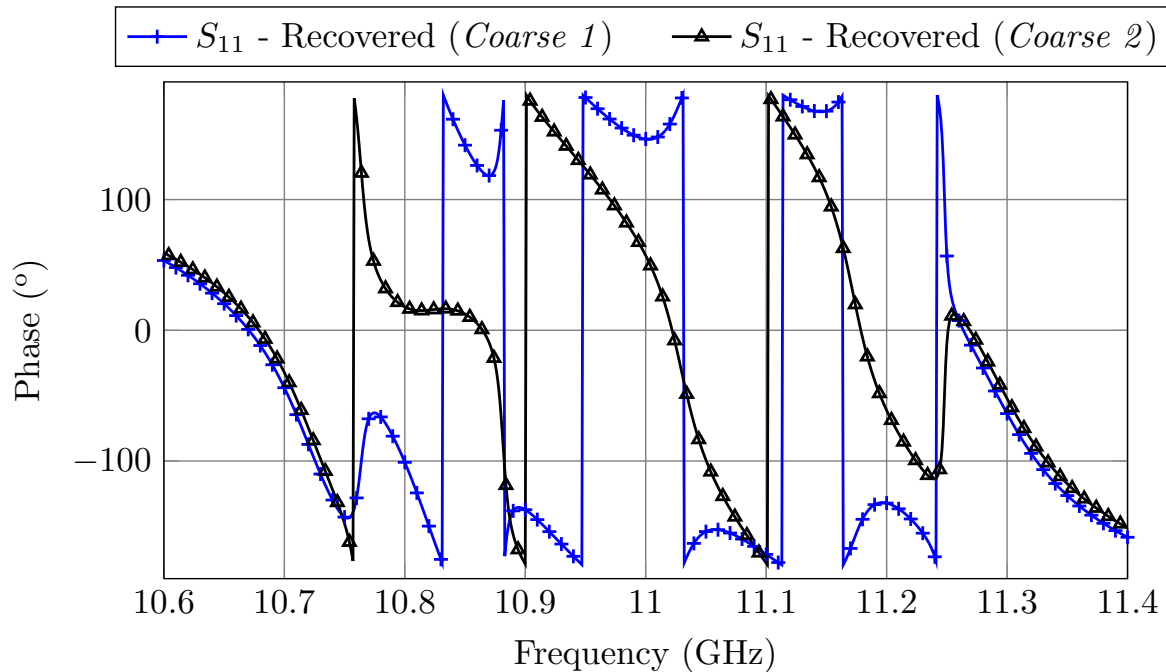


Figure 4.26: Phase of the S11 parameter for both *coarse* models.

2. Once the same magnitude has been recovered, check the phases of the S11 parameter in both models. If they differ, that means we just obtained the wrong solution. In order to compensate it, we only have to invert the input and the output of the *coarse* filter, and then proceed as before.

4.5 Other possible *coarse* models

Even though in the past sections we have used waveguide-based *coarse* models, the same procedures can be applied using any other type of *coarse* model. In this section, we will tune a 4-pole inductive waveguide filter, like the one shown in Fig. 4.27, using two different *coarse* models and then we will compare the results.

The filter is centered at 12 GHz. It has a bandwidth of 200 MHz and a return loss of 25 dB. It will also be manufactured using milling and thus, it should include rounded corners (2 mm radius). The tuners in this case have a radius of 1 mm, and their design penetration is 2 mm. In the following subsections, we will compare the results obtained with two different *coarse* models, a waveguide model and one based on transmission lines and inverters.

Since all tuning procedures have already been validated with measured hardware,

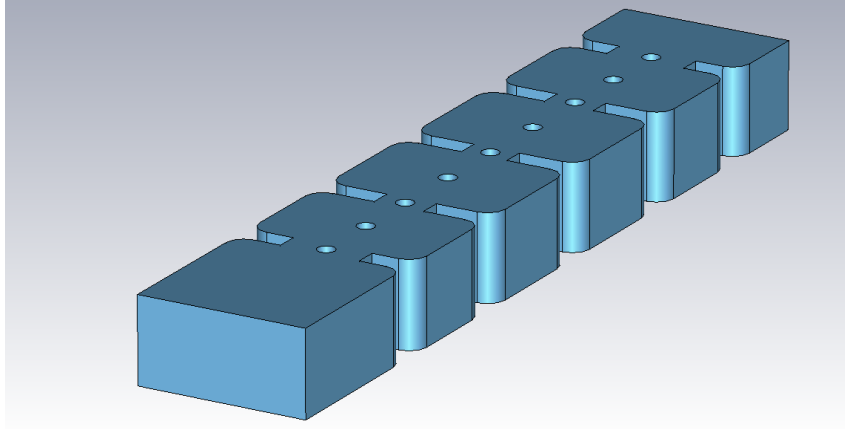


Figure 4.27: Waveguide 4-pole filter to be tuned.

Table 4.8: Performance of Procedure IV.

TC	TF	AD	TB	NI	AI	$Total$	$Total + Extra$
0.117 s	6.1 s	73	1 min 13 s	3	414	3 min. 38 s.	9 min. 38 s.

we will not manufacture this specific filter. Instead, we will apply random deviations to the nominal dimensions to simulate the manufacturing errors. The deviations have been obtained from a normal distribution of mean $\mu = 0$ and standard deviation $\sigma = 100 \mu\text{m}$. Fig. 4.28 shows the initial performance of the filter after applying the deviations, and setting all tuning elements to the design penetration depth. As we can see, the performance is severely detuned.

4.5.1 Using a waveguide *coarse* model

We will now apply Procedure IV (see Section 4.2.4 for additional details) to tune the filter using a waveguide-based *coarse* model. The procedure is as follows:

1. Estimate the mapping matrix between the waveguide dimensions of the *coarse* model shown in Fig. 4.29 and the penetrations of the tuning elements of the low precision model that includes regular tuners, as shown in Fig. 4.30.
2. Tune the filter following the procedure described in Section 4.2.4.

Fig. 4.31 shows how the filter is tuned in three ASM iterations. Table 4.8 shows the performance of this procedure. In this case, we have assumed that the time necessary to ‘modify’ all tuning elements is around 2 minutes ¹.

¹The time required to modify all tuners in the 6-pole was around 3 minutes. We estimate that if this filter was indeed manufactured, it would take us around 2 minutes to change all tuners.

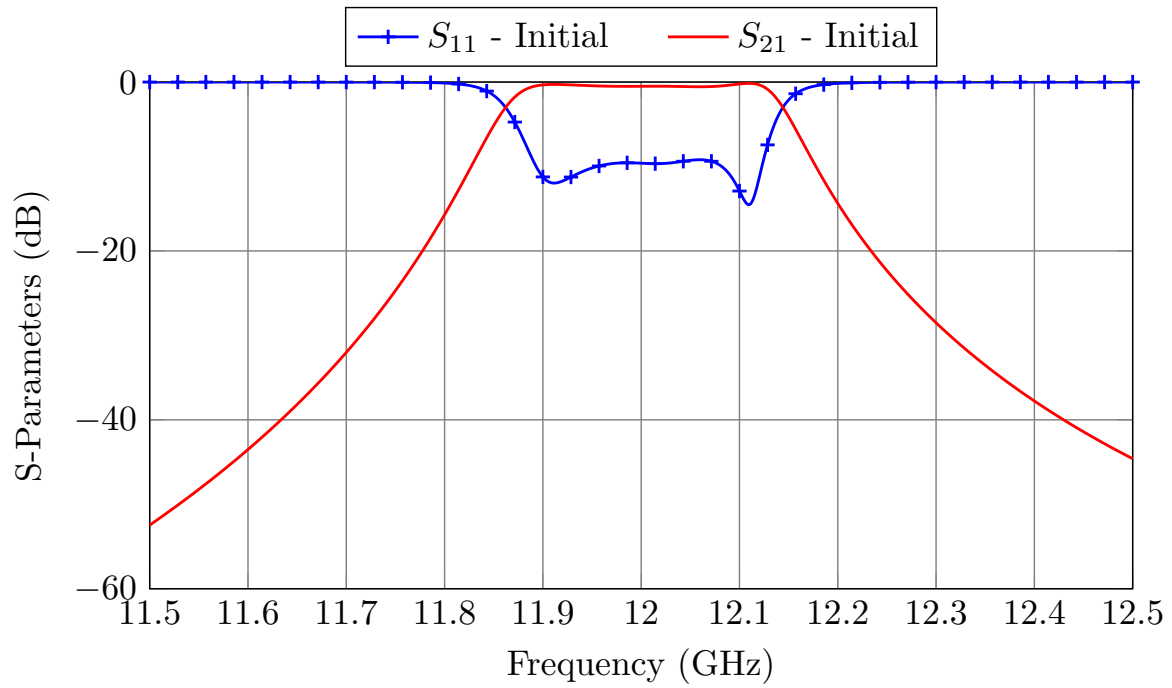


Figure 4.28: Initial state of the filter. As we can see, it is very detuned.

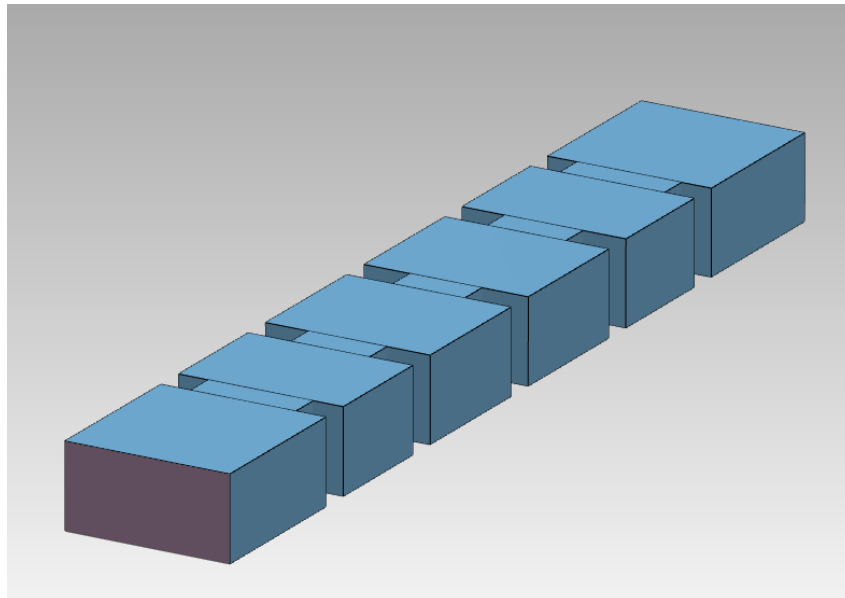


Figure 4.29: Waveguide *coarse* model of the filter.

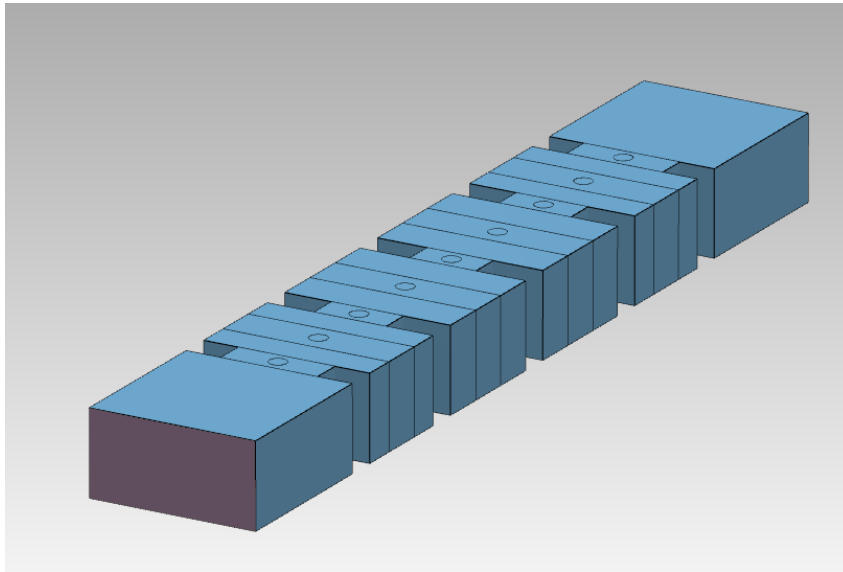


Figure 4.30: Low precision model of the filter that considers tuning elements.

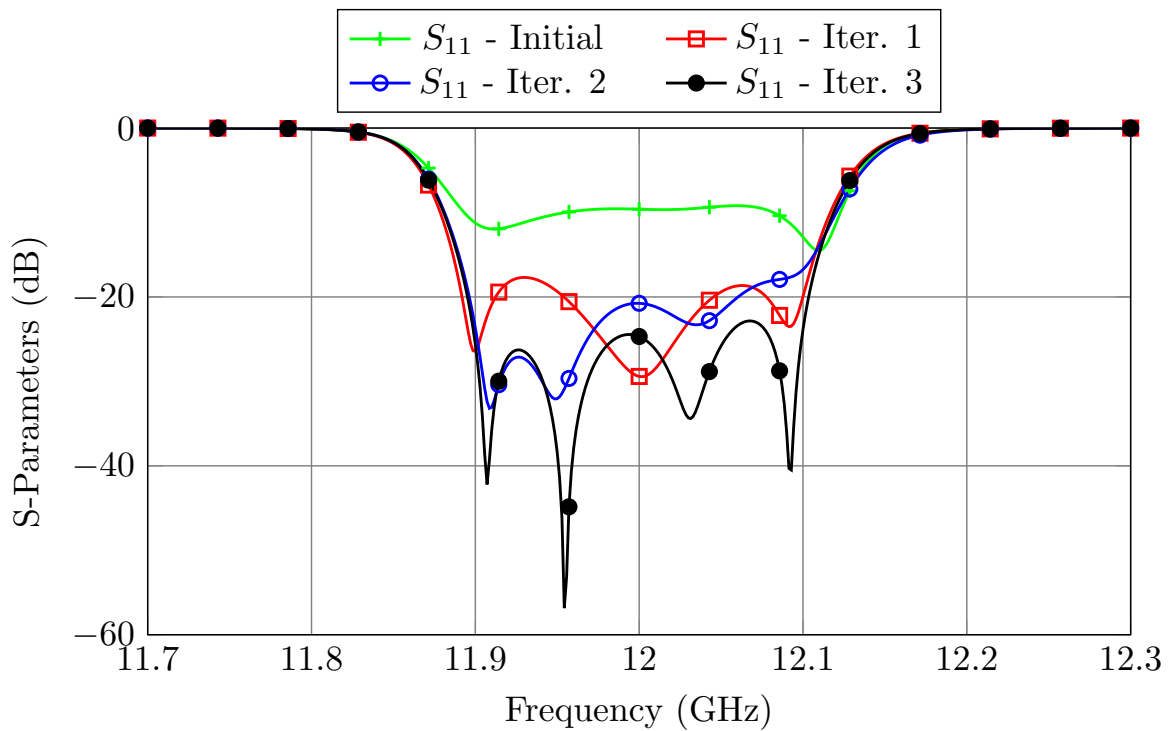


Figure 4.31: Procedure IV: Filter's performance after every ASM iteration. The *coarse* model used is a waveguide-based model.

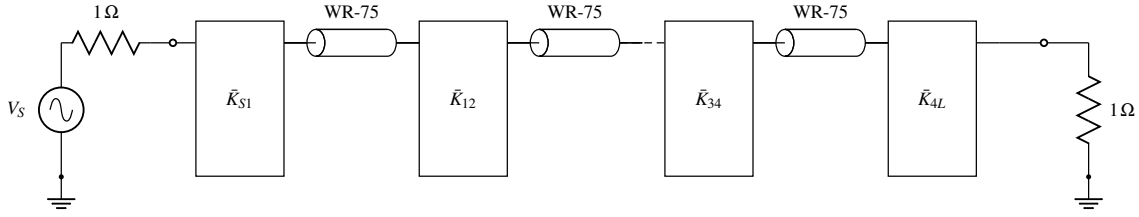


Figure 4.32: *Coarse* model based on transmission lines and inverters.

Table 4.9: Performance of Procedure IV using a *coarse* model based on transmission lines and inverters.

TC	TF	AD	TB	NI	AI	$Total$	$Total + Extra$
0.06 s	6.1 s	213	1 min 34 s	5	856	5 min. 50 s.	15 min. 50 s.

4.5.2 Using a *coarse* model based on transmission lines and inverters

We will now apply Procedure IV using a *coarse* model based on transmission lines and inverters as the one shown in Fig. 4.32. The model in this case is simulated in Microwave Office. The procedure is the same as before:

1. Estimate the mapping matrix that links the parameters of the *coarse* model (the distributed model) with the penetrations of the tuning elements of the low precision model shown in Fig. 4.30.
2. Tune the filter following the procedure described in Section 4.2.4.

Fig. 4.33 shows the tuning process for this case. Five iterations are needed in this case to tune the filter. Table 4.9 shows the performance of the method. There are several details that are worth noting:

- The *coarse* model based on transmission lines and inverters is almost twice as fast as the waveguide-based model.
- Recovering the measured (in this case, simulated) performance takes more simulations in the distributed model.
- The waveguide-based model is able to tune the filter in fewer iterations.
- The most time consuming task in this example is to actually modify the tuners.

Due to the previous points, the procedure that uses the waveguide-based *coarse* allows for a faster filter tuning. However, the main reason why we prefer to use low precision waveguide models without tuners as *coarse* models is that a *waveguide-based coarse model will always be able to recover exactly the measured performance*. The only difference between our *coarse* and measured (or *fine* model) is that the latter includes tuning elements (and/or rounded corners). Apart from that, both models are identical.

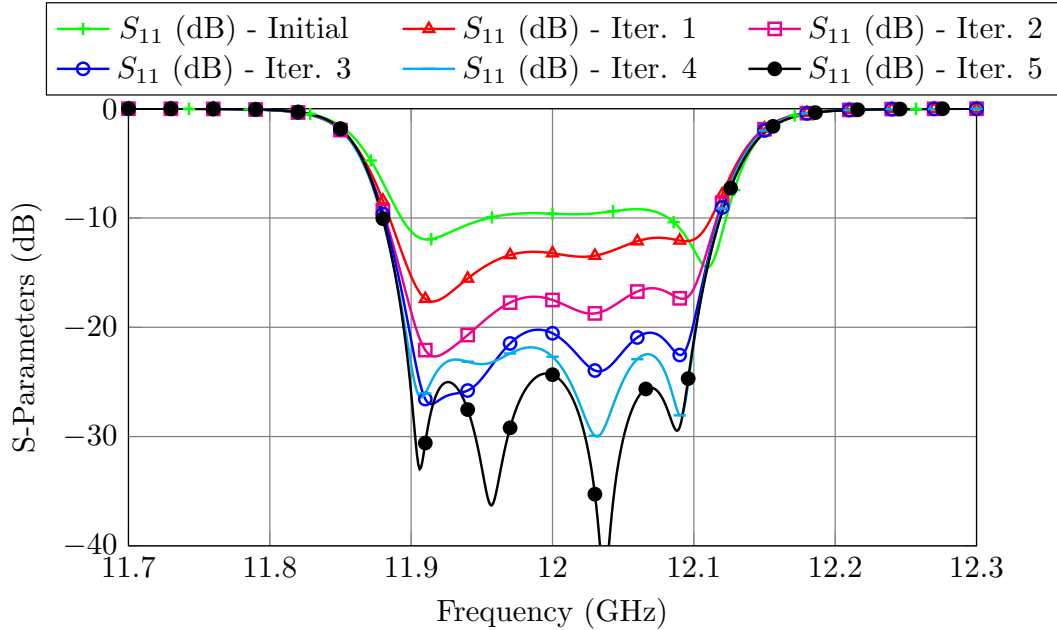


Figure 4.33: Procedure IV: Filter’s performance after every ASM iteration. The *coarse* model used is based on transmission lines and inverters.

On the other hand, the distributed model considers *ideal* impedance inverters. We can indeed implement the impedance inverters with apertures, but we can only match their magnitude and phase at one single frequency [13]. When we try to recover the ‘measured’² performance using a distributed model, it is not usually possible to recover exactly the same performance as it is shown in Fig. 4.34. The performances are similar, but not identical. However, when we use a waveguide-based *coarse* model, we can recover exactly the same performance (see Fig. 4.35).

Even though this is not critical for simple in-line filters, this issue may cause convergence issues for more complex filters. In that case, another variant of SM should be used with these distributed models, like implicit space mapping [30]. However, if we use a waveguide *coarse* model, we can always apply the procedure as is, without further changes.

²Note that in this particular case, we have not manufactured the filter. The ‘measured’ performance is, in fact, obtained by simulation.

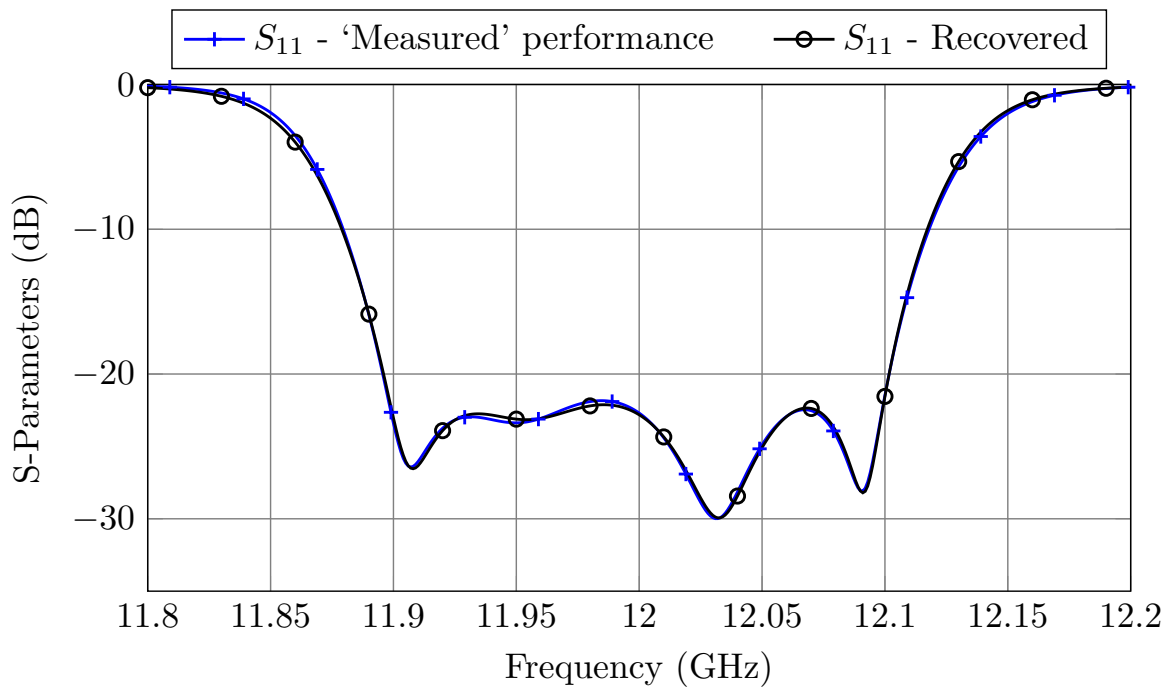


Figure 4.34: Recovering the ‘measured’ performance with a distributed model.

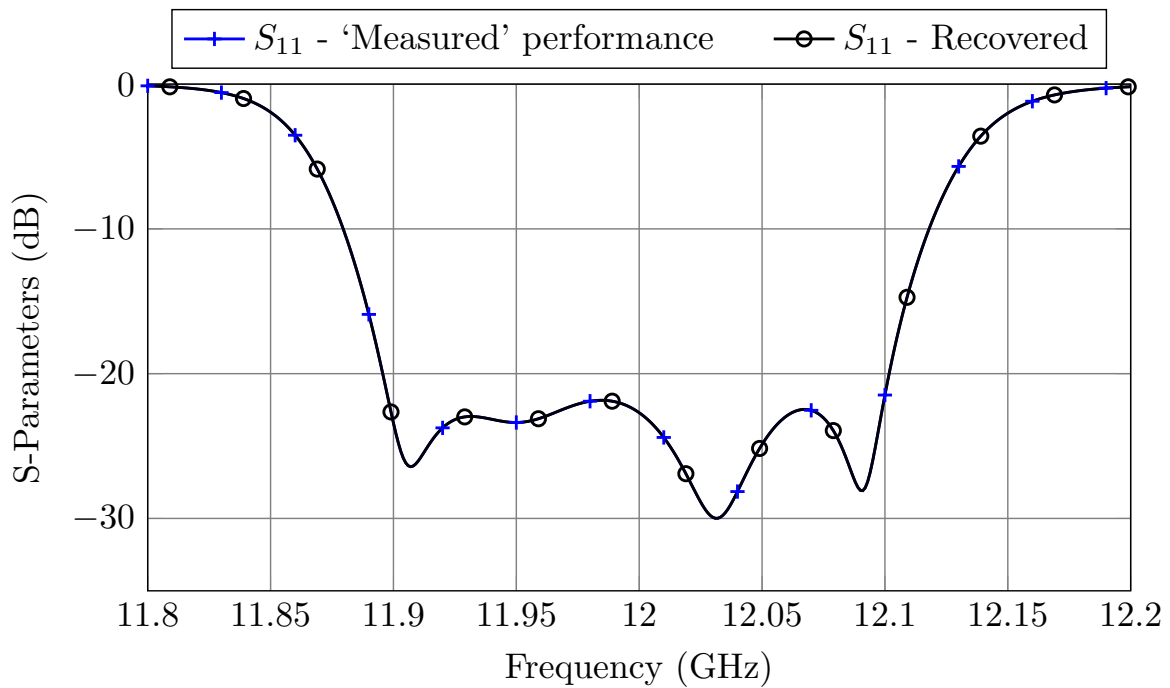


Figure 4.35: Recovering the ‘measured’ performance with a waveguide-based *coarse* model.

4.6 Conclusions

We have shown how Space Mapping techniques can effectively be used to facilitate, and essentially automatize, the cumbersome tuning stage of a microwave filter. Furthermore, the techniques discussed have been fully validated by tuning a 6-pole inductive filter.

Five different ASM-based procedures have been compared. In the first one (Procedure I), which is only used as a reference, the tuning elements of the *coarse* model are optimized until the measured performance is matched and then, the real tuners are modified according to the One-Step ASM equations. In the rest of the procedures, the *coarse* model does not include tuning elements and, therefore, it is necessary to estimate the mapping matrix that relates the penetration of the tuners of the real filter with the waveguide dimensions of the *coarse* model. We have proved that this estimation can be performed by simulation with different models. In Procedure II we used a computationally expensive model to perform this task while, in Procedure III, we proved that the same result can also be achieved if we used a low precision model that includes tuning elements. In Procedure IV we showed that we can use a reduced optimization space in order to estimate the mapping matrix. Finally, in Procedure V, we showed that the mapping matrix can be estimated directly, measuring the performance of the filter with the VNA.

Furthermore, we have discussed the important role that the phase of the response plays in the process, and we have provided an efficient approach to recover each of the measured responses without being affected by local minima.

Finally, we have shown how other *coarse* models can also be used. We have tuned a waveguide 4-pole filter using both a waveguide model and a *coarse* model based on transmission lines and inverters. We have discussed the limitations of using distributed models, and we have seen how the waveguide-based *coarse* models are not affected by the same limitations.

Novel Folded Multi-Band Filters

Multi-band filters have recently become an attractive approach to implement complex satellite payloads [52, 53]. A number of non-contiguous channels may, in fact, be amplified together and sent through the same satellite beam to cover a particular area, while rejecting specific interleaved channels. The most common approaches to design multi-band filters are:

- Using circulators to add or drop the various channels.
- Cascading a bandpass filter and one (ore more) band-stop filter(s).
- Using transmission zeros to separate a higher order bandpass filter into lower order channels.
- Using resonators with multiple modes.
- Using a manifold-based approach to combine the filter channels.

Recently in [66], it was shown that the well-known multiplexer design technique described in [9] could be used to design multi-band filters in a manifold configuration. Due to the importance of this paper in the rest of the chapter, we will now discuss this contribution in more detail.

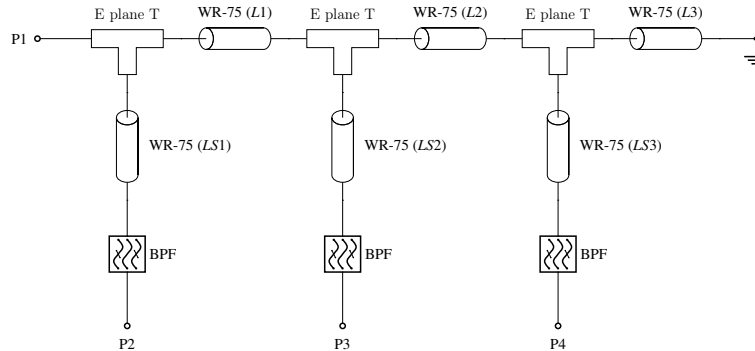


Figure 5.1: Manifold-based multiplexer.

5.1 Multi-band filters in a manifold configuration

According to [66], in order to design an N -band filter we can proceed as follows:

1. First design an N channel multiplexer following the well-known multiplexer design procedure in [9], [12]:
 - (a) Design the independent filter channels.
 - (b) Optimize exclusively the interjunction spacings ($L1$, $L2$ and $L3$ of Fig. 5.1).
 - (c) Optimize exclusively $L1$ and $LS1$.
 - (d) Repeat the previous step for all channels.
 - (e) If the multiplexer does not converge to the desired response, go back to step (c) and optimize an additional parameter per filter.

With this approach, the design parameters of each channel are optimized progressively, starting from the ones that are closer to the manifold. If instead of this strategy we tried to optimize all design variables at the same time, the optimizer would most likely get stagnated near a local minimum.

2. After designing the multiplexer, the N -band filter is simply obtained by mirroring the complete structure in the center of the filter channels, as shown in Fig. 5.2.
3. A final optimization of all design parameters is generally required. This step, however, is not computationally expensive because the performance of the N -band filter is, normally, very close to the target.

This technique was used in [66] to design a tri-band filter in WR-75. The channels were centered, respectively, at 11, 11.5 and 12 GHz and they all had a bandwidth of 100 MHz. Fig. 5.3 shows the topology of the filter that was manufactured and Fig. 5.4 shows its response.

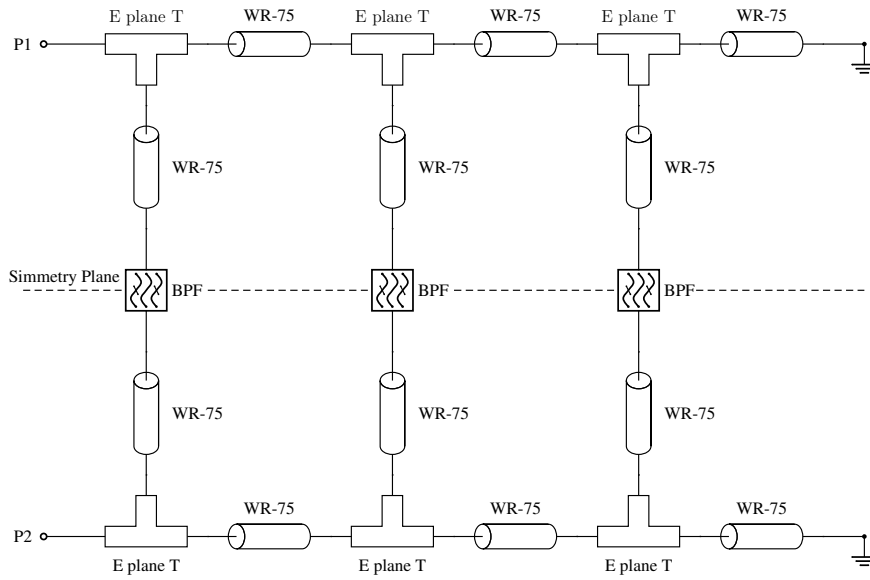


Figure 5.2: Manifold-based N-band filter.

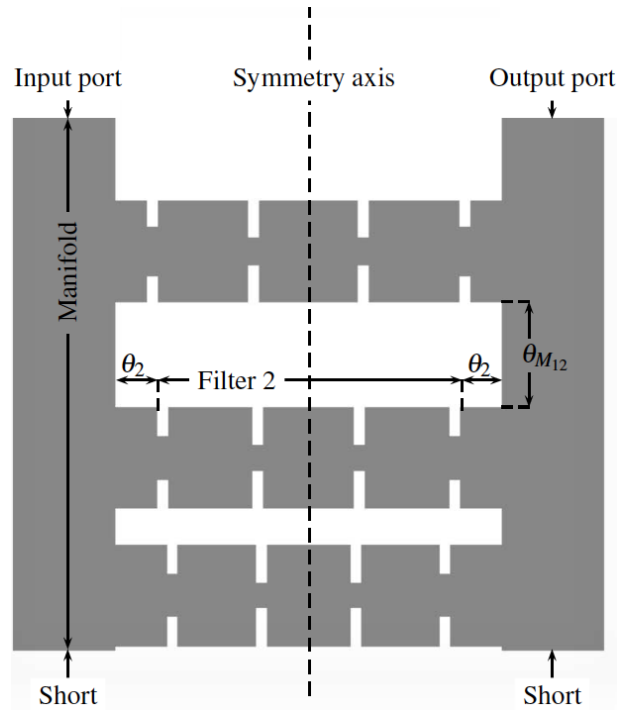


Figure 5.3: Topology of the tri-band filter designed in [66].

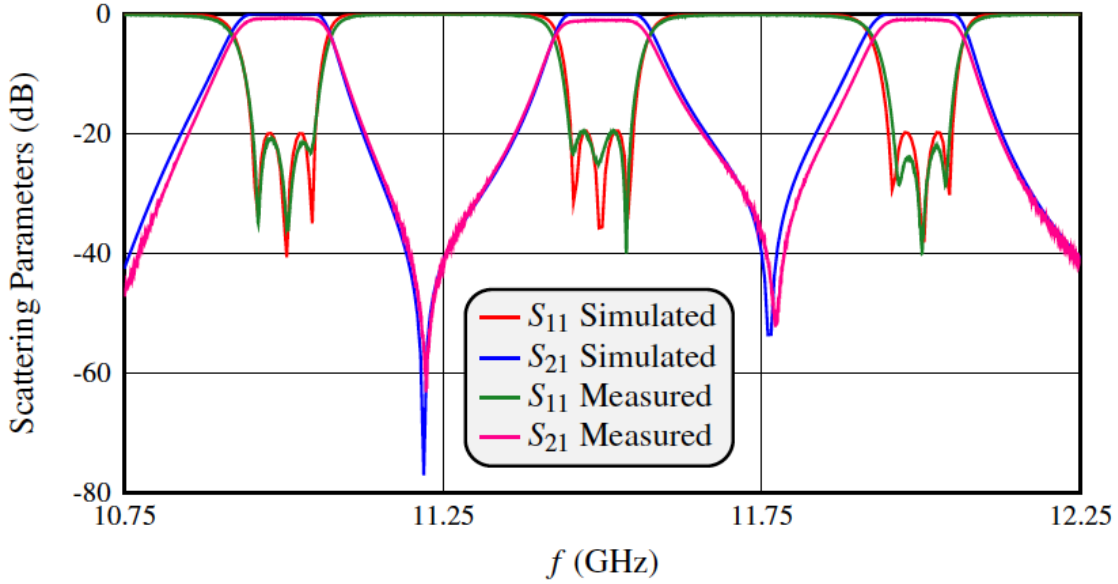


Figure 5.4: Performance of the tri-band filter designed in [66].

This is indeed a simple and effective design procedure. There are, however, some limitations regarding the physical realization of the filters:

- All channels must be of the same length. This requirement was guaranteed in [66] by enforcing the following condition:

$$L_s^{(i)} = L_{\text{half}} - L_1^{(i)} - \frac{L_2^{(i)}}{2} - t_1^{(i)} - t_2^{(i)} \quad \forall i = 1, 2, 3 \quad (5.1)$$

where $L_s^{(i)}$ is the length of the stub of the i -th channel, $L_1^{(i)}$ and $L_2^{(i)}$ are the lengths of the first and second cavity, and $t_1^{(i)}$ and $t_2^{(i)}$ are the thicknesses of the first and second aperture.

The stubs also increase the weight of the filter. In addition, enforcing the length constraint is especially challenging if the filter channels do not have similar characteristics. For example, it would not be possible to have filter channels with a different order.

- Finally, it is not possible to introduce cross-couplings between non-adjacent resonators, and thus, we cannot design channels with transmission zeros.

In this chapter we propose a novel topology that overcomes these limitations, and that still maintains the benefits of the original method regarding the flexibility in the number of channels, the frequency spacing and IL behavior. To validate the new topology

that we propose, we have also designed and manufactured a tri-band waveguide filter obtaining excellent agreement between measurements and simulations. The results of our investigation have been published in the following journal:

- J. C. Melgarejo, S. Cogollos, M. Guglielmi and V. E. Boria, "A New Family of Multiband Waveguide Filters Based on a Folded Topology," in *IEEE Transactions on Microwave Theory and Techniques*, vol. 68, no. 7, pp. 2590-2600, July 2020.

5.2 Proposed topology

The solution that we propose to overcome the limitations of [66], is simply to fold each filter channel in the center, as shown in Fig. 5.5:

- Folding each individual filter in the center removes the equal-length constraint, and eliminates the need for additional waveguide stubs. This is because the input and output ports of each channel are in the same plane (see Fig. 5.5). The filters can then be added to a double manifold to easily implement N -band filters. Fig. 5.6 shows the topology for a tri-band filter. Additionally, the channel filters can have different orders.
- Cross-coupling windows can also be easily implemented between non-adjacent resonators to introduce transmission zeros.

5.3 Specifications

The specifications that we have used for our tri-band filter design are as follows:

- Input and output: WR-75.
- Central frequency for the channels: 11, 12 and 13 GHz.
- Bandwidth of each channel: 200, 300 and 400 MHz.
- Order of the filter channels: $N = 6$.
- Every channel has two TZs, one below and one above its pass band.
- Rounded corners (2 mm radius, to account for the milling process).
- Commercial tuners with a radius of 0.9 mm in every cavity and inductive aperture.

It is important to note that, with our approach, there are no frequency or bandwidth restrictions. We could have chosen different values for the bandwidths, frequency spacing and order of the channels¹. The complete filter assembly has been manufactured by

¹Furthermore, by choosing odd order channels we could have introduced additional transmission zeros between adjacent bands due to the phase difference of the signal going through the filters. This is not used in this example to test the limitations (signal rejection) between adjacent bands in the worst-case scenario.

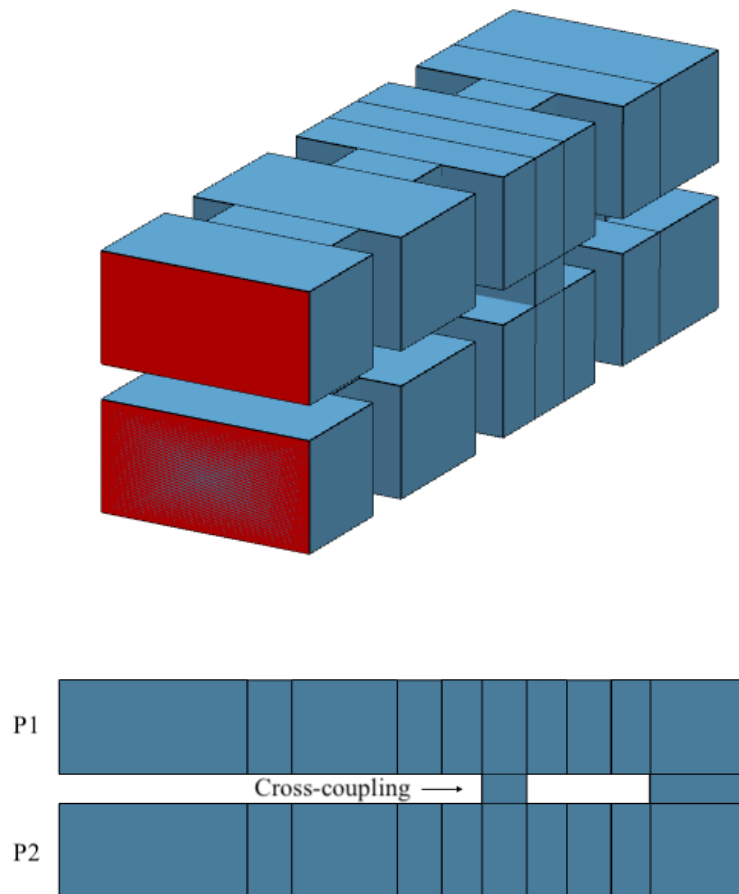


Figure 5.5: Proposed topology for the filter channels. Top: Perspective view of the filter. Bottom: Lateral view of the filter.

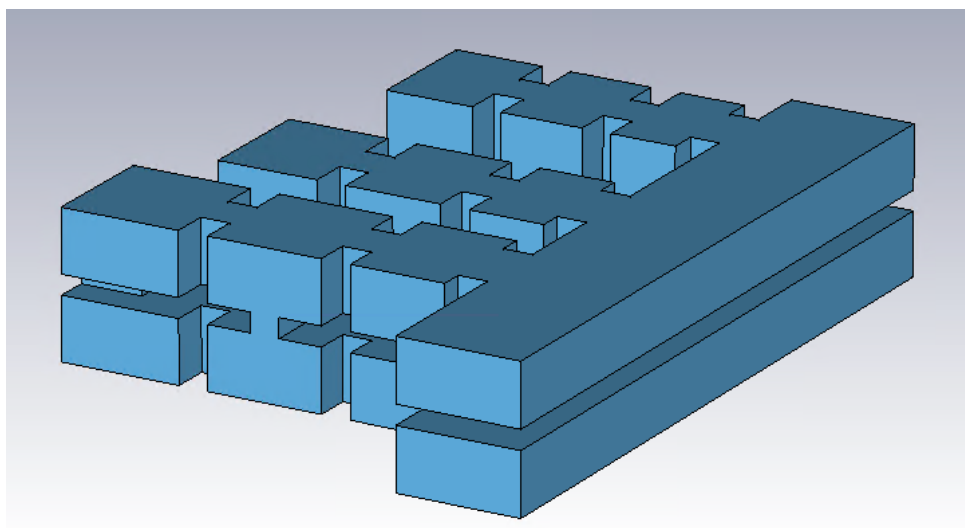


Figure 5.6: Proposed topology for the tri-band filter.

H-plane milling in three pieces: a body, a top and a bottom cover.

In the next section, we will describe in detail the complete design procedure, which basically consists of only two steps:

1. Design a low precision model of the complete filter that does not include rounded corners or tuning elements.
2. Then use the Step-by-Step ASM procedure described in Chapter 3 to obtain the final high-precision model of the filter that includes all non-ideal factors (tuners and rounded corners).

The low precision model has been obtained with FEST3D. For the final high-precision model we have used CST Microwave Studio. Table 5.1 contains the simulation settings used for both models.

5.4 Design of the independent channels

5.4.1 Folded filters without TZs

As in [66], the design of an N -band filter starts with the design of the independent channels. We begin our design with models based on transmission lines and inverters that provide the desired Chebyshev responses. We will then follow the procedure described in [17] to obtain the in-line waveguide models (see Fig. 5.7). Fig. 5.8 shows the response of each independent filter channel.

Table 5.1: Accuracy settings used for tri-band filter.

Coarse Model	
Simulator	FEST3D
Accessible modes	10
Number of basis functions	30
Green's function terms	300
Fine Model	
Simulator	CST Microwave Studio
Solver	Frequency Domain Solver
Frequency Sweep	General Purpose
Mesh refinement	11, 12 and 13 GHz
Error Threshold	0.005
Maximum number of iterations	20

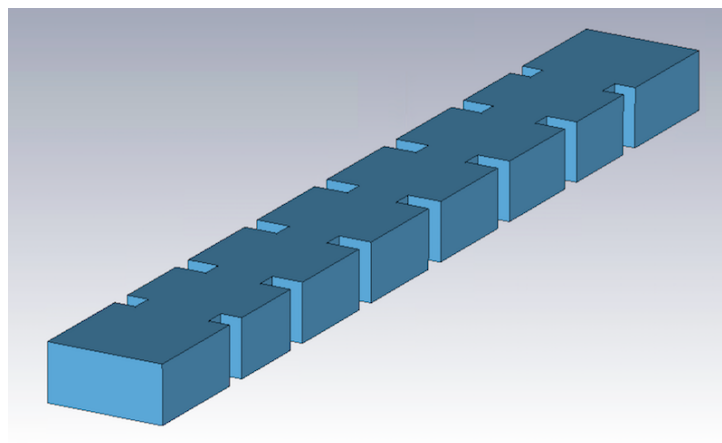


Figure 5.7: In-line 6-pole filter.

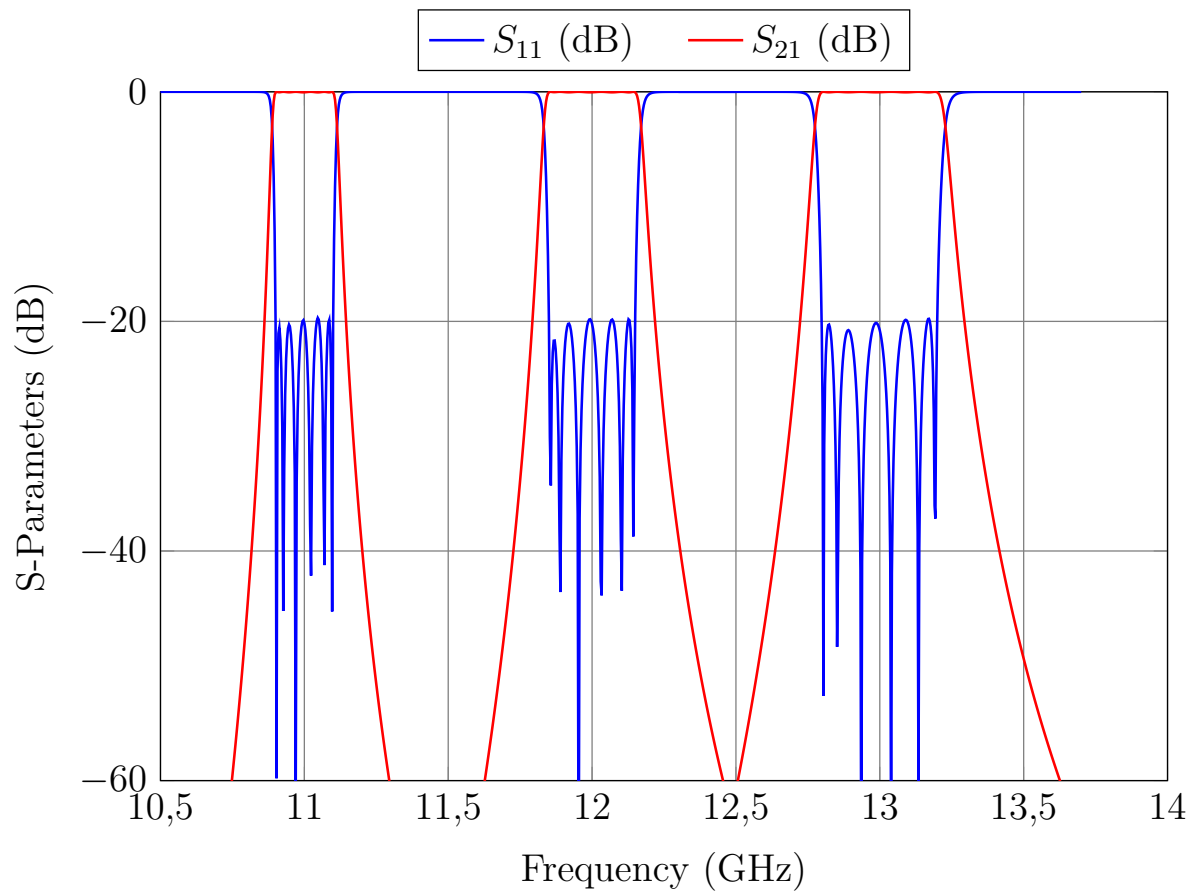


Figure 5.8: Performance of the independent in-line filters.

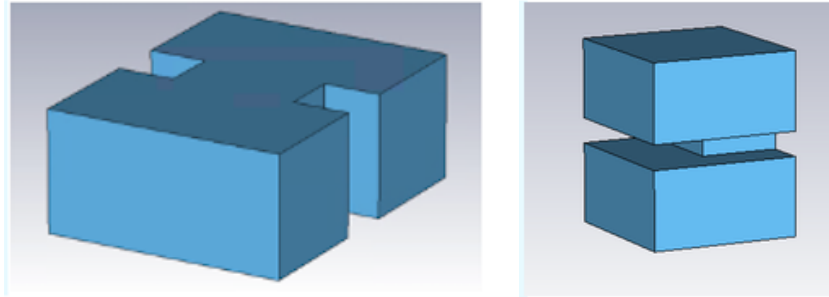


Figure 5.9: Left: Central aperture of the in-line filter. Right: Central aperture of the folded filter.

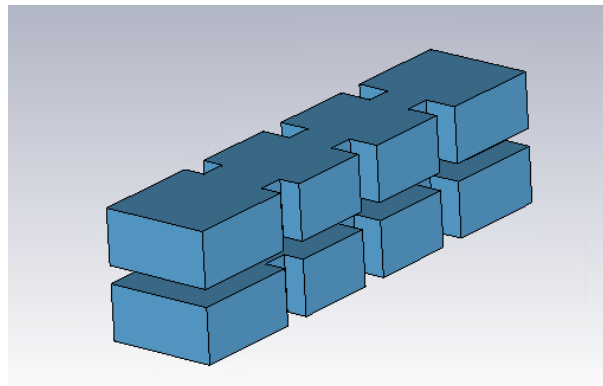


Figure 5.10: Folded filter without TZs.

Once the in-line filters have been designed, they need to be folded along their center. Fig. 5.9, left, shows the central iris of the in-line filter and Fig. 5.9, right, shows the central iris for the folded structure. It is necessary to optimize the latter until the performance (in module and phase) of the in-line aperture is recovered. To do this we need to optimize three parameters, namely, the height, the width and the thickness of the aperture.

The thickness of the aperture will determine the separation between the two halves of the filter, and it will also have an impact on the coupling level of the cross-couplings. If we use a low value (for example, 1 mm), both sides of the filter will be too close, and that will force us to use very narrow cross-coupling windows that may be difficult to manufacture with standard milling. Setting the thickness to 3 mm will ensure that the cross-coupling windows can be easily manufactured. Since to control the coupling level we only need one parameter, we decided to fix the height of the window to 9.525 mm.

After a short optimization of the two relevant parameters (the width of the central aperture and the length of the resonators to which it is attached) the folded filter (shown in Fig. 5.10) provides, essentially, the same performance as the in-line filter.

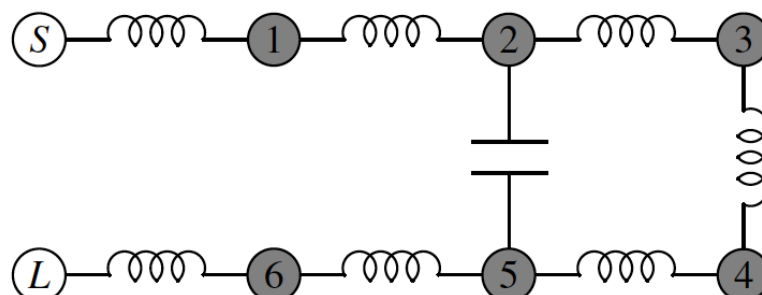


Figure 5.11: Multipath coupling diagram for a 2-5 cross-coupling.

5.4.2 Folded filters with TZs

In order to introduce the transmission zeros, we now need to open a cross-coupling between non-adjacent resonators. The transmission zeros appear when multiple paths of the signal are combined in a destructive way, or equivalently, when there is a 180° difference in the phase of the signals. If the cross-coupling is added between the second and fifth resonator (as shown in Fig. 5.11), we will introduce two transmission zeros, one below and one above the pass band. A more detailed explanation regarding phase shifts in the coupling windows and resonators can be found in [87].

Fig. 5.5 shows the filter with the cross-coupling between resonators two and five. The thickness of the window is the separation between the sides of the filter (3 mm) and the coupling level is controlled by the height of the window. A simple procedure to find the optimum height of the window is as follows:

1. Start with a short window of, for example, 1 mm high. The TZs at this point will be very far from the passband.
2. Optimize the length of the resonators connected to the capacitive coupling, and the widths of the apertures that are closest to the cross-coupling to recover the desired in-band performance.
3. After the previous step, the performance of the filter will be very close to the target response. However, if necessary, optimize the rest of the parameters to recover an equiripple response.
4. Finally, increase the height of the capacitive cross-coupling to change the position of the TZs and, if necessary, go back to step 2.

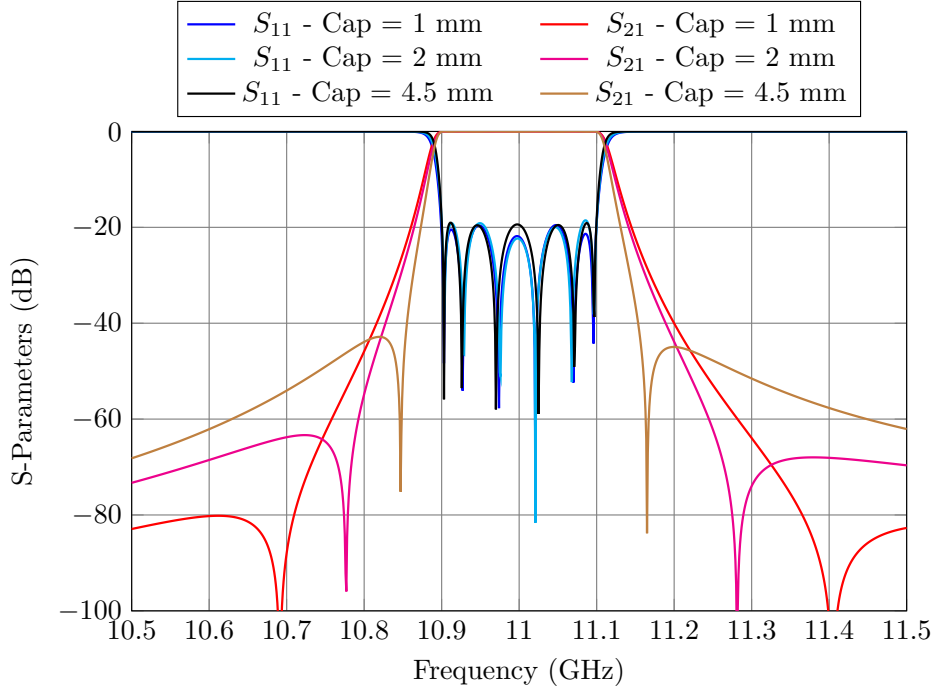


Figure 5.12: Performance of one of the channels for different cross-couplings.

These steps are repeated until the transmission zeros are located at the desired frequencies. In our case, the target performance is obtained for a height of 4.5 mm. Fig. 5.12 shows the performance of one of the channels for different heights of the capacitive window.

This process is repeated for all channels of the tri-band filter. Fig. 5.13 shows the performance of the independent channels. Fig. 5.14 shows that the filter are more selective due to the presence of the TZs. Now that the independent channels have been designed, we can proceed with the design of the tri-band filter.

5.5 Design of the tri-band filter

At this point, we could apply the design procedure described in [66], namely:

1. Obtain the three-channel multiplexer following the well-known procedure described in [9], [12].
2. Obtain the tri-band filter mirroring the multiplexer (along the center of the filter channels).
3. Finally, optimize all design parameters slightly.

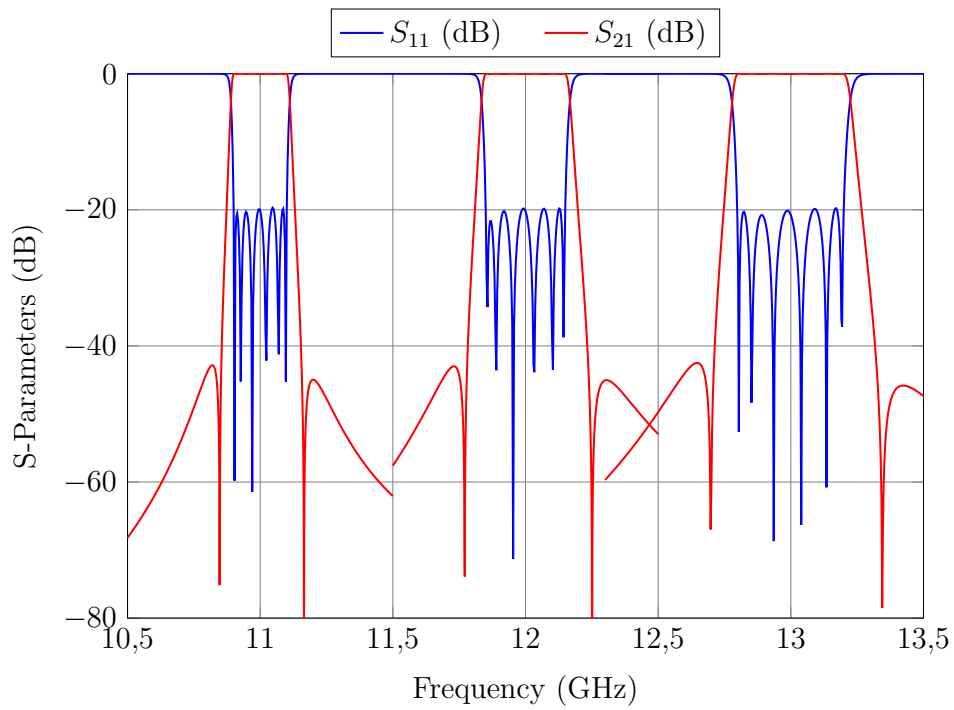


Figure 5.13: Performance the independent channels.

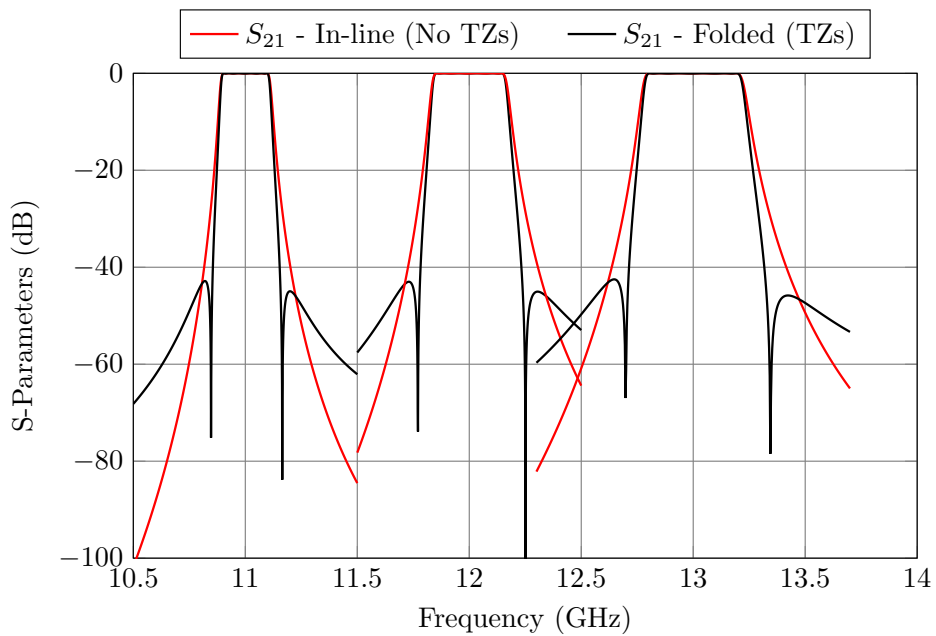


Figure 5.14: Performance the independent channels with and without TZs.

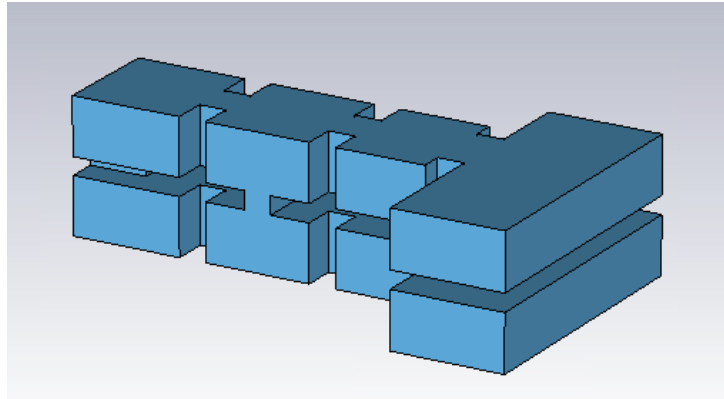


Figure 5.15: First channel connected to a double manifold terminated in short circuits.

However, it is not strictly necessary to follow these steps. As an alternative, we can design the tri-band filter assembly at once. In this case, the design procedure is as follows:

1. Add the narrowest filter to two manifolds terminated in short circuits as shown in Fig. 5.15 and optimize, exclusively, the distance to the short circuits and the width of the first aperture of the filter. Fig. 5.16 shows the performance of the filter after this step. As it is stated in [9], a good starting point for the length of the stub is $\lambda_g/4$.
2. After that, add the next filter to the manifold (as shown in Fig. 5.17) and optimize the separation between the channels and the first aperture of the newly added filter. A good starting point for the channel separation is $\lambda_g/2$. Finally, optimize simultaneously the four parameters we have considered so far: the widths of the first apertures and the stubs of the manifold. Fig. 5.18 shows the performance of the filter after this step.
3. Finally, add the third channel to the manifold (as in Fig. 5.19) and repeat the previous step. After an optimization process using only six parameters, the performance of the filter is shown in Fig. 5.20.
4. Finally, follow the well-known multiplexer design strategy of [9] to fine tune the filter performance. Fig. 5.21 shows the optimized performance of the low precision model.

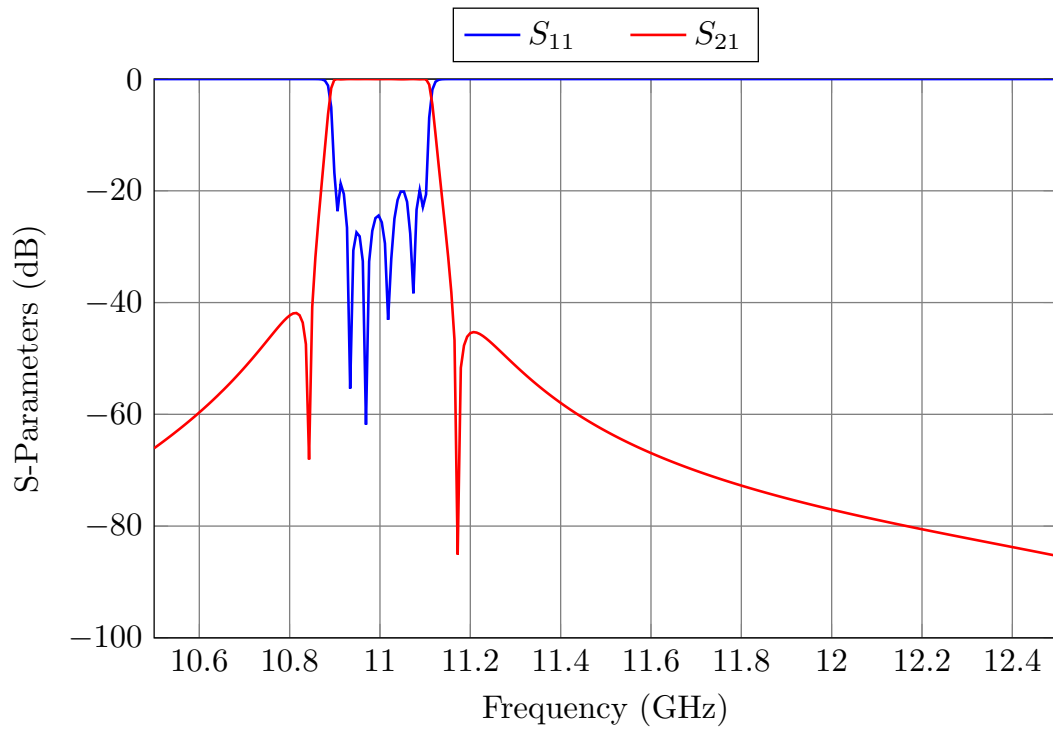


Figure 5.16: Performance of the filter after connecting it to a double manifold.

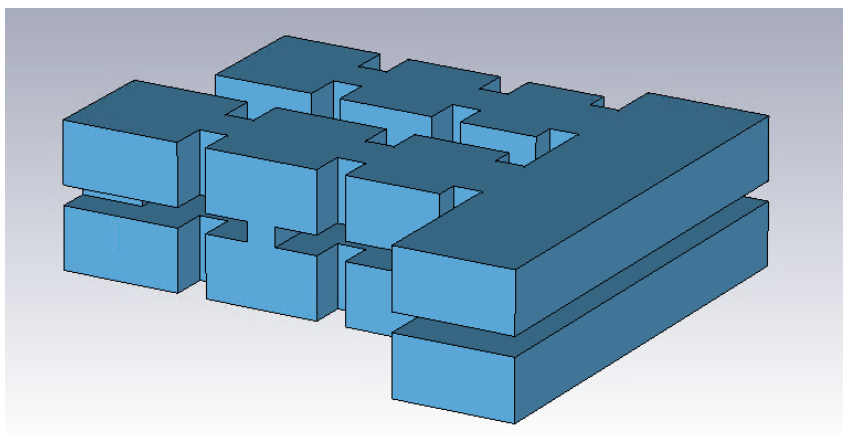


Figure 5.17: Structure after adding the second filter channel.

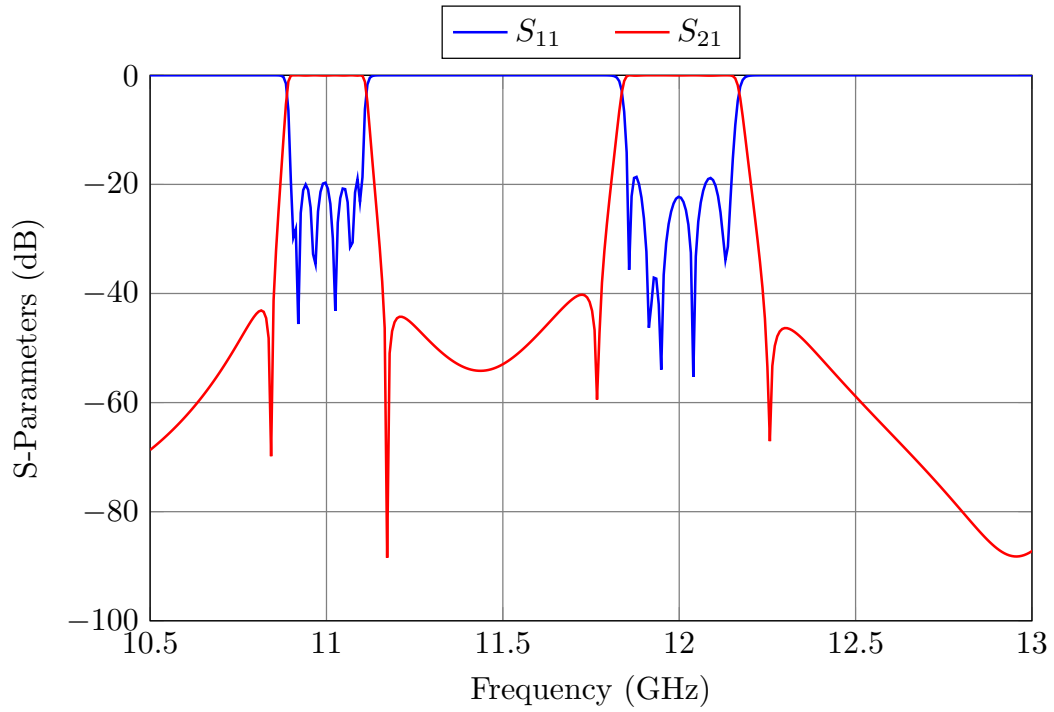


Figure 5.18: Performance of the filter after connecting the second channel to the double manifold.

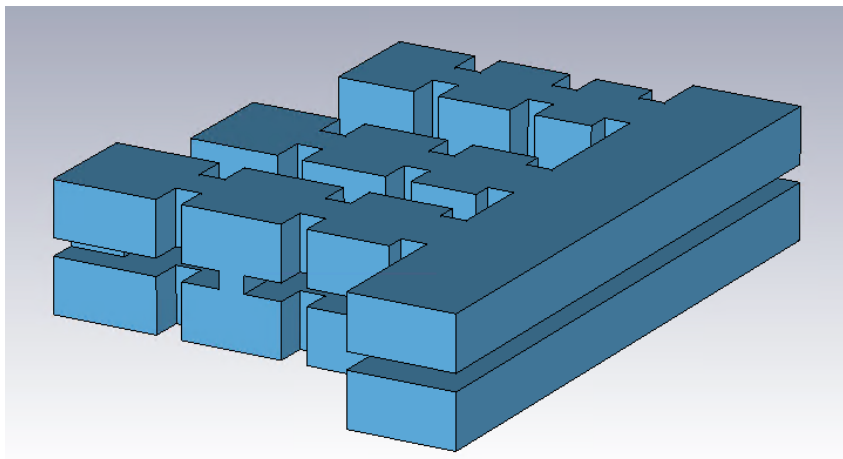


Figure 5.19: Structure after adding the third filter channel.

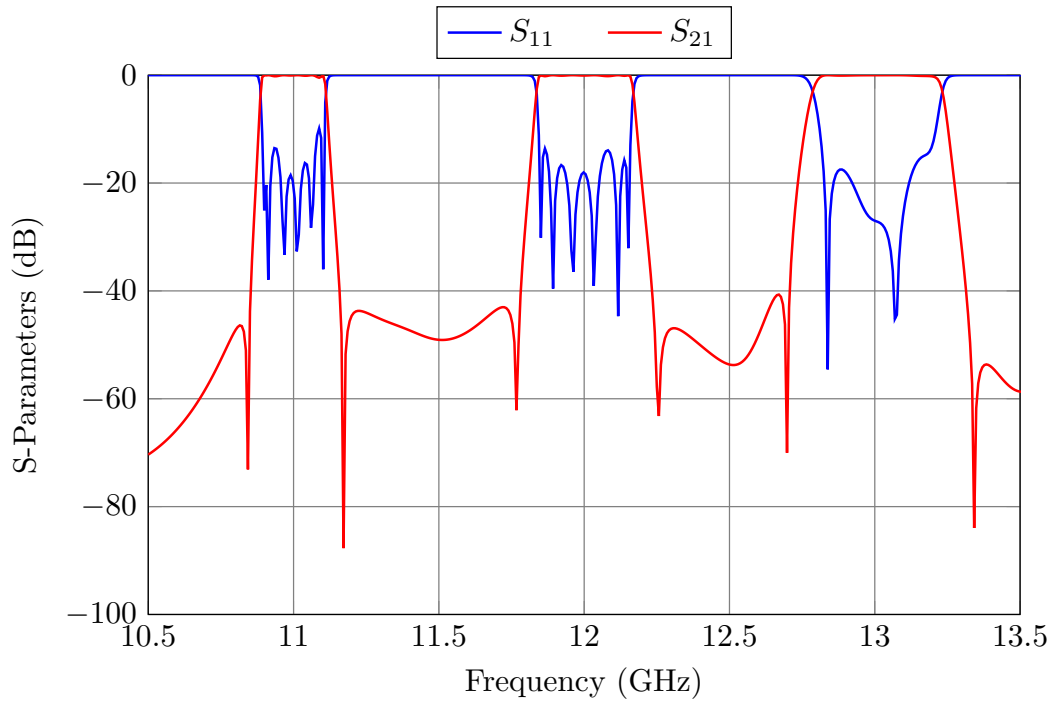


Figure 5.20: Performance of the filter after connecting the third channel to the double manifold.

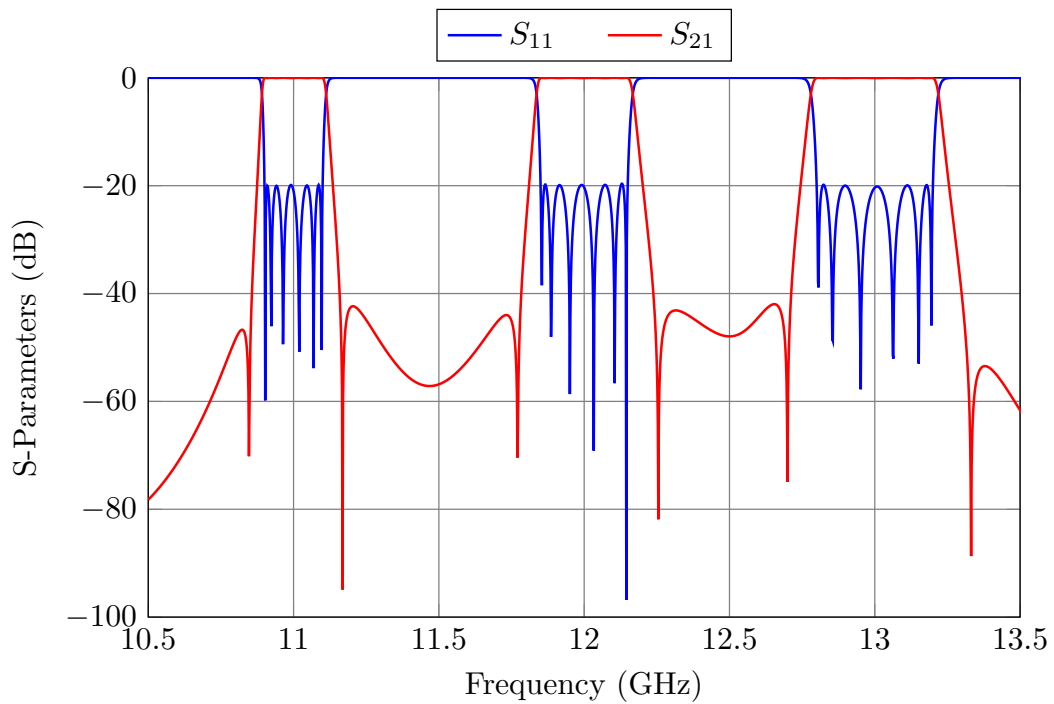


Figure 5.21: Optimized performance of the low-precision model.

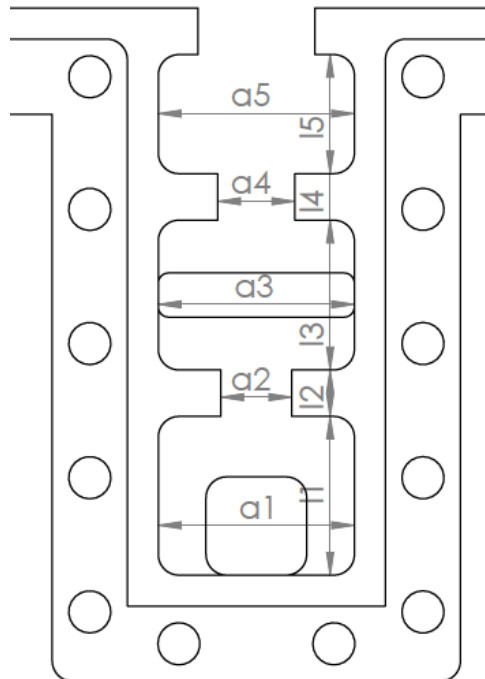


Figure 5.22: Closing M4 screws and pressure well.

5.6 Practical considerations

5.6.1 Closing screws

As already discussed, the filter will be manufactured in three parts: a body and two covers. A solid block of aluminum will be machined from two directions (top and bottom) in order to obtain the body of the filter. We will then need to assemble the body and covers using M4 screws.

In order to ensure a good electric contact between the pieces, we need to include a pressure well (go to Appendix A for additional details) around the closing M4 screws, as shown in Fig. 5.22. However, in the design process we noticed that the channels were too close to each other, and therefore, we decided to move the central channel to the other side of the manifold as shown in Fig. 5.23.

This barely affects the performance of the filter, as shown in Fig. 5.24. The central channel can be easily optimized in order to recover the equiripple performance shown in Fig. 5.21.

Up to this point, we have not provided any details concerning the actual manufacturing of the filters. Appendix A provides a detailed description on how to draw the

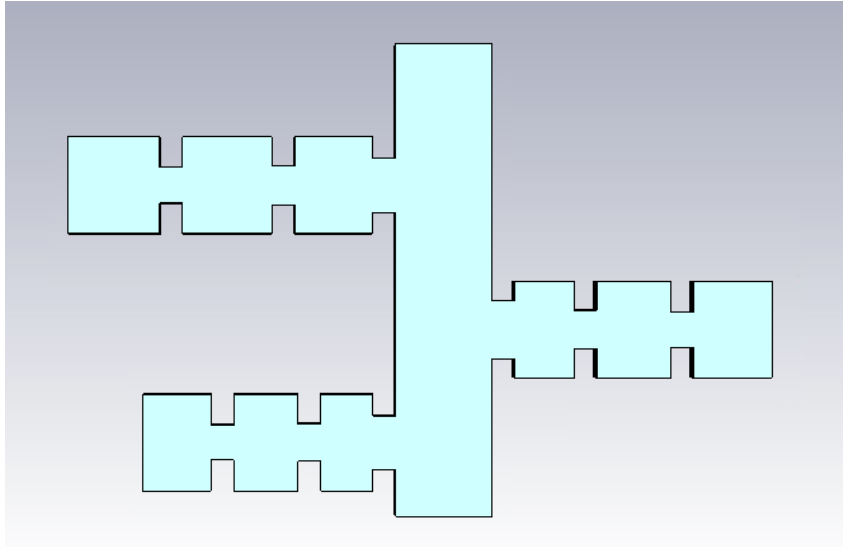


Figure 5.23: Final structure after changing the central channel to the opposite side.

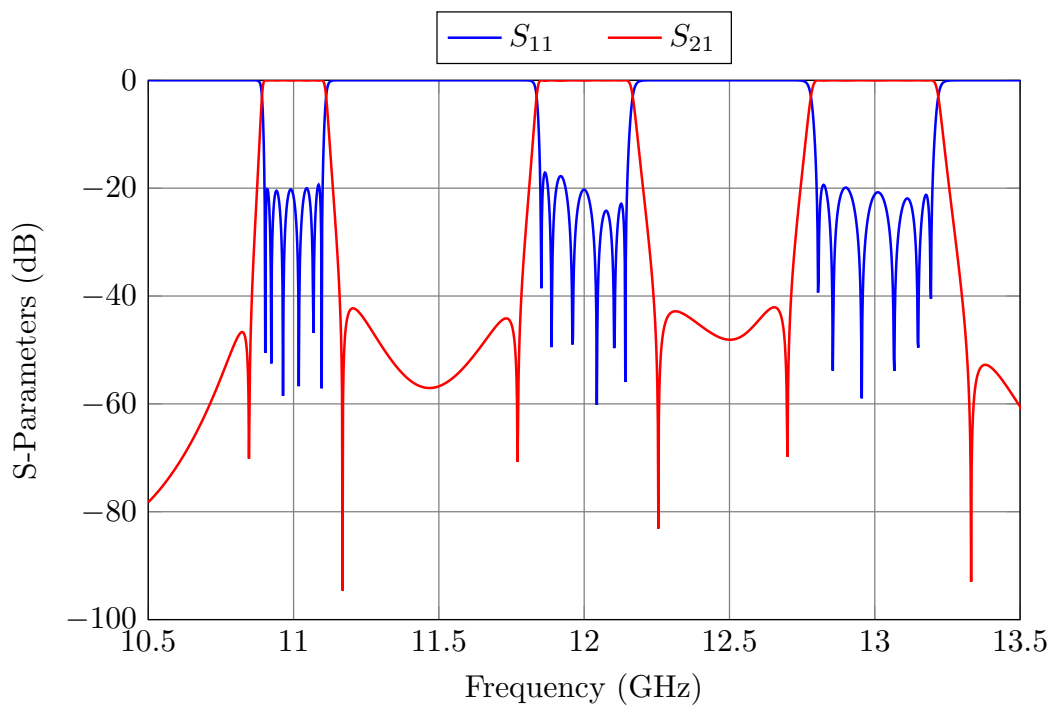


Figure 5.24: Performance of the filter after flipping the central channel.

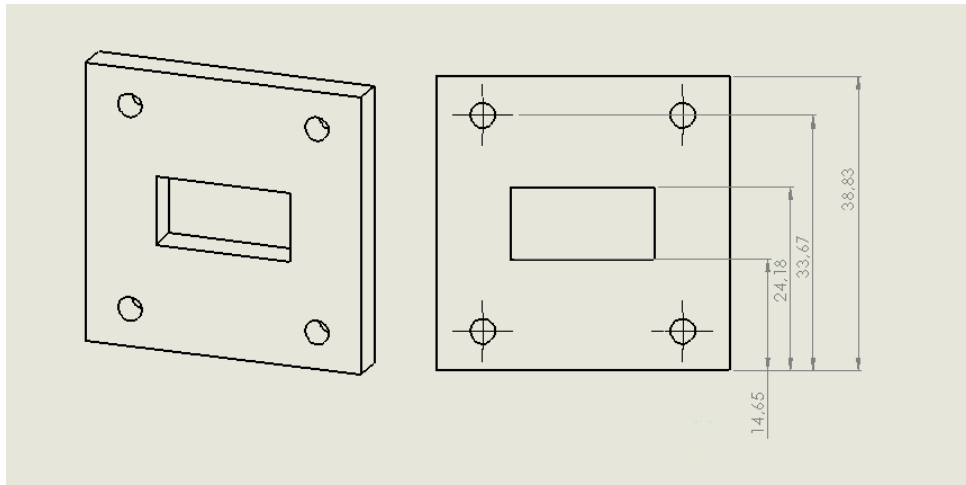


Figure 5.25: Flanges for WR-75. All annotations are in mm.

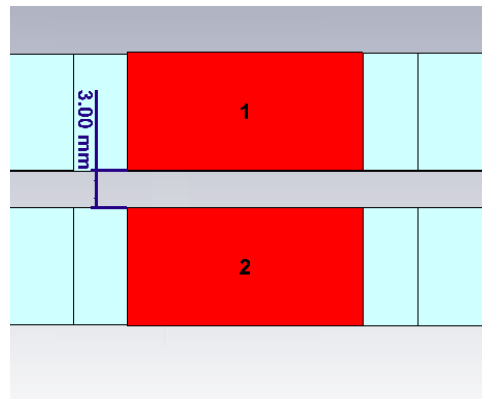


Figure 5.26: Lateral view of the filter. The ports are marked in red.

manufacturing plans with Solid Works for the folded 6-pole folded filter shown in Chapter 3, which is actually the first channel of the tri-band filter.

5.6.2 Flanges

The filter will be fed by two WR-75 waveguides, as mentioned in Section 5.3. Fig. 5.25 shows the standard dimensions for a WR-75 waveguide. However, both sides of the filter are only separated by 3 mm (as shown in Fig. 5.26). In order to feed the filter with standard WR-75 flanges, we have added two H-plane bends as shown in Fig. 5.27.

It is important to note that we can design these bends separately, minimizing the return loss at the frequency of interest (10.5-13.7 GHz). In this case, the optimum dimensions for the inner and outer radius are 5.45 and 24.51 mm, respectively.

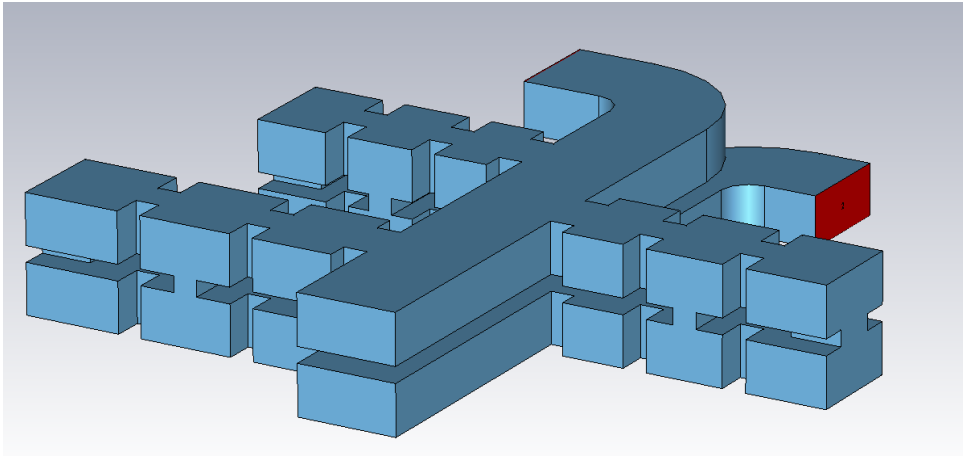


Figure 5.27: Two H-plane bends have been added to the filter, so that it can be fed with standard WR-75 flanges.

5.7 High-precision simulations

After the low precision model is designed we can perform a yield analysis to determine whether the filter requires tuning elements or not. From a normal distribution of mean $\mu = 0$ and standard deviation of $\sigma = 10 \mu\text{m}$, we obtain a data set of $N \times 1$ vectors (N being the total number of design parameters of the filter) that represent the manufacturing deviations. Out of the 300 vectors, only 6 comply with the design specifications. Fig 5.28 shows the the performance of the first channel after applying the first 10 deviations (out of 300).

It is therefore obvious that the tri-band filter needs tuning elements. A commercial tuner with 0.9 mm radius has been added to the center of each cavity, and inductive aperture. However, no tuning elements have been added to the capacitive couplings. In order to allow for future bidirectional adjustments, all tuners have been set to a fixed penetration of 1 mm. At this point, the rounded corners have also been included in the hardware. Fig. 5.29 shows the final high precision model of the filter.

For this stage of the design, we will use CST Microwave Studio with the settings shown in Table 5.1. The transition from the low-precision model in FEST3D to the high-precision model can be effectively performed using the Step-by-Step ASM procedure described in Chapter 3. The procedure is as follows:

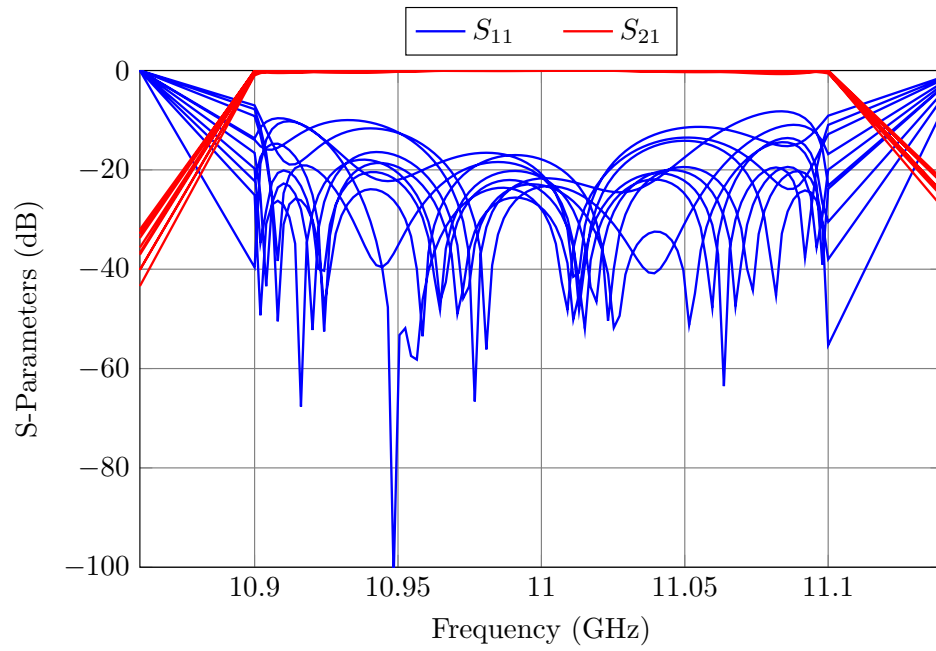


Figure 5.28: Yield analysis.

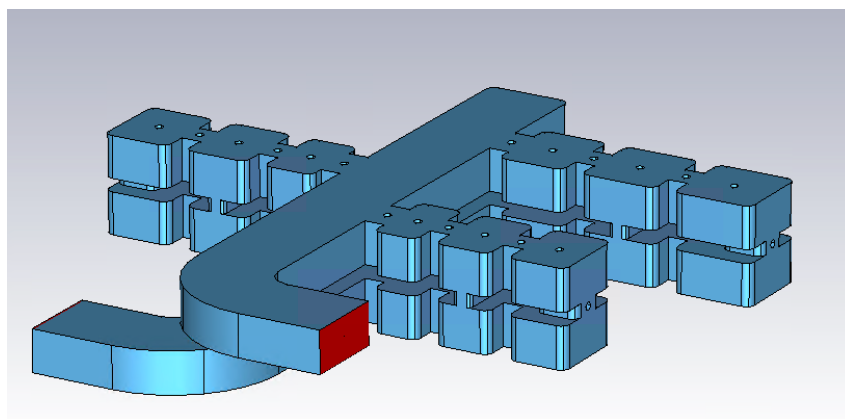


Figure 5.29: Final high-precision model of the tri-band filter.

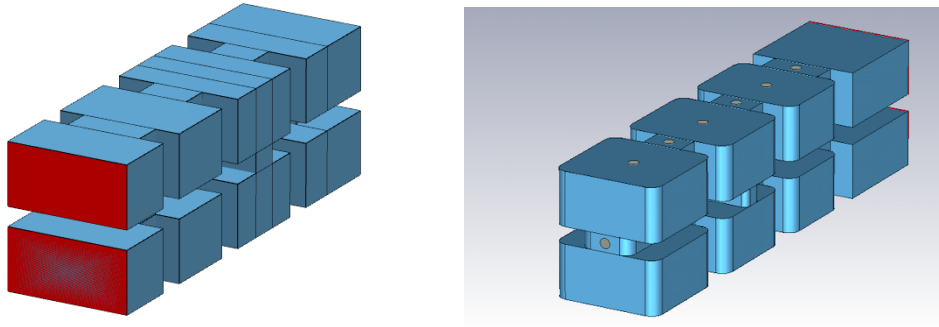


Figure 5.30: Left: *Coarse* model of one of the filter channels. Right: *Fine* model.

1. We will first extract each filter channel from the manifold to treat them separately. Fig. 5.30 (left) shows one of the filter channels. This structure will provide the reference performance that the high-precision model of the filter [shown in Fig. 5.30 (right)] should match.
2. For each of the channels, perform the Step-by-Step ASM procedure described in Section 3.3.2. After an optimization process in which several *coarse* and *fine* models are used, the *fine* structure of Fig. 5.30 will provide the target performance. Fig. 5.31 shows the performance obtained for the second filter channel.
3. Add the filters to the manifold obtaining the structure of Fig. 5.29. Since each filter channel has already been optimized, the performance of the filter will be very close to the desired response, as shown in Fig. 5.32.
4. Finally, perform an ASM iteration using the *coarse* model shown in Fig. 5.23 and the *fine* model shown in Fig. 5.29. Note that the *coarse* model does not include the flanges, as they do not change the response of the filter. Fig. 5.33 shows the final performance of the high-precision model.

5.8 Experimental validation

The tri-band filter was finally manufactured in three parts by milling a block of aluminum. A 10 μm silver-plating finish was added to reduce the effect of ohmic losses. This in turn will decrease the manufacturing accuracy. However, this is not a problem because we are using tuning elements. Fig. 5.34 shows both the body and covers of the filter.

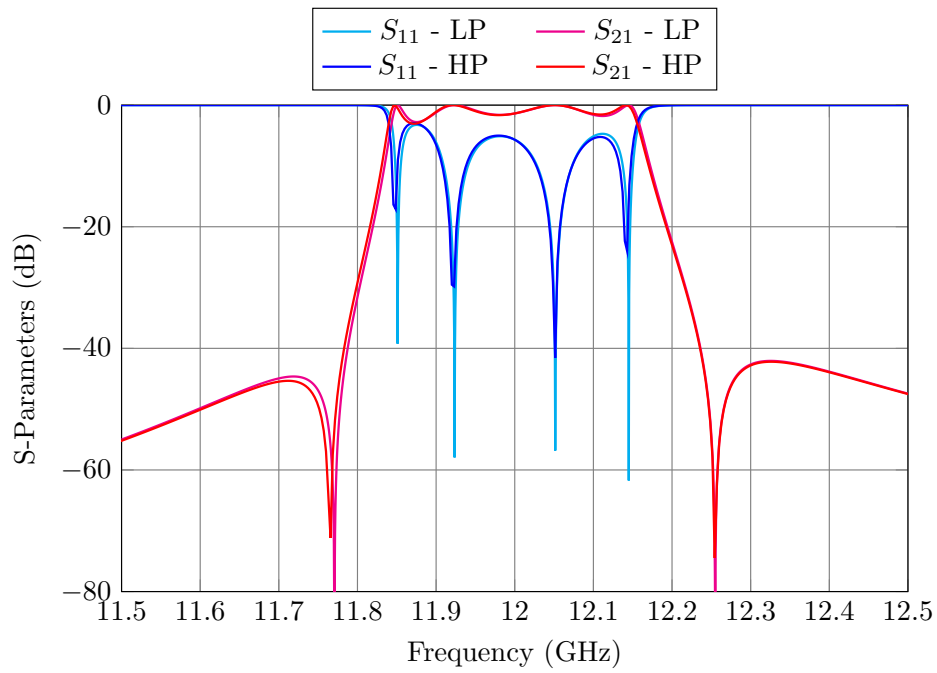


Figure 5.31: Performance of the low and high-precision models for the second filter channel.

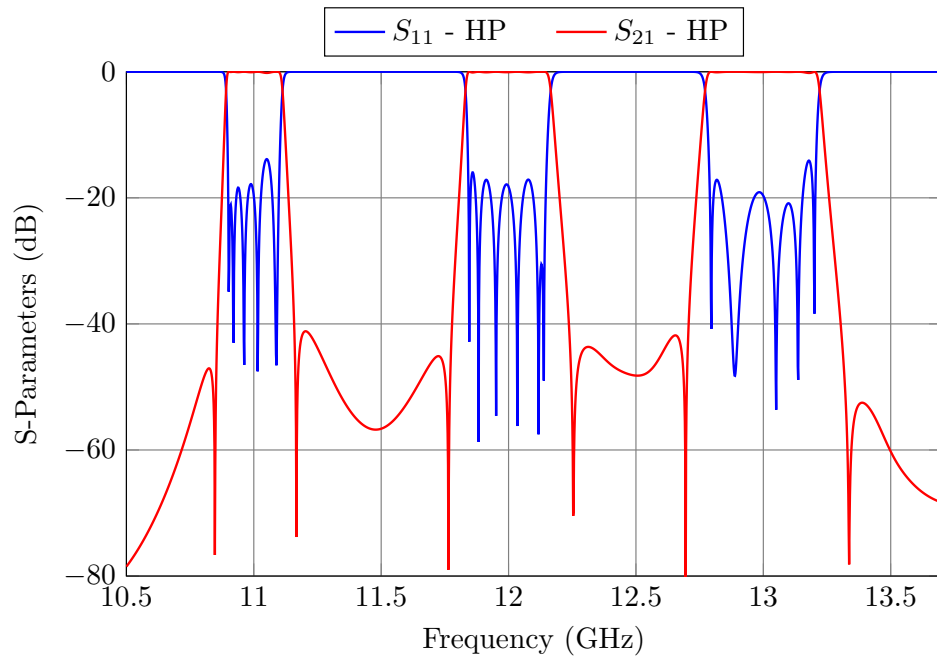


Figure 5.32: Performance of the high-precision model after adding the filter channels to the manifold.

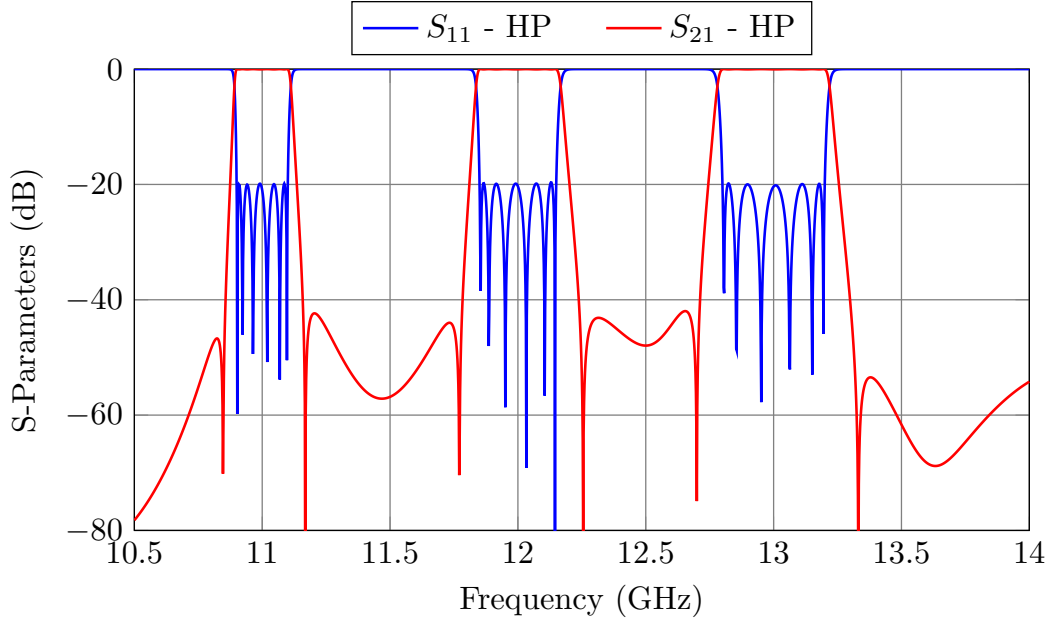


Figure 5.33: Final performance of the high-precision model.

Table 5.2: Parameters of the combined analysis.

$max(error)$	$min(error)$	Average Error	Standard Deviation
38 μm	10 μm	12.7 μm	27 μm

5.8.1 CMM measurements of the filter

After the filter was manufactured, we measured the actual filter dimensions using a coordinate-measuring machine (CMM). This was done in order to evaluate the errors introduced in the manufacturing process.

The manufacturer provided us with a csv spreadsheet with the optical measurements of the filter. For each side of every filter channel we were given the following measurements: a1, l1, a2, l2, a3, l3, a4, l4, a5 and l5 (see Fig. 5.35). In total, that makes it 60 X-Y plane measurements (20 per channel). We also had 10 measurements in Z (depths) at different points. We could obtain an estimation of the manufacturing errors subtracting these CMM measures from the nominal dimensions of the filter.

5.8.1.1 Combined analysis

Table 5.2 shows the key parameters of the manufacturing errors. Specifically, it shows the maximum and minimum absolute error, the average error and the standard deviation. Looking at these parameters we can conclude that:

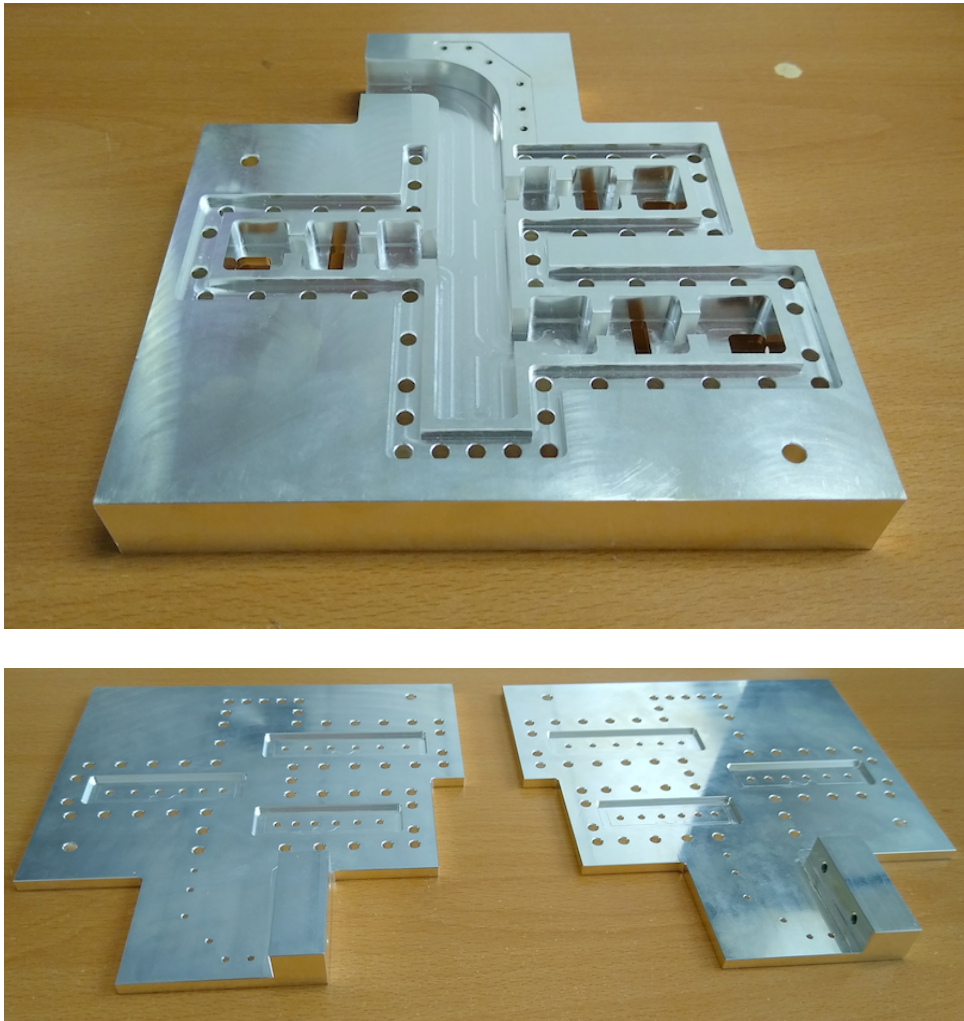


Figure 5.34: Top: Body of filter. Bottom: Top and bottom covers of the filter.

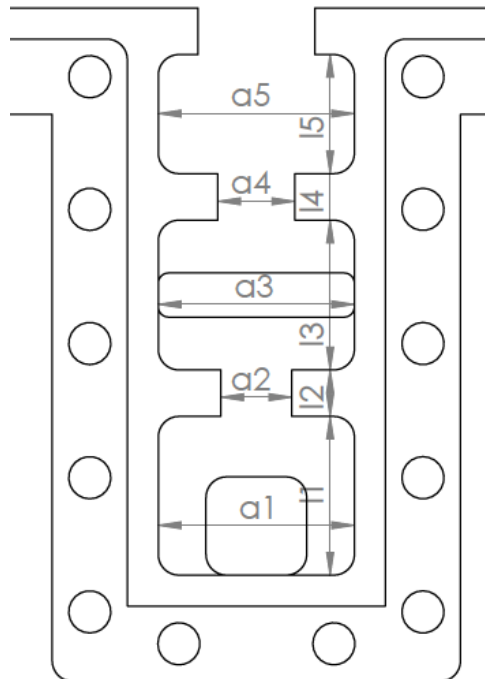


Figure 5.35: CMM measurements of each filter channel.

- The maximum error is smaller than the $50 \mu\text{m}$, which is the precision we agreed at with the manufacturer. We will be able to compensate these errors with the tuning elements.
- The standard deviation is very large and the average error is not near $0 \mu\text{m}$.

The results do not follow a normal distribution centered at 0 mm , which is what we expected. Fig. 5.36 shows the histogram of the errors. In the 70 error samples, there is not a single entry with absolute value below $10 \mu\text{m}$. We can also see that positive errors (48 out of 70) are more frequent than the negative errors (22 out of 70).

5.8.1.2 Separate analysis

In the previous section we analyzed all the errors at the same time. We had, in fact, assumed that the X-Y errors and the Z errors behaved in a similar way. This, however, appears not to be the case. If we think about the process to machine the filter, we can assume that:

- The X and Y errors must be related because the mechanics of both movements is the same. It is safe to assume that the CNC (computer numerical control) machine will behave similarly along the X and Y axis.
- The movement in the Z axis may follow a different distribution.

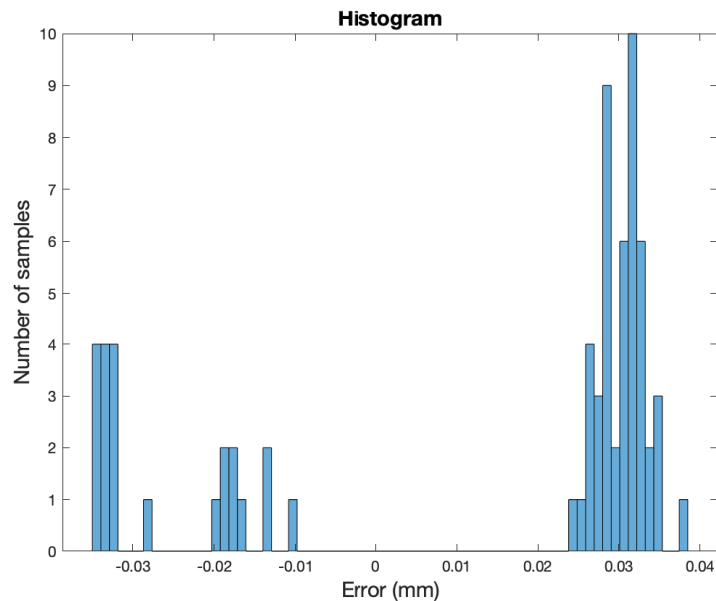


Figure 5.36: Histogram of the errors.

Table 5.3: Key parameters of the Z errors.

$\max(\text{error})$	$\min(\text{error})$	Average Error	Standard Deviation
$28 \mu\text{m}$	$10 \mu\text{m}$	$-17.6 \mu\text{m}$	$4.8 \mu\text{m}$

The manufacturer confirmed that this assumption is in fact, true. The physical components of the CNC machine involved in moving the arm in the X and Y axis have similar mechanisms. However, the movement in the Z axis involves a different set of components. We will, therefore, separate the original dataset into two separate ones: an X-Y dataset of 60 samples and a Z dataset of 10 samples.

We will first analyze the errors in Z. It is important to note that we only have 10 samples and therefore, the results are not very representative. Table 5.3 shows the key parameters. Specifically, it shows the absolute maximum and minimum values, the average error and the standard deviation.

Fig. 5.37 shows the histogram for the Z deviations. In this case, the values are more evenly distributed between $-28 \mu\text{m}$ y $-10 \mu\text{m}$. There is a resemblance between the histogram of the data and a normal distribution of mean $-17.6 \mu\text{m}$ and standard deviation of $4.8 \mu\text{m}$. Even though we do not have enough data points to make a proper inference, we can clearly see that all Z errors are negative, and centered around $-18 \mu\text{m}$. This suggests that there is a bias in the Z axis, and the cutting tool did not remove as much aluminum as it should have.

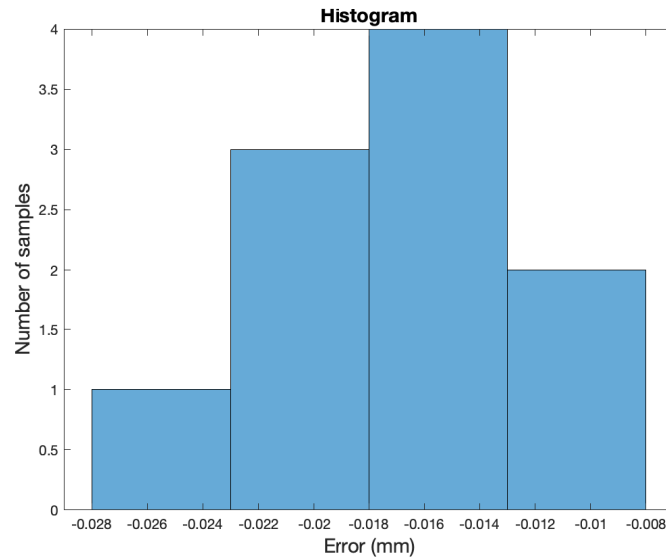


Figure 5.37: Histogram for the Z errors.

Table 5.4: Key parameters of the X-Y errors

$\max(\text{error})$	$\min(\text{error})$	Average Error	Standard Deviation
$38 \mu\text{m}$	$24 \mu\text{m}$	$17.8 \mu\text{m}$	$25.8 \mu\text{m}$

We will now analyze the X-Y errors. The dataset in this case is larger, so we will be able to draw better conclusions. Table 5.4 shows the key parameters. The key parameters alone do not provide much insight, but when we visualize the data (Fig. 5.38) we can clearly see that:

- There are no errors smaller than $24 \mu\text{m}$ (in absolute value). This clearly shows that, again, there is a bias in the errors.
- We can see an cluster of errors around $+30$ and $-30 \mu\text{m}$. There must be a reason for this.
- Out of the 60 samples, there are 48 positive errors (the dimensions were wider or longer than they were supposed to) and 12 negative errors.

Since there are fewer negative than positive errors, we will first focus on these values. Fig. 5.39 shows the X-Y errors for one of the channels (for both sides). Out of all the errors, the four negative ones belong to l2 and l4 (in both sides), which correspond to the lengths of the apertures that have been measured. This behavior is repeated for the other two channels.

If we analyze the errors considering the type of each element (width and length of

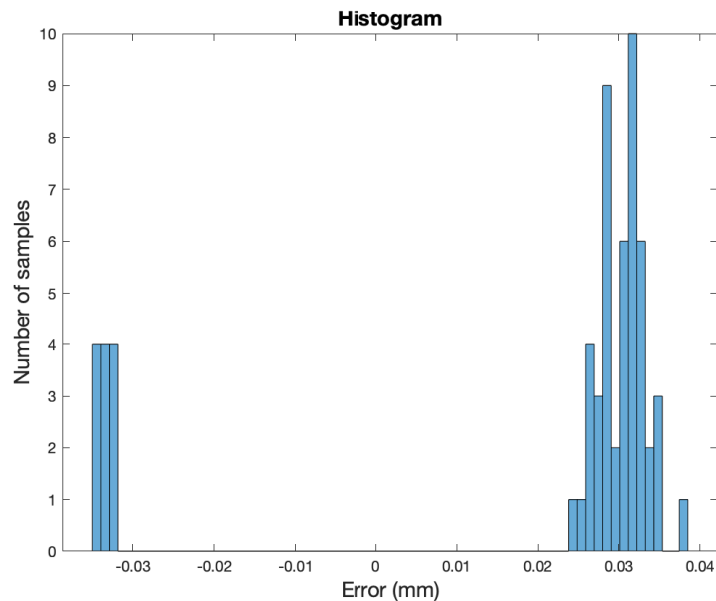


Figure 5.38: Histogram for the X-Y errors.

apertures or resonators) we conclude that:

- The errors of the widths a_i $i = 1, \dots, 5$ are **all positive**. This happens for all filters: the widths of all cavities and apertures are slightly wider than they should. **The errors are always positive.**
- If we check the lengths of the resonators (l_1 , l_3 y l_5), the same thing happens. **The errors are always positive.**
- Finally, we can observe that the errors of the lengths of the coupling windows (l_2 y l_4) **are always negative.**

These results strongly suggest that there is a bias in the errors of $30 \mu\text{m}$: the cutting tool removes more metal than it should. The reason why some of the errors are positive and some are negative is straightforward. Let us consider the milling process itself, starting from the first cavity (whose length and width are given respectively by l_5 and a_5):

1. The cutting tool removes more metal than it should and, therefore, the first resonator results slightly longer and wider than it should have been (positive errors). Fig. 5.40 (left) shows the directions in which the cutting tool moves.
2. The next aperture is then milled. The width(a_4) is slightly wider than it should. Since the aperture is opened from the ends (it is connected to the cavities), the cutting tool cannot alter the thickness. Fig. 5.40 (center) shows the directions in

Dimension	Model dimension	Measured dimension	Error
a1	19,05	19,078	0,028
a2	6,88	6,906	0,026
a3	19,05	19,078	0,028
a4	7,47	7,499	0,029
a5	19,05	19,076	0,026
l1	15,38	15,41	0,03
l2	4,5	4,466	-0,034
l3	14,52	14,546	0,026
l4	4,5	4,465	-0,035
l5	11,54	11,575	0,035

Dimension	Model dimension	Measured dimension	Error
a1	19,05	19,076	0,026
a2	6,98	7,011	0,031
a3	19,05	19,077	0,027
a4	7,49	7,523	0,033
a5	19,05	19,08	0,03
l1	18,2	18,227	0,027
l2	4,5	4,467	-0,033
l3	17,45	17,475	0,025
l4	4,5	4,465	-0,035
l5	15,23	15,262	0,032

Figure 5.39: Top: Manufacturing errors in the top side of the first filter channel. Bottom: Manufacturing errors in the bottom side.

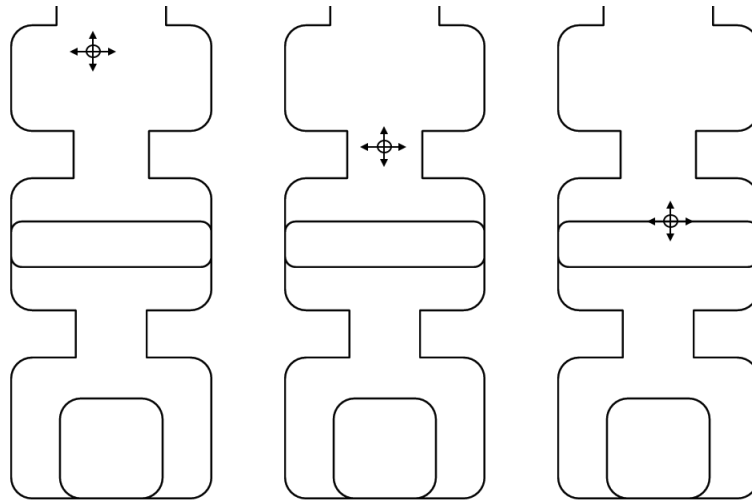


Figure 5.40: Cutting tool directions for the first cavity, first aperture and second cavity.

which the cutting tool moves.

3. For the second resonator (a_3 , l_3) the same thing happens. It is longer and wider than it should have been (positive errors). Fig. 5.40, right, shows the machining directions.
4. The errors in the thicknesses of the apertures are 100 % correlated to the errors in the cavities that are connected to them (the correlation is -1). If the cutting tool makes l_5 y l_3 longer than they should have been, it is indirectly shortening l_4 .

We can eliminate the negative X-Y errors from the analysis, since now we know that these errors are completely determined by the dimensions of the adjacent cavities. Fig. 5.41 shows the histogram of the positive errors. It seems reasonable to say that we now have a gaussian distribution of mean $30.5 \mu\text{m}$, and standard deviation of $3 \mu\text{m}$.

It is interesting to note that, if we did have this data before manufacturing the filter, we could easily have pre-compensated the nominal dimensions:

- We would have made all apertures and cavities $30.5 \mu\text{m}$ narrower.
- We would have made all cavities $30.5 \mu\text{m}$ shorter.

With these corrections, we would have been able to reduce the maximum error by **5 times** without any cost. Fig. 5.42 shows the histogram of the corrected errors. From this point on, therefore, it is strongly advisable to discuss with the manufacturers possible modifications to the dimensions of the filter to correct possible biases in manufacturing errors.

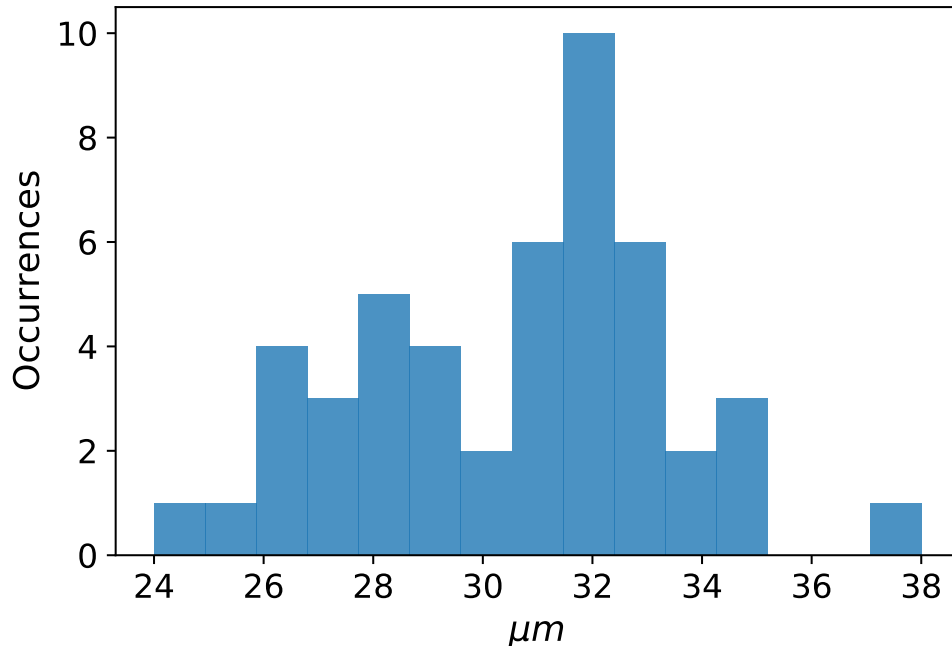


Figure 5.41: Histogram of the positive X-Y errors.

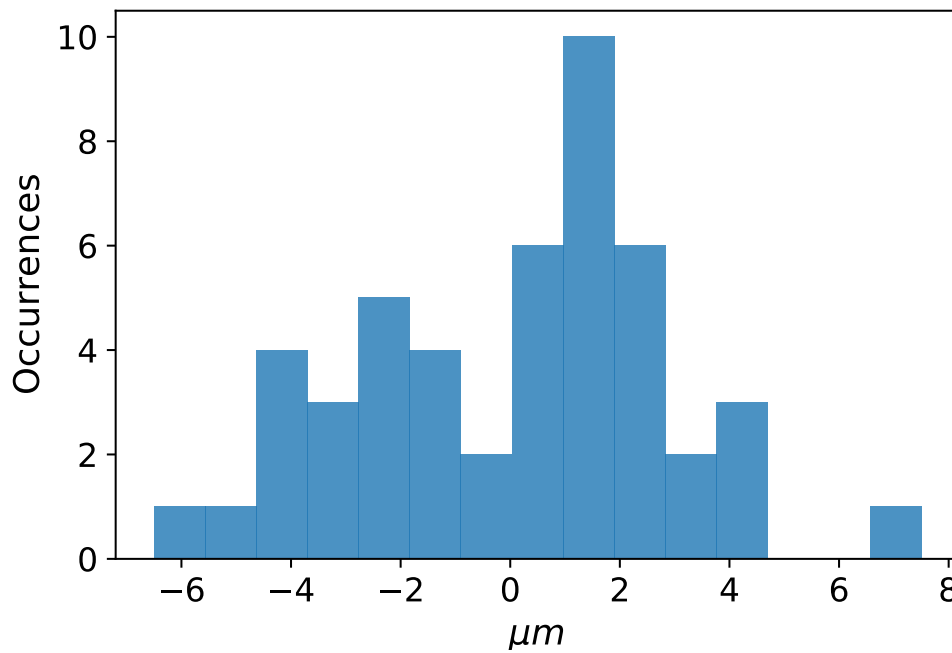


Figure 5.42: Histogram of the positive X-Y errors (compensated).

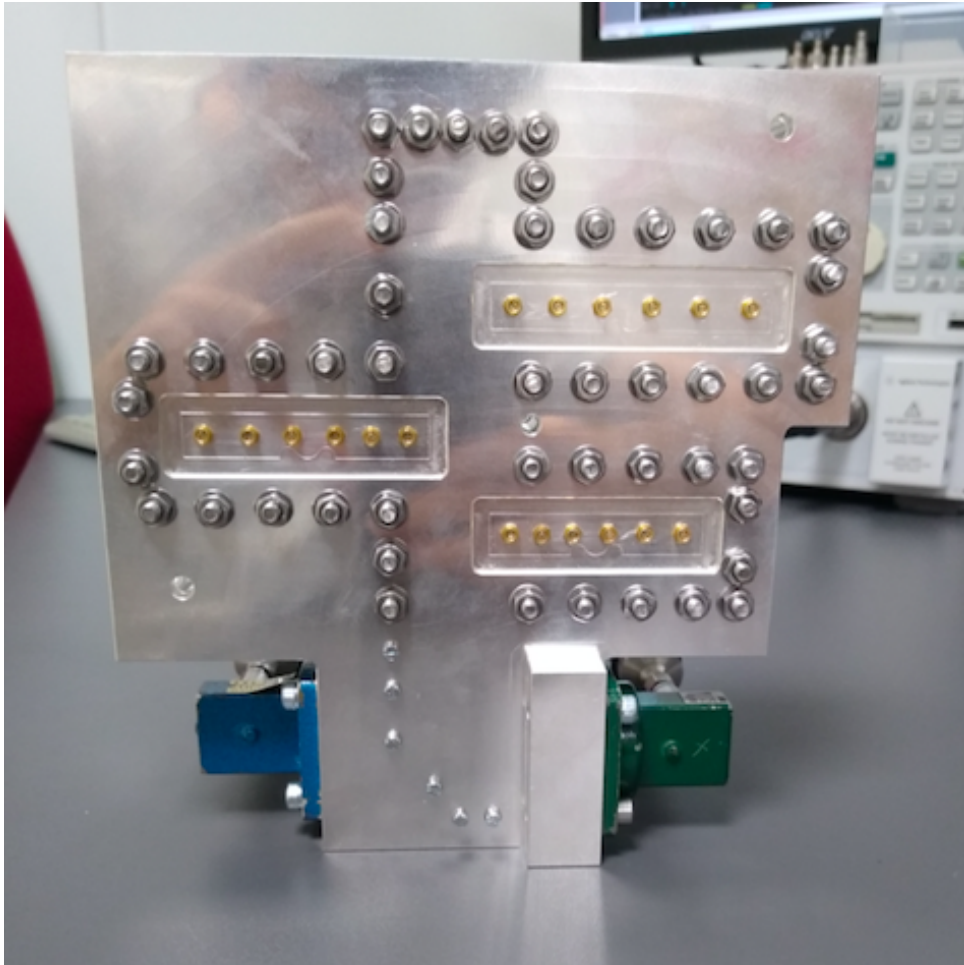


Figure 5.43: Assembled filter fed with WR-75 waveguides.

5.8.2 Measurements

Fig. 5.43 shows the assembled filter, already fed by two WR-75 waveguides. Fig. 5.44 shows the measured broadband performance of the filter after the tuning process. As we can see, there is an excellent match between the simulated and measured performance: all lobes have been properly recovered, and the transmission zeros have not moved despite the fact that we did not include tuners in the capacitive cross-couplings. Two spurious signals appear at 14.48 and 14.88 GHz, however, they are well above the working frequency and in any case, their attenuation is greater than 30 dB.

Fig. 5.44 shows a zoom of the transmission parameter so that we can compare the simulated and measured insertion losses. The simulations were performed in CST using a lossy material with the conductivity of silver. The measured insertion losses at the center of each channel are 0.49, 0.21 and 0.17 dB, respectively.

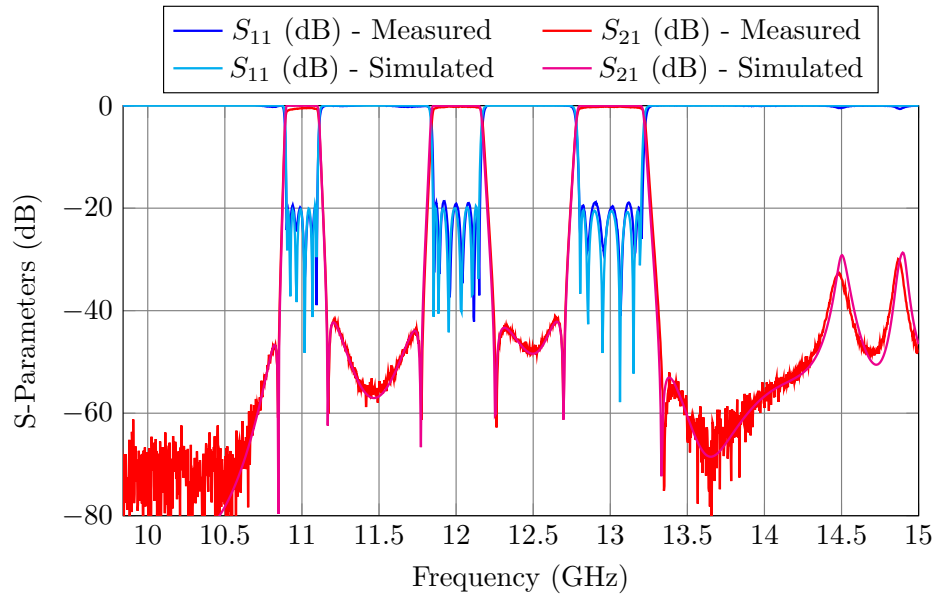


Figure 5.44: Measured performance of the tri-band filter compared to the CST simulation.

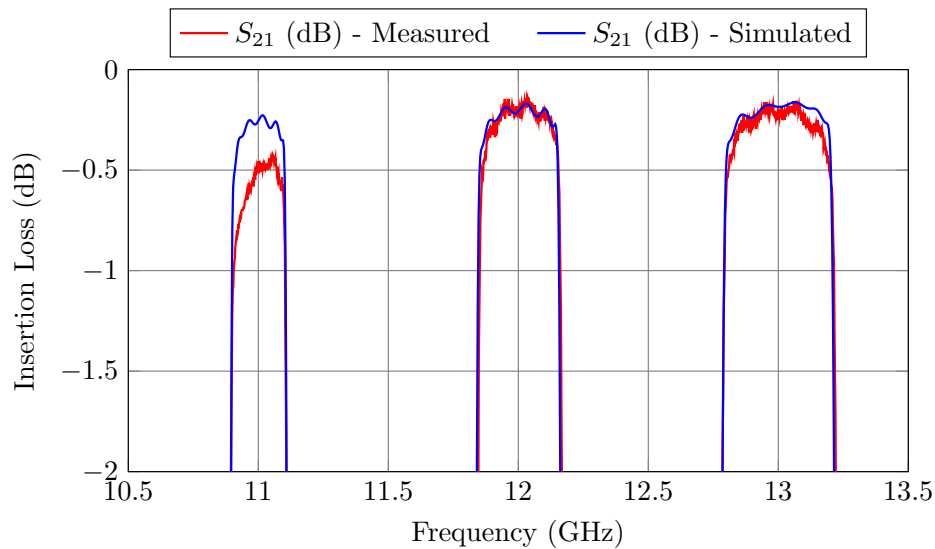


Figure 5.45: Insertion loss of the filter compared to the simulated losses in CST.

5.9 Conclusion

In this chapter, we have proposed a new folded topology for N -band filters based on a manifold approach. The folded topology overcomes the limitations of previous implementations, while maintaining all the typical advantages of the manifold approach: low insertion loss, flexibility in the frequency spacing, number of channels, etc.

The key feature of this approach is that the filters are folded along their center, thus removing all length constraints. Each filter channel can be completely different (different order, BW, TZs) depending on the specific application requirements.

Another key feature of the approach that we propose is the inherent flexibility in terms of number of channels. This is because the optimization strategy that we have used in our design has been widely employed for manifold multiplexers with a high number of channels (up to 20 channels).

Reconfigurable Waveguide Components

The current evolution trend of modern communication systems is toward higher data rates, higher channel frequencies, and dynamic adaptability to customer demands. In this context, therefore, tunable and (or) reconfigurable microwave components, and filters in particular, are currently of great research interest.

As already discussed in Chapter 2, the most common approaches to design tunable and reconfigurable filters are:

- Modifying the physical dimensions of the filters, using, for example, movable walls [67–69].
- Using metallic (or dielectric) screws to modify the electric field inside a resonator or an aperture [70, 71].
- Combining mechanical switches and microwave filters [12].

If the tuning range of a filter with movable end walls or metallic (or dielectric) screws is wide enough, we can change the filter's bandwidth and/or its center frequency. However, we cannot alter its order or shape. Therefore, the most flexible solution is to combine different filters using switches.

Most switches are based on mechanical rotatory systems [75], or use semiconductor technology [78] and MEMS [76, 88]. Recently, in [89–91], a new approach to design waveguide switches was proposed. The switches were based on alternating short and open circuits in the signal path of a waveguide. A similar unconventional approach was used

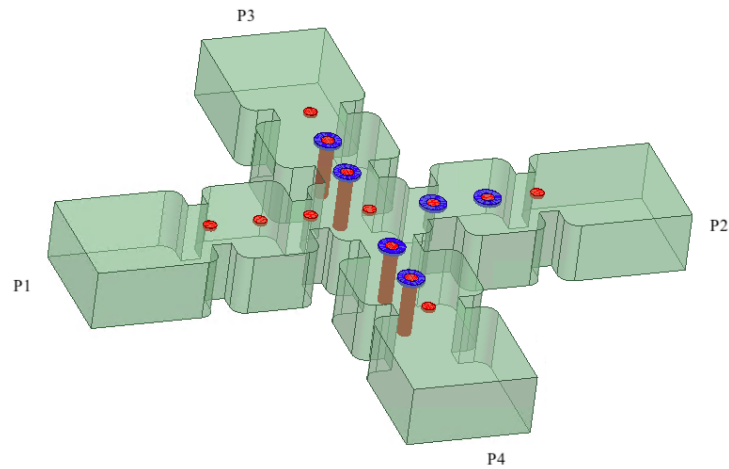


Figure 6.1: Possible implementation of the Filter & Switch. It behaves at the same time as a 3-pole filter and as a 1P3T switch.

in [11], where a new device that integrates the functions of microwave filter and waveguide switch (F&S) was proposed. Due to the importance of this device, we will discuss this contribution in more detail.

6.1 Filter & Switch based on MTPs

Fig. 6.1 shows an implementation of the F&S. It simultaneously behaves as a three-pole filter and as a 1P3T (one-pole triple-throw) switch. The F&S has one input branch (labeled P1 in Fig. 6.1) and three output branches (P2, P3 and P4). They all are connected to a central waveguide resonator. The apertures and cavity of the first branch (P1) have professional tuners that can be manually adjusted, whereas the rest of the branches include *modified tuning pins* (MTPs).

The key aspect of the F&S is the introduction of the MTPs. Each MTP (Fig. 6.2) has two states: an ON (or tuned) and an OFF (or detuned) state. The ON state is obtained by removing the inner pin [Fig. 6.2 (b)] from the hollowed M4 screw [Fig. 6.2 (a)]. The OFF state is obtained by inserting the inner pin until it touches the bottom of the waveguide. The hollowed M4 screws are used to compensate the manufacturing errors and correctly adjust each cavity and iris of the filter.

By removing/inserting some of the MTPs, it is possible to select different paths of the signal. For example, if the MTPs of branches 3 and 4 are set to the OFF state [as in Fig. 6.3 (top)], the attenuation at ports 3 and 4 is above 55 dB [as shown in Fig. 6.3 (bottom)]. If the MTPs of branches 2 and 4 are set to the OFF state, the active

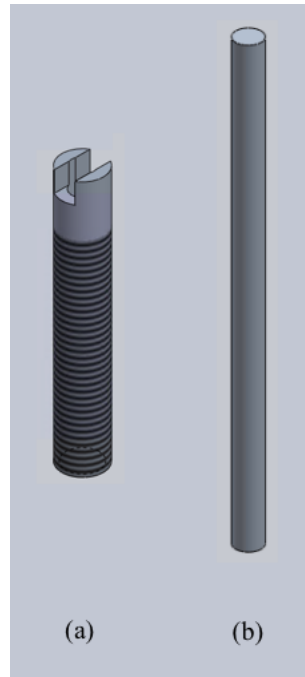


Figure 6.2: Modified Tuning Pins: (a) A hollow M4 screw that can be manually adjusted to tune a cavity or an iris; (b) An inner pin that can be inserted in the middle of the hollow M4 screw in order to short circuit a cavity or an iris.

path of the F&S is the path P1-P3 (as shown in Fig. 6.4).

The main advantage of this topology is that it can be remotely operated. In fact, the authors of [11] demonstrated the remote operation of the F&S using simple linear servomotors shown in Fig. 6.5 (top). These actuators are controlled by an Arduino as shown in Fig. 6.5 (bottom). It is important to note that whereas classic rotary switches need to be very precise (which in turn, makes them expensive and bulky), the servomotors only need to extract the very lightweight pins from the MTPs without concerning about the precision of the movement: once the inner pin is out from the MTP, its actual height with respect to the cavity/aperture does not alter the electromagnetic response of the filter.

The goal of this chapter is to significantly extend the results demonstrated in [11], showing that MTPs can also be effectively used to design reconfigurable filters with discrete states. In addition to theory, the measured results of two reconfigurable filters are also discussed. Furthermore, a reconfigurable diplexer is also demonstrated. Measured results for all the hardware discussed in this chapter are compared very favorably with simulations, thereby fully validating all of the novel structures that we propose.

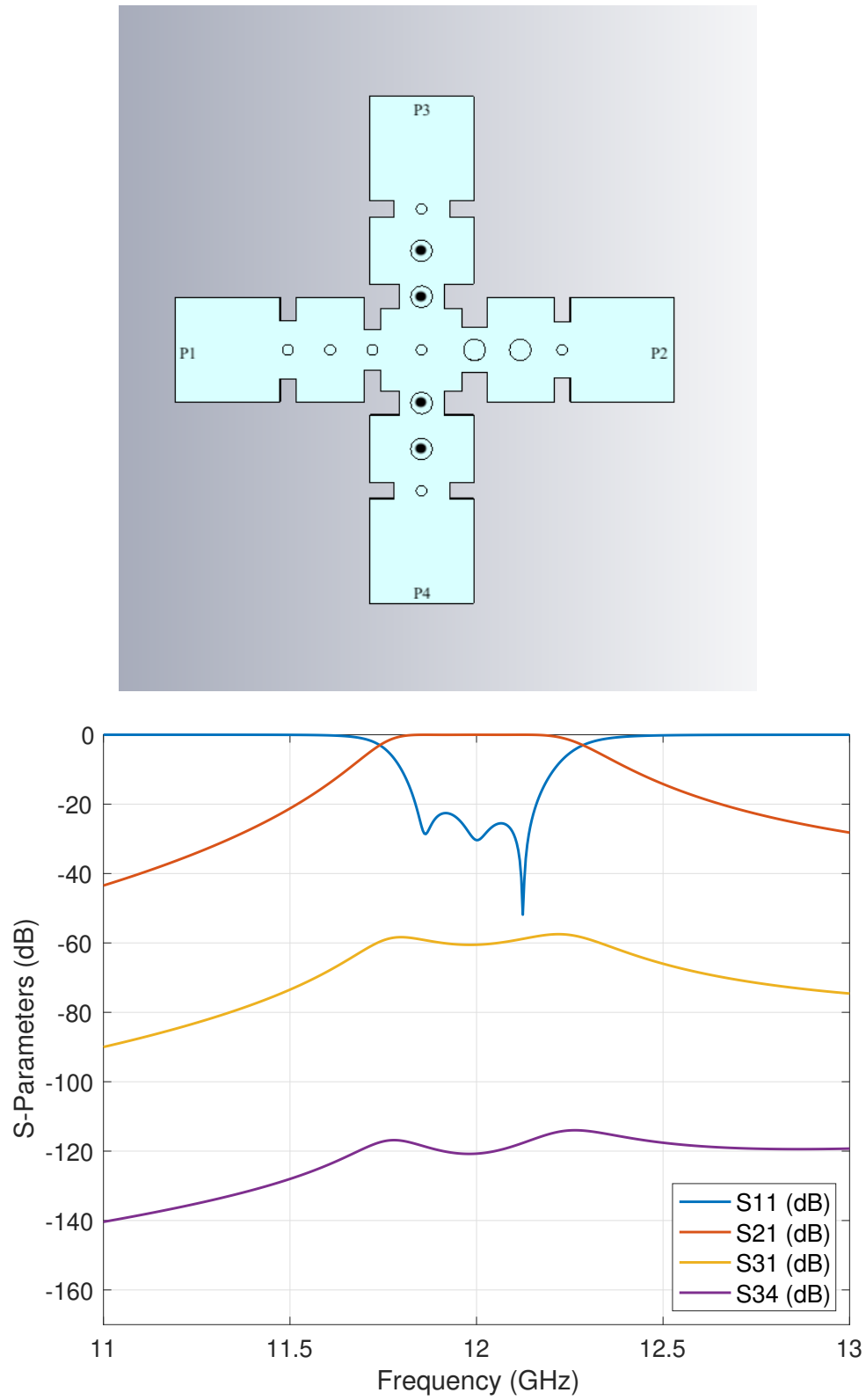


Figure 6.3: Path P1-P2 of the F&S. Top: The black circles in the MTPs of branches P3 and P4 indicate that they are set to the detuned state. Bottom: Performance of the F&S.

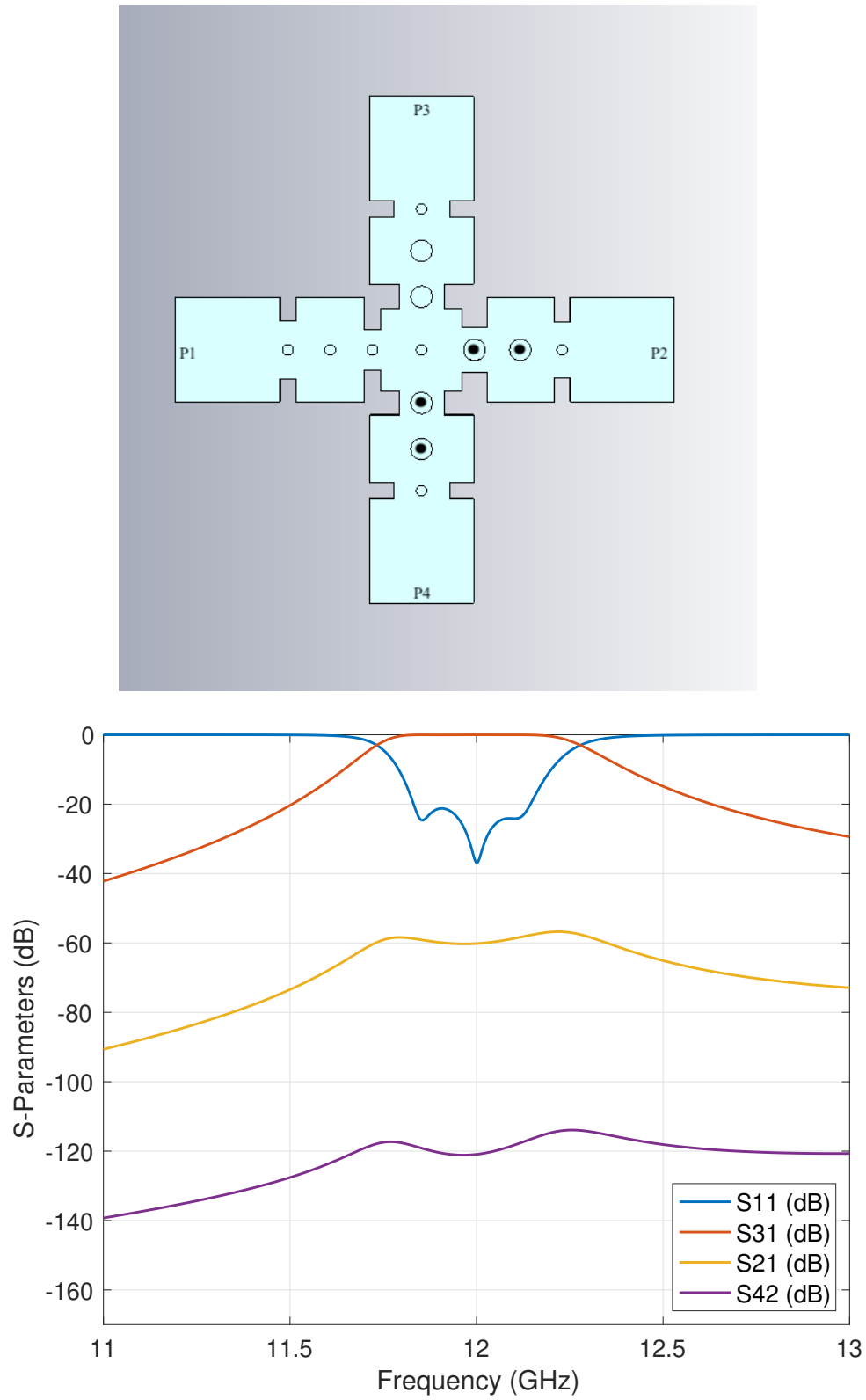


Figure 6.4: Path P1-P3 of the F&S. Top: The black circles in the MTPs of branches P2 and P4 indicate that they are set to the detuned state. Bottom: Performance of the F&S.

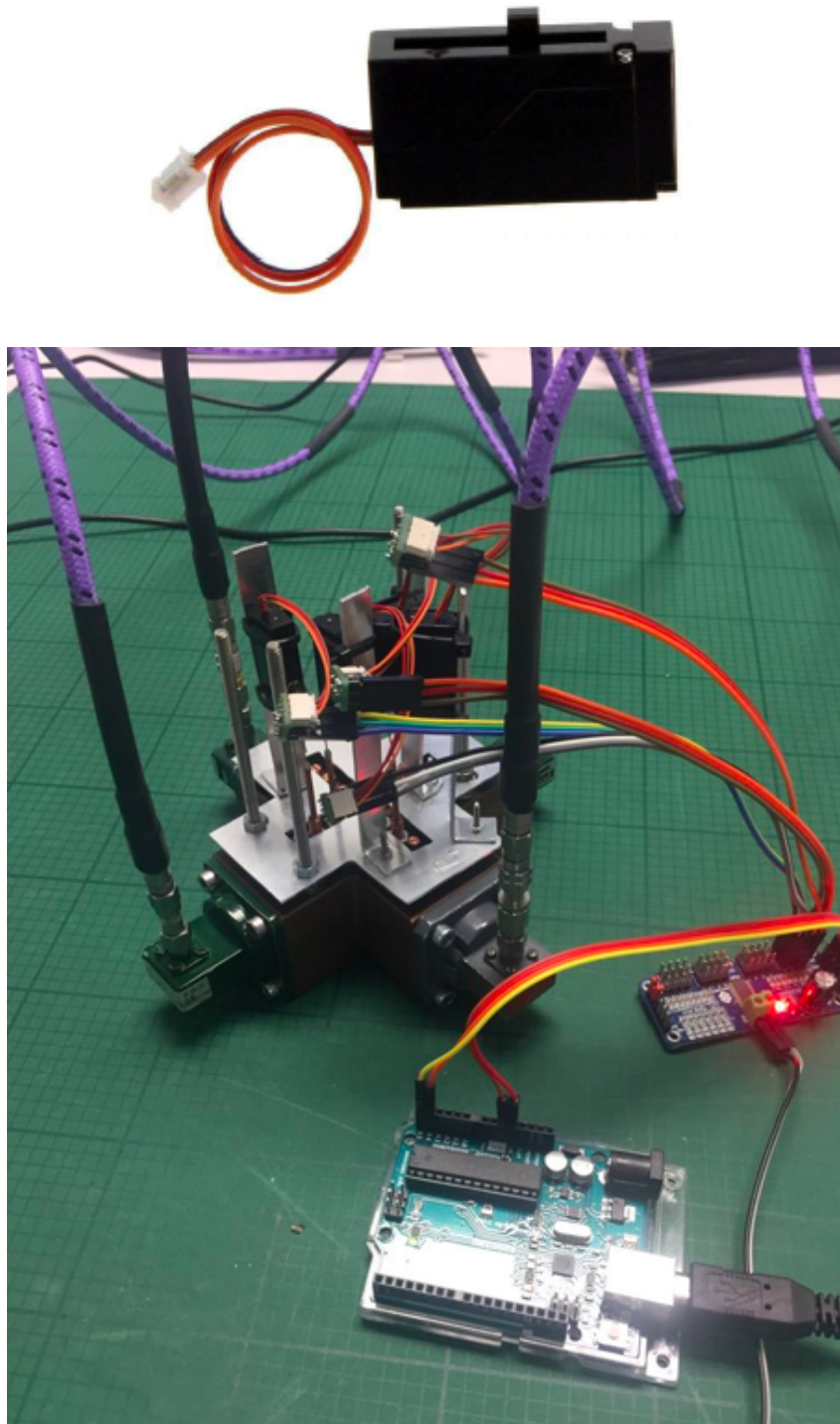


Figure 6.5: Remote operation of the F&S. Top: Servomotor used to lower and lift the inner pin of the MTPs. Bottom: The actuators are controlled by an Arduino.

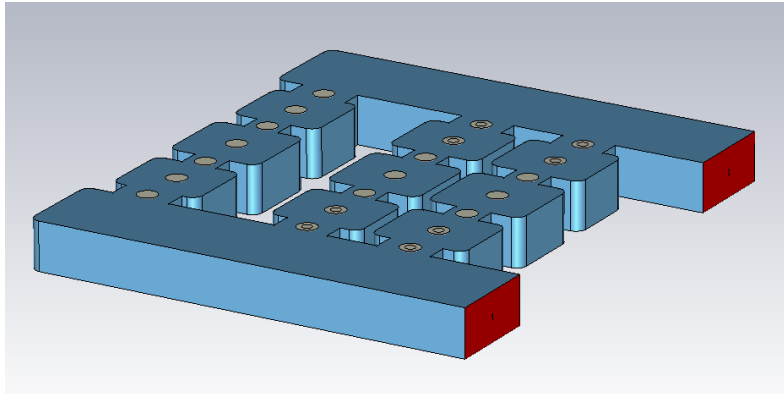


Figure 6.6: Reconfigurable waveguide filter topology.

6.2 Reconfigurable Waveguide Filters

The topology that we propose to implement reconfigurable waveguide filters is shown in Fig. 6.6. The key components of the structure are the MTPs [11] (Fig. 6.2).

The structure is essentially composed by a set of filters that are activated or deactivated using the MTPs. By removing (ON state) or inserting (OFF state) the inner pins of specific MTPs we can, in fact, select the different filter channels (or states), thereby obtaining a different filter performance. Fig. 6.7 shows how to select each discrete state switching the MTPs.

As shown in [11], the MTPs can be remotely lifted and lowered using simple servomotors. The same remote control operation can also be implemented in our structure, so that it becomes effectively a remotely operated reconfigurable filter. Important features of this approach are:

- Every filter is designed independently. The various specifications can, therefore, be completely different. This is indeed a great degree of flexibility.
- Compared to the standard solution of separate waveguide filters and mechanical (rotary) switches, this solution is lighter and significantly less expensive.
- The same basic idea can also be used to obtain very complex reconfigurable devices, like diplexers, as it will later be shown in Section 6.7.

The complete design procedure is discussed in the next section.

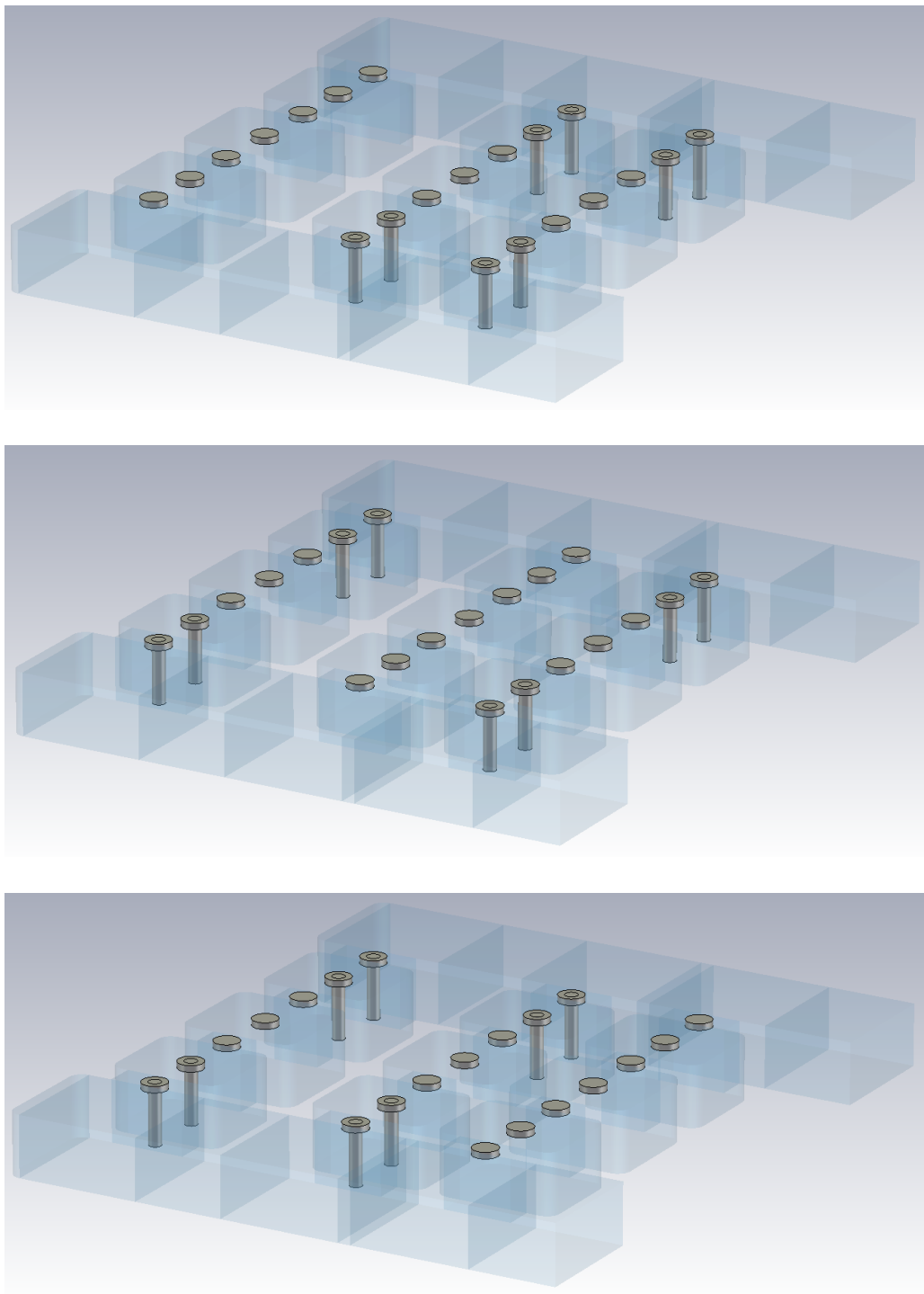


Figure 6.7: State selection. Top: MTP configuration for the first state. Central: MTP configuration for the second state. Bottom: MTP configuration for the third state.

6.3 Specifications and design procedure

As illustrative examples, we discuss in this section the design of two reconfigurable waveguide filters (Filter A and Filter B) with different specifications. The target specifications for Filter A are as follows:

- Input/output waveguide: WR-75.
- Return Loss ≥ 20 dB.
- Three discrete states:
 - State 1: $f_0 = 10.875$ GHz ; $BW = 125$ MHz; $N = 3$.
 - State 2: $f_0 = 11$ GHz ; $BW = 125$ MHz; $N = 3$.
 - State 3: $f_0 = 11.125$ GHz; $BW = 125$ MHz; $N = 3$.

The target specifications for Filter B are as follows:

- Input/output waveguide: WR-75.
- Return Loss ≥ 25 dB.
- Three discrete states:
 - State 1: $f_0 = 11$ GHz ; $BW = 62.5$ MHz; $N = 3$.
 - State 2: $f_0 = 11$ GHz ; $BW = 125$ MHz; $N = 3$.
 - State 3: $f_0 = 11$ GHz; $BW = 250$ MHz; $N = 3$.

Both filters will be manufactured in two pieces using milling (body and cover) and, therefore, we must also consider round corners (2 mm) in all the cavities. The design is carried out, for convenience, in two stages:

1. Stage 1: Obtain a low-accuracy model of the filter (LA). The LA filter will not consider round corners or tuning elements. It is important to note that the purpose of the MTP is twofold: the outer part, the hollowed M4 screw, is used to tune the cavities or apertures, whereas the inner pin is used to switch between the ON/OFF states. At this stage of the design, we do not need to simulate the outer part of the MTPs.
2. Stage 2: Obtain a high-accuracy model of the filter (HA). The HA structure will include rounded corners and MTPs. At this point, we will consider the whole MTP (outer and inner parts).

In the first stage of the design, we will use the commercial simulator FEST3D with the setup shown in Table 6.1. This setup will allow us to perform simulations in a very short time. In the first stage of the design we will need to perform hundreds of simulations in the optimization loop in order to achieve the desired performance. Choosing an efficient simulator for this task will greatly speed up the design process.

Once the LA filter has been designed, we will need to include the features we omitted

Table 6.1: Accuracy settings used for Filters A and B.

Coarse Model	
Simulator	FEST3D
Accessible modes	10
Number of basis functions	30
Green's function terms	300
Fine Model	
Simulator	CST Microwave Studio
Solver	Frequency Domain Solver
Frequency Sweep	General Purpose
Mesh refinement	11 (or 10.875 or 11.125) GHz
Error Threshold	0.005
Maximum number of iterations	20

in the previous step (rounded corners and MTPs). The simulator we have used for this stage is CST Microwave Studio. Even though the simulations of the HA filter will take much longer, we can easily make the transition from the LA to the HA model using an Aggressive Space Mapping (ASM) based strategy [22], [30], [35] or the Step-by-Step method described in Chapter 3. Using ASM, the majority of the simulations required to go from the LA to the HA model will be performed in the fast, LA model.

6.4 Design procedure for Filter A

The first step in the LA design is to obtain the independent channel filters. We therefore start with a model based on transmission lines and inverters that provides the desired Chebyshev response for each channel [13]. We then apply the synthesis procedure described in [17] to obtain the waveguide model for each filter as shown in Fig. 6.8.

It is important to note that, as shown in Fig. 6.6, the three channel filter must have the same length in order to fit our topology. There are three possible options:

- We can use stubs to couple the filters to the manifold and include these stubs in the optimization process as it was previously done in [66].
- We can fix the length of the resonators and optimize their widths. With this option we can couple the channel filters directly to the manifold and reduce the footprint of the filter.
- We can fold the filters along their center, as we did in Chapter 5, and bypass completely the problem.

For the sake of simplicity, we have chosen the second option. Fig. 6.9 shows the in-line performance of the three independent channel filters (or states).

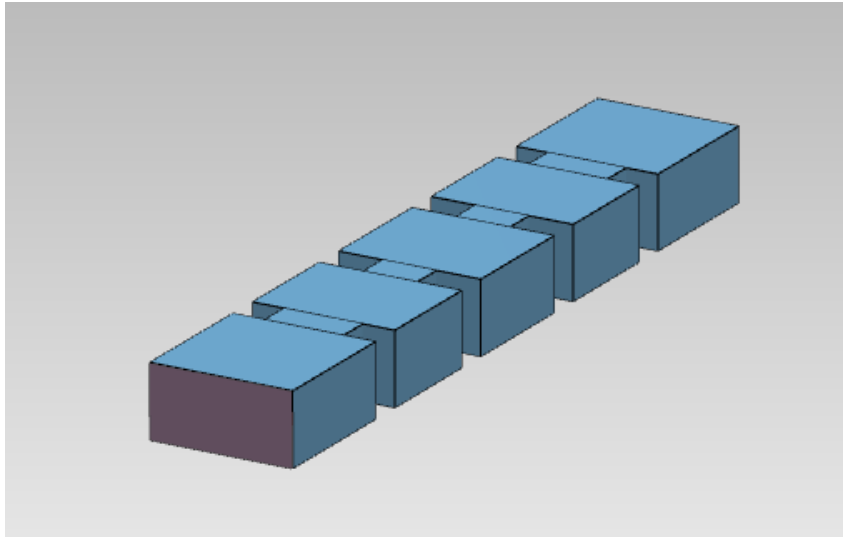


Figure 6.8: Waveguide filter channel.

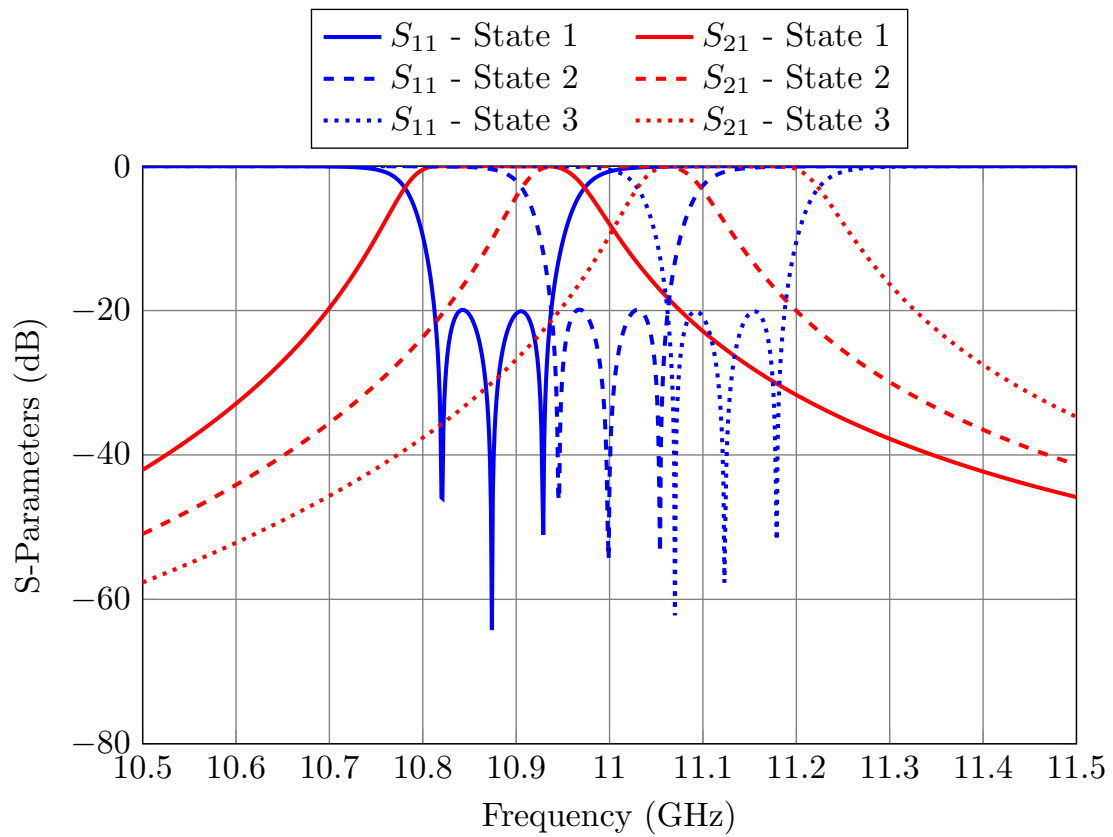


Figure 6.9: Performance of the independent filters. These are the three possible discrete states of the reconfigurable filter (Filter A).

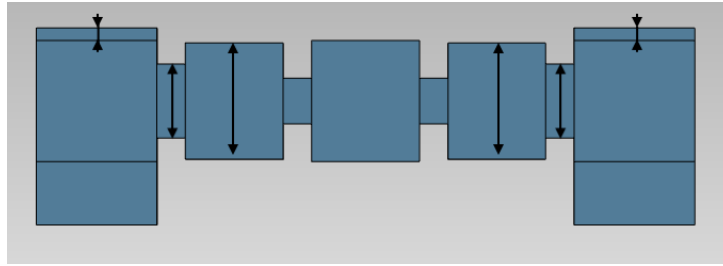


Figure 6.10: Step 1: Join the first filter channel to the manifold and optimize the distance to the short circuit and the widths of the first two elements of the filter. The parameters that are optimized are shown with arrows.

After designing the independent filters, we can add them to the manifold using the following procedure:

1. Add the first filter to the manifold as in Fig. 6.10, and optimize the distance to the short circuit and the widths of the first aperture and cavity of the filter. Fig. 6.11 shows the response of the filter after this step.
2. Set the MTPs of the first filter to the OFF state and add the second filter to the manifold as shown in Fig. 6.12 (top). Note that after setting the first filter's MTPs to the OFF state, the central part of the first channel does not affect the response of the active channel and thus, we can save some time if we do not simulate it [Fig. 6.12 (bottom)]. It is important to remember that we do not need to simulate the whole MTPs, we only need to consider the inner pins to short circuit the inactive filter. Fig. 6.13 shows the performance of the filter after optimizing the distance between the channels and the first two elements of the newly added filter.
3. Repeat the previous step until all the channels/states have been added. Fig. 6.14 shows the filter at this point and Fig. 6.15 shows its simulated performance.
4. After all the channels have been added, it is necessary to perform another optimization for the first two channels/states. These iterations are necessary because the filters added in Steps 2 and 3 are loading (slightly) the active filter. After a rapid optimization process, we obtain the performance shown in Fig. 6.16.

After designing the LA filter, we can apply any of the variations of ASM mentioned before to obtain the HA model shown in Fig. 6.17. The HA model must include round corners in every cavity, as well as the (hollow) M4 screws of the MTPs. The M4 screws will be fixed at a depth of 1 mm in order to allow for future bidirectional adjustments. In SM terminology, the HA model will be the *fine model* and the LA model will be our *coarse model*. The fastest way to apply the Step-by-Step approach in this case is as follows:

1. Extract the individual filters of the LA model, obtaining three in-line filters (as

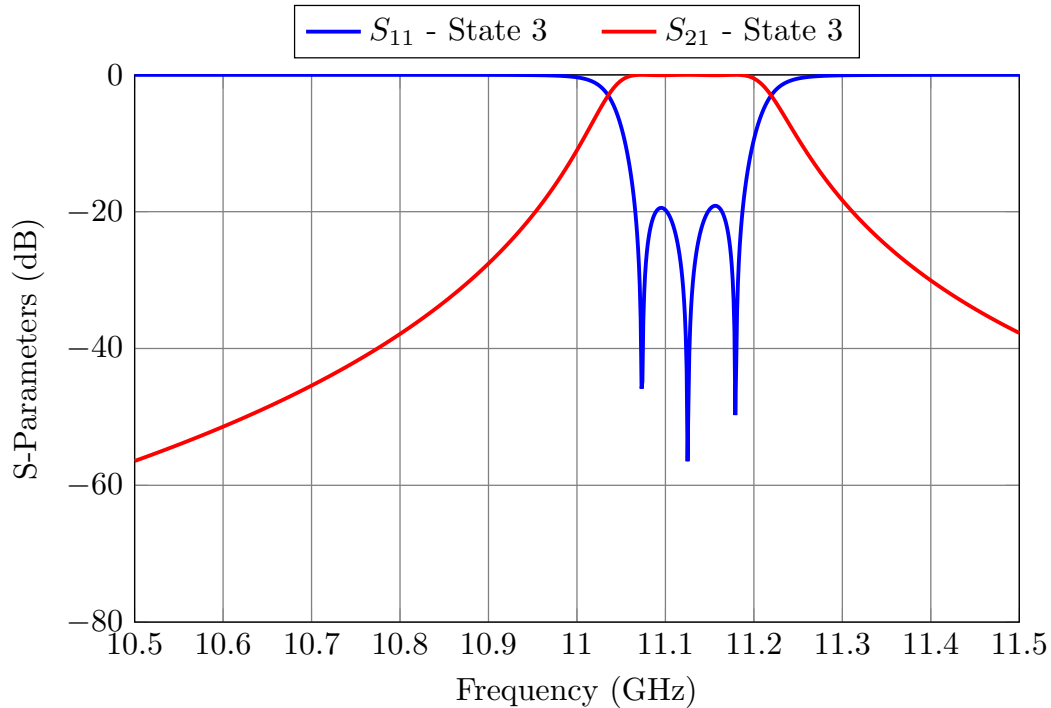


Figure 6.11: Response of the filter after performing Step 1.

the one shown in Fig. 6.8).

2. Apply the Step-by-Step approach described in Chapter 3 until the high-accuracy version of the filters that include rounded corners and tuning elements (M4 hollowed screws) has been recovered.
3. Combine the high accuracy filter channels to obtain the HA model of the reconfigurable filter (shown in Fig. 6.17).
4. Finally, perform an additional OS-ASM iteration for each filter channel using the *coarse* model of Fig. 6.14 and the *fine* model of Fig. 6.17.

After following the previous procedure, the HA model meets the required specifications (see Fig. 6.18). This concludes the design of Filter A.

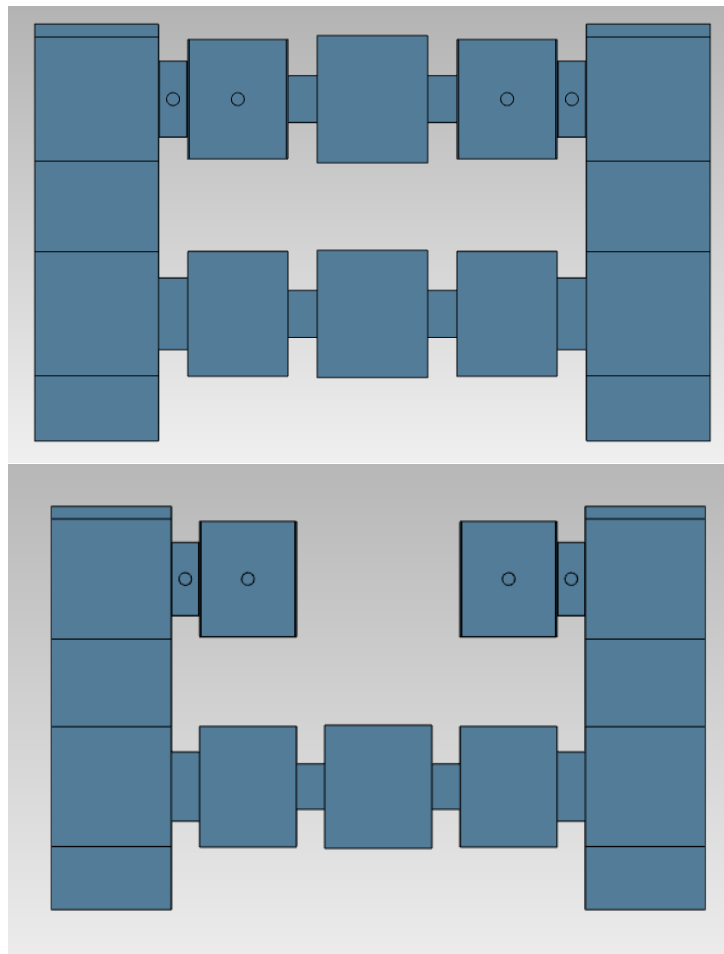


Figure 6.12: Filter structure after performing Step 2. Top: Complete structure. Bottom: Reduced structure. Due to the MTPs, the complete and reduced structure provide the same performance.

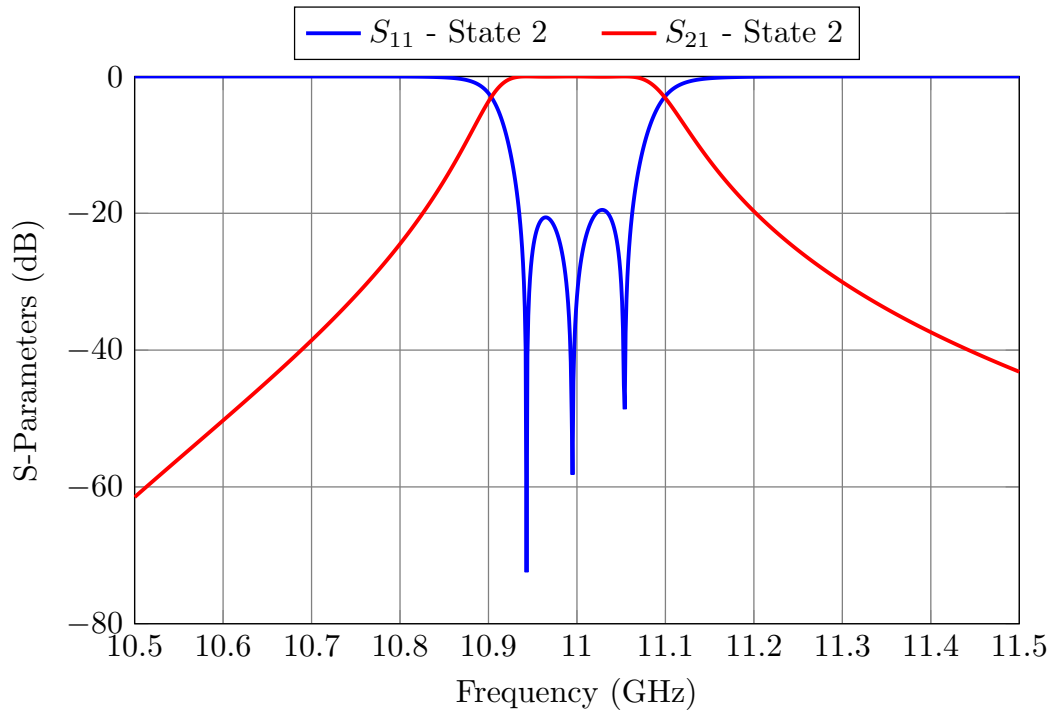


Figure 6.13: Response of the filter after performing Step 2.

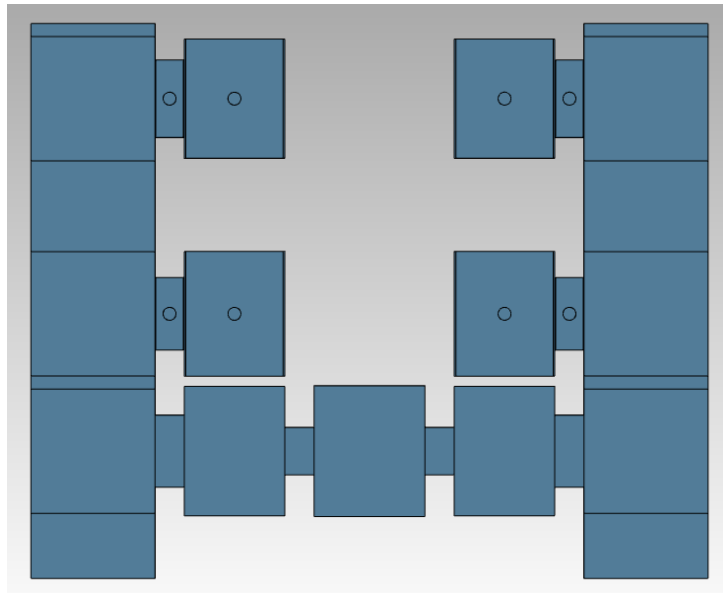


Figure 6.14: Step 3: Set the MTPs of the second filter to the OFF state and add the third filter to the manifold.

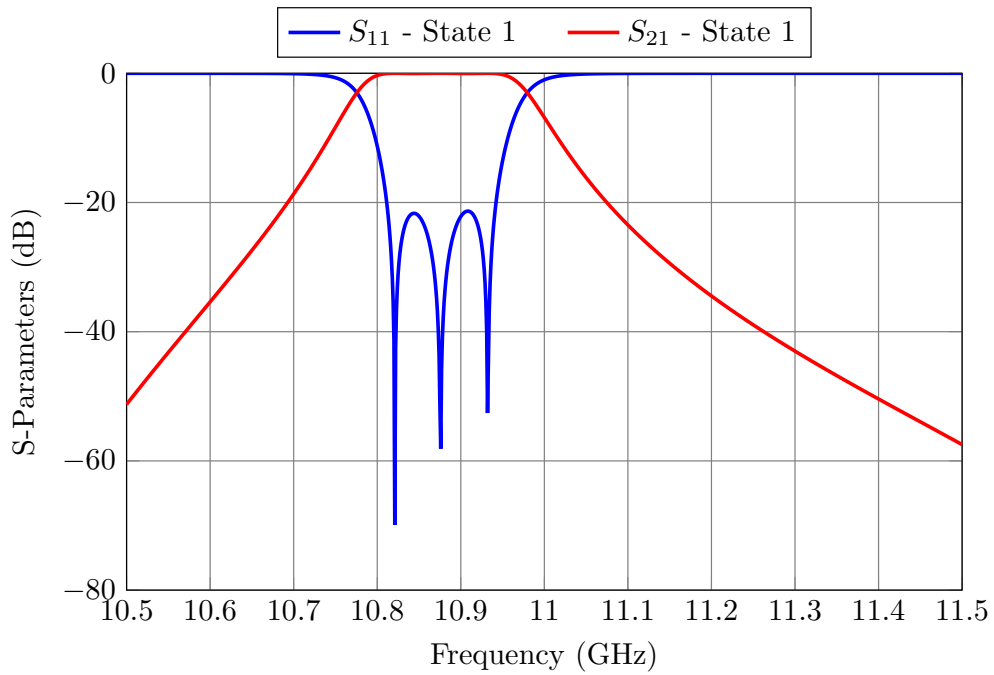


Figure 6.15: Response of the filter after performing Step 3.

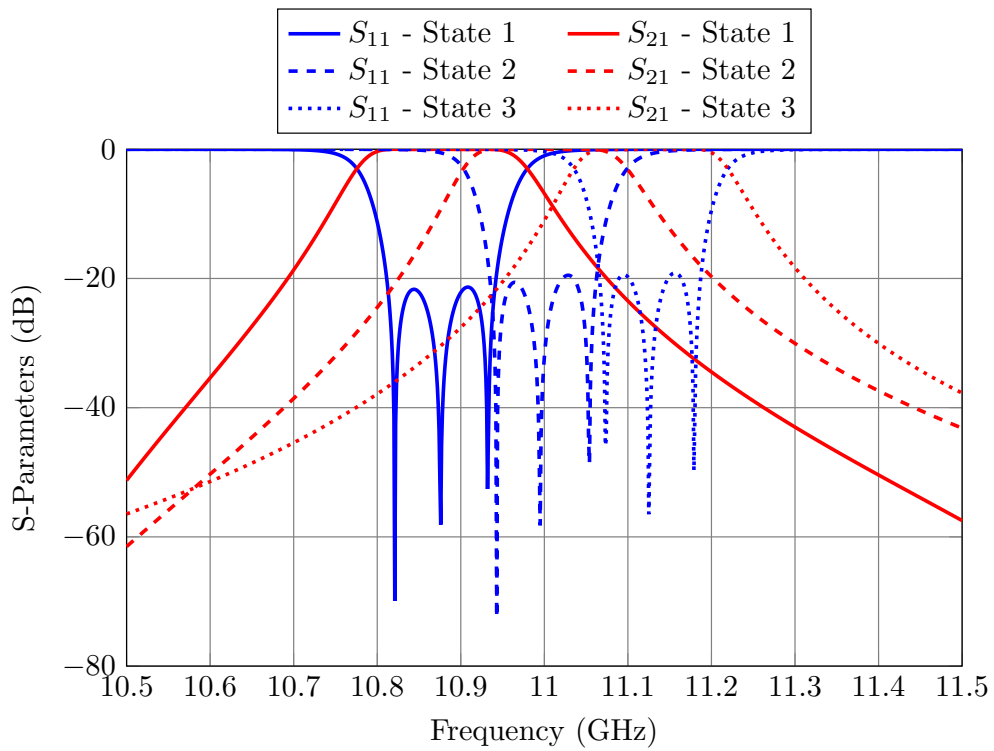


Figure 6.16: Performance of the LA filter.

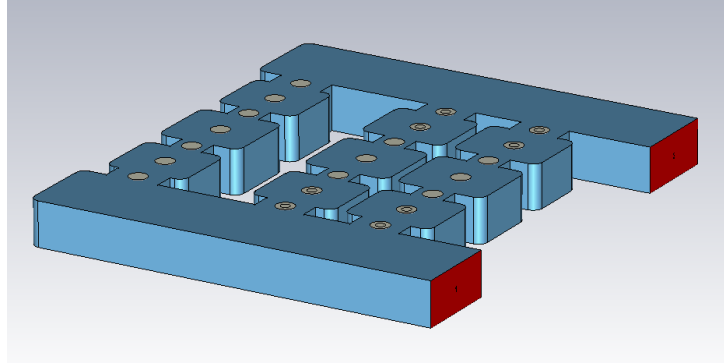


Figure 6.17: Final high-precision model for Filter A.

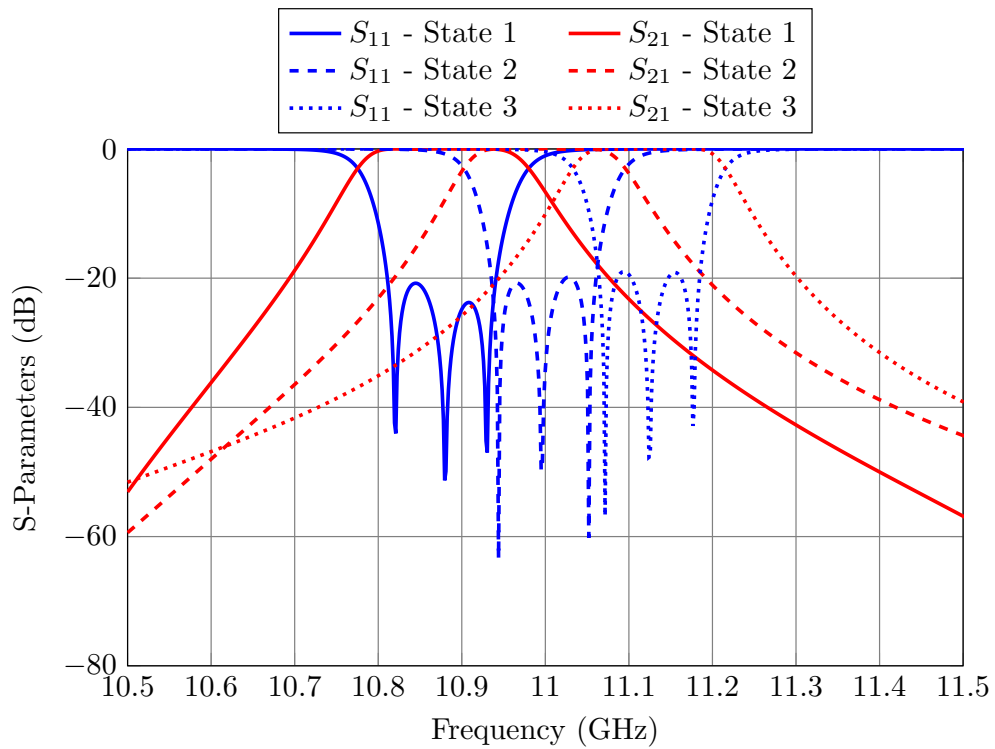


Figure 6.18: Performance of the high-accuracy model of Filter A.

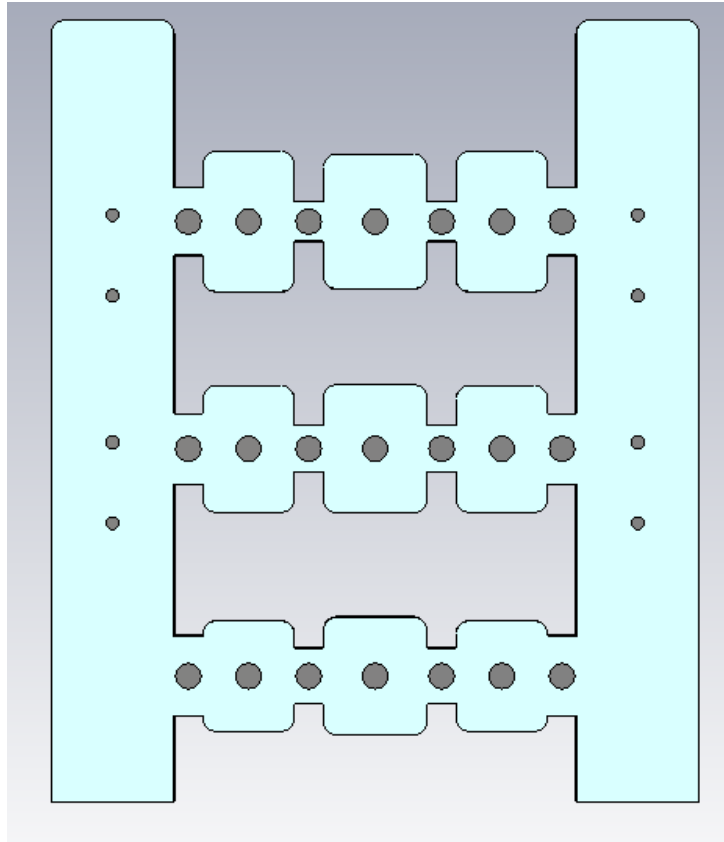


Figure 6.19: Proposed topology for Filter B. In this case, we have also included MTPs in the manifold.

6.5 Design procedure for Filter B

During the design of Filter A, we observed that the *length* of the manifold could introduce design problems. As it is well-known, connecting a short circuited manifold to a filter can generate transmission zeros. As the length to the short circuit of the manifold increases, the transmission zeros generated become more difficult to control. A simple solution to this problem is to add MTPs to the manifold. Filter B uses this approach (see Fig. 6.19). Including MTPs in the manifold has two advantages:

- We can now easily control the distance between the channels. The filter will be manufactured in two pieces (body and cover) that will be assembled using closing screws. If we can add more space between the filters, we can also insert additional screws (see Fig. 6.20), and this will help to decrease the insertion losses introduced by the filters.
- The design becomes simpler because we can control (or eliminate) more easily the transmission zeros generated by the manifold.

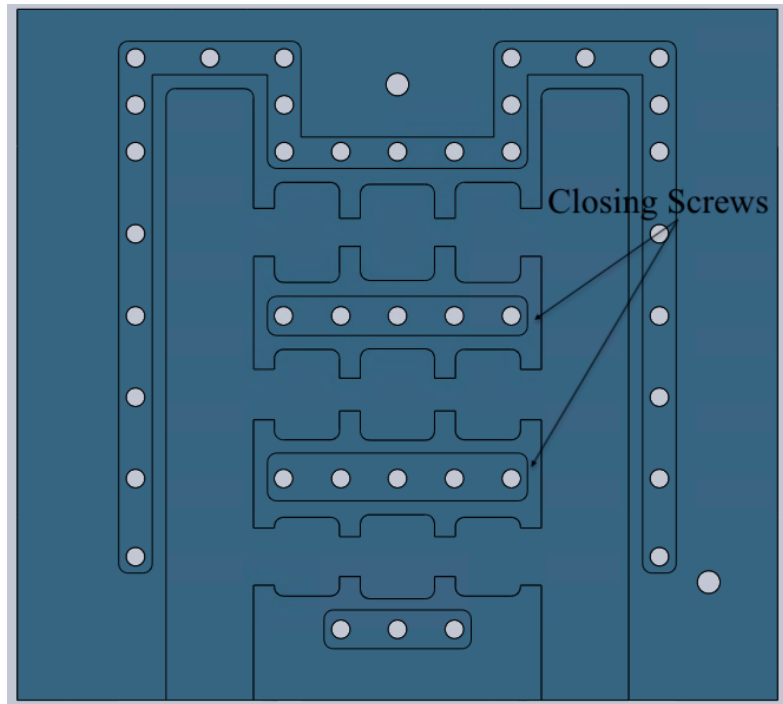


Figure 6.20: Closing screws of Filter B.

The design of Filter B is similar to the design of Filter A:

1. Design the independent filter channels. Following the same approach as in the previous case, we have fixed the lengths of the resonators, and we have optimized their widths.
2. Add the filters to the manifold one at a time.
3. Once all the filters have been added, perform an additional optimization for the first and second filters. Fig. 6.21 shows the LA model for the second state and Fig. 6.22 shows its performance.
4. Once the LA model has been designed, use ASM to obtain the HA model shown in Fig. 6.19. Fig. 6.23 shows the simulated performance of the HA filter.

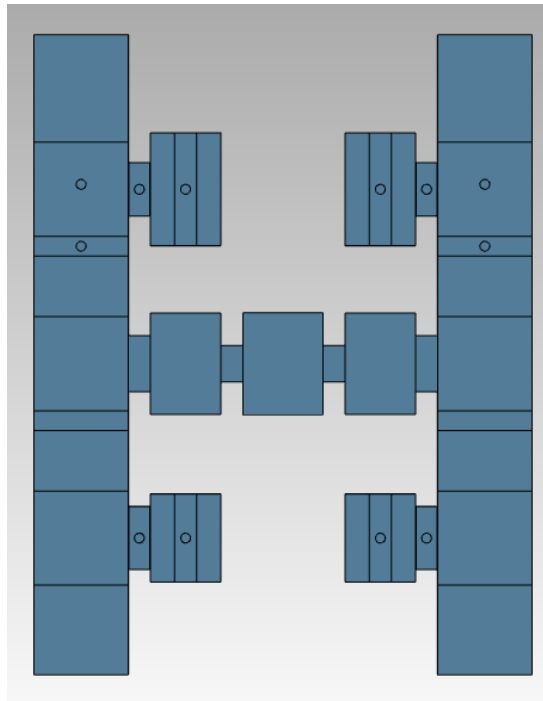


Figure 6.21: LA model of Filter B for the second state.

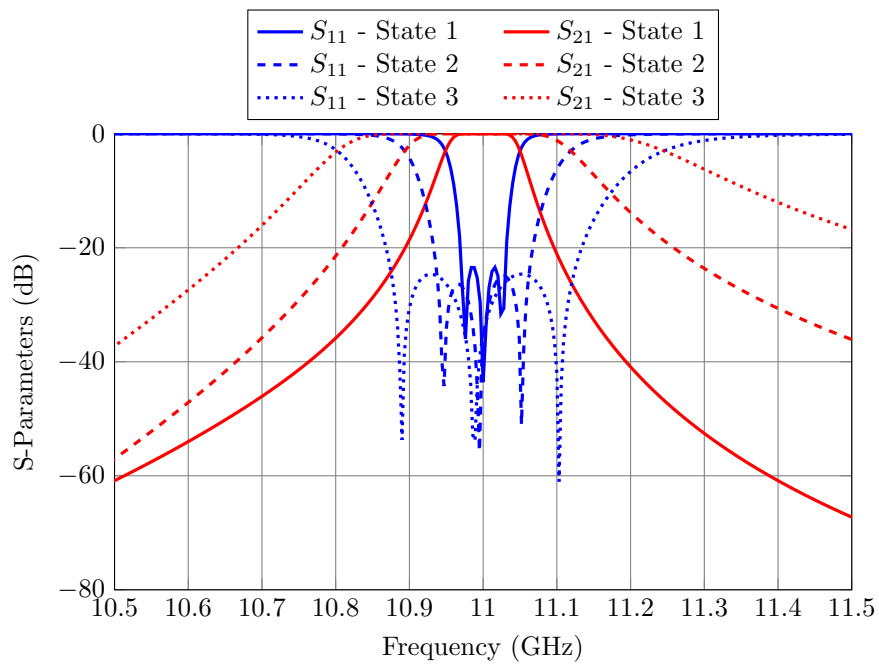


Figure 6.22: Performance of the LA model for Filter B.

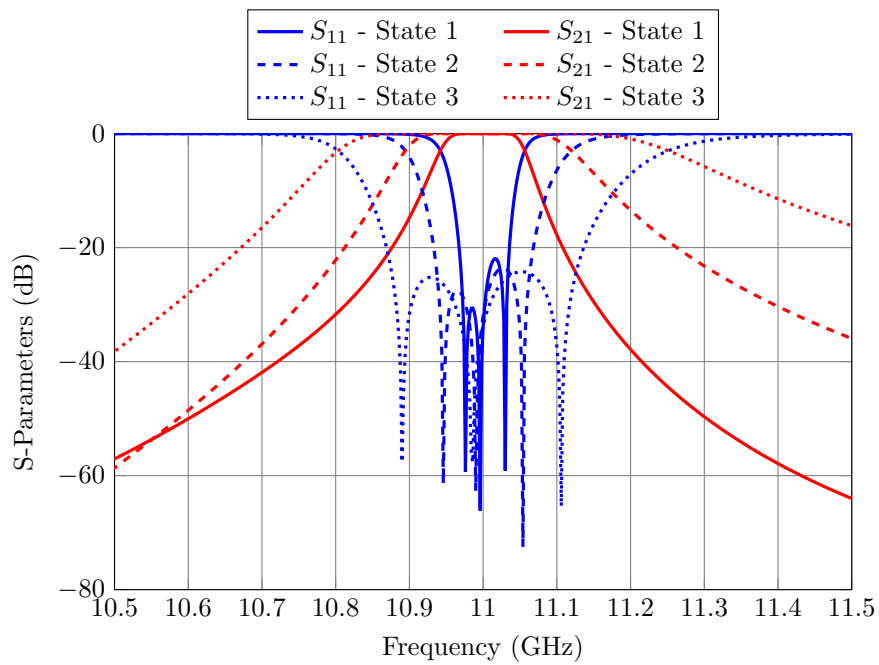


Figure 6.23: Performance of the HA model for Filter B.

6.6 Experimental Validation

After designing two reconfigurable filters, we decided to manufacture Filter B, since it is the most complex of the two filters: the channels are placed at the same central frequency and it includes additional MTPs in the manifold.

The filter was manufactured by H-plane milling in two pieces of aluminum: body and cover (as shown in Fig. 6.24). For the manufacture we used a low cost process with tolerances between 100 and 200 μm .

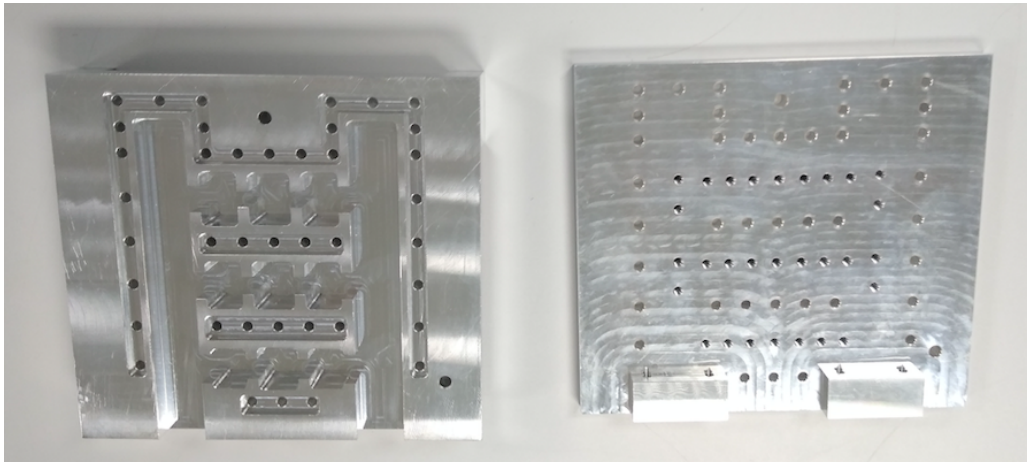


Figure 6.24: Body and cover of Filter B. Both pieces have been manufactured in aluminum.

Fig. 6.25 to Fig. 6.27 show the measured performance compared to the ideal high-precision model simulations. As we can see, the level of agreement between the simulations and measurements is excellent, thereby validating both the proposed topology and the design process.

6.7 Reconfigurable Diplexer

The reconfigurable filter topology we just discussed can also be used to design more complex devices. As an example, we demonstrate in this section how to design a reconfigurable diplexer with two discrete states. Fig. 6.28 shows the two states of the diplexer. The diplexer specifications are as follows::

- Input/Output: WR-75.
- State 1:
 - $f_{01} = 10.9075$ GHz; $BW = 125$ MHz; $N = 5$; $RL \geq 25$ dB.
 - $f_{02} = 11.155$ GHz; $BW = 250$ MHz; $N = 5$; $RL \geq 25$ dB.

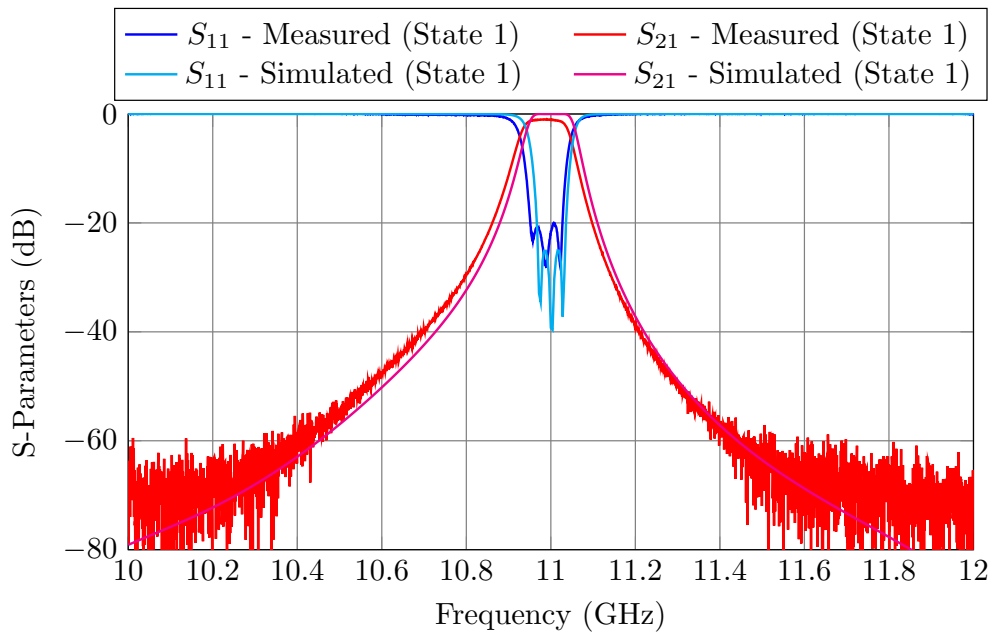


Figure 6.25: Measured performance of Filter B (State 1).

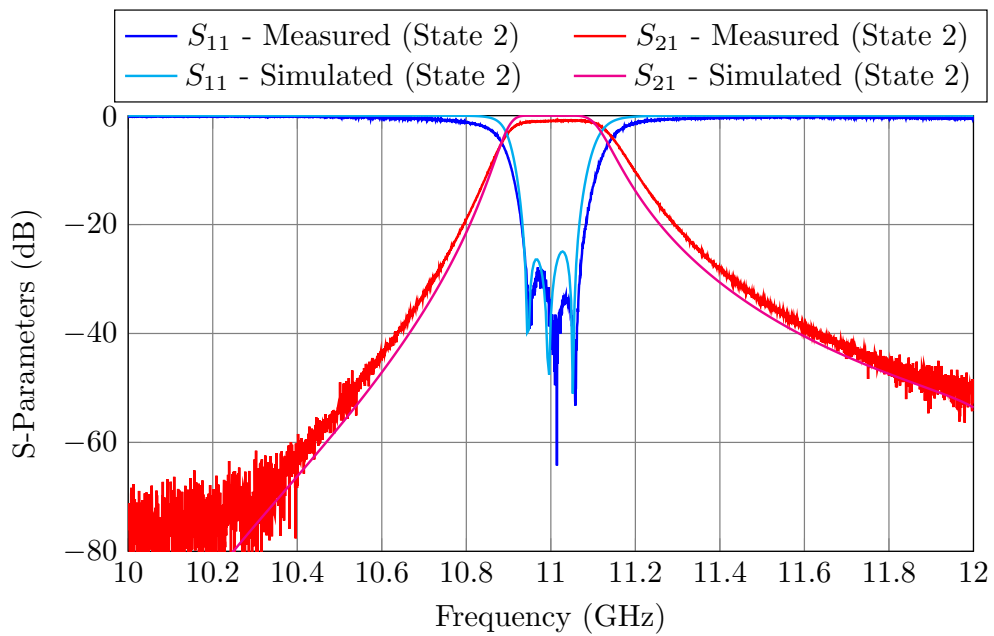


Figure 6.26: Measured performance of Filter B (State 2).

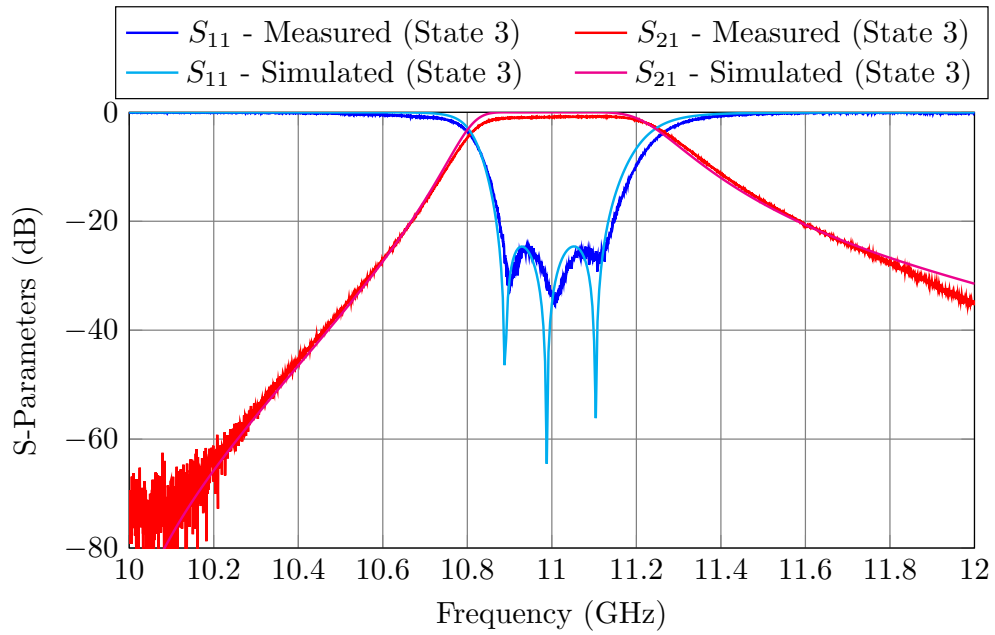


Figure 6.27: Measured performance of Filter B (State 3).

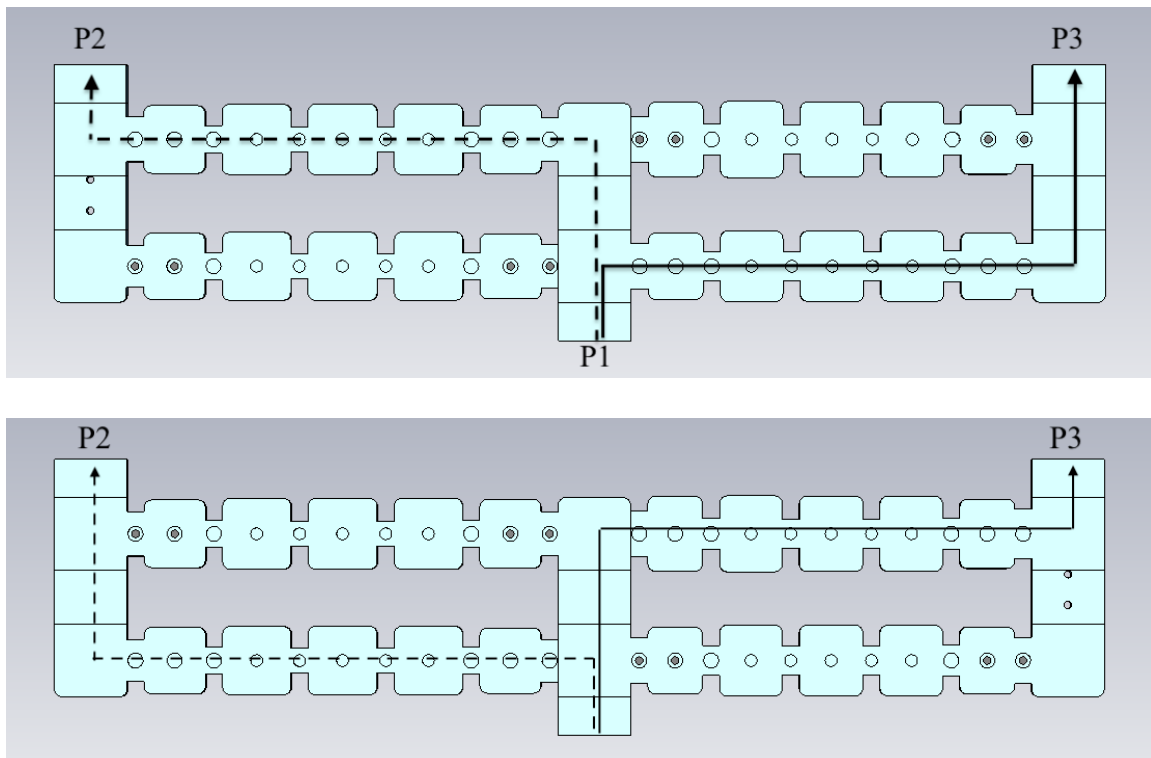


Figure 6.28: Reconfigurable diplexer. The two paths of the signal have been drawn. Top: Top view of the first state. Bottom: Top view of the second state.

- State 2:
 - $f_{01} = 10.845$ GHz; $BW = 250$ MHz; $N = 5$; $RL \geq 25$ dB.
 - $f_{02} = 11.0925$ GHz; $BW = 125$ MHz; $N = 5$; $RL \geq 25$ dB.

A multiplexer can be considered as contiguous when the separation between the channels (assuming that all have the same bandwidth) is less than $0.25 \times BW$ [12]¹. We have chosen the central frequencies so that there are 60 MHz between the channels (≈ 250 MHz $\times 0.25$).

The design is again carried out in two stages: the design of the low-accuracy (LA) model, and the desing of the high-accuracy (HA) model. The setup for the simulators is the same as in Section 6.3.

6.7.1 Design procedure for the LA diplexer

The design procedure for the LA diplexer is as follows:

1. Design two independent diplexers. The reconfigurable diplexer is then obtained combining the two manifold diplexers shown in Fig. 6.29. The two diplexers can be designed using the procedures described in [9] and [12]. As we did for the reconfigurable filters, we will optimize the widths of the apertures, and the widths of the cavities (instead of their lengths). Fig. 6.30 shows the performance of the isolated diplexers.
2. Combine the independent diplexers to form a 4-port device, as shown in Fig. 6.31. We then optimize the first aperture and cavity of each branch in order to recover the performance we had in the previous step. We can perform these optimizations with the whole structure [Fig. 6.31 (top)] or with a reduced structure [Fig. 6.31 (bottom)]. Due to the presence of the MTPs, both structures provide the same performance. We can, therefore, use the reduced structure in order to speed up the optimization process. After a very short optimization, we obtain the performance shown in Fig. 6.32.

¹This empirical rule assumes that all channels have the same bandwidth.

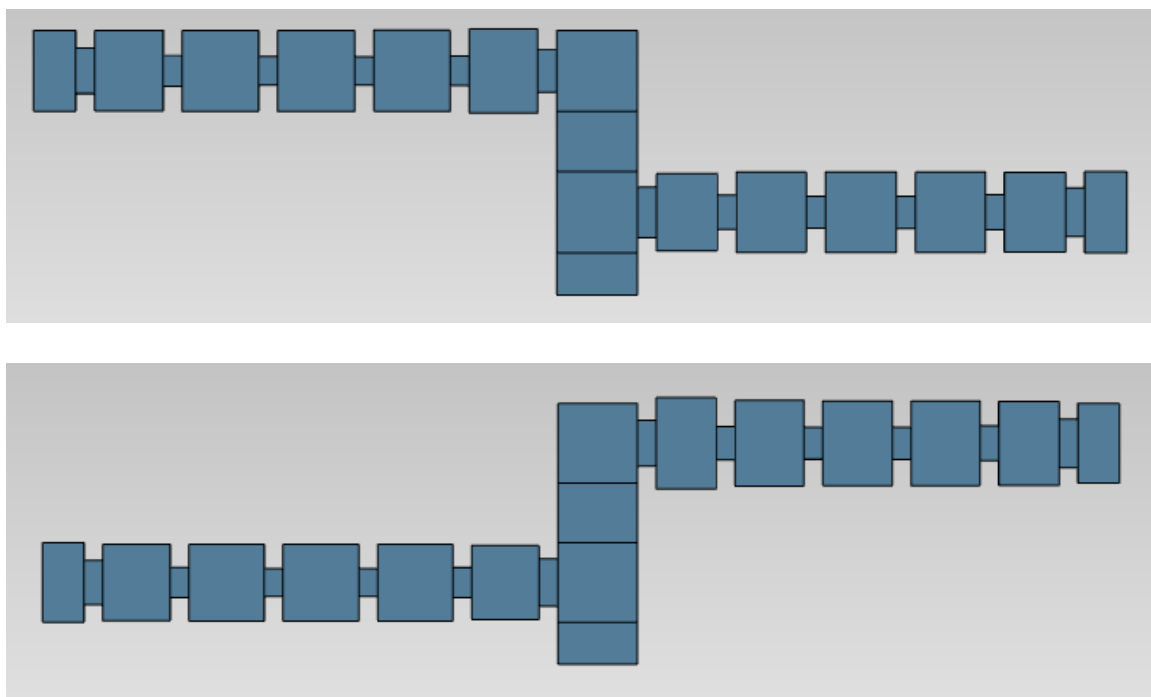


Figure 6.29: Independent diplexers. Top: The response of this isolated diplexer is the goal for the first state of the reconfigurable diplexer. Bottom: The response of this isolated diplexer is the goal for the second state of the reconfigurable diplexer.

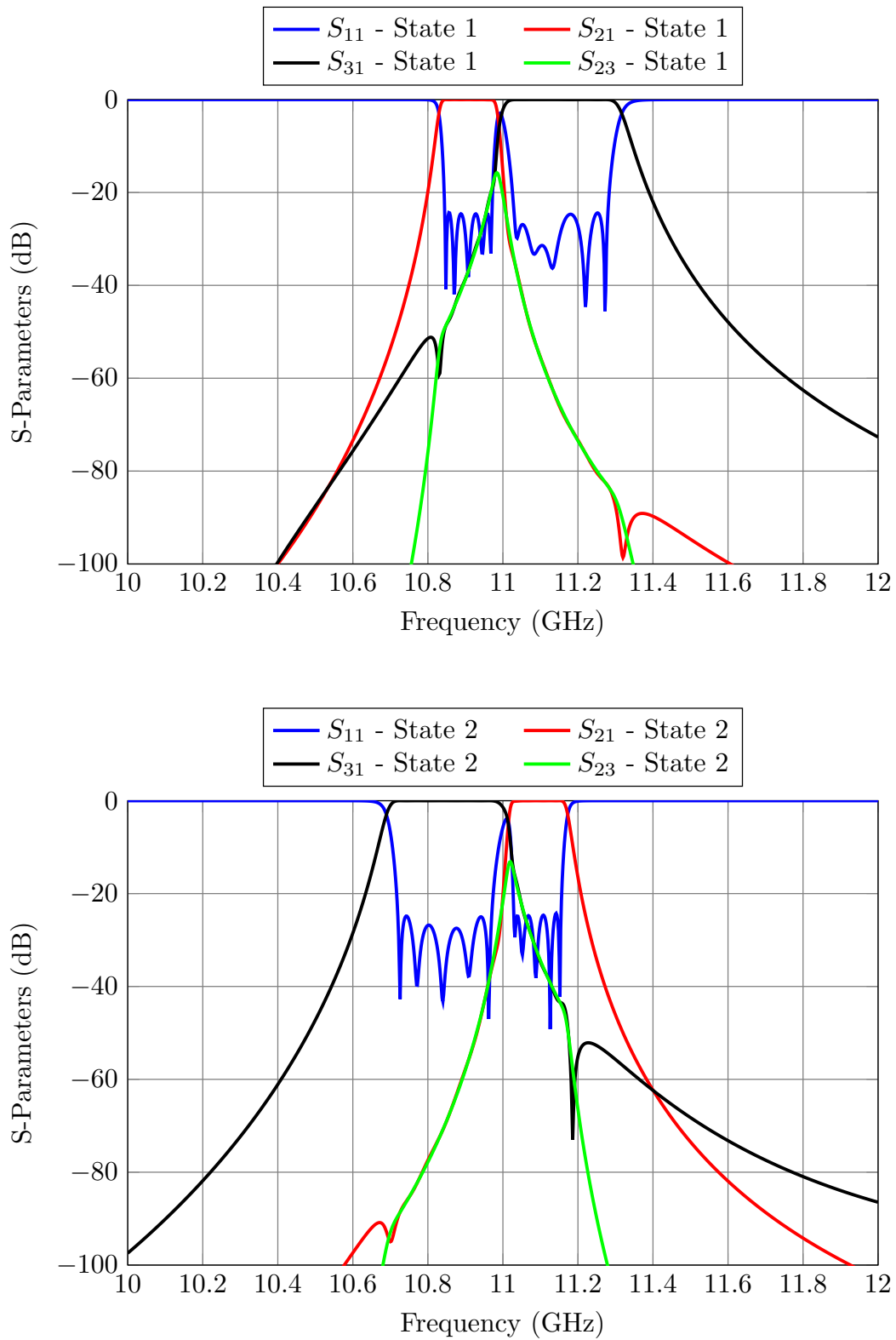


Figure 6.30: Performance of the isolated diplexers. Top: State 1. Bottom: State 2.

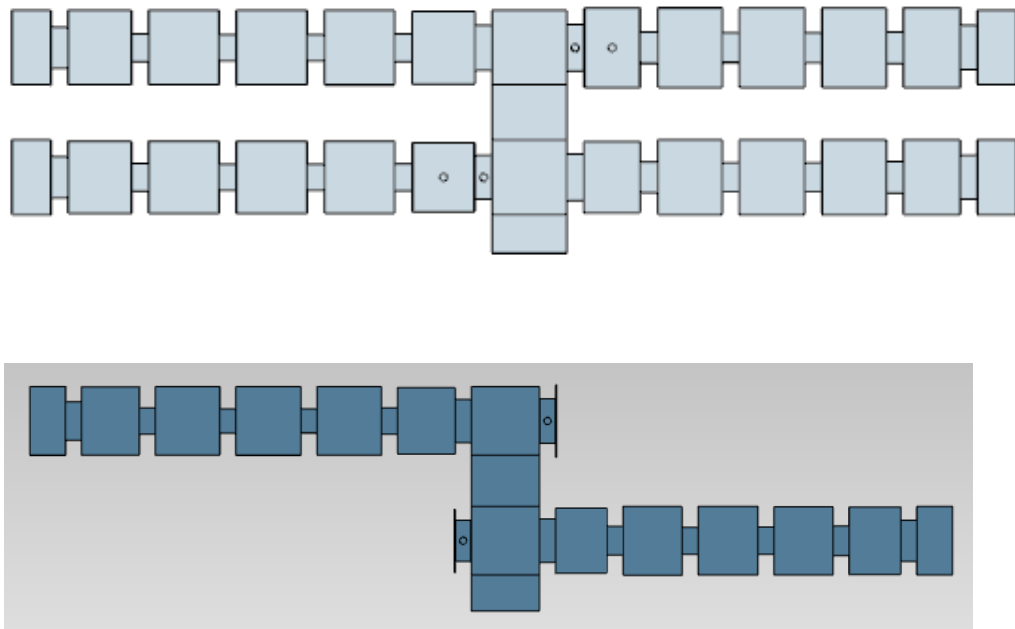


Figure 6.31: Combination of the independent diplexers. Top: Considering the whole diplexer. Bottom: Considering a reduced circuit.

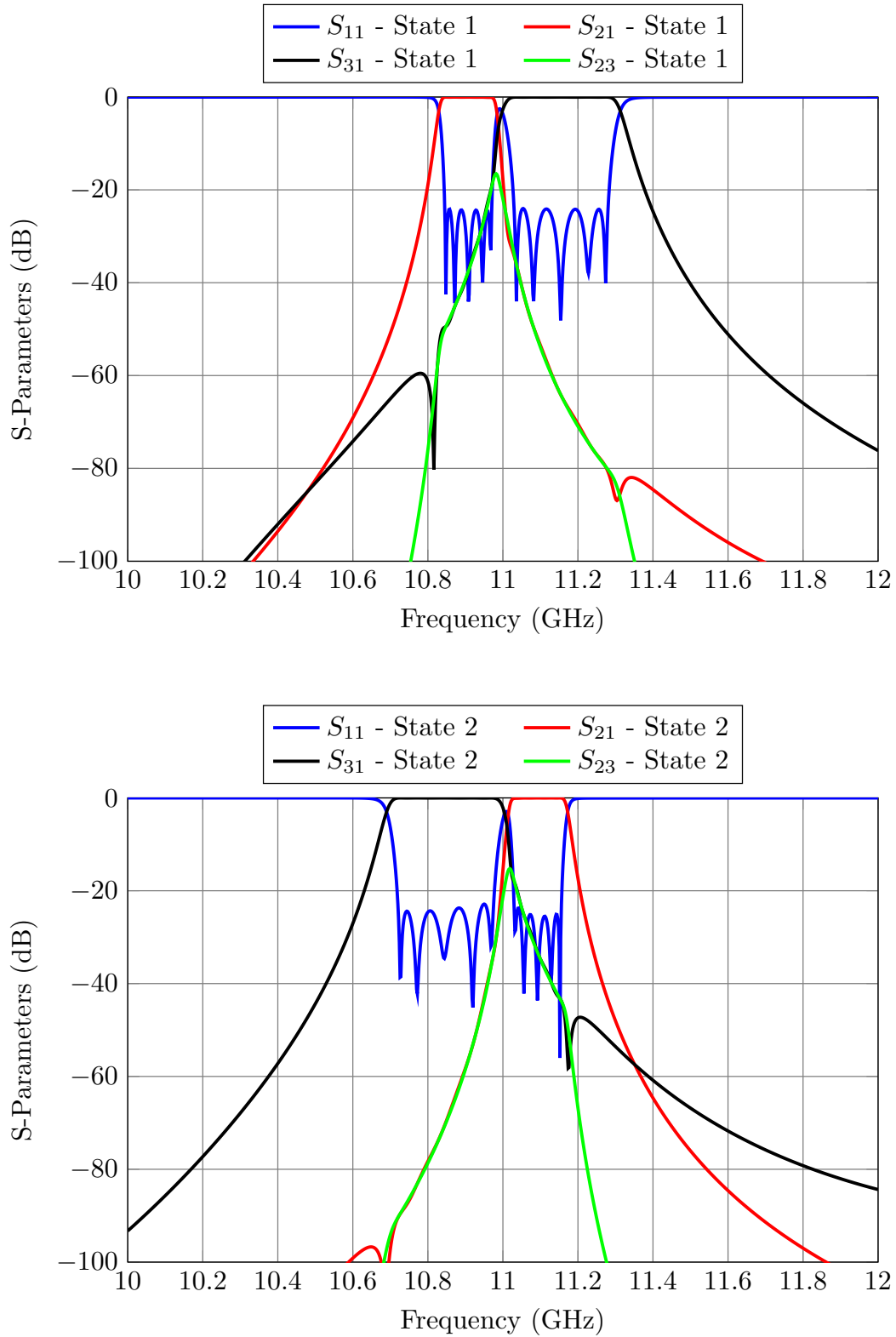


Figure 6.32: Performance of the 4-port device. Top: State 1. Bottom: State 2.

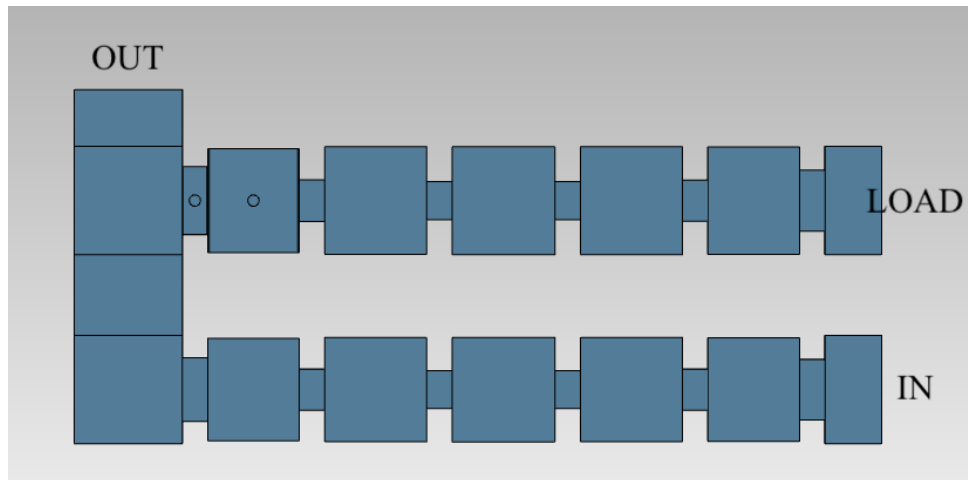


Figure 6.33: Combination of the common outputs of the branches (part 1).

3. Combine the common outputs of the branches. For each branch we can proceed as follows:
 - (a) Add the initial filter channels (the ones we had before designing the independent duplexers) to a manifold and set the MTPs of one of the filters to the OFF state (see Fig. 6.33). After that, optimize the elements of the active filter that are closest to the manifold (the first aperture and cavity) in order to recover the ideal filter performance (see Fig. 6.34). It is important to note that in this case, it was not necessary to optimize the distance to the short circuit of the lateral manifold (as shown in Fig. 6.33, that distance is 0 mm). Optimizing the first aperture and cavity of the filter was enough to recover the target performance.
 - (b) Switch the state of the MTPs and add a pin to short circuit the manifold (see Fig. 6.35). Optimize the elements of the active filter that are closest to the manifold and the position of the pin. After a short optimization, we obtain the performance shown in Fig. 6.36². As we can see, there is a peak in the S_{21} parameter around 11.8 GHz that resembles a transmission zero. If we simulated the same structure considering aluminum losses, we would see that the S_{11} also decreases at this frequency. The pin we added to the manifold behaves like an inductive aperture and, therefore, there is now a new cavity between the pin and the short-circuited end of the manifold. The

²As in the previous case, we included the short circuit pin at a 0 mm distance from the active filter. If we had not been able to recover the target performance optimizing the first aperture and cavity of the active filter, we would have also modified the position of the short circuit pin.

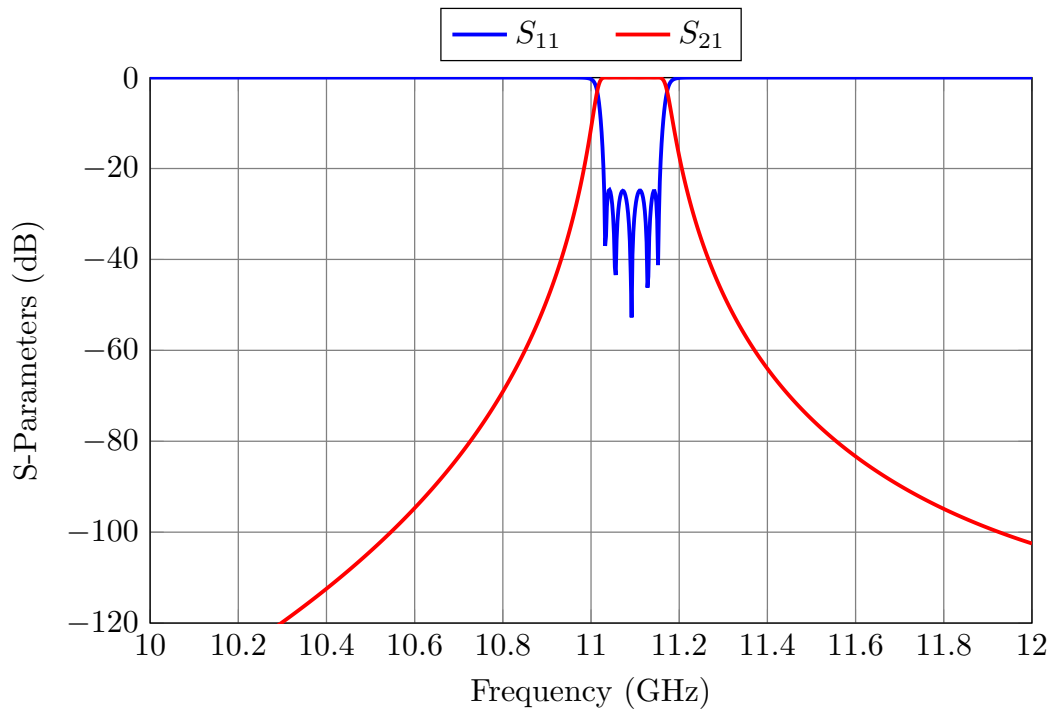


Figure 6.34: Performance of the structure shown in Fig. 6.33 after a short optimization.

second mode of the new cavity is resonating at 11.8 GHz (see Fig. 6.37) introducing the unexpected resonance peak. It is necessary to include an additional pin in the manifold to ensure that the resonance falls out of the frequency of interest. After adding the pin shown in Fig. 6.38, the cavities of the manifold resonate at 9.62 and 14 GHz. The peak at 11.8 GHz (see Fig. 6.39) has been successfully eliminated.

4. The final step is to combine half of the structures from Steps 2 and 3. Fig. 6.40 shows the LA model of the diplexer for the two possible states. Fig. 6.41 shows their performances.

In conclusion, the design of the reconfigurable diplexer consists of designing two separated diplexers which are then combined with a simple step-by-step procedure.

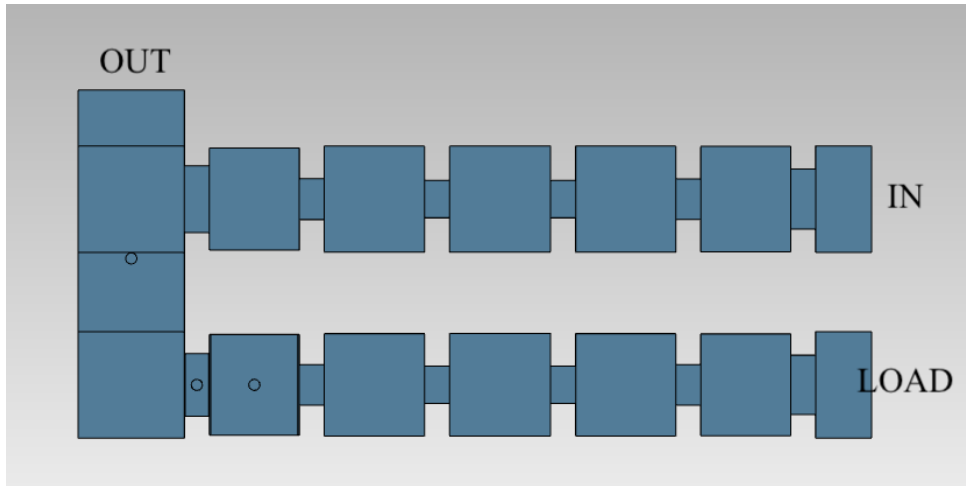


Figure 6.35: Combination of the common outputs of the branches (part 2).

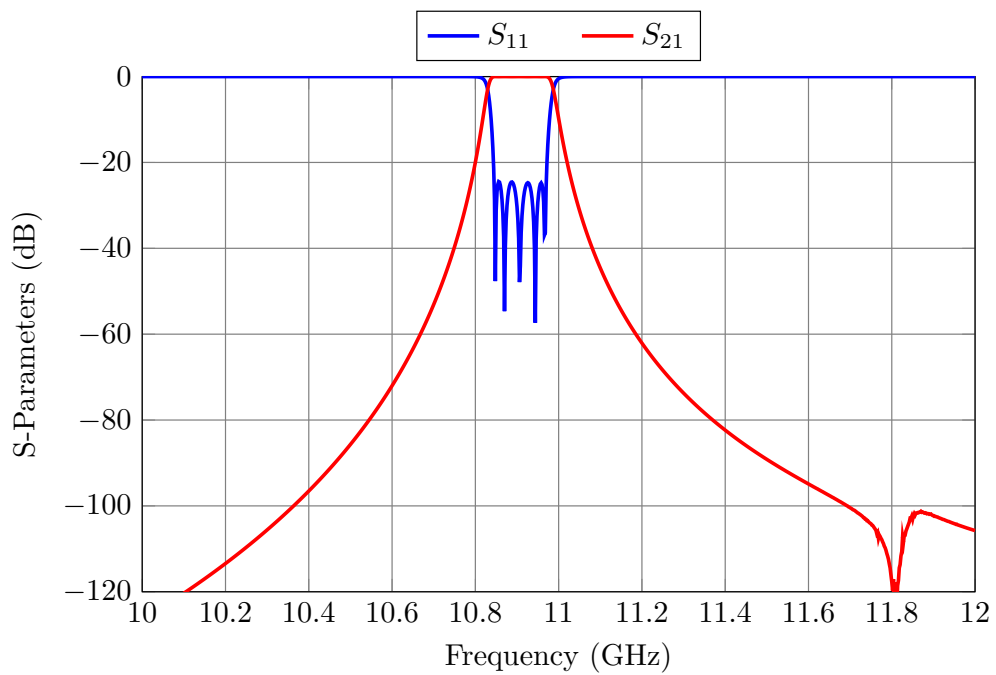


Figure 6.36: Performance of the structure shown in Fig. 6.35 after a short optimization.

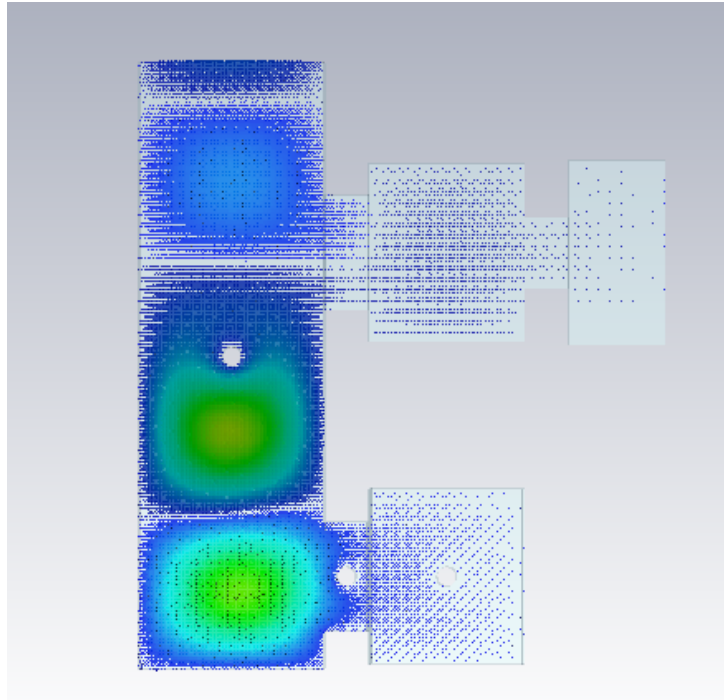


Figure 6.37: E-field at 11.8 GHz of Fig. 6.35.

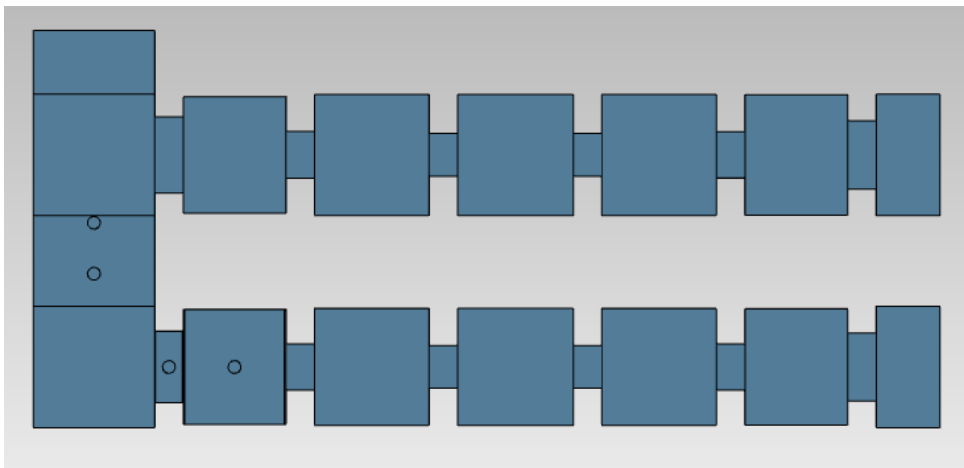


Figure 6.38: Introducing an additional pin to short circuit the manifold eliminates the resonance at 11.8 GHz.

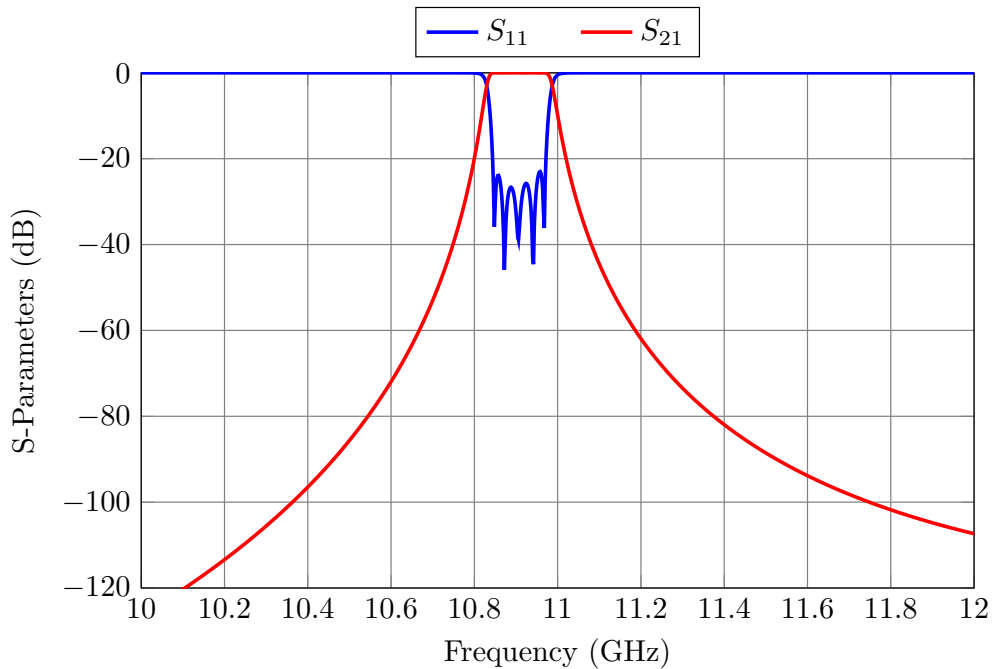


Figure 6.39: Performance of the structure shown in Fig. 6.38.

6.7.2 Design procedure for the HA diplexer

Once the LA diplexer has been designed, we can follow the same ASM-based procedure described in Chapter 3 (Step-by-Step ASM) to obtain the HA model including round corners in all cavities, MTPs, and regular tuners (see Fig. 6.42).

One interesting point is that designing the diplexer and the reconfigurable filters (see Section 6.4), we realized that it is not necessary to include MTPs in every cavity and aperture. We have, therefore, used MTPs in the first and last three elements of every branch (24 MTPs in total). Standard commercial tuners are used in all other cavities and apertures (20 in total).

The fastest approach to obtain the HA diplexer is as follows:

1. Extract the filter channels from the LA model and apply the Step-by-Step procedure to obtain the high-precision filter channels that include rounded corners and tuning elements (the hollowed M4 screws).
2. Then, combine the high-precision filters to obtain the structure shown in Fig. 6.42.
3. Using the *coarse* model(s) shown in Fig. 6.40 and the *fine* model(s) shown in Fig. 6.42, apply as many ASM iterations as needed in order to recover the target performance.

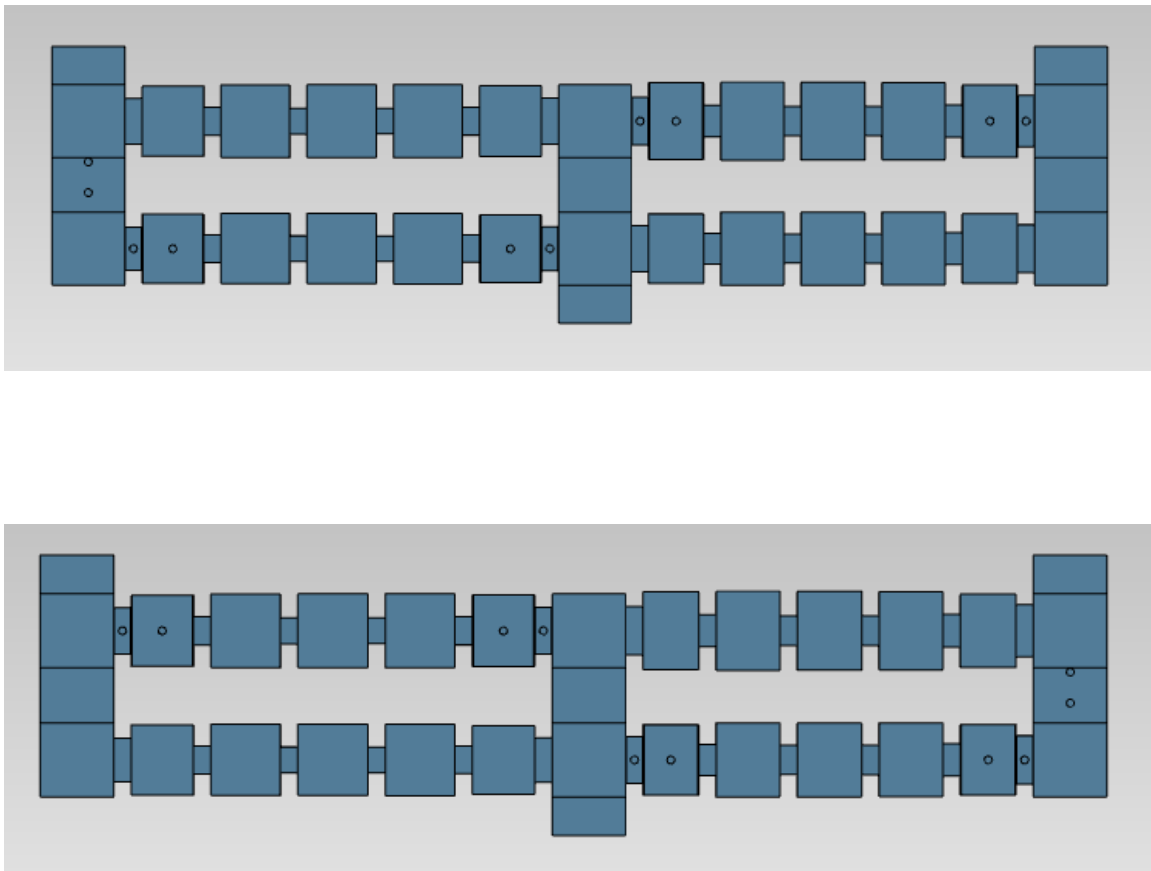


Figure 6.40: Low precision model of the reconfigurable diplexer. Top: LA model of the first state. Bottom: LA model of the second state.

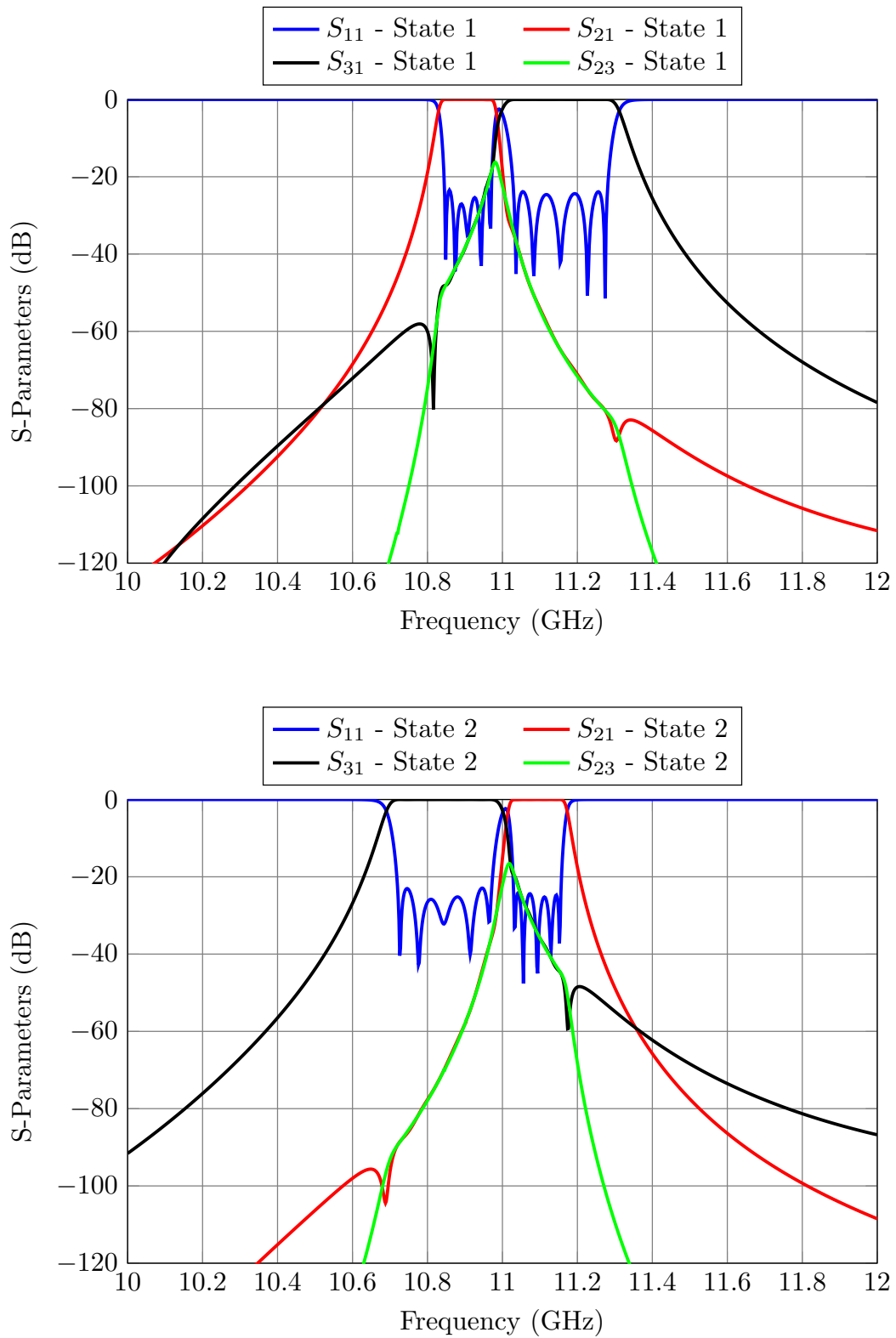


Figure 6.41: Performance of LA reconfigurable diplexer. Top: State 1. Bottom: State 2.

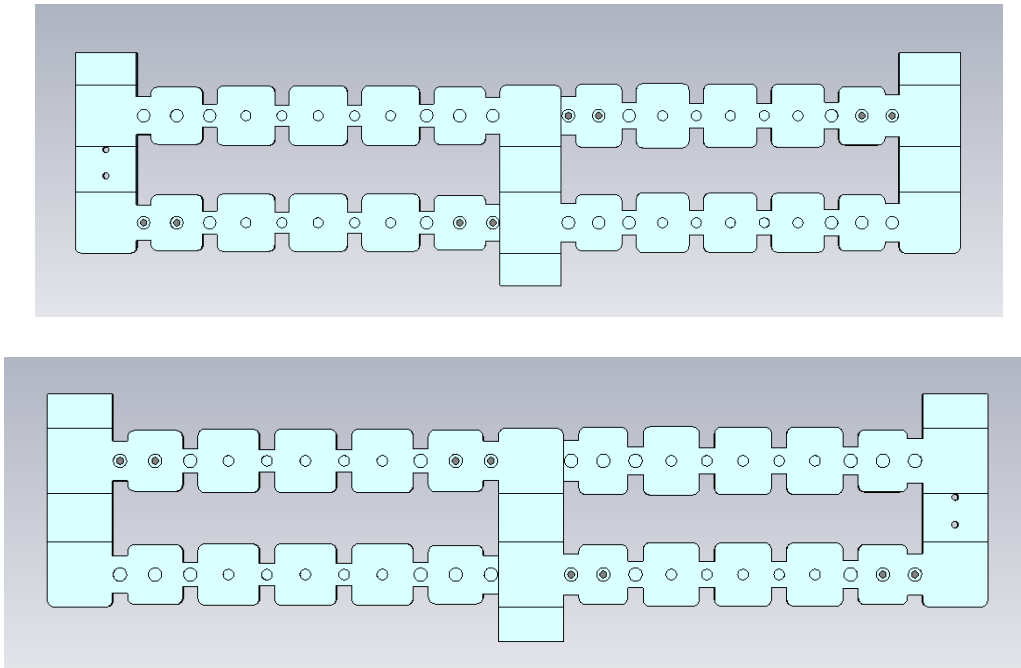


Figure 6.42: High accuracy model for the reconfigurable diplexer. Top: Top view of the first state. Bottom: Top view of the second state.

In this case, after three ASM iterations per diplexer, the HA model provides the performance shown in Figs. 6.43 and 6.44 for the first and second state, respectively.

6.8 Experimental Validation

The reconfigurable diplexer was manufactured, using aluminum, in two parts: body and cover. Fig. 6.45 shows the assembled filter already connected to standard WR-75 waveguides. Figs. 6.46 and 6.47 show the measured performances for State 1 and 2, respectively. As we can see, there is an excellent agreement between the simulated and measured performances of the diplexer. Even though, due to the low manufacturing accuracy, we were not able to recover an equiripple response for State 2, all S11 lobes are visible, and the return loss is greater than 23 dB. The losses for the narrower filters are around 1.3 and 1.2 dB, respectively. The losses for the wider filters are around 0.8 and 1 dB, respectively. These results completely validate both the topology and the design process of the reconfigurable diplexer.

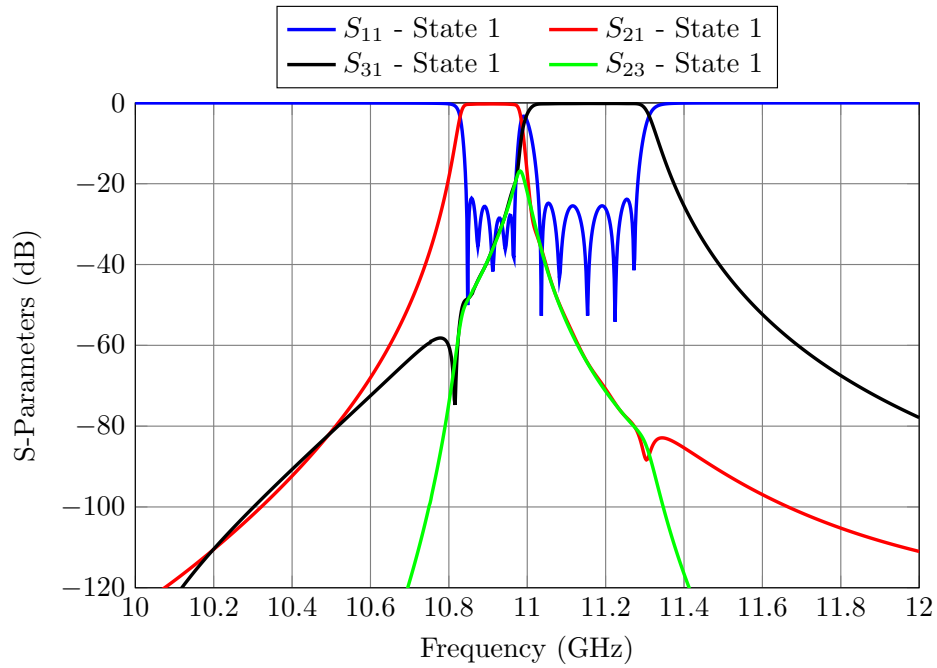


Figure 6.43: Performance of the HA reconfigurable diplexer (State 1)

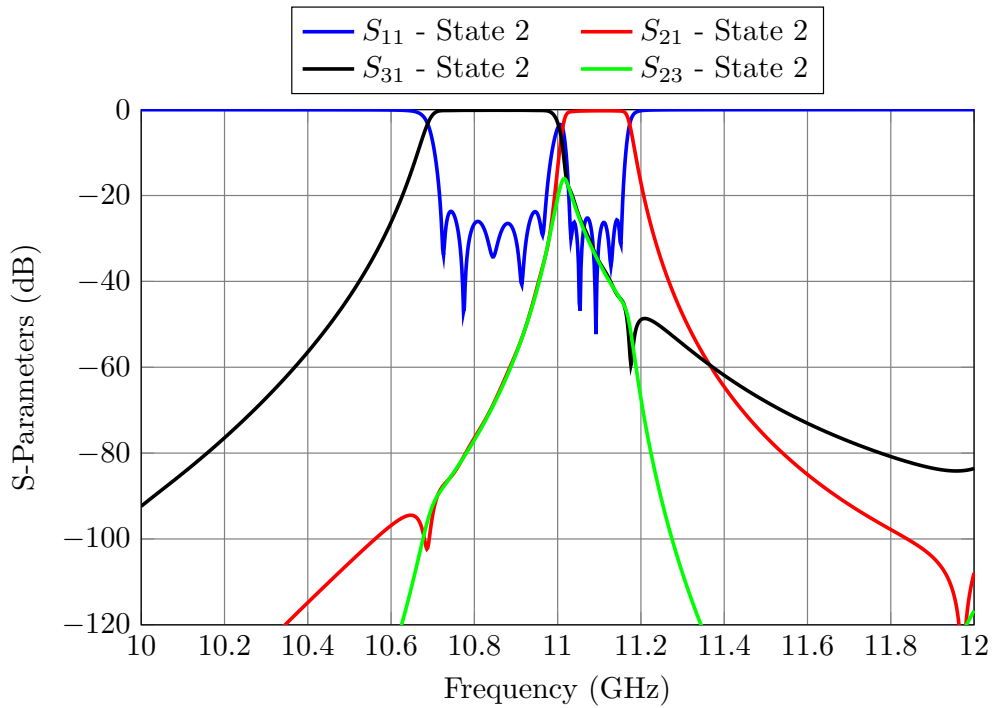


Figure 6.44: Performance of the HA reconfigurable diplexer (State 2).

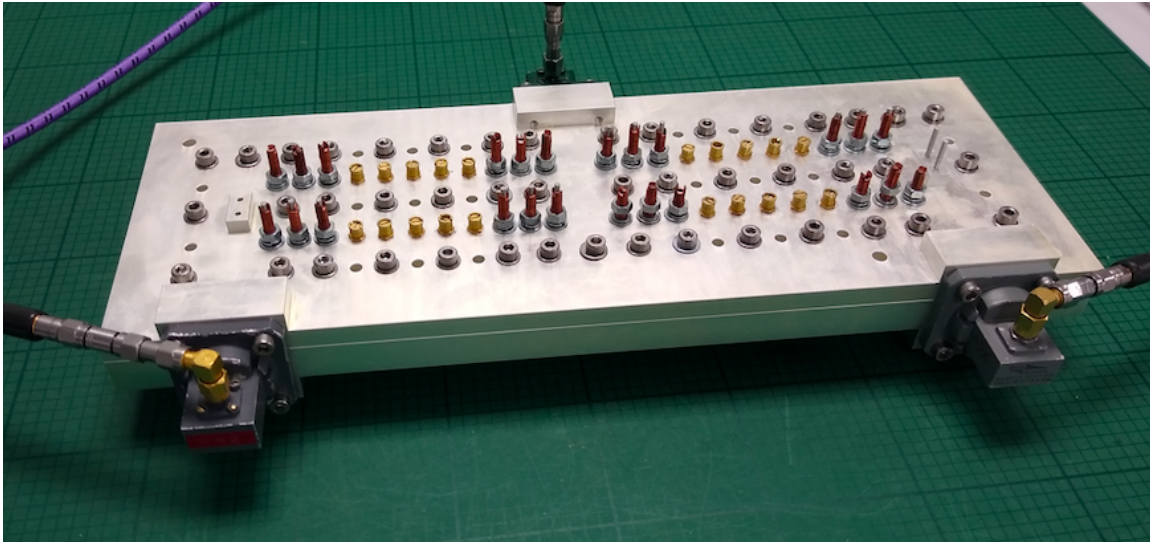


Figure 6.45: Reconfigurable diplexer already fed with WR-75 waveguides.

6.9 Conclusions

In this chapter we have discussed a novel topology for reconfigurable filters. We have, in fact, shown that, using MTPs, it is possible to design reconfigurable filters with a number of discrete states. We have also shown that this approach is very flexible since each filter channel can be completely different. Furthermore, it is important to note that although we have used as a proof-of-concept simple in-line filters, we can also use the same approach with folded filters to implement transmission zeros.

Furthermore, the reconfigurable filters can be operated remotely with a minimum additional weight and cost. In this context, it is important to note that the solution that we have discussed does not require high-precision displacement mechanisms. A simple linear actuator can, in fact, be used to change the position of the inner pins of the MTPs.

Finally, we have also shown experimental results for a reconfigurable filter with three discrete states and for a diplexer with two states. The agreement between simulations and measurements is excellent in all cases, thereby fully validating both the hardware and the design procedures.

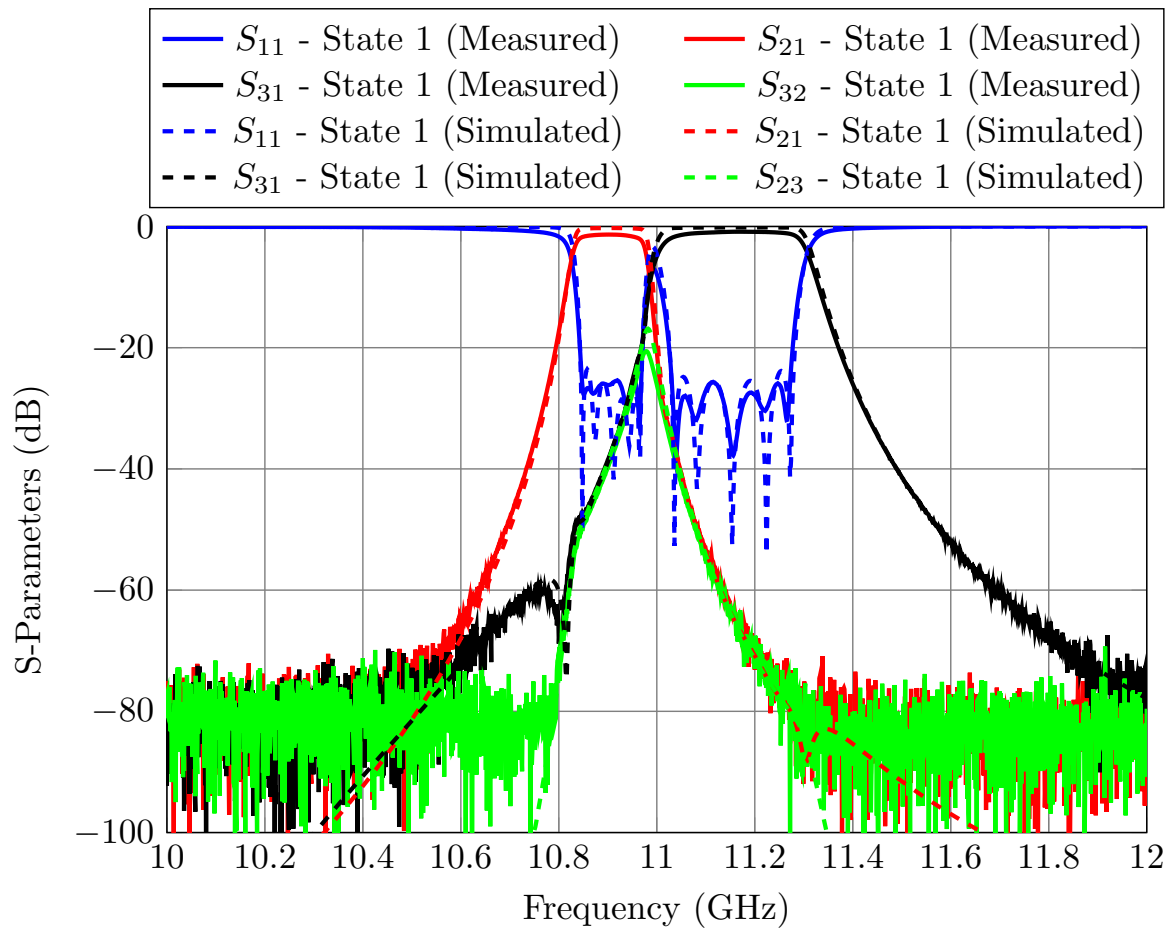


Figure 6.46: Measured performance of the reconfigurable diplexer (State 1).

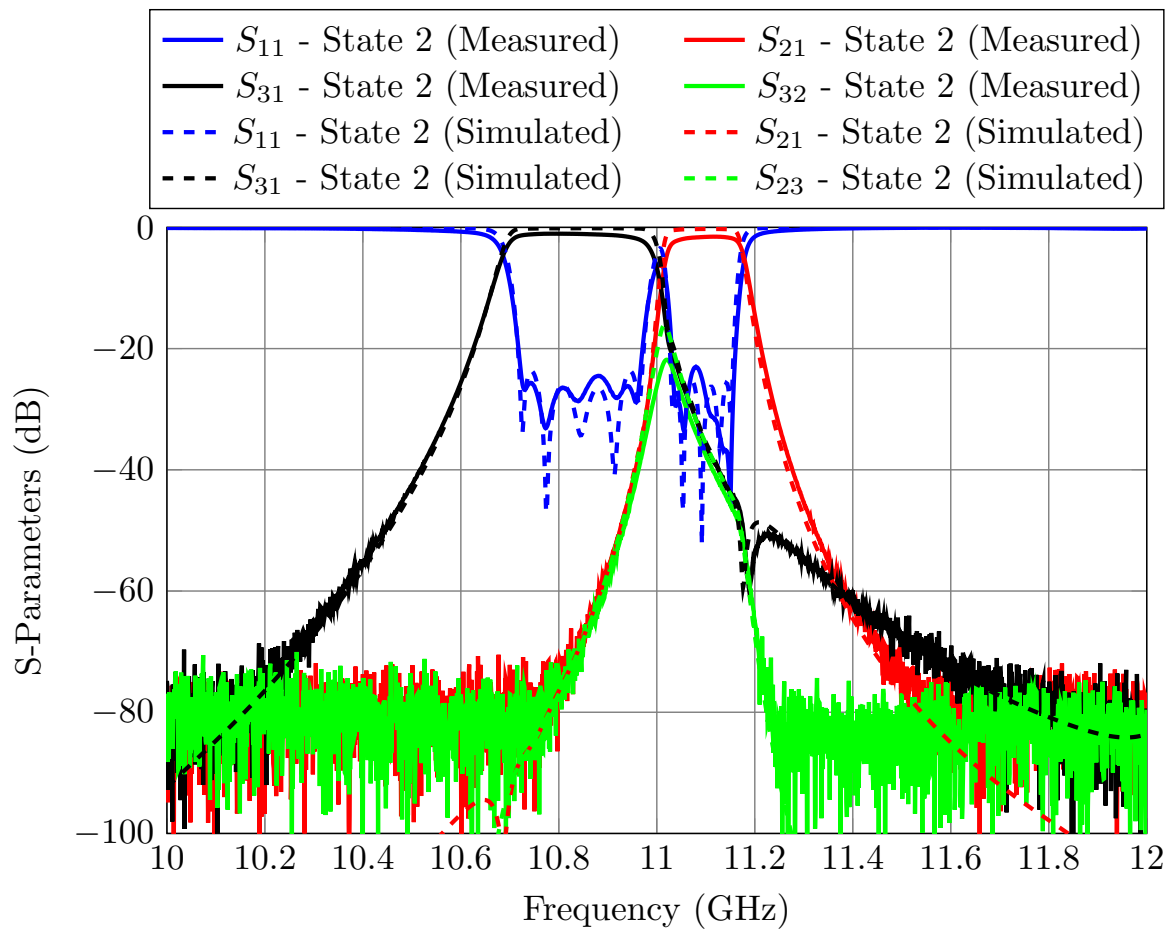


Figure 6.47: Measured performance of the reconfigurable diplexer (State 2).

Conclusions and Future Work

7.1 Conclusions

In this doctoral thesis, we have provided a number of theoretical and practical contributions to the state-of-the-art of microwave filters, for both ground and space applications. In this chapter, we will first provide a summary of our major achievements and contributions, and then we will propose a number of possible future research areas.

The first topic that we have discussed is a novel procedure based on the Aggressive Space Mapping (ASM) optimization method. The advantage introduced by the Step-by-Step procedure is that it allows us to easily include all non-ideal factors (tuning elements and rounded corners) in the design process with substantially less computational effort than its predecessors. The key of the proposed method is that the non-ideal factors are added in sets of two or three elements at a time, thereby greatly simplifying all needed computations and reducing the chances of finding local minima in the optimization process. As compared to the current state-of-the-art of ASM, namely, the so-called One-Step ASM, the proposed procedure is more robust and much faster, especially for complex filter topologies.

In addition, we have also clearly demonstrated the advantages introduced by the new procedure with the design of four different microwave filters. Both Step-by-Step and One Step ASM have been used for the design of each filter, namely: a standard 6-pole inductive filter in rectangular waveguide, a folded 6-pole filter with a capacitive cross-coupling, a 4-pole folded filter with a cross-coupling, and a 5-pole filter based on dual-mode resonators. For the simplest filter (the in-line 6-pole waveguide filter), the Step-by-Step procedure is

1.83 times faster than One Step ASM. For the rest of the filters our method is 6.3, 10.6 and 5.3 times faster, respectively, than One-Step ASM. The more complex the filter to be designed is, the greater are the benefits of the Step-by-Step approach.

The next contribution that we have discussed is a simple and effective solution to the cumbersome task of tuning microwave filters. The method that we propose is again based on SM. The key feature of the procedure we have developed is that it exploits the filter's simulation models. In particular, our approach allows us to evaluate the relation (or mapping) between the penetrations of the tuning elements of the filter and the dimensions of a computationally efficient model. Since this relation is established by simulation, we can obtain the mapping around the optimal tuned response. This mapping can then be used very effectively to tune the actual filter without needing to update it after every iteration.

The tuning procedure we have proposed has been validated by tuning an inductive 6-pole waveguide filter. Several enhancements of the basic method have also been discussed in order to further accelerate and simplify the tuning process.

The next contribution that we have described in this thesis is a new topology to design multi-band filters that can be used to easily design hardware with an arbitrary number of bands. The proposed topology has been validated by designing, manufacturing and measuring a tri-band filter.

The new folded topology overcomes the limitations of its in-line predecessor: since the filters are folded, it is no longer necessary to guarantee any type of length constraint and we can easily introduce transmission zeros in every channel. Furthermore, the design process that we have discussed is based on the well-known optimization strategy for manifold multiplexers and thus, it can be used to design multi-band filters with as many channels as required. We believe that this approach is the best solution available in terms of flexibility, scalability and ohmic losses.

Finally, the last contribution that we have discussed is the design of a family of filters that can be reconfigured remotely. The key feature of the novel topology that we propose is the use of modified tuning pins (MTPs) that can be operated remotely to activate and deactivate different paths of the signal. The MTPs can be effectively seen as a low-cost mechanical switch that can be easily added to any type of structure. The benefits introduced by our contribution are that the filters for each state can be completely different, they can be designed independently from each other, and that the MTPs do not require expensive high-precision actuators.

As a verification, we have designed two reconfigurable filters with three discrete states. One of the filters has also been manufactured and measured. In addition to simple

filters, we have also designed, manufactured and measured a reconfigurable diplexer with two discrete states. All measured results have been found to be in excellent agreement with the high-precision simulations, thereby fully validating both the novel hardware and the design techniques.

7.2 Future work

The research work described in this thesis can effectively be used as a starting point for future research. Several areas could indeed be explored. In particular:

- **New optimization domains.** Until now, in all the ASM-based procedures we have discussed, we have generally used the magnitude of the S_{11} and S_{21} in the recovery process. It may be beneficial to completely change the optimization domain and move, for instance, to the complex plane where filters are characterized in terms of poles and zeros. It has been proved that if the error functions used in the ASM recovery process are re-written in terms of the filter's poles and zeros, the effect of local minima decreases drastically. As a consequence, gradient-based optimization algorithms could be used, potentially speeding the design process even more.
- **Filter tuning.** In our work, we have clearly shown that SM can be used to tune an inductive filter in rectangular waveguide very efficiently. It would be interesting to extend the basic tuning procedure we discussed to more complex filtering structures and technologies, such as dual-mode filters, coaxial filters with a folded topology, in-line filters with transmission zeros (based on resonant coupling irises) or to GGW (groove gap waveguide) filters.
- **Reconfigurable filters.** It would be interesting in this context to continue the development of more complex reconfigurable filters based on MTPs such as coaxial filters, low-pass corrugated filters or circular waveguide dual-mode filters, and to partner up with an actual industrial manufacturer to develop a commercial version of our basic concept for both ground and space applications. It would also be interesting to develop a family of MTPs with a dielectric outer part. The metallic inner pin will activate and deactivate the different paths of the signal, and the outer dielectric part could be used to continuously tune each of the possible states.
- **Multi-band filters.** A further interesting extension of the work described in this thesis could be the exploration of reconfigurable multi-band filters based on the use of MTPs in multi-band filter structures.

Manufacturing Plans with Solid Works

A.1 Filter example

This appendix contains a detailed description of how to prepare the manufacturing plans in Solid Works for a folded 6-pole filter with a cross-coupling. Fig. A.1 shows the final filter designed with CST, whose performance is shown in Fig. A.2

Since the filter has been folded along its center, it will be manufactured by H-plane milling in three pieces: a body and two covers. There are several things to notice about this filter:

- The concave corners have a radius of 2 mm.
- There is a manifold connected to the input/output of the filter. This prototype was manufactured to test the insertion loss of the most restrictive channel of the tri-band filter shown in Chapter 4 and, therefore, we wanted to include the effect of the double manifold.
- The filter includes professional tuners (see Fig. A.3). It is important to note that whereas the cylinder that actually goes inside the filter has a radius of 0.9 mm, the diameter of the outside part of the tuner has a radius of 1.35 mm.
- The three pieces will be assembled using passing M4 screws tightened with nuts.

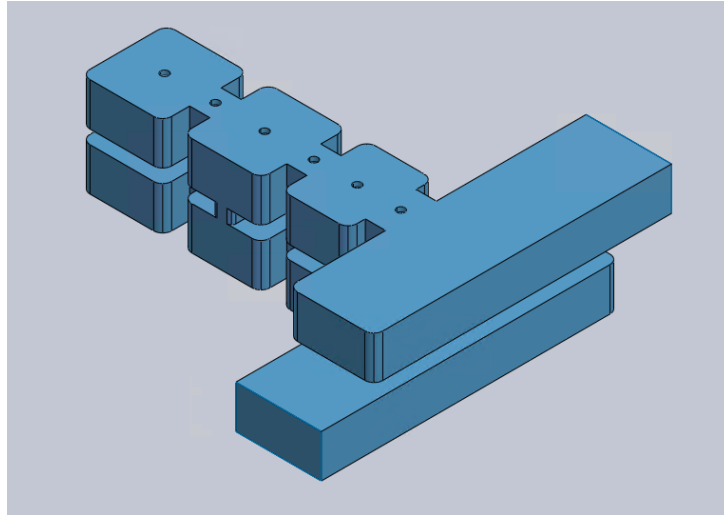


Figure A.1: Folded 6-pole filter with a capacitive a cross-coupling.

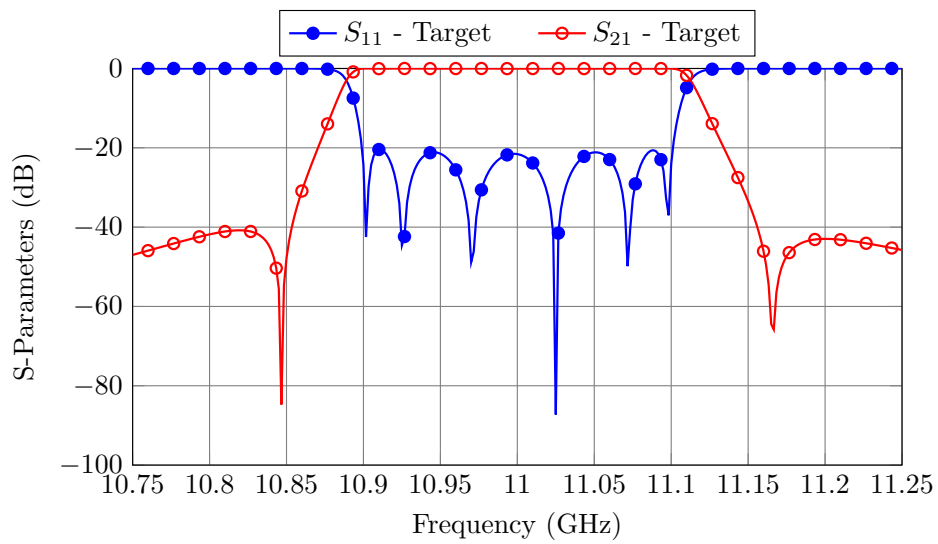


Figure A.2: Target performance for the filter.

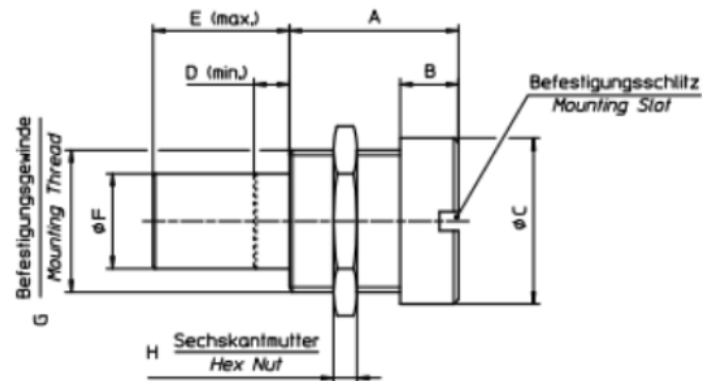


Figure A.3: Professional tuner.

A.2 General idea

Solid Works is a 3D modeling CAD tool that can be used to generate the manufacturing plans the CNC machines require. In this section, we will provide a very detailed guide on how to draw these plans step by step. The general process goes as follows:

- Insert the structure of the model in a solid block, and then subtract it to obtain a block that has been hollowed with the shape of the filter.
- Then add all the holes of the screws that are necessary to close and align the filter.
- Finally, separate this hollowed block with several holes into a body and cover(s).

A.3 3D plans

In this section we will exhaustively describe each of the steps mentioned before. The complete process goes as described next:

1. After the filter is designed, export its geometry as a STEP file so that it can be opened with Solid Works.
2. Then select the surface of the tuners (which were set to a depth of 1 mm) and add an *Extrude Base* operation (*Features/Extrude Base*). Then, sketch circles in the tuners' holes as shown in Fig. A.4 (left) and exit the sketch so that the *Extrude Base* menu appears [Fig. A.4 (right)]. Set the height of the extruded volume (in this case 6 mm). It is important that the extruded base is merged into the existing solid.
3. Repeat the previous operation for the top, bottom and side of the filter (one of the tuning elements is in the aperture where the filter is folded). At the end of this process we will have one solid as shown in Fig. A.5.

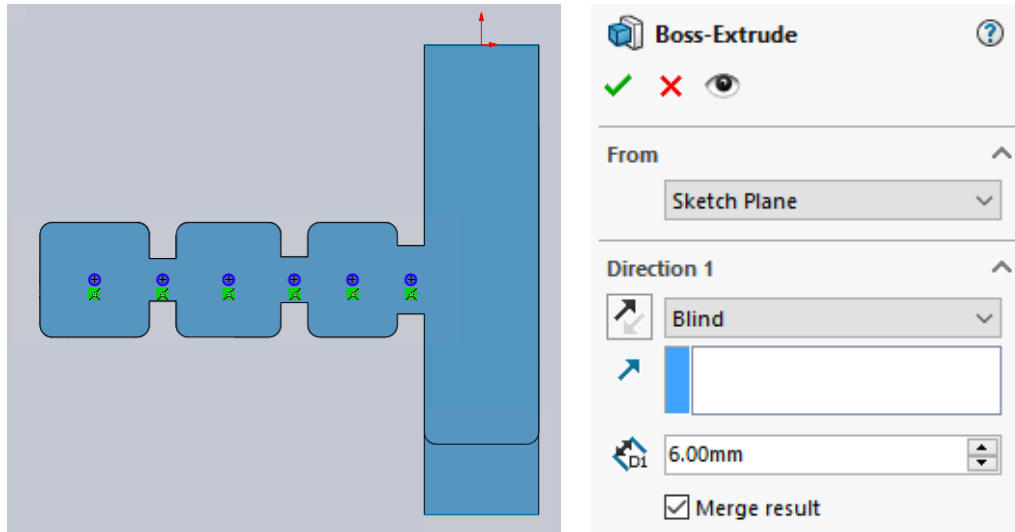


Figure A.4: Left: Draw circles in the tuner's holes. Right: Boss-Extrude's menu.

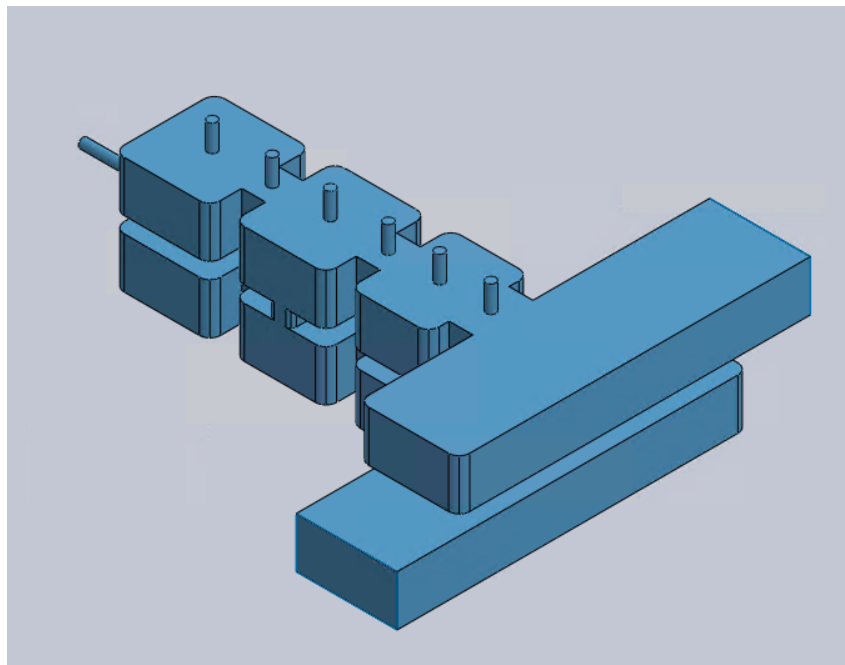


Figure A.5: Solid structure at the end of Step 3.

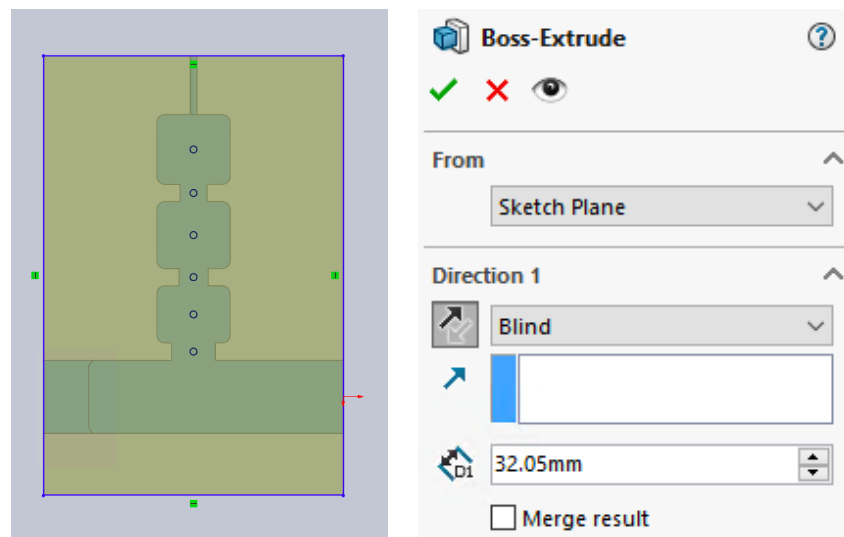


Figure A.6: Left: Draw a rectangle that contains the filter. Right: Boss-Extrude's menu.

4. Add a rectangular box that contains the filter. In order to do so, select the top of one of the cylinders added in the previous step (to define the plane in which we will perform the next operation) and add another *Extrude Base* operation. Draw a rectangle that contains the filter and exit the sketch [Fig. A.6 (left)]. At this point it is important **not to merge** the results [see Fig. A.6 (right)]. At this point we will have two solids: a box that contains the filter, and the filter itself.
5. Then subtract the filter from the box with a *Combine* operation. Fig. A.7 (left) shows how to perform the subtraction and Fig. A.7 (right) shows the result. We can see that the block has been hollowed. We can clearly see the importance of adding the cylinders of Step 2: after the subtraction operation the holes for the tuning element are present.
6. Add the standard flanges for WR-75. Fig. A.8 shows the standard flanges for WR-75 with its dimensions in mm. In this case, it is necessary to add a rectangle on what will be the top and bottom covers (see Fig. A.9).
7. The input and output waveguides will be attached with threaded M4 screws, and thus, we must include them with an *Extrude Cut* operation (see Fig. A.10). Fig. A.11 shows the final solid that includes the flanges.

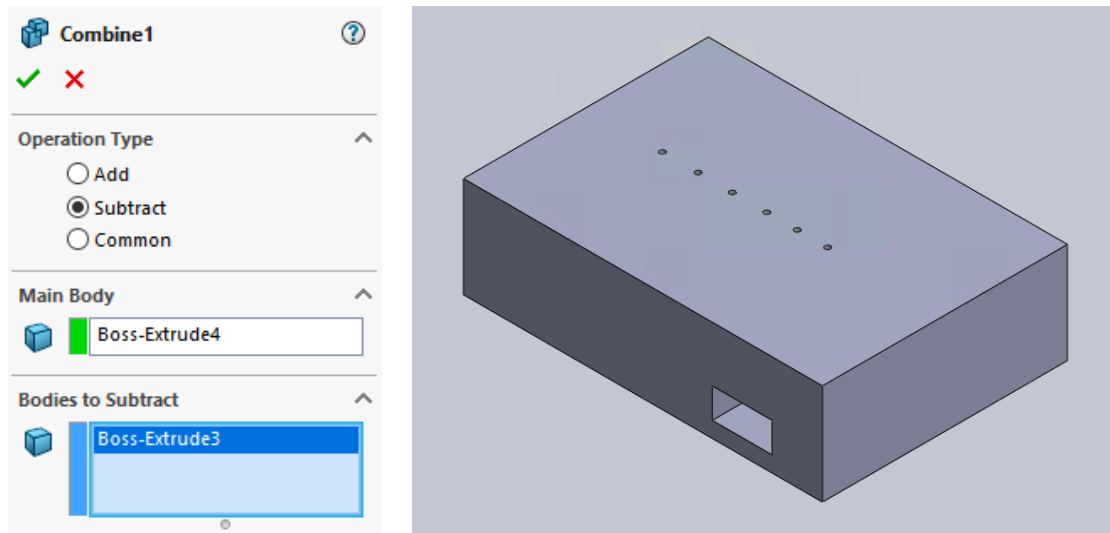


Figure A.7: Left: *Combine*'s menu. Right: Hollowed solid with the shape of the filter.

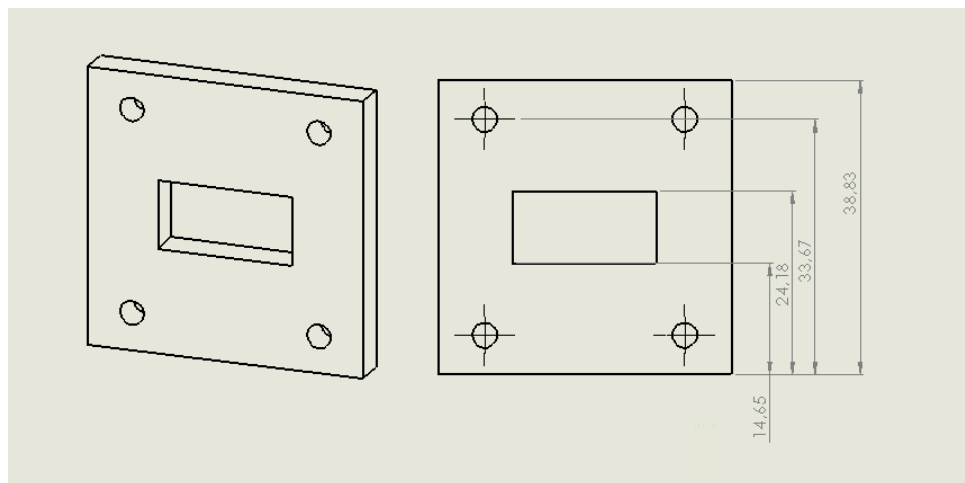


Figure A.8: Flanges for WR-75. All annotations are in mm.

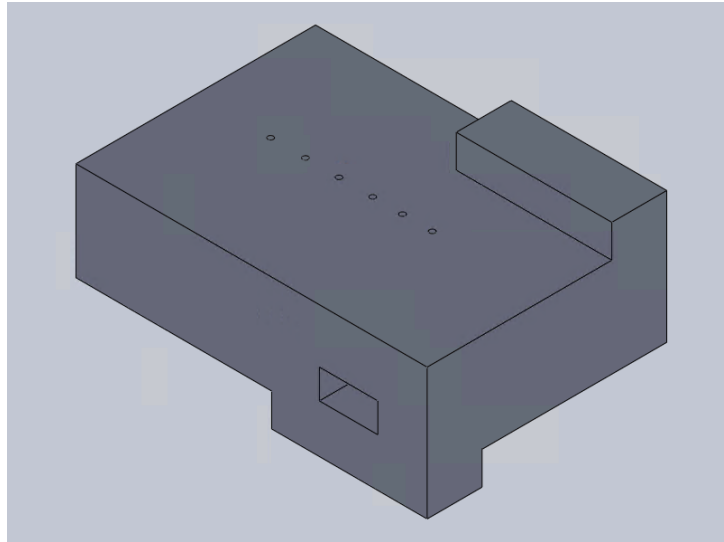


Figure A.9: Add additional rectangles to fit the standard flanges.

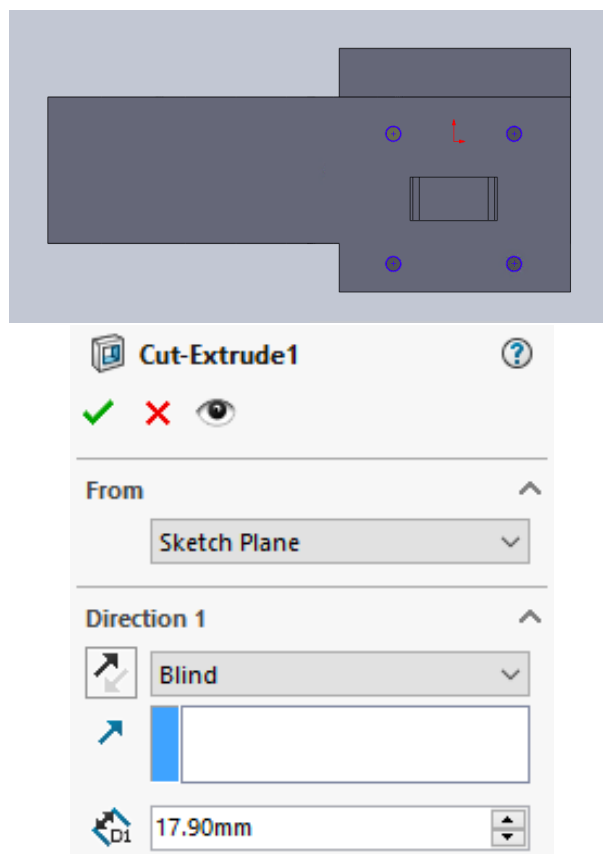


Figure A.10: Top: M4 threaded holes ($\phi = 1.65$ mm). Bottom: *Extrude Cut*'s menu.

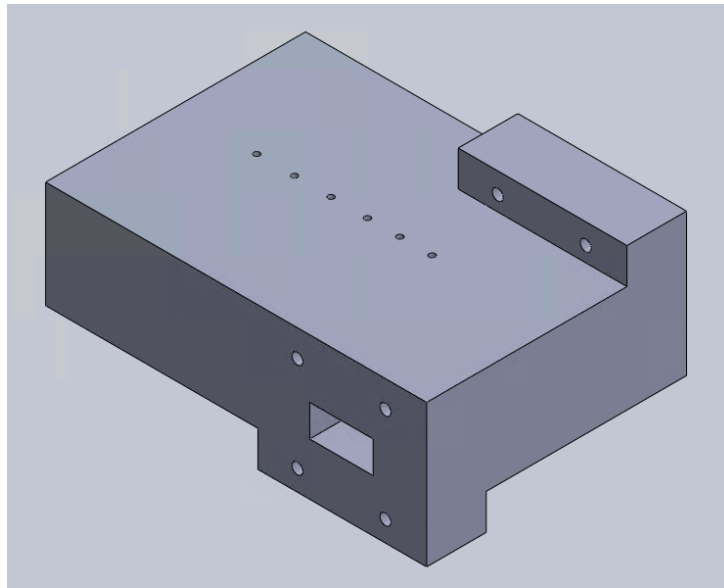


Figure A.11: Solid that includes standard WR-75 flanges.

8. Add the following holes with an *Extrude Cut* operation:
 - Passing M4 holes ($\phi = 4.085$ mm). As mentioned before, the three pieces will be assembled together using passing M4 screws. Each M4 will go through the top cover, body and bottom cover of the filter and we will use nuts to tighten the screws. These M4 screws must surround the filter to ensure a good electric contact between the body and the covers. In this case, we will use 15 screws [see Fig. A.12 (top)].
 - Threaded M2 holes ($\phi = 1.61$ mm). The output of the filter has been flipped in order to fit the standard flanges (without using H-plane bends) (see Fig. A.1). In order to ensure a good electric contact near the two short circuits of the manifold, we need to include two threaded M2 screws [see Fig. A.12 (top)].
 - Alignment pins ($\phi = 5$ mm). These pins are used to align the three pieces before tightening the closing screws. In this case, we will use two alignment pins [see Fig. A.12 (top)].

We need to perform four different *Extrude Cut* operations: one for the passing M4 screws and the alignment pins (that go through the hole solid) and one for each M2 hole (since they do not go through the whole solid). Fig. A.12 (bottom) shows the resulting piece after this step.

9. Separate the solid in three pieces: a body and the two covers¹. Fig. A.13 shows the body and top cover (the bottom one is identical).

¹This can be done with an *Extrude Cut* operation.

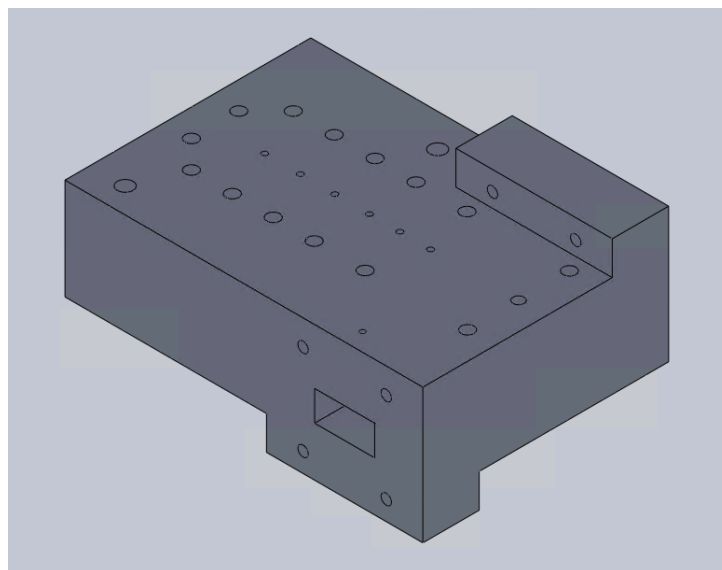
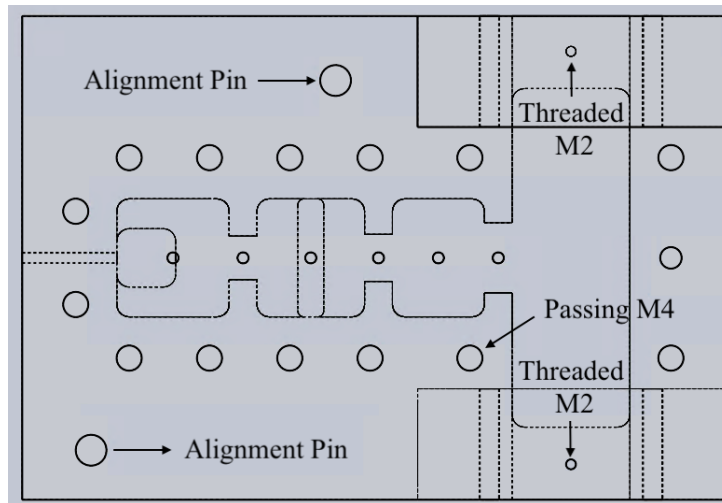


Figure A.12: Top: Different holes to be added. Bottom: Resulting piece after Step 8.

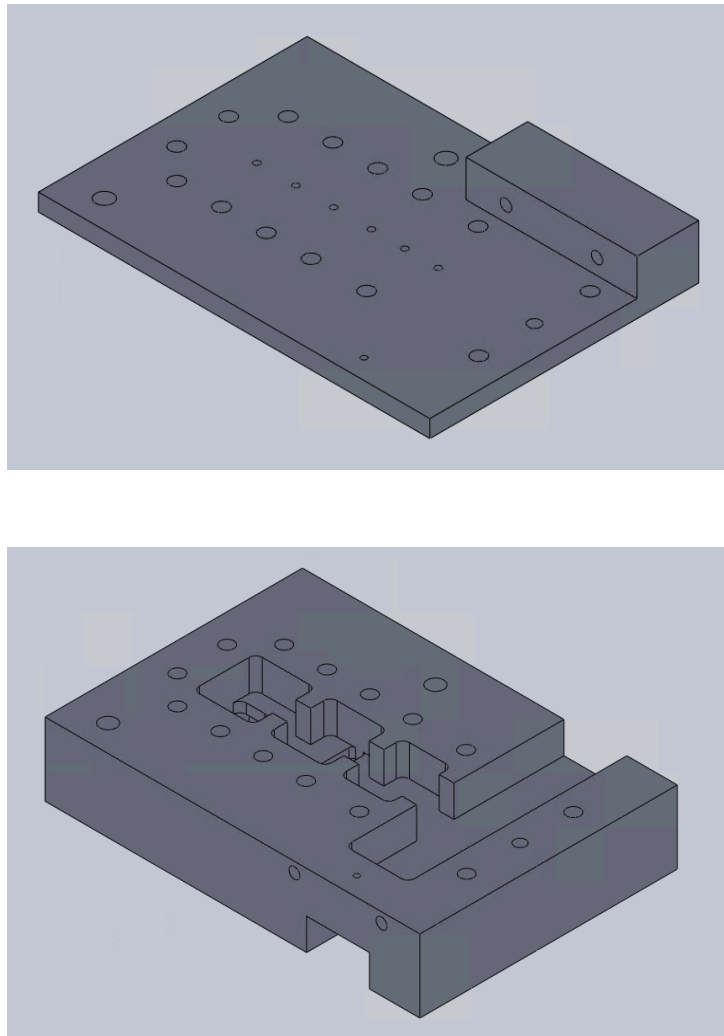


Figure A.13: Top: Top cover of the filter. Bottom: Body of the filter.

10. Add pressure wells to the body. The covers of the filter will not be completely smooth and therefore, in order to guarantee that the best possible electric contact, we must add these wells². One *Extrude Cut* operation is needed to include the pressure wells. Fig. A.14 shows the resulting body of the filter.
11. There are two additional modifications that must be done in the covers:
 - Modify the diameter of the tuners. We started to draw the manufacturing plans from the STEP file and thus, the current diameter of the holes for the tuners corresponds to the part that actually is used to tune the filter (diameter of 1.8 mm). We need to modify these holes to the proper diameter (2.7 mm).
 - Erase some material from the cover so that the tuners fit. The tuners that we will use are shorter than 5 mm (thickness of the covers) and therefore, we need to eliminate some material so that the tuners can be used.

Fig. A.15 shows the top and bottom covers of the filter. Note that some material has also been removed from the bottom cover, it is just not visible from the orientation of the piece.

12. After following the previous steps, the 3D plans are ready to be sent to the filter manufacturer. Along with the Solid Work plans, it is also recommended to include a pdf file specifying how the holes should be (the metric and if the hole needs to be threaded or not). Solid Works allows us to do this in a very simple way:
 - (a) Generate a drawing from each 3D piece (*File/Make drawing from part*).
 - (b) Then, Solid Works will ask us which views we want to add to the drawing (top, bottom, isometric etc.).
 - (c) Finally, we will add some annotations with the characteristics of the holes.

Fig. A.16 shows an example of one of the drawings.

All these files can be sent to the filter manufacturer. If we had sent the original STEP file (Fig. A.1), they would have charged us for all the hours that are needed to perform Steps 1- 12, and the price of manufacturing the filter would have been increased substantially.

²The pressure wells can be around 2-4 mm deep.

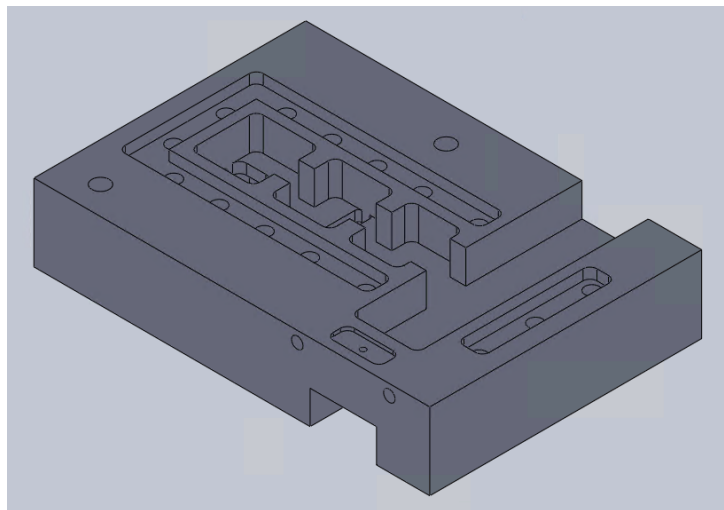
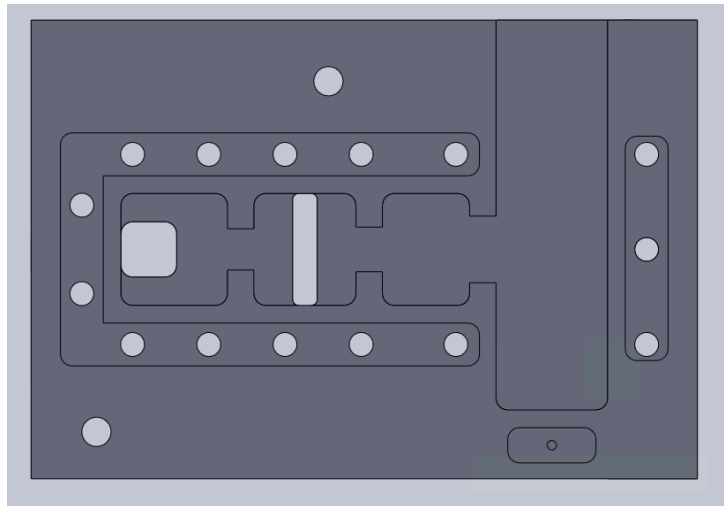


Figure A.14: Body of the filter.

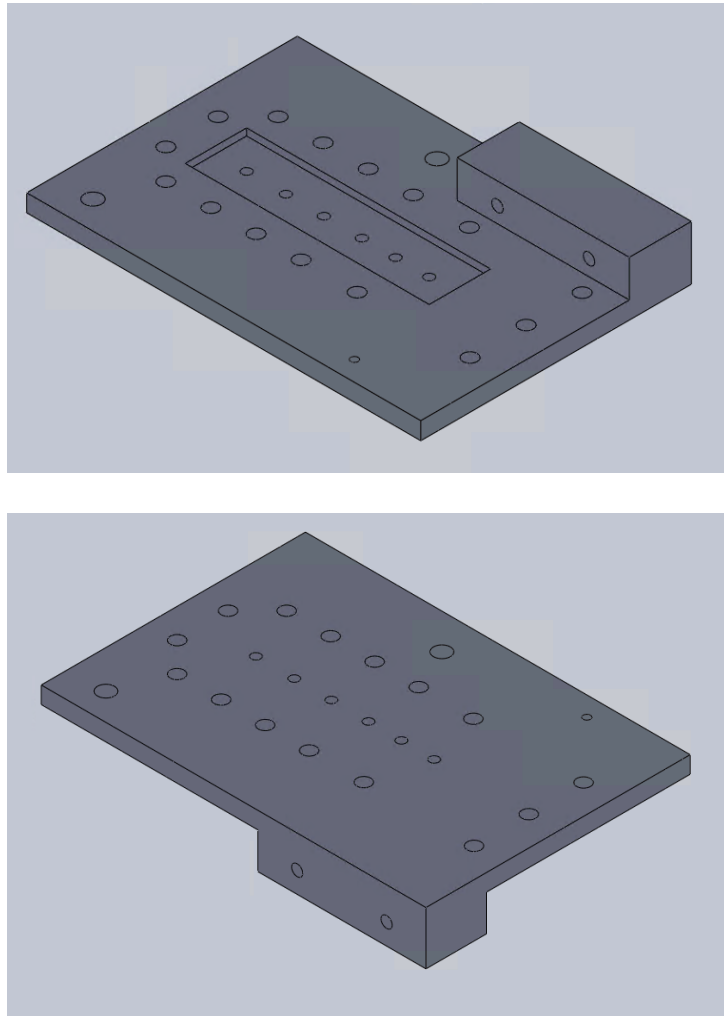


Figure A.15: Top: Top cover of the filter. Bottom: Bottom cover of the filter.

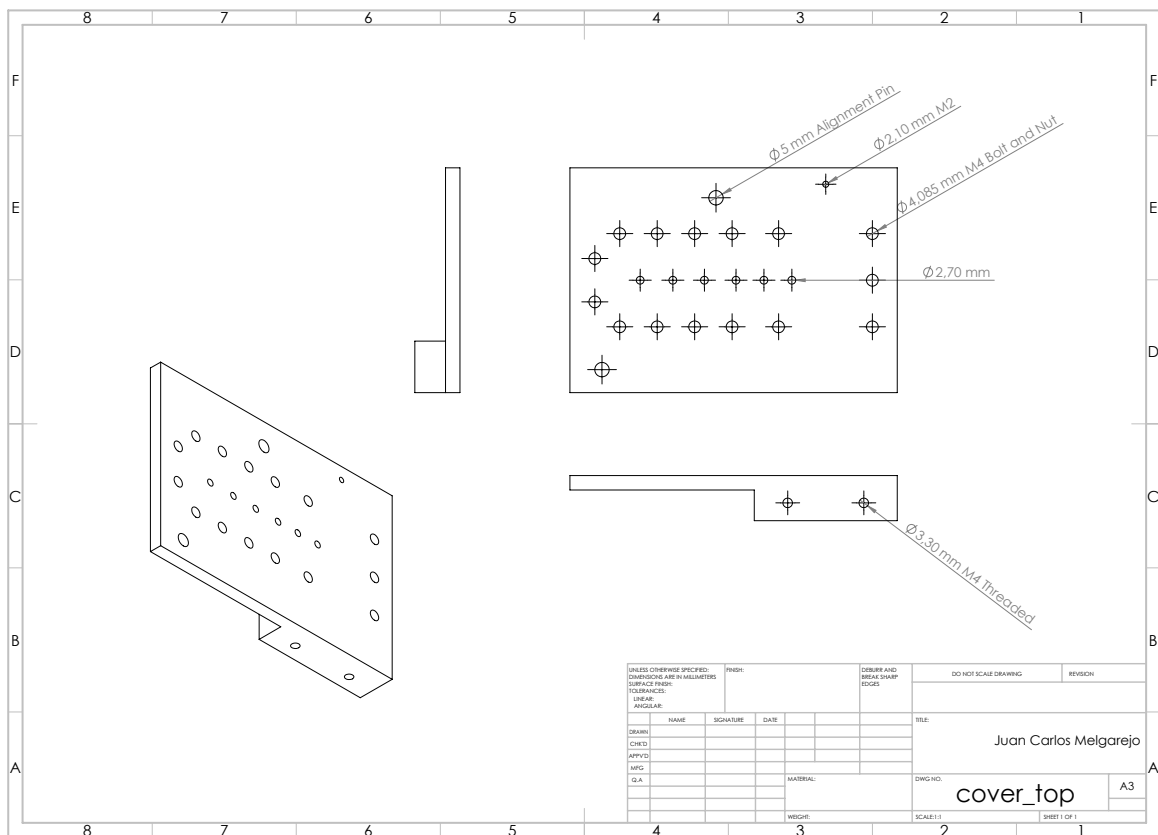


Figure A.16: Drawing for the top cover.

Appendix B

Publications

The main and novel results of this doctoral thesis have resulted in a total number of four scientific publications, which are distributed into two journal papers and two contributions to international conferences. There are also two articles that are currently awaiting review.

B.1 Journal publications

- J. C. Melgarejo, J. Ossorio, S. Cogollos, M. Guglielmi, V. E. Boria and J. W. Bandler, "On space mapping techniques for microwave filter tuning," in *IEEE Transactions on Microwave Theory and Techniques*, vol. 67, no. 12, pp. 4860-4870, Dec. 2019.
- J. C. Melgarejo, S. Cogollos, M. Guglielmi and V. E. Boria, "A New Family of Multiband Waveguide Filters Based on a Folded Topology," in *IEEE Transactions on Microwave Theory and Techniques*, vol. 68, no. 7, pp. 2590-2600, July 2020.

B.2 Conference publications

- J.C. Melgarejo, M. Guglielmi, S. Cogollos and V. Boria, "An efficient microwave filter design procedure based on space mapping", in *2020 50th European Microwave Conference (EuMC)*, Jan. 2021, pp. 743-746.
- J. C. Melgarejo, M. Guglielmi, S. Cogollos and V. E. Boria, "Space mapping for tuning microwave waveguide filters," in *2019 IEEE MTT-S International Microwave Symposium Digest*, Boston, MA, USA, 2019, pp. 353-356.

Bibliography

- [1] J. W. Bandler, R. M. Biernacki, Shao Hua Chen, P. A. Grobelny, and R. H. Hemmers, “Space mapping technique for electromagnetic optimization,” *IEEE Transactions on Microwave Theory and Techniques*, vol. 42, no. 12, pp. 2536–2544, Dec. 1994.
- [2] E. S. A. (ESA), *Strategic Research Agenda*. European Space Technology Platform, July 2011.
- [3] J. R. M. Vaughan, “Multipactor,” *IEEE Transactions on Electron Devices*, vol. 35, no. 7, pp. 1172–1180, July 1988.
- [4] V. E. Semenov, E. I. Rakova, I. M. Nefedov, I. A. Shereshevski, N. K. Vdovicheva, R. Udiljak, D. Anderson, M. Lisak, and J. Puech, “Multipactor breakdown in waveguide irises,” in *2009 IEEE International Vacuum Electronics Conference*, April 2009, pp. 321–322.
- [5] J. W. Bandler, R. M. Biernacki, Shao Hua Chen, R. H. Hemmers, and K. Madsen, “Electromagnetic optimization exploiting aggressive space mapping,” *IEEE Transactions on Microwave Theory and Techniques*, vol. 43, no. 12, pp. 2874–2882, Dec. 1995.
- [6] J. C. Melgarejo, M. Guglielmi, S. Cogollos, and V. E. Boria, “An efficient microwave filter design procedure based on space mapping,” in *2020 50th European Microwave Conference (EuMC)*, Jan. 2021, pp. 743–746.
- [7] J. C. Melgarejo, M. Guglielmi, S. Cogollos, and V. E. Boria, “Space mapping for tuning microwave waveguide filters,” in *2019 IEEE MTT-S International Microwave Symposium Digest*, June 2019, pp. 353–356.

- [8] J. C. Melgarejo, J. Ossorio, S. Cogollos, M. Guglielmi, V. E. Boria, and J. W. Bandler, “On space mapping techniques for microwave filter tuning,” *IEEE Transactions on Microwave Theory and Techniques*, vol. 67, no. 12, pp. 4860–4870, Oct. 2019.
- [9] R. J. Cameron and M. Yu, “Design of manifold-coupled multiplexers,” *IEEE Microwave Magazine*, vol. 8, no. 5, pp. 46–59, Oct. 2007.
- [10] J. C. Melgarejo, S. Cogollos, M. Guglielmi, and V. E. Boria, “A new family of multi-band waveguide filters based on a folded topology,” *IEEE Transactions on Microwave Theory and Techniques*, vol. 68, no. 7, pp. 2590–2600, May 2020.
- [11] J. Ossorio, J. C. Melgarejo, V. E. Boria, and M. Guglielmi, “On the integration of microwave filters and waveguide switches,” *IEEE Microwave and Wireless Components Letters*, vol. 31, no. 3, pp. 265–268, March 2021.
- [12] R. Cameron, R. Mansour, and C. Kudsia, *Microwave Filters for Communication Systems: Fundamentals, Design and Applications*. Wiley, 2007.
- [13] S. Cogollos, *Fundamentos de la Teoría de Filtros*. Universitat Politècnica de València, 2016.
- [14] V. Belevitch, “Chebyshev filters and amplifier networks,” *Wireless Engineer*, vol. 29, pp. 106–110, Apr. 1952.
- [15] G. Matthaei, L. Young, and E. Jones, *Microwave Filters, Impedance-matching Networks, and Coupling Structures*. Artech House Books, 1980.
- [16] M. Guglielmi, R. Sorrentino, and G. Conciauro, *Advanced Modal Analysis: CAD Techniques for Waveguide Components and Filter*, 1st ed. John Wiley & Sons, Inc., 1999.
- [17] M. Guglielmi and A. A. Melcon, “Novel design procedure for microwave filters,” in *1993 23rd European Microwave Conference (EuMC)*, Sept. 1993, pp. 212–213.
- [18] W. Banzhaf, P. Nordin, R. Keller, and F. Francone, *Genetic Programming - An Introduction*. Morgan Kaufmann, 1998.
- [19] G. Madey, X. Xiang, S. E. Cabaniss, and Y. Huang, “Agent-based scientific simulation,” *Computing in Science and Engineering*, vol. 2, no. 01, pp. 22–29, Jan. 2005.
- [20] X.-S. Yang, *Nature-Inspired Optimization Algorithms*. Academic Press, Sept. 2020.

-
- [21] M. Bakr, J. Bandler, K. Madsen, and J. Søndergaard, "Review of the space mapping approach to engineering optimization and modeling," *Optimization and Engineering*, vol. 1, pp. 241–276, Aug. 2000.
- [22] J. W. Bandler, R. M. Biernacki, S. H. Chen, R. H. Hemmers, and K. Madsen, "Aggressive space mapping for electromagnetic design," in *1995 IEEE MTT-S International Microwave Symposium Digest*, vol. 3, May 1995, pp. 1455–1458.
- [23] C. G. Broyden, "A class of methods for solving nonlinear simultaneous equations," *Mathematics of Computation*, vol. 19, no. 92, pp. 577–593, Oct. 1965.
- [24] J. W. Bandler, R. M. Biernacki, S. H. Chen, and D. Omeragic, "Space mapping optimization of waveguide filters using finite element and mode-matching electromagnetic simulators," in *1997 IEEE MTT-S International Microwave Symposium Digest*, vol. 2, June 1997, pp. 635–638.
- [25] E. Diaz Caballero, J. Morro, A. Belenguer, H. Esteban, and V. Boria, "CAD technique for designing H-plane waveguide filters considering rounded corners," in *2013 IEEE MTT-S International Microwave Symposium Digest*, Jan. 2013, pp. 1–3.
- [26] M. A. Ismail, D. Smith, A. Panariello, Y. Wang, and M. Yu, "EM based design of large-scale dielectric resonator multiplexers by space mapping," in *2003 IEEE MTT-S International Microwave Symposium Digest*, vol. 1, Jan. 2003, pp. 291–294.
- [27] M. Brumos, V. E. Boria, M. Guglielmi, and S. Cogollos, "Correction of manufacturing deviations in circular-waveguide dual-mode filters using aggressive space mapping," in *2014 44th European Microwave Conference (EuMC)*, Oct. 2014, pp. 624–627.
- [28] S. Cogollos, C. Carceller, M. Taroncher, V. Boria, M. Guglielmi, C. Vicente, and M. Brumos, "Correction of manufacturing deviations in waveguide filters and manifold multiplexers using metal insertions," *International Journal of Microwave and Wireless Technologies*, vol. 7, no. 3-4, pp. 219–227, 2015.
- [29] J. W. Bandler, Q. S. Cheng, S. A. Dakroury, A. S. Mohamed, M. H. Bakr, K. Madsen, and J. Søndergaard, "Space mapping: the state of the art," *IEEE Transactions on Microwave Theory and Techniques*, vol. 52, no. 1, pp. 337–361, Sept. 2004.
- [30] J. E. Rayas-Sanchez, "Power in simplicity with ASM: Tracing the aggressive space mapping algorithm over two decades of development and engineering applications," *IEEE Microwave Magazine*, vol. 17, no. 4, pp. 64–76, Apr. 2016.

- [31] R. Lehmensiek and P. Meyer, “An efficient adaptive frequency sampling algorithm for model-based parameter estimation as applied to aggressive space mapping,” *Microwave and Optical Technology Letters*, pp. 71–78, Jan. 2000.
- [32] M. A. Ismail, K. G. Engel, and Ming Yu, “Multiple space mapping for RF T-switch design,” in *2004 IEEE MTT-S International Microwave Symposium Digest*, vol. 3, June 2004, pp. 1569–1572.
- [33] J. V. Morro, P. Soto, H. Esteban, V. E. Boria, C. Bachiller, M. Taroncher, S. Cogollos, and B. Gimeno, “Fast automated design of waveguide filters using aggressive space mapping with a new segmentation strategy and a hybrid optimization algorithm,” *IEEE Transactions on Microwave Theory and Techniques*, vol. 53, no. 4, pp. 1130–1142, Apr. 2005.
- [34] J. Ossorio, J. Vague, V. E. Boria, and M. Guglielmi, “Efficient implementation of the aggressive space mapping technique for microwave filter design,” in *2017 47th European Microwave Conference (EuMC)*, Dec. 2017, pp. 644–647.
- [35] J. Ossorio, J. C. Melgarejo, V. E. Boria, M. Guglielmi, and J. W. Bandler, “On the alignment of low-fidelity and high-fidelity simulation spaces for the design of microwave waveguide filters,” *IEEE Transactions on Microwave Theory and Techniques*, vol. 66, no. 12, pp. 5183–5196, Dec. 2018.
- [36] J. B. Ness and V. A. Lenivenko, “Design and manufacture of exact waveguide filters,” in *2000 Asia-Pacific Microwave Conference Proceedings*, Dec. 2000, pp. 507–511.
- [37] V. Boria, M. Guglielmi, and P. Arcioni, “Accurate CAD for dual mode filters in circular waveguide including tuning elements,” in *1997 IEEE MTT-S International Microwave Symposium Digest*, vol. 3, Aug. 1997, pp. 1575–1578.
- [38] R. V. Snyder, “Practical aspects of microwave filter development,” *IEEE Microwave Magazine*, vol. 8, no. 2, pp. 42–54, May 2007.
- [39] A. Lindner and E. Biebl, “A manual tuning method for coupled cavity filters,” in *2006 European Microwave Conference (EuMC)*, 2006, pp. 1340–1342.
- [40] A. Lindner, H. Kugler, and E. Biebl, “Manual filter tuning by cloning frequency domain data,” in *2007 37th European Microwave Conference (EuMC)*, Dec. 2007, pp. 329–331.
- [41] V. Miraftab and R. R. Mansour, “Computer-aided tuning of microwave filters using fuzzy logic,” in *2002 IEEE MTT-S International Microwave Symposium Digest*, vol. 2, June 2002, pp. 1117–1120.

-
- [42] V. Miraftab and R. R. Mansour, “Automated microwave filter tuning by extracting human experience in terms of linguistic rules using fuzzy controllers,” in *2006 IEEE MTT-S International Microwave Symposium Digest*, June 2006, pp. 1439–1442.
- [43] V. Miraftab and R. R. Mansour, “Tuning of microwave filters by extracting human experience using fuzzy logic,” in *2005 IEEE MTT-S International Microwave Symposium Digest*, June 2005, pp. 1605–1608.
- [44] A. R. Mirzai, C. F. N. Cowan, and T. M. Crawford, “Intelligent alignment of waveguide filters using a machine learning approach,” *IEEE Transactions on Microwave Theory and Techniques*, vol. 37, no. 1, pp. 166–173, Jan. 1989.
- [45] J. Zhou and J. Huang, “Intelligent tuning for microwave filters based on multi-kernel machine learning model,” in *2013 IEEE International Symposium on Microwave, Antenna, Propagation and EMC Technologies for Wireless Communications*, Dec. 2013, pp. 259–266.
- [46] J. Zhou, B. Duan, and J. Huang, “Influence and tuning of tunable screws for microwave filters using least squares support vector regression,” *International Journal of RF and Microwave Computer-Aided Engineering*, pp. 422 – 429, July 2010.
- [47] J. Zhou, B. Duan, and J. Huang, “Support-vector modeling of electromechanical coupling for microwave filter tuning,” *International Journal of RF and Microwave Computer-Aided Engineering*, vol. 23, Jan. 2013.
- [48] L. Accatino, “Computer-aided tuning of microwave filters,” in *1986 IEEE MTT-S International Microwave Symposium Digest*, June 1986, pp. 249–252.
- [49] L. Bi, W. Cao, W. Hu, and M. Wu, “Intelligent tuning of microwave cavity filters using granular multi-swarm particle swarm optimization,” *IEEE Transactions on Industrial Electronics*, pp. 1–10, Dec. 2020.
- [50] S. Li and P. D. Laforge, “A post-fabrication tuning method for a varactor-tuned microstrip filter using the implicit space mapping technique,” in *2015 IEEE MTT-S International Microwave Symposium Digest*, June 2015, pp. 1–4.
- [51] A. Rodriguez, J. V. Morro, J. Selga, M. Sans, J. Ossorio, M. Guglielmi, F. Martín, and V. E. Boria, “Robust optimization and tuning of microwave filters and artificial transmission lines using aggressive space mapping techniques,” in *2017 IEEE MTT-S International Microwave Symposium Digest*, June 2017, pp. 1501–1504.
- [52] S. Holme, “Multiple passband filters for satellite applications,” in *20th AIAA International Communication Satellite Systems Conference and Exhibit*, May 2002.

- [53] M. Uhm, K. Ahn, I. Yom, and J. Kim, "A triple-passband waveguide filter with dual-mode resonators for Ka band satellite applications," in *24th AIAA International Communications Satellite Systems Conference*, June 2006.
- [54] L. Zhu, R. R. Mansour, and M. Yu, "Triple-band cavity bandpass filters," *IEEE Transactions on Microwave Theory and Techniques*, vol. 66, no. 9, pp. 4057–4069, Sept. 2018.
- [55] L. Tsai and C. Hsue, "Dual-band bandpass filters using equal-length coupled-serial-shunted lines and Z-transform technique," *IEEE Transactions on Microwave Theory and Techniques*, vol. 52, no. 4, pp. 1111–1117, Apr. 2004.
- [56] G. Macchiarella and S. Tamiazzo, "Design techniques for dual-passband filters," *IEEE Transactions on Microwave Theory and Techniques*, vol. 53, no. 11, pp. 3265–3271, Nov. 2005.
- [57] M. Mokhtaari, J. Bornemann, K. Rambabu, and S. Amari, "Coupling-matrix design of dual and triple passband filters," *IEEE Transactions on Microwave Theory and Techniques*, vol. 54, no. 11, pp. 3940–3946, Nov. 2006.
- [58] S. Bila, R. J. Cameron, P. Lenoir, V. Lunot, and F. Seyfert, "Chebyshev synthesis for multi-band microwave filters," in *2006 IEEE MTT-S International Microwave Symposium Digest*, June 2006, pp. 1221–1224.
- [59] L. Zhu, R. R. Mansour, and M. Yu, "Triple-band dielectric resonator bandpass filters," in *2017 IEEE MTT-S International Microwave Symposium Digest*, June 2017, pp. 745–747.
- [60] J. A. Ruiz-Cruz, M. M. Fahmi, and R. R. Mansour, "Dual-resonance combline resonator for dual-band filters," in *2012 IEEE MTT-S International Microwave Symposium Digest*, June 2012, pp. 1–3.
- [61] J. A. Ruiz-Cruz, M. M. Fahmi, and R. R. Mansour, "Triple-conductor combline resonators for dual-band filters with enhanced guard-band selectivity," *IEEE Transactions on Microwave Theory and Techniques*, vol. 60, no. 12, pp. 3969–3979, Dec. 2012.
- [62] S. Amari and M. Bekheit, "A new class of dual-mode dual-band waveguide filters," *IEEE Transactions on Microwave Theory and Techniques*, vol. 56, no. 8, pp. 1938–1944, Aug. 2008.

-
- [63] L. Zhu, R. R. Mansour, and M. Yu, "Compact waveguide dual-band filters and diplexers," *IEEE Transactions on Microwave Theory and Techniques*, vol. 65, no. 5, pp. 1525–1533, May 2017.
- [64] L. Zhu, R. R. Mansour, and M. Yu, "A compact waveguide quasi-elliptic dual-band filter," in *2019 IEEE MTT-S International Microwave Symposium Digest*, June 2019, pp. 1179–1182.
- [65] R. R. Mansour and P. D. Laforge, "Multiband superconducting filters," in *2016 IEEE MTT-S International Microwave Symposium Digest*, June 2016, pp. 1–4.
- [66] S. Cogollos, P. Micó, J. Vague, V. E. Boria, and M. Guglielmi, "New design methodology for multiband waveguide filters based on multiplexing techniques," in *2017 IEEE MTT-S International Microwave Symposium Digest*, June 2017, pp. 741–744.
- [67] U. Rosenberg, R. Beyer, P. Krauß, T. Sieverding, P. M. Iglesias, and C. Ernst, "Remote controlled high-Q cavity filters providing center frequency and bandwidth re-allocation," in *2017 IEEE MTT-S International Microwave Workshop Series on Advanced Materials and Processes for RF and THz Applications*, Sept. 2017, pp. 1–3.
- [68] U. Rosenberg, R. Beyer, P. Krauß, T. Sieverding, A. Papanastasiou, M. Pueyo-Tolosa, P. M. Iglesias, and C. Ernst, "Reconfigurable doublet dual-mode cavity filter designs providing remote controlled center frequency and bandwidth re-allocation," in *2016 46th European Microwave Conference (EuMC)*, Oct. 2016, pp. 532–535.
- [69] U. Rosenberg, R. Beyer, P. Krauß, T. Sieverding, P. M. Iglesias, and C. Ernst, "Omux approach providing re-configuration of contiguous/non-contiguous channel allocations with variable frequencies and bandwidths," in *2016 46th European Microwave Conference (EuMC)*, Oct. 2016, pp. 536–539.
- [70] J. Ossorio, J. Vague, V. E. Boria, and M. Guglielmi, "Exploring the tuning range of channel filters for satellite applications using electromagnetic-based computer aided design tools," *IEEE Transactions on Microwave Theory and Techniques*, vol. 66, no. 2, pp. 717–725, Nov. 2018.
- [71] J. Ossorio, V. E. Boria, and M. Guglielmi, "Dielectric tuning screws for microwave filters applications," in *2018 IEEE MTT-S International Microwave Symposium Digest*, June 2018, pp. 1253–1256.
- [72] C. Arnold, J. Parlebas, and T. Zwick, "Reconfigurable waveguide filter with variable bandwidth and center frequency," *IEEE Transactions on Microwave Theory and Techniques*, vol. 62, no. 8, pp. 1663–1670, July 2014.

- [73] C. Arnold, J. Parlebas, R. Meiser, and T. Zwick, "Fully reconfigurable manifold multiplexer," *IEEE Transactions on Microwave Theory and Techniques*, vol. 65, no. 10, pp. 3885–3891, Apr. 2017.
- [74] E. Laplanche, N. Delhote, A. Périgaud, O. Tantot, S. Verdeyme, S. Bila, D. Pacaud, and L. Carpentier, "Tunable filtering devices in satellite payloads: A review of recent advanced fabrication technologies and designs of tunable cavity filters and multiplexers using mechanical actuation," *IEEE Microwave Magazine*, vol. 21, no. 3, pp. 69–83, Feb. 2020.
- [75] COMDEV, *COMDEV Space Group*. Canada: Cambridge, 2010.
- [76] M. Daneshmand and R. R. Mansour, "RF MEMS satellite switch matrices," *IEEE Microwave Magazine*, vol. 12, no. 5, pp. 92–109, July 2011.
- [77] L. Pelliccia, F. Cacciamani, R. Sorrentino, P. Farinelli, P. Ligander, and O. Persson, "High-Q MEMS-tunable waveguide filters in K-band," in *2012 42nd European Microwave Conference (EuMC)*, Nov. 2012, pp. 273–276.
- [78] F. Gentili, L. Urbani, G. Bianchi, L. Pelliccia, and R. Sorrentino, "p-i-n-Diode-based four-channel switched filter bank with low-power TTL-compatible driver," *IEEE Transactions on Microwave Theory and Techniques*, vol. 62, no. 12, pp. 3333–3340, Oct. 2014.
- [79] J. W. Bandler, Q. S. Cheng, S. A. Dakrouy, A. S. Mohamed, M. H. Bakr, K. Madsen, and J. Sondergaard, "Space mapping: the state of the art," *IEEE Transactions on Microwave Theory and Techniques*, vol. 52, no. 1, pp. 337–361, Jan 2004.
- [80] G. Crevecoeur, L. Dupré, L. Vandebossche, and R. Van de Walle, "Reconstruction of local magnetic properties of steel sheets by needle probe methods using space mapping techniques," *Journal of Applied Physics*, vol. 99, Apr. 2006.
- [81] J. Wu, Y. Dong, J. He, and J. Deng, "An ameliorated aggressive space mapping based on responses error," in *2012 International Workshop on Microwave and Millimeter Wave Circuits and System Technology*, Apr. 2012, pp. 1–4.
- [82] J. Xu, X. Luo, L. zu Cao, and R. shan Chen, "Optimization of coaxial dielectric resonator filter with aggressive space mapping," in *2012 Asia Pacific Microwave Conference Proceedings*, Dec. 2012, pp. 229–231.
- [83] A. Cunliffe and L. E. S. Mathias, "Some perturbation effects in cavity resonators," *Journal of the Institution of Electrical Engineers*, vol. 1950, no. 10, Oct. 1950.

- [84] J. Ossorio, J. C. M. Lermas, S. Cogollos, V. E. Boria, and M. Guglielmi, “Waveguide quadruplet diplexer for multi-beam satellite applications,” *IEEE Access*, vol. 8, pp. 110 116–110 128, June 2020.
- [85] A. San-Blas, M. Guglielmi, J. C. Melgarejo, A. Coves, and V. E. Boria, “Design procedure for bandpass filters based on integrated coaxial and rectangular waveguide resonators,” *IEEE Transactions on Microwave Theory and Techniques*, vol. 68, no. 10, pp. 4390–4404, Aug. 2020.
- [86] S. Li, X. Fan, P. D. Laforge, and S. C. Qingsha, “Space mapping post-fabrication tuning of 3d printed air-filled waveguide filter,” in *2017 IEEE MTT-S International Microwave Symposium Digest*, June 2017, pp. 1635–1637.
- [87] J. B. Thomas, “Cross-coupling in coaxial cavity filters - a tutorial overview,” *IEEE Transactions on Microwave Theory and Techniques*, vol. 51, no. 4, pp. 1368–1376, Apr. 2003.
- [88] M. Daneshmand, R. R. Mansour, and N. Sarkar, “RF MEMS waveguide switch,” *IEEE Transactions on Microwave Theory and Techniques*, vol. 52, no. 12, pp. 2651–2657, July 2004.
- [89] J. A. Ruiz-Cruz, M. M. Fahmi, and R. R. Mansour, “Compact four-port rectangular waveguide switches based on simple short circuit loads,” in *2011 IEEE MTT-S International Microwave Symposium Digest*, June 2011, pp. 1–4.
- [90] J. A. Ruiz-Cruz, M. M. Fahmi, and R. R. Mansour, “Single-pole six-throw waveguide switch embedded in a seven port loaded junction,” in *2013 IEEE MTT-S International Microwave Symposium Digest*, Jan. 2013, pp. 1–4.
- [91] J. A. Ruiz-Cruz, M. M. Fahmi, and R. R. Mansour, “Single-pole multiple-throw waveguide switch for twelve output ports (sp12t),” in *2014 44th European Microwave Conference (EuMC)*, Dec. 2014, pp. 468–471.